Seismic structure beneath the Central Andes revealed by full waveform inversion

Yajian Gao

GFZ Helmholtz Centre Potsdam

Dissertation

zur Erlangung des akademischen Grades

Doktor der Naturwissenschaften (Dr. rer. nat.)

Freie Universität Berlin

vorgelegt im Fachbereich Geowissenschaften

Freie Universität Berlin

Berlin, 2021

Dissertation eingereicht am: 10. Dezember 2021
Disputation am: 11. März 2022

Prüfungskommission:
Prof. Dr. Eline Le Breton (Vorsitz)
Prof. Dr. Serge Shapiro
Prof. Dr. Frederik Tilmann
Prof. Dr. Andreas Fichtner
Dr. Stine Gutjahr

Erstgutachter: Prof. Dr. Frederik Tilmann (FU Berlin und GFZ, Potsdam, Germany)

Zweitgutachter: Prof. Dr. Andreas Fichtner (ETH, Zürich, Switzerland)

To my parents for their understanding and support, to my grandfather who loved me but passed away unfortunately after I reached Germany.

Zusammenfassung

Der westliche Rand des südamerikanischen Kontinents ist eine aktive Subduktionszone, die als Prototyp für die Subduktionszonen des 'Anden-Typs' bekannt ist. Die Anden erstrecken sich über mehr als 6000 km entlang des Kontinentalrandes. Die vorherrschenden tektonischen Prozesse in den Zentralanden sind die Verformung des Hochplateaus sowie die Subduktion der Nazca-Platte unter Chile und Westargentinien, welche zu einer starken Verkürzung und Verdickung der Kruste sowie zu Magmatismus und wiederkehrender Delamination der unteren Kruste und des lithosphärischen Mantels im Back-Arc Bereichs geführt haben. Die Art der krustalen und lithosphärischen Verformung wird auch durch den Neigungswinkel der abtauchenden Nazca-Platte beeinflusst. Die Wechselwirkungsmechanismen zwischen der Kontinentalen Platte und der abtauchenden Nazca-Platte sind jedoch noch immer nicht im Detail verstanden. In meiner Dissertation verwende ich die Methode der Multi-Scale Full Waveform Inversion (FWI), um die Kruste und die Struktur des oberen Mantels mit Hilfe von seismischen Wellen abzubilden. Ziel ist es, die Wechselwirkungen zwischen der Platte und dem zentralen Andenplateau abzubilden.

In der ersten Studie habe ich FWI auf die Wellenformdaten von 117 Erdbeben angewendet, welche zunächst im langperiodischen (40–80 s) Bereich über mehrere Iterationen bis hinunter zum Periodenbereich von 12–60 s invertiert wurden. Ziel war es, die seismische Struktur der nördlichen Zentralanden, welche die Subduktionszone mit normaler Neigung von Südperu bis Zentralchile abdecken, abzubilden. Die subduzierte Nazca-Platte wurde im oberen Mantel deutlich abgebildet und weist Variationen des Neigungswinkels von Norden nach Süden auf. Bänder niedriger Geschwindigkeiten, die in der Kruste und im Bereich des Mantelkeils abgebildet wurden, weisen auf ein intensives partielles Schmelzen der Kruste bzw. Hydrierung des Mantelkeils unter dem vorderen Vulkanbogen hin. Sie stehen auch im Zusammenhang mit der starken Dehydrierung der subduzierenden Nazca-Platte und der darin verorteten Erdbeben mittlerer Tiefe. Diese Bänder mit niedriger seismischer Geschwindigkeit werden bei Breitengraden von 19.8°-21°S sowohl in der Kruste als auch im obersten Mantel unterbrochen. Zusammen mit der Abwesenheit von aktiven Vulkanen in diesem Bereich deutet dies auf ein geringeres Ausmaß, sowohl des Krustenschmelzens, als auch der Hydrierung des Mantelkeils hin, welche mit einer schwachen Dehydrierung der Nazca-Platte einhergeht. Die Variation in der von Nord nach Süd verlaufenden lithosphärischer Hochgeschwindigkeitsanomalie unterhalb des Back-Arcs ermöglicht einen Einblick in die Entwichlung der Zentralanden. Eine ausgedehnte Hochgeschwindigkeitsschicht in Lithosphärentiefen unter dem südlichen Altiplano deutet darauf hin, dass, gefolgt von der Delamination der autochthonen Lithosphäre, eine Unterschiebung des Brasilianischen Schildes stattgefunden hat. Im Gegensatz dazu weisen ein steil nach Westen abfallender Hochgeschwindigkeitsblock und niedrige Geschwindigkeiten im lithosphärischen Mantel unter dem südlichen Puna-Plateau auf den anhaltenden lithosphärischen Delaminationsprozess hin.

In einer zweiten Studie habe ich Daten von 134 Erdbeben zur Durchführung von FWI genutzt und bin dabei von Daten mit noch längerer Periode (60-120 s) bis 12-100 s ausgegangen. In dieser Studie wird ein neues seismisches Geschwindigkeitsmodell für die südlichen Zentralanden abgeleitet, das die flachen Pampean- und die angrenzenden steilen Payenia-Subduktionssegmente abdeckt. Starke fokussierte Niedriggeschwindigkeitsanomalien in der Kruste deuten auf partielle Schmelzen im

Payenia-Segment entlang des Vulkanbogens hin, während schwächere Niedriggeschwindigkeitsanomalien, welche eine breite Zone innerhalb des Pampean-Segments abdecken, möglicherweise auf Restschmelzen in der Vergangenheit hinweisen. Das Ausdünnen und Zerreißen der flachen Nazca-Platte unterhalb des Pampean-Segments wird durch Lücken in der Hochgeschwindigkeitszone entlang der Inlandsprojektion des Juan-Fernandez-Rückens abgeleitet. Eine Hochgeschwindigkeitsanomalie im oberen Mantel unterhalb der mit flachem Winkel subduzierenden Platte wird als ein Relikt der Nazca-Platte interpretiert, was auf einen früheren Plattenabbruch während des Abflachungsprozesses hinweist, der durch den Auftrieb des Juan-Fernandez-Rückens ausgelöst wurde. Im Payenia-Segment werden großräumige Niedriggeschwindigkeitsanomalien über und unter der wieder steil subduzierenden Nazca-Platte mit der Öffnung des Mantelkeils und dem asthenosphärischen Fluss unter der Platte in Verbindung gebracht.

Summary

The current western margin of the South American continent is an active subduction orogeny, which is famous for the 'Andean-type' subduction. The Andes orogeny extends more than 6000 km along the margin. The Central Andes is governed by plateau-style deformation and the subduction of the Nazca plate below Chile and western Argentina, which has caused drastic crustal shortening and thickening, magmatism and periodical back-arc lithosphere and lower crust delamination. The deformation is also influenced by the periodical dip angle variations of the Nazca plate. However, the interaction zone between the overriding plate and the subducting Nazca slab is still enigmatic. In my dissertation, I use earthquake multi-scale full waveform inversion (FWI) to image the crust and upper mantle structure providing new robust images to resolve the interactions between the slab and the Central Andean plateau.

First, I performed FWI using 117 earthquakes to investigate the seismic structure for the northern Central Andes which cover the normal-dip subduction zone from southern Peru to central Chile, proceeding from long period data (40–80 s) over several steps down to 12–60 s. In this study, the subducting Nazca slab is clearly imaged in the upper mantle, with dip-angle variations from the north to the south. Bands of low velocities in the crust and mantle wedge indicate intense crustal partial melting and hydration of the mantle wedge beneath the frontal volcanic arc, respectively. They are also linked to the vigorous dehydration from the subducting Nazca plate and intermediate-depth seismicity within the slab. These low-velocity bands are interrupted at 19.8°–21° S, both in the crust and uppermost mantle with an absence of active volcanoes, hinting at the lower extent of crustal partial melting and hydration of the mantle wedge, associated with the weak dehydration from the Nazca plate. The variation of lithospheric high-velocity anomalies below the backarc from north to south allows insight into the evolutionary foundering stages of the Central Andes. An extended high-velocity layer at lithospheric depths beneath the southern Altiplano suggests underthrusting of the leading edge of the Brazilian Shield following the removal of the autochthonous lithosphere. In contrast, a steeply westward dipping high-velocity block and low-velocity lithospheric uppermost mantle beneath the southern Puna plateau hints at the ongoing lithospheric delamination.

Second, I took advantage of 134 events to perform FWI and started from even longer period data 60-120 s to 12-100 s. In this study, a new seismic velocity model for the southern Central Andes is derived, covering the Pampean flat and adjacent Payenia steep subduction segments. Strong focused crustal low-velocity anomalies indicate partial melts in the Payenia segment along the volcanic arc, whereas weaker low-velocity anomalies covering a wide zone in Pampean possibly indicate remnant melts in the past. Thinning and tearing of the flat Nazca slab below the Pampean is inferred by gaps in the high-velocity slab along the inland projection of the Juan-Fernandez-Ridge. A high-velocity anomaly in the upper mantle below the flat slab is interpreted as a relic Nazca slab segment, which indicates an earlier slab break-off during the flattening process, triggered by the buoyancy of the Juan-Fernandez-Ridge. In Payenia, large-scale low-velocity anomalies atop and below the re-steepened Nazca slab are associated with the re-opening of the mantle wedge and sub-slab asthenospheric flow, respectively.

Declaration

Hiermit versichere ich, dass ich die vorliegende Dissertation ohne unzulässige Hilfe Dritter und ohne Benutzung anderer als der angegebenen Literatur angefertigt wurde. Die Stellen der Arbeit, die anderen Werken wörtlich oder inhaltlich entnommen sind, wurden durch entsprechende Angaben der Quellen kenntlich gemacht. Diese Arbeit hat in gleicher oder ähnlicher Form noch keiner Prüfungsbehörde vorgelegen.

I hereby declare that except where specific reference is made to the work of others, the contents of this dissertation are original and have not been submitted in whole or in part for consideration for any other degree or qualification in this, or any other university. This dissertation is my own work and contains nothing which is the outcome of work done in collaboration with others, except as declared specified in the text.

Yajian Gao

Potsdam, 1st Dec. 2021

Contents

Chapter 1

Introduction

1.1 Motivation

The current western margin of the South American continent is an active subduction orogeny, the Andes, extending for more than 6000 km. The Central Andes (Figure 1.1) is governed by plateau-style deformation and the subduction of the Nazca plate along the Central Andes has resulted in drastic crustal shortening (Oncken et al., 2006), thickening (Yuan et al., 2000; Heit et al., 2007a, 2008a), magmatism (Wörner et al., 1992; Kay et al., 1994; Wörner et al., 2000; Kay & Mpodozis, 2002; Kay & Coira, 2009) and lithospheric delamination (Kay & Kay, 1993; Whitman et al., 1996; Allmendinger et al., 1997; Beck & Zandt, 2002; Schurr et al., 2006; Bianchi et al., 2013; Beck et al., 2015; Scire et al., 2015a; Garzione et al., 2017; Chen et al., 2020). The age of the subducting Nazca plate is ∼45–50 Ma at the trench (Müller et al., 2008) as it enters the subduction zone with a convergence rate of 61–65 mm/yr (Norabuena et al., 1999; Angermann et al., 1999) beneath northern Chile. The subduction of the Nazca plate initiated around 70-80 Ma and it is thought to have reached the lower mantle beneath the Central Andes ∼50 Ma ago, according to a recent plate reconstruction based on slab unfolding scheme (Chen et al., 2019). The widest part of the Central Andean orogen is between 15° and 27°S, where the subduction angle is 20°-30°, flanked southwards and northwards by the flat subduction segments, where the subducted Nazca plate flattens out to become nearly horizontal, in the Peru and Pampean flat subduction segments, respectively. Further south is the Payenia segment (34° S - 37°S), the subduction has been dominated by current steep subduction since 5-4 Ma (Kay & Mpodozis, 2002; Ramos & Folguera, 2009) while it was flat subduction before 5 Ma, which resulted in a complete cycle from crustal thickening and mountain uplift to extensional collapse and normal faulting (Ramos et al., 2014). The large scale dip-angle variations during the last 30 Ma beneath the north and central Chile are thought to be related to the southward migration of the Juan Fernandez Ridge (Gutscher et al., 2000; Kay & Mpodozis, 2002; Ramos & Folguera, 2009; Chen et al., 2019), which is a seamount ridge that originated from the Juan Fernandez Hotspot (Yáñez et al., 2001; Yáñez et al., 2002; Bello-González et al., 2018). The subduction of Juan Fernandez Ridge beneath the South American plate is attributed to be responsible for the periodical flat subduction from the north to south including the historical flat subduction beneath North Chile (15°S to 27°S, 40-12 Ma) and the current Pampean flat subduction. The southward migration of the Juan Fernandez Ridge with flat subduction period is supposed to close the mantle wedge corner and cause the inland migration and even cessation of the volcanic arc (Ramos & Folguera, 2009; Kay & Coira, 2009; Beck et al., 2015).

The interactions of the slab angle variations and the continental lithosphere have been hotly debated for the last decades including the deformation pattern, crustal shortening process and continental lithosphere foundering style. For example, the formation of the current Central Andean Plateau is thought to be linked to lithospheric foundering beneath the Central Andes (Kay & Kay, 1993; Kay et al., 1994; Beck & Zandt, 2002; McQuarrie et al., 2005; Garzione et al., 2006; DeCelles et al., 2015).

Although many researchers agree on the existence of lithospheric foundering in the Central Andes, there remain vigorous debates on its mechanisms, scale, pattern, timing and surface expression.

Meanwhile, more recent geodynamic modeling works indicate the causes of the dip angle variations are far more complicated than the single dominant force originating from the migration of the buoyant oceanic mountain (hotspot) ridges. For the global flat subduction, several factors are attributed to affect the flattening process of the slab: (1) increased buoyancy related to the presence of seamount chains or oceanic plateaus, or simply the young age of the oceanic plate (Yáñez et al., 2001; Gans et al., 2011; Huangfu et al., 2016; Hu et al., 2016; Liu & Currie, 2016); (2) plate suction forces from the overriding plate due to the cold and/or overthickened overriding plate with increased viscosity (Manea et al., 2012; Rodríguez-González et al., 2012; Bishop et al., 2017); (3) movement of the overriding plate towards the trench (trench retreat) will result in significant shallowing of the dip angle if the retreat rate is faster than the sink rate of the slab (Schepers et al., 2017; Manea et al., 2017; Liu & Currie, 2016); (4) mantle convection flow including mantle plumes provides over-pressure below the slab (Boutelier & Cruden, 2008; Rodríguez-González et al., 2014). Thus in order to decipher the key questions involving the interaction of the subducting Nazca slab and continental plate, a robust large-scale high-resolution seismic velocity model covering the whole Central Andes subduction system is the prerequisite. The seismic structure of the crust and upper mantle beneath the whole Central Andes has been investigated by many tomographic studies, including regional body wave tomography (Husen et al., 2000; Schurr & Rietbrock, 2004; Schurr et al., 2006; Koulakov et al., 2006; Comte et al., 2016; Huang et al., 2019), teleseismic tomography (Heit et al., 2008a; Bianchi et al., 2013; Scire et al., 2015a,b, 2017; Portner et al., 2020; Rodríguez et al., 2021) and surface wave and ambient noise tomography (Porter et al., 2012; Calixto et al., 2013; Ward et al., 2013, 2014; Delph et al., 2017; Antonijevic et al., 2016; Ward et al., 2016, 2017). Previous teleseismic and global tomography results revealed a continuous subducted Nazca slab from the uppermost mantle down to the lower mantle (Heit et al., 2008a; Ritsema et al., 2011; Scire et al., 2015a; Lei et al., 2020; Portner et al., 2020; Rodríguez et al., 2021) with a potential slab tear at the southeastern edge of the Pampean flat subduction zone (Portner & Hayes, 2018; Portner et al., 2020). However, teleseismic tomography cannot easily separate anomalies in the crust and uppermost mantle due to smearing along steep ray paths, such that the starting model and crustal corrections can exert a strong influence on the final results in this depth range. In contrast, local and regional earthquake tomography can provide more details for the crust and upper mantle in the selected regions but lacks resolution for the deeper parts. In some of these aforementioned regional tomographic studies, the upper part of the Nazca slab is visible as a relatively continuous high velocity anomaly beneath the Central Andes and various back-arc seismic structures were also imaged (Schurr et al., 2006; Bianchi et al., 2013; Chen et al., 2020). However, these studies were limited to small specific regions according to the footprints of the temporary seismic arrays, typically differing among each other in many methodological details, which makes margin-wide comparisons difficult. For the Pampean flat subduction zone, the flat structure of the Nazca plate beneath the Pampean is difficult to resolve due to the low sensitivity of vertical ray paths from the teleseismic tomography. Thus, the flat portion is demonstrated as low velocity merged with the sub-slab asthenosphere in many teleseismic tomography results.

Thus in order to obtain larger scale models for the study domain covering the interaction zone of the slab and the overriding plate but without losing details in the crust and upper mantle, multi-scale full waveform inversion is adopted to image the seismic structure which fully considers the propagation of the seismic waves within the Earth medium, as a result, body wave and multimode surface waves, frequency dependence, waveform healing, anisotropy and attenuation could be naturally and coherently incorporated. A wealth of information could be extracted through the direct comparison between the observed and accurate synthetic 3-D wavefield. With the developments of high-performance computing, it has now become practical to simulate seismic wave propagation in complex 3-D Earth models using

numerical methods such as Spectral-Element method (e.g. Komatitsch & Tromp, 1999; Afanasiev et al., 2019) or Finite-Difference (e.g. Alterman & Karal, 1968; Zhang et al., 2012b). Most importantly, accurate simulations of seismic wave propagation through laterally heterogeneous models allow the calculation of accurate finite-frequency kernels with the adjoint method (Chen et al., 2007b; Fichtner et al., 2010; Tape et al., 2010). Meanwhile, multi-scale full waveform inversion starts from long period surface wave data and migrates to higher frequency body wave and surface wave trains, which mitigates the risk of convergence to only local minima. Thus multi-scale full waveform inversion scheme is a high-end and suitable technique for imaging tectonic active parts of the earth, like the Central Andes. We collect seismic waveform data from the previous temporary and permanent network stations deployed between 1988 and 2018 and integrate them into two multi-scale three-dimensional full waveform inversion (FWI) (Simutė et al., 2016; Krischer et al., 2018b; Blom et al., 2020) to infer the seismic structure within the crust and upper mantle.

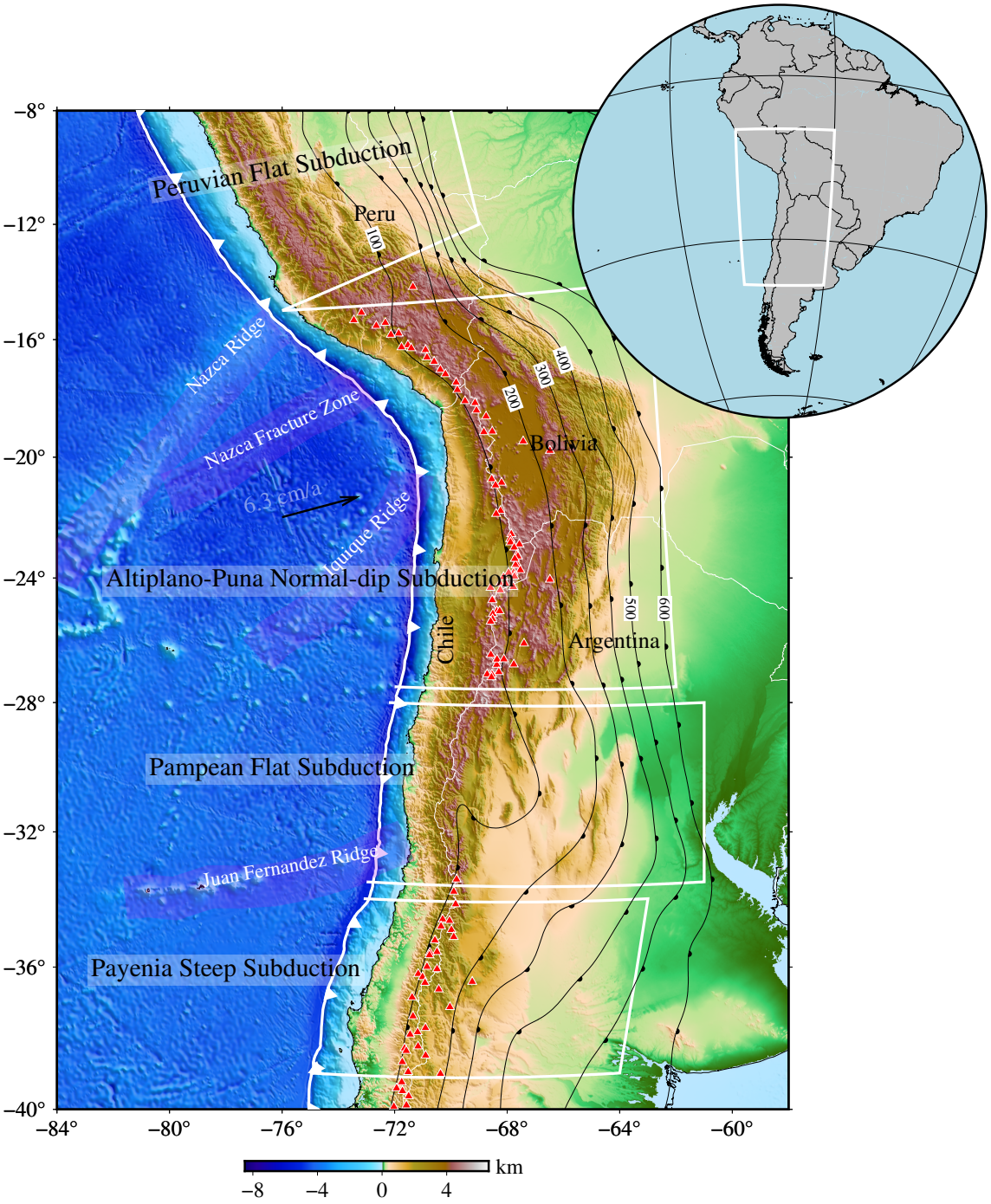

Fig. 1.1: Map of Central Andes. Red triangles denote Holocene volcanoes (retrieved from Global Volcanism Program, Smithsonian Institution, Venzke (2013)). Topography data is extracted from the ETOPO1 Global Relief Model (Amante & Eakins, 2009); the white saw-tooth line denotes the position of the trench. Inset marks the position of our study region in the South America; black lines represent the slab contours, retrieved from the Slab2.0 global subduction zone model (Hayes et al., 2018). Four subduction segments are listed from north to south including Peruvian Flat subduction, Altiplano-Puna Normal-dip subduction, Pampean Flat subduction and Payenia Steep subduction.

1.2 Thesis contributions

The present work in this thesis consists of 6 chapters and two appendices. The main structure of each chapter is described as follows:

Chapter 2 presents the tectonic context including the geological history of the Central Andean Plateau, periodical evolution of the subduction angles of the Nazca Plate and the magmatism evolution.

Initially, I aim to decrypt the present constellation of the subducting Nazca slab with different dip angles beneath the Central Andes to clarify their tectonic affinity and history, including Peruvian flat subduction zone beneath Peru and Bolivia, normal-dip subduction beneath northern Chile and western Argentina, Pampean flat subduction and Payenia dip subduction beneath central-southern Chile.

Chapter 3 presents the numerical modeling methods for seismic wave propagation and adjoint theory with multiple misfit functionals.

In this chapter, I firstly illustrate two popular numerical methods for solutions of the seismic equation including Finite-Difference (FD) and Spectral-Element (SEM). I developed a simple 2D P-SV plane isotropic seismic wave simulation code based on Seismo-live project (Krischer et al., 2018a) to simulate the propagation of high frequency seismic waves in the subducting plate with low velocity oceanic crust. Specfem2D (Tromp et al., 2008) is used to illustrate the propagation of seismic waves through a high velocity anomaly in the mantle through the SEM method. Then I briefly revisit the Adjoint Theory following Fichtner et al. (2006a,b) and Fichtner (2010) which is the theoretical cornerstone for the full waveform inversion of this thesis. Five popular misfit functions with their corresponding adjoint sources are presented and tested for body wave and surface wave trains based on the simulations using SEM code.

Chapter 4 presents the published paper concerning the interaction between the current dip subduction of the Nazca plate and the Central Andean plateau (Gao et al., 2021a) as below:

Gao, Y., Tilmann, F., Herwaarden, van, D.-P., Thrastarson, S., Fichtner, A., Heit, B., et al. (2021). Full waveform inversion beneath the Central Andes: Insight into the dehydration of the Nazca slab and delamination of the back-arc lithosphere. Journal of Geophysical Research: Solid Earth, 126, e2021JB021984. https://doi.org/10.1029/2021JB021984

This chapter incorporates the methods of seismic wave simulation based on 3D Earth medium based on the SEM code Salvus (Afanasiev et al., 2019) and detailed model update schemes including Conjugate-Gradient (Fletcher & Reeves, 1964) and Limited-memory Broyden–Fletcher–Goldfarb–Shanno algorithm (LBFGS, Liu & Nocedal, 1989). Large-scale Seismic Inversion Framework 2.0 (LASIF) (Thrastarson et al., 2021) developed by the coauthors Dirk-Philip van Herwaarden and Sölvi Thrastarson is used and adapted to generate the input files for the simulation and inversion. Seismic waveforms are retrieved from 26 permanent and temporary networks deployed in Central Andes. Seismicity catalogs from Sippl et al. (2018) and ISC-EHB (`http://www.isc.ac.uk/isc-ehb/`) are used for comparison with the seismic velocity model. I collected and processed the seismic data using LASIF and ObsPy (Krischer et al., 2015b) and I wrote the manuscript and prepare all figures with contributions from my co-authors including my supervisor Frederik Tilmann, second supervisor Xiaohui Yuan, Benjamin Heit, Andreas Fichtner and Bernd Schurr. Dirk-Philip van Herwaarden and Sölvi Thrastarson also provided suggestions on the manuscript and code for the inversion.

Chapter 5 presents the published paper concerning the Pampean flat subduction zone and Payenia normal-dip subduction zone (Gao et al., 2021b) as below:

Gao, Y., Yuan, X., Heit, B., Tilmann, F., van Herwaarden, D.-P., Thrastarson, S., et al. (2021). Impact of the Juan Fernandez Ridge on the Pampean flat subduction inferred from full waveform inversion. Geophysical Research Letters, 48, e2021GL095509. https://doi.org/10.1029/2021GL095509

In this chapter, I mainly follow the same method and workflow from Chapter 4 but migrate the

study area to the Pampean flat and Payenia normal-dip subduction zone. Seismic waveforms recorded by 23 permanent and temporary networks are used for this study. Seismicity catalogs from Sippl et al. (2021) and ISC-EHB (`http://www.isc.ac.uk/isc-ehb/`) are also used for comparison with the model. I collected and processed the seismic data and wrote the manuscript and prepare all figures with contributions from my co-authors including my supervisor Frederik Tilmann, second supervisor Xiaohui Yuan, Benjamin Heit, Andreas Fichtner and Bernd Schurr and many suggestions from Dirk-Philip van Herwaarden and Sölvi Thrastarson. Except for coauthors, fruitful discussions about the geodynamic process with Dr. Lara S, Wagner, Prof. Lijun Liu, Dr. Jiashun Hu and Xiaowen Liu also contribute to this chapter.

Chapter 6 Conclusion and outlook

This chapter especially for the outlook is mainly inspired by discussions with my coauthors including supervisor Prof. Frederik Tilmann, Prof. Andreas Fichtner, Dr. Xiaohui Yuan, Dr. Benjamin Heit, Dr. Bernd Schurr and discussions with Prof. Barbara Romanowicz, Prof. Lijun Liu, Dr. Chao Lv, etc.

Appendix A Supplementary for Chapter 4

Appendix B Supplementary for Chapter 5

Chapter 2

Tectonic Context

During the Late Mesozoic-Cenozoic time frame, the western margin of South America has been influenced by the subducting Farallon-Nazca Plate which suffered different stages involving cyclic changes of the dip angle, slab break-off and penetration into the lower mantle. According to the plate reconstruction model (e.g. Wright et al., 2016; Chen et al., 2019), the current phase of Farallon-Nazca Plate subduction began at the northern edge of the Andes (at 5°S) during the Late Cretaceous (ca. 83 Ma) and propagated southwards reaching the southern Andes (40°S) by the Late Cenozoic era (55 Ma, Figure 2.1 and 2.2). Since 23.5 Ma, the Farallon Plate was fragmented into Nazca Plate subducting beneath the South America Plate and Cocos Plate subducting beneath the Central America Plate (Figure 2.1). Farallon-Nazca subduction was not always continuous but was punctuated by episodes of divergence between 80 Ma and 55 Ma, south of 35 °S (Chen et al., 2019). The southward migration of the Nazca Plate implied by these models also demonstrates that there would have been more than 3,000 km of subducted Nazca Plate that would have presumably piled up and already anchored into the lower mantle in the northern part of Andes (north of 30°S), whereas in the southern part of Andes (south of 30°S) the subducted Nazca Plate was much shorter and would not be expected to have extended into the deep lower mantle according to plate unfolding and global tomography studies (Chen et al., 2019; Li et al., 2008).

Except for the southward migration of the Nazca Plate, cyclic temporal and spatial variations of the dip angle possibly further dominate the Andean orogeny and plateau evolution (Kay & Mpodozis, 2002; Ramos & Folguera, 2009; Kay & Coira, 2009; Beck et al., 2015; Ward et al., 2017) and were related to the migration of the oceanic ridges (Yáñez et al., 2001; Gutscher et al., 2000; Antonijevic et al., 2015), including both the Nazca Ridge and the Juan Fernandez Ridge (Kopp et al., 2004). The current western margin of South America from Peru (5°S) to southern Chile (36°S) is mainly composed of two flat subduction segments including the Peruvian flat subduction zone (5°S- 14°S, Rosenbaum et al., 2005) and Pampean flat subduction zone (28°S- 33°S, Ramos et al., 2002), and two steep subduction segments including the southern Peru-northern Chile steep subduction (16°S-27°S) and the Payenia steep subduction (33° -36°S, Figure 1.1). Meanwhile, historical flat subduction existed in the past (Kay & Abbruzzi, 1996; Kay & Coira, 2009; Ramos & Folguera, 2009) including the Altiplano flat subduction (40-32 Ma to 27-18 Ma, Ramos & Folguera, 2009; Beck et al., 2015), the Puna flat subduction (18-12 Ma, Ramos & Folguera, 2009) and the Payenia flat subduction (13-5 Ma, Ramos & Folguera, 2011; Ramos et al., 2014). In the following subsections we will briefly introduce the tectonic evolution of the whole Central Andes since 40 Ma and the related dip angle variations of the Nazca Plate.

2.1 Peruvian flat subduction

This segment is associated with the subduction of the aseismic Nazca Ridge and the Inca Plateau (Figure 1.1). The onset timing of the Nazca Ridge collision with the Peruvian western margin was around 11.2 Ma at about 11°S and moved southward to its current position (Hampel, 2002; Rosenbaum et al., 2005;

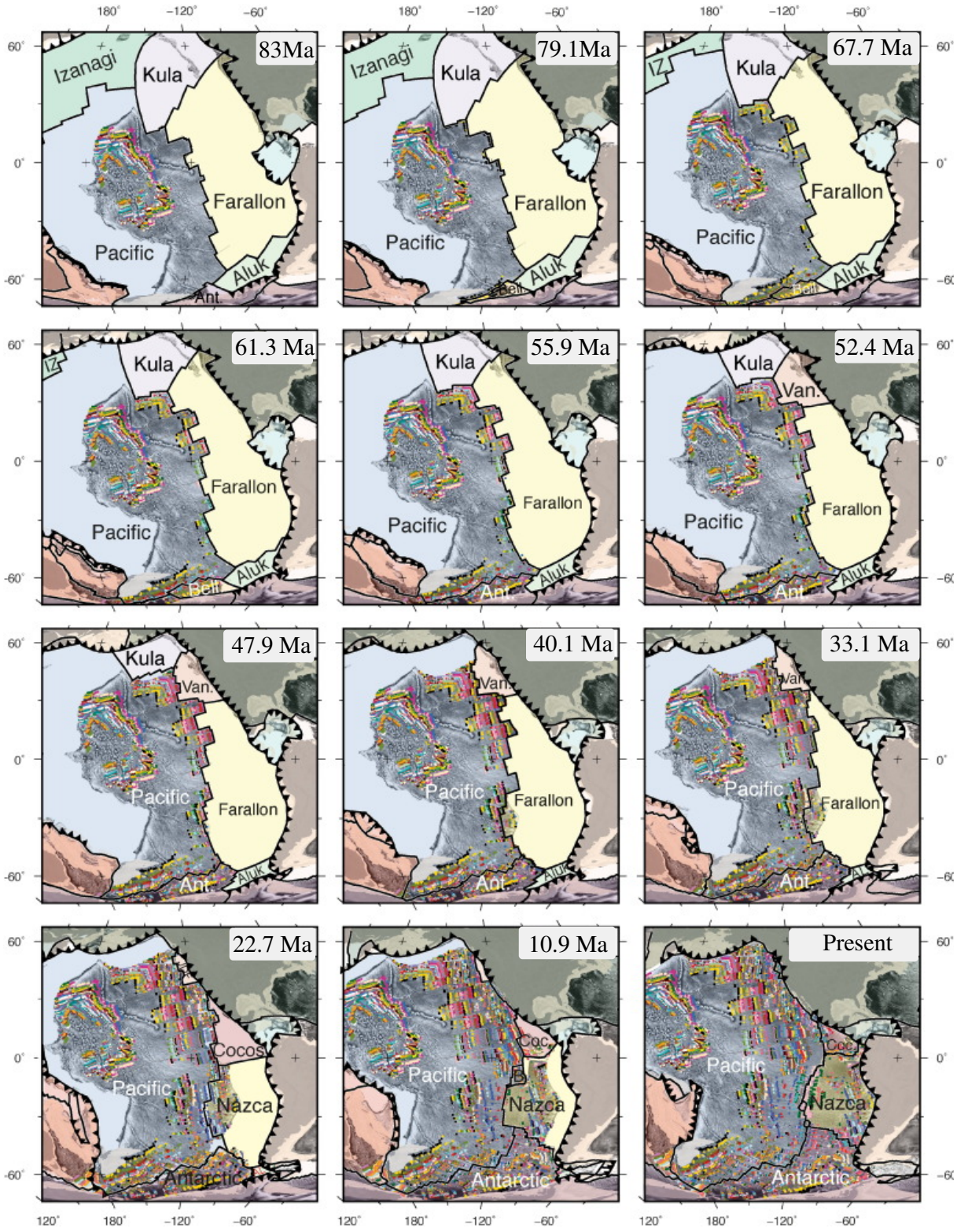

Fig. 2.1: Reconstruction of the Pacific basin since 83 Ma, shown at times corresponding to major seafloor spreading isochrons or major reorganisation events within the Pacific basin. Marine gravity anomalies (Sandwell et al., 2014) are reconstructed to highlight presently preserved oceanic crust. The compilation of magnetic identifications from the GSFML repository (Seton et al., 2014) is shown as coloured circles. Ant: Antarctica; B: Bauer microplate; Bell: Bellingshausen; Coc: Cocos; IZ: Izanagi; JDF: Juan de Fuca; Van: Vancouver. Figure is modified from Wright et al. (2016)

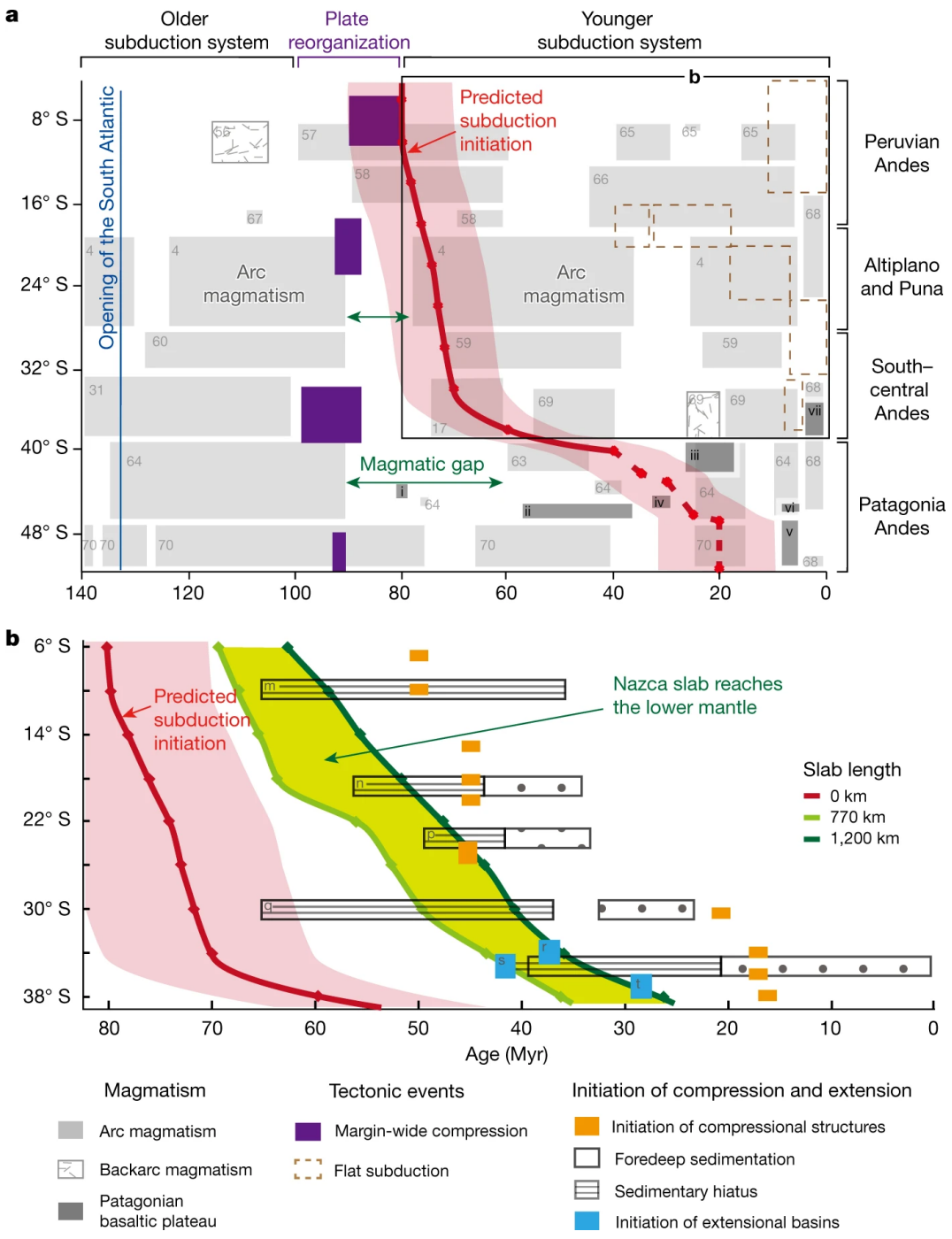

Fig. 2.2: (a) The onset of Nazca subduction and a comparsion with Andean magmatism. The thick red line highlights the southward propagation of the initiation of Nazca subduction predicted by plate reconstruction, at the latitudes shown by the red dots. Model predictions within the less-well-imaged area (south of 40°S) are shown by a red dashed line. Purple rectangles show the Andean margin-wide compressional event in the Late Cretaceous (Tunik et al., 2010). Light grey rectangles show arc-related magmatism and striped rectangles show backarc magmatism. The green arrows highlight the magmatic gap that occurred before the predicted Nazca slab initiation. Dark grey rectangles are Patagonian basaltic plateaus (Kay et al., 2004; Folguera et al., 2009). i, Tres Picos Prieto basalts; ii, Belgrano basalts; iii, Somuncura basalts; iv, Kankel basalts; v, Meseta de la Muerte basalts; vi, Pico Truncado basalts; vii, Payenia basalts. Brown dashed boxes show previously proposed flat subduction events (Ramos & Folguera, 2009). (b) Reconstructed subducted Nazca slab lengths. The red line and shading shows the initiation of Nazca subduction, as in (a). The light green and dark green lines show the times at which subducted Nazca slab lengths reached 770 km and 1,200 km (Peru-like), respectively. The lime green area between the two green lines indicates our inferred minimum time range for the subducted Nazca slab to reach the lower mantle (which lies at a depth of 660 km) at each latitude. Geological evidence for the initiation of compressional structures is represented by orange rectangles (Schepers et al., 2017). This figure is retrieved from Chen et al. (2019)

Ramos & Folguera, 2009). The Peruvian segment also coincides with an area lacking of volcanism since at least the Late Miocene times (Rosenbaum et al., 2005). The cessation (ca. 12 Ma) of magmatism in the northern part of the flat slab correlates with the complete subduction of the Inca Plateau and the arrival of the Nazca Ridge (Antonijevic et al., 2015; Bishop et al., 2017). The cessation of the main magmatic activity in the volcanic arc is followed by the emplacement of minor crustal melts of acidic composition and the magmatic lull following the Nazca Ridge subduction began at the end of the Miocene (Ramos & Folguera, 2009) (Ramos and Folguera, 2009a). Through seismology constraints, the flat Nazca slab beneath Peru is believed to be the shallowest along the ridge while to the northwest of the ridge, the slab is sagging, tearing and re-initiating normal-dip subduction (Gutscher et al., 1999; Antonijevic et al., 2015, 2016).

2.2 Normal-dip subduction beneath Central Andes with past flat subduction footprints

The dip angle variations beneath the Central Andes are highly related to the subduction of the Juan Fernandez Ridge. A detailed comparison between the location of the Juan Fernandez Ridge relative to the South American plate from the last 40 Ma and the volcanism and deformation pattern was discussed in Yáñez et al. (2001),Ramos & Folguera (2009) and Kay & Coira (2009). This segment including the Altiplano and Puna high plateau represents a zone of the past flat subduction and current steep subduction regime. Currently, the Altiplano and Puna region together constitute the second-largest high plateau in the world, the Central Andean Plateau (Figure 2.3), which is also the only one that formed under a subduction regime. The Altiplano Plateau (AP), in the northern part of the Central Andes, is characterized by a single internally drained basin with an average rather uniform elevation around 3800 m, whereas the southern part of the Central Andes is occupied by the Puna Plateau (PN), which exhibits a higher altitude around 4500 m with more rugged relief, enclosing a series of internally drained basins. The Central Andean Plateau is flanked to the west by the Western Cordillera (WC) and to the east by the Eastern Cordillera (EC), followed by the Subandean Ranges (SA), the Santa Barbara System (SB) and the Sierras Pampeanas (SP) tectonic provinces from the north to the south (Figure 2.3). The formation of the current Central Andean Plateau is thought to be linked to lithospheric foundering beneath the Central Andes (Kay & Kay, 1993; Kay et al., 1994; Beck & Zandt, 2002; McQuarrie et al., 2005; Garzione et al., 2006; DeCelles et al., 2015). Although many researchers agree on the existence of lithospheric foundering in the Central Andes, the mechanisms, scale, pattern, timing and surface expression are still under debate. The tectonic history of the eastern margin of the Central Andes exhibits north-south variations, which might provide an insight into the lithospheric foundering processes. North of 24°S, deformation in the EC has occurred between ∼40 and 15 Ma (McQuarrie et al., 2005; Oncken et al., 2006) before migrating to the SA after 10 Ma, forming a thin-skinned fold and thrust belt (Allmendinger & Gubbels, 1996; Allmendinger et al., 1997; Sobolev & Babeyko, 2005; Garzione et al., 2017; Ibarra et al., 2019). In contrast, south of 24°S, the backarc deformation becomes thick-skinned in the SB and finally changes to the basement-cored uplift in the SP (Allmendinger & Gubbels, 1996; Allmendinger et al., 1997; Sobolev & Babeyko, 2005; Oncken et al., 2006; Garzione et al., 2017).

A flat-slab subduction period was recorded in southern Peru and northern Bolivia (16°S - 19°S) within the northern part of the Altiplano. Several factors provide evidence of the period of flat subduction: (1) rapid cessation of the magmatism arc between 45 and 35 Ma; (2) widespread deformation and crustal thickening in the EC; (3) lack of igneous rocks of this age that represents the heat advection by fluids at 38 Ma before the activity of the Subandean fold and thrust belt (James & Sacks, 1999; Ramos & Folguera, 2009; Kay & Coira, 2009). These processes were explained by a shallowing of the subducted

slab that became sub-horizontal at about 35 Ma and lasted until 25 Ma. Similarly, between 20°S-27°S, the flat or shallow subduction of the Nazca slab during 26-18 Ma caused the cessation of the magmatism (Kay & Coira, 2009; Ramos & Folguera, 2009; Beck et al., 2015), crustal shortening and deformation of the southern Altiplano and Puna (Oncken et al., 2006; Allmendinger et al., 1997).

The re-steepening of the Nazca slab was illustrated by widespread bimodal volcanism where rhyolite and basalts covered a wide area. As a result, great volumes of rhyolites up to 530 km^3 erupted on the current Altiplano and western slope of the Eastern Cordillera. The hydrated overriding lithosphere due to the flat subduction dehydration is believed to be thermally eroded by the hot asthenosphere related to the following steepening of the Nazca slab and re-opening of the mantle wedge (Kay & Coira, 2009; Ramos & Folguera, 2009). Meanwhile, backarc lithospheric delamination and the Subandean thrusting were active after the re-steepening of the Nazca Plate. Similar to the Southern Altiplano, the asthenospheric flow connected with the hydrated lithosphere and contributed to the piecemeal delamination, accompanied by the formation of large rhyolitic calderas and ignimbrite fields in the Puna plateau.

In Figure 2.4, the reconstructed Juan Fernandez Ridge migration history indicates that the ridge could be divided into three sections including the earlier subduction (prior to 25 Ma) with a south-north trending beneath northern Altiplano, the northeast trending section (25-10 Ma) beneath the Altiplano-Puna and late east-west trending section (12 Ma - now) beneath the Pampean region. The northeast trending ridge section arrived under the southern Altiplano arc at 23 Ma and lasted to 12 Ma, occupying the entire arc region and leaving the Altiplano and northern Puna arc by 10-8 Ma. The amagmatic flat-slab period and a high deformation rate in the Altiplano (Oncken et al., 2006; Kay & Coira, 2009; Bello-González et al., 2018) correspond to the subduction of the north-south trending section and the flat slab stage passed with the arrival of the northeast-trending section but the slab dip remained shallow until the ridge passed to the south at around ca. 12 Ma. The north-south ridge segment subduction can account for a long period of flat subduction and the change at 25 Ma caused the recovery of the volcanism (Figure 2.5) across the region (Kay & Coira, 2009). The intense thrusting (Oncken et al., 2006; Kay & Coira, 2009) in the Eastern Cordillera accompanied the passage of the north-south segment (28-18 Ma) and the deformation rate increased beneath the Western and Central Altiplano as the passage of the northeast ridge segment (18-12 Ma). The thrusting front was transferred into the Subandean Belt as the ridge crest was leaving the backarc at ca. 10 Ma. After the passage of the north-east segment, the Nazca Plate under the southern Altiplano re-steepened accompanied by the giant Los Frailes ignimbrite field between 10 and 7 Ma. The Puna region mainly was exposed to the passage of the northeast segment subduction as the ignimbrite erupted mainly after the ridge has passed at around 6-5 Ma. The best example is the eruption of the Cerro Galan ignimbrite and its large caldera (Kay & Coira, 2009). During the resteepening of the slab, thick eclogitic mafic lower crust and lithosphere delaminated from the continental upper plate (Figure 2.5).

2.3 Pampean flat subduction, deformation and volcanism

The Pampean segment is located between 27°S and 33°S (Figure 2.6). It has the highest topography of the Main Andes coinciding with the central part of the Pampean flat slab. Tectonically uplifted areas contain Miocene to Late Paleozoic rocks above 6000 m (Ramos et al., 2002; Ramos & Folguera, 2009). In this region, Cenozoic tectonics have resulted in the development of the Fore-Arc, Domeyko Cordillera, Frontal Cordillera, Precordillera and the associated Sierras Pampeanas in the eastward foreland region from the west to the east. The initial arrival of the west-east segment of the Juan Fernandez Ridge is around 12 Ma. The volcanic gap in the Quaternary volcanic arc of the Andes indicates cold subduction due to the flat slab. The shifting and subsequent cessation of the magmatic arc moved from the west to the east and from the north to the south, complete cessation at around 5 Ma. The beginning of the

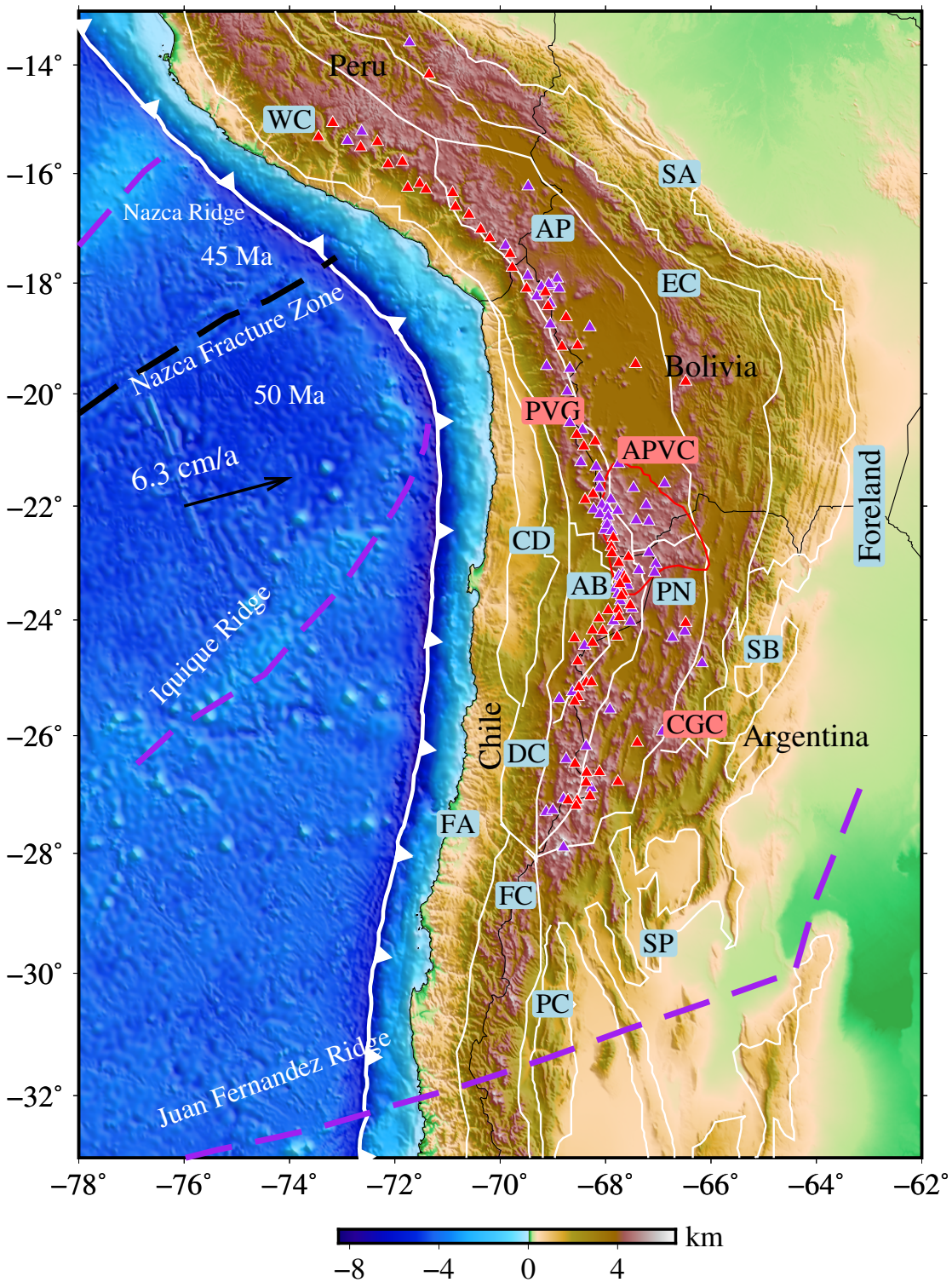

Fig. 2.3: Tectonic settings of the North Central Andes (modified from Tassara (2005)), including the forearc (FA), Central Depression (CD), Domeyko Cordillera (DC), Atacama Basin(AB), Frontal Cordillera (FC), Western Cordillera (WC), Altiplano (AP), Eastern Cordillera (EC), Puna (PN), Precordillera (PC), Subandean Ranges (SA), Santa Barbara system (SB), Sierras Pampeanas (SP); Altiplano-Puna Volcanic Complex (APVC, enclosed by the red line). Cerro Galan Caldera (CGC); Pica Volcanic Gap (PVG). The purple dashed lines represent three major oceanic Ridges, including the Nazca Ridge, Iquique Ridge and Juan Fernandez Ridge. The reconstruction of the trace of the subducted Juan Fernandez Ridge has been taken from Yáñez et al. (2001). Red and purple triangles denote Holocene and Pleistocence volcanoes, respectively(retrieved from Global Volcanism Program, Smithsonian Institution, Venzke (2013)). Topography data has been retrieved from the ETOPO1 Global Relief Model Amante & Eakins (2009); the white saw-tooth line denotes the position of the Trench.

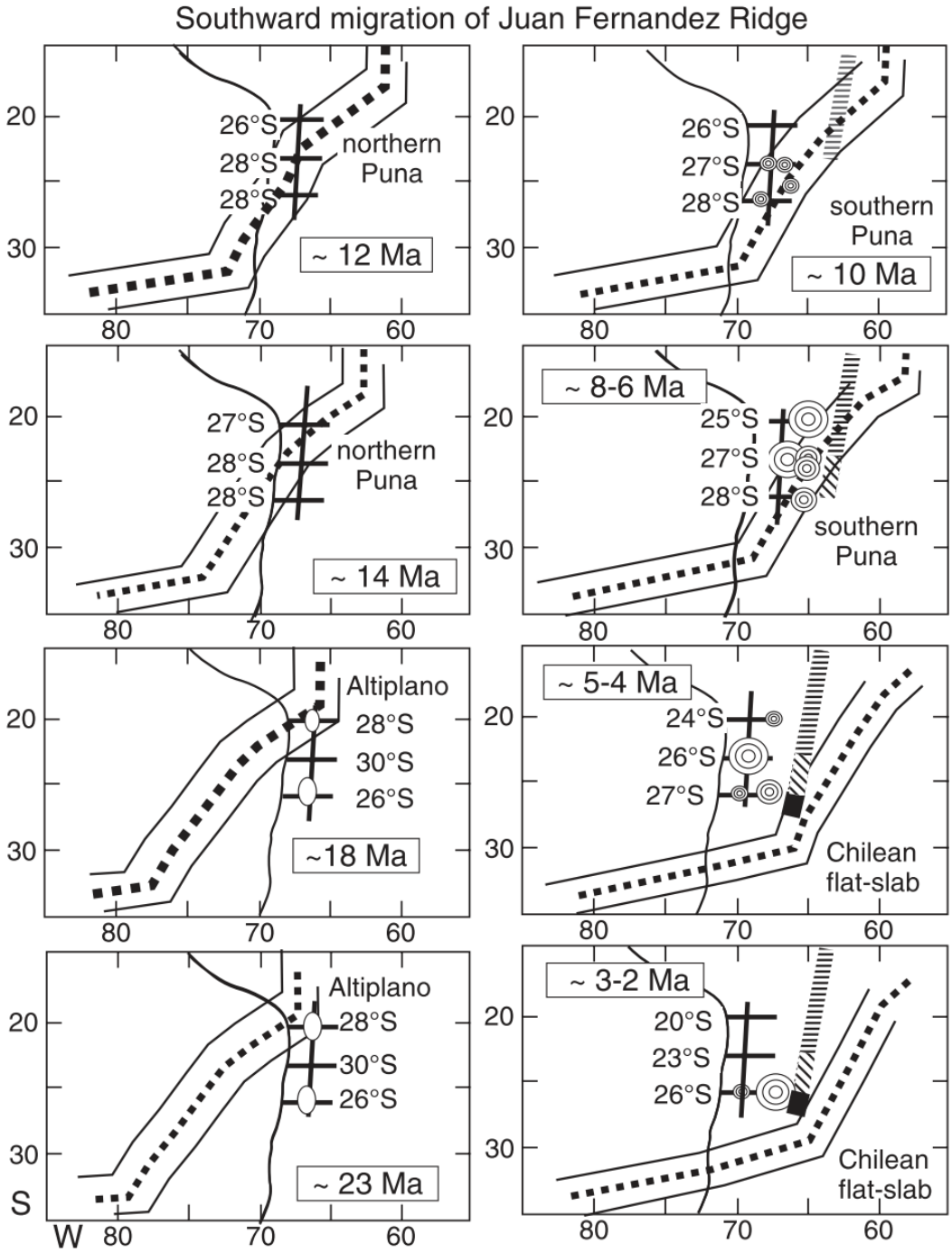

Fig. 2.4: Southward migration of the Juan Fernandez Ridge from the model of Yáñez et al. (2001) for the Altiplano at 20°S, the northern Puna at 23°S, and the southern Puna at 26°S. The trace of the Juan Fernandez Ridge is the heavy dotted line bracketed by solid lines at 100 km on each side. The other solid line is the continental margin used for reference to adjust for cumulative convergence by Yáñez et al. (2001). The coarser lines from the reference margin extend to the Los Frailes Ignimbrite in the Altiplano, the Coranzulí ignimbrite in the northern Puna, and the Cerro Galán ignimbrite in the southern Puna, respectively. The vertical crosscutting line shows the approximate position of the frontal arc. The numbers in degrees next to the line are the modern latitudinal equivalents in Figure 2.3. The white ellipses show regions of important early Miocene ignimbrites. The concentric circles represent the intermediate to giant ignimbrites, which are scaled for size. The broad line shows the Subandean belt (horizontal striped part), the Santa Barbara zone (slanted line part), and the Sierras Pampeanas (black part). As discussed in the text, the slab dips, magmatic pattern, and uplift of the ranges to the east show a broad correspondence to the southward passage of the ridge. Extracted from Kay & Coira (2009).

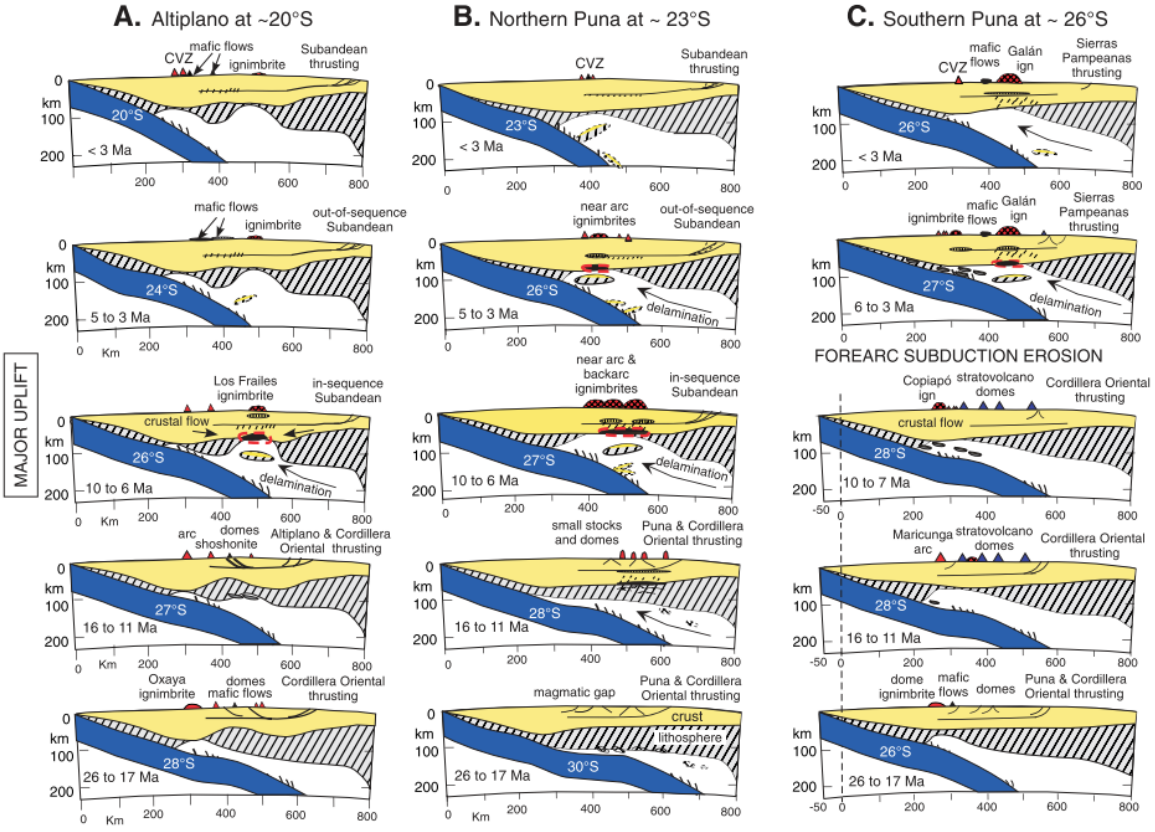

Fig. 2.5: Lithospheric-scale sections showing proposed sequence of Neogene events leading to the observed magmatic and deformation features of the (A) southern Altiplano, (B) northern Puna, and (C) southern Puna regions. The geometry of the subducting plate is based on profiles of the modern subducting plate in Figure 2.3 at the latitude indicated on the downgoing slab. The latitude chosen for the slab profile is largely based on the distribution and chemistry of the overlying volcanic centers as discussed in the text. Arrows indicate regions of decompression melting above steepening slabs. Wavy lines above the slabs represent zones of dehydration. Vertical dashed line in C shows the area added to the east of the modern trench to account for the material removed during a peak in forearc subduction-erosion between 7 and 3 Ma. CVZ: Central Volcanic Zone; ign: ignimbrite. From Kay & Coira (2009).

broken foreland stage coincided with the eastward advancing front of the shallowing Nazca slab beneath the retroarc area accompanied by the large subsidence rates during the Middle Miocene inception of the Pampean flat-slab (Ramos et al., 2002).

For the deformation, synorogenic deposit age studies show a southward diachronic beginning of the basement block uplift from 7 Ma (at 27°S) to 2.5 Ma (at 33°S). The main deformation phases and uplift of the thin and thick-skinned fold and thrust belts of the Principal Cordillera (Fore-Arc area) occurred between 20 Ma and 8.6 Ma and the uplift of the Frontal Cordillera overlapped the last stages of the Principal Cordillera deformation at ca. 9 Ma (e.g. Ramos et al., 2002; Ramos & Folguera, 2009). The rapid propagation of the thrust front occurred 2 Ma later after the collision of the Juan Fernandez Ridge (11-12 Ma) at this latitude. Uplift of the Precordillera by tectonic inversion of pre-existing normal faults and basement uplifts of the Sierras Pampeanas in the vicinity of 33°S occurred from 2.6 Ma to the present (Ramos et al., 2002; Ramos & Folguera, 2009).

For the volcanism (Figure 2.4 - 2.5), Late Oligocene to Early Miocene volcanism across the Pampean flat-slab region is characterized by voluminous magmas erupted in association with intra-arc basins and sporadic occurrence of backarc basalts to mafic and andesitic volcanism (Kay & Mpodozis, 2002; Ramos et al., 2002; Kay & Coira, 2009; Ramos & Folguera, 2009). The onset of the Juan Fernandez Ridge subduction is recorded as the northeast trending segment of the ridge in the northern flat-slab region at

around 12 Ma. Volcanism at that time includes a variation in the volcanic style from a chain of andesitic stratovolcanic centers to isolated dacitic dome complexes accompanied by an increase in backarc volcanism (Kay & Coira, 2009). Following these events, andesitic volcanism terminated along the flat-slab margin at 9-8 Ma as the east-west segment of the ridge track advanced near 31°S. The expansion of the arc magmatism is first associated with a second dehydration front (Kay & Coira, 2009). The main Middle Miocene arc was characterized by large volumes of andesites and dacites in the Principal Cordillera whereas in the Precordillera at 130 km east of the main arc, small volcanic centers and subvolcanic bodies were emplaced. The shifting and subsequent cessation of the magmatic arc simultaneously moved from west to east and from north to south ending at around 5 Ma. The last subduction-related volcanism occurred more than 750 km east of the trench. The occurrence of adakitic magmatism has also been attributed to slab melting (Gutscher et al., 2000; Hu et al., 2016) or intrusion of the basaltic arc magmas (Kay & Kay, 2002). The Middle to Late Miocene adakitic volcanoes include the Famatina Mogotes Group (FMG, Kay & Mpodozis 2002) and Gualcamayo Igneous Complex (GIC, D´Annunzio et al. 2018).

2.4 Payenia normal-dip subduction with past flat subduction footprints

In the southern Central Andes of Mendoza and northern Neuquen (33°S-37°S, Figure 2.6), recent fieldwork, geochronological data and petrological studies have shown a distinct pattern in terms of the interaction among the timing of deformation, type of volcanic activity and changes in the tectonic regime. This pattern is linked to an original normal-to-thin crust in the main Andes and huge and extensive basaltic floods in the retroarc foreland region. This segment is characterized by the low elevation of the Principal Cordillera (less than 3000 m), in comparison with the Pampean section to the north where the Frontal and Principal Cordillera exceeds 6900 m. The main Andes at these latitudes were uplifted as a result of the Miocene contraction along with the Neuquen System, which is characterized by fold and thrust belt (Ramos et al., 2014) . The arc-related rocks were emplaced more than 550 km away from the trench during Late Miocene times, suggesting a shallow subduction process was in place during that time (Ramos & Folguera, 2009; Ramos et al., 2014)

In addition, the main phase of deformation in the eastern section of the Neuquen System is inferred to have occurred between 13-10 Ma, indicating a genetic relationship between the initial phase of arc expansion, uplift of the main Andes, sedimentation in the adjacent foreland basin and breaking of the foreland area. However, during the Late Miocene-Early Pliocene times (8-4 Ma), this crustal compression changed to an extensional regime with the development of extensional troughs across the area that had previously recorded arc expansion. The extensional collapse was also accompanied by flooding of the huge basaltic Payenia Volcanic Complex in the foreland province which was developed in the last 2 Ma. These two contrasting stages of deformation and arc dynamics point to a scenario that there was a progressive shallowing subduction from 15 to 5 Ma which was followed up by a sudden slab steepening during the last 4 Ma, associated with the partial collapse of the orogeny at these latitudes (Ramos et al., 2014).

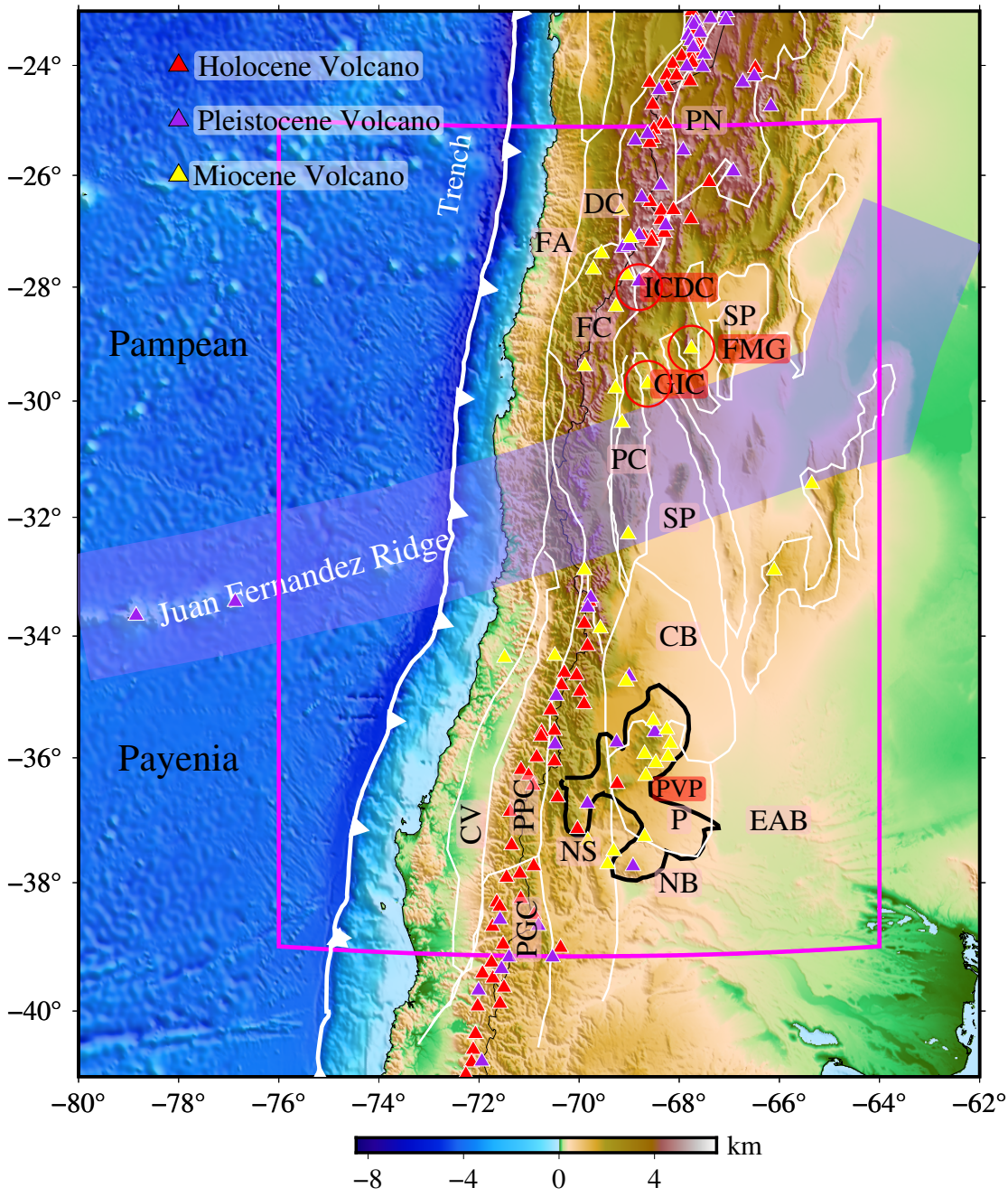

Fig. 2.6: Tectonic settings of the South Central Andes, Major morphotectonic provinces are modified from Tassara et al. (2006); Piceda et al. (2020)). Fore-Arc (FA), Domeyko Cordillera (DC), Frontal Cordillera (FC), Puna (PN), Precordillera (PC), Subandean Ranges (SA), SierrasPampeanas (SP), Patagonian Cordillera (PGC), Principal Cordillera (PPC), Central Valley (CV), Neuquen Basin (NB), Neuquen System (NS) Payenia Craton (P), Payenia Volcanic Province (PVP, black line), Incapillo Caldera and Dome Complex (ICDC), Famatina Mogotes Group (FMG), Gualcamayo Igneous Complex (GIC). Black solid line denotes the Payenia Volcanic Province (Ramos & Folguera, 2011). White saw-tooth line denotes the trench. Topography data is retrieved from ETOPO1 Global Relief Model (Amante & Eakins, 2009).

Chapter 3

Theory and Method

3.1 Introduction

This chapter briefly presents the theoretical background of Adjoint Full Waveform Tomography based on the numerical modeling for the elastic wave equation in the 2D P-SV plane. As mechanical waves propagate through a medium, they are imprinted by the information of the medium. Through investigating the character of the waves recorded by a number of detectors, the information carried by the seismic waves can be retrieved and used to image the interior structure of the medium.

In the seismology and exploration area, ray theory has been widely adopted in early tomographic studies due to its simplicity and efficiency and provides the seismologists initial knowledge of the velocity structure of the earth. Based on the assumption of large-scale weak and lateral heterogeneities and infinite high frequency, the seismic waves propagate only along the geometrical raypath between the source and receivers. The assumptions of ray theory become less valid when the seismic wavelength larger than the heterogeneities of the medium. In other words, it is almost impossible for ray theory to explain phenomena such as wave-front healing and other finite-frequency diffraction effects. In order to account for these phenomena, finite-frequency sensitivity kernels have been calculated through Born scattering (e.g. Tarantola, 1988; Chen et al., 2007a). The finite-frequency kernel includes volumetric sensitivities in the vicinity of the ray path. The classic banana-doughnut theory incorporates the paraxial ray approximation to account for finite-frequency effects for body waves (Dahlen et al., 2000) and was followed by finite-frequency surface wave kernel developed by surface wave summation (Zhou et al., 2004) and normal mode summation (Zhao et al., 2000; Capdeville, 2005; Zhao & Jordan, 2006). Due to its efficiency and effectiveness in finite-frequency, especially for the long period surface waves, finite-frequency tomography has been successfully applied for global and regional tomography work (e.g. Montelli et al., 2004; Zhou et al., 2006; Liu & Zhou, 2016; Portner et al., 2020; Rodríguez et al., 2021). However, the classic finite-frequency tomography is mainly based on analytical solutions using one-dimensional models, which means lateral heterogeneities are not included in the wavefield computation. Thus debates exist on the accuracy of the classic finite-frequency theory due to the strong heterogeneous properties of the interior of the Earth (de Hoop & van Der Hilst, 2005). In order to characterize the wavefield propagation in 2D and 3D heterogeneous media, multiple numerical modeling methods were proposed such as Finite-Difference (e.g. Alterman & Karal, 1968; Zhang et al., 2012b), Pseudo-Spectral (e.g. Kosloff & Baysal, 1982; Igel, 1999), Finite-Element (e.g. Lysmer & Drake, 1972; Akcelik et al., 2002), Spectral-Element (e.g. Komatitsch & Tromp, 1999; Afanasiev et al., 2019) and Discontinuous Galerkin (e.g. Dumbser et al., 2007; Brossier et al., 2009).

Based on Born scattering theory, there are generally two ways to compute the finite-frequency kernels using numerical solver: scattering integral and adjoint method. Zhao et al. (2005) pioneered the scattering integral method to calculate finite-frequency kernels through Finite-Difference solver in a 3D model, followed by various applications in recent years (e.g. Chen et al., 2007b; Zhang et al., 2007). The adjoint

Table 3.1: List of notational conventions

Symbols	interpretation
$\mathbf{A} \cdot \mathbf{B}$	inner or dot product
$\mathbf{A} : \mathbf{B}$	contraction over two adjacent indices, e.g., $\Sigma_{i,j=1}^{n} A_{i,j} B_{i,j}$
$< \mathbf{A} >$	integration over time and space
$\mathbf{A} \otimes \mathbf{B}$	tensor or dyadic product
$\Im m$	imaginary part of a complex
$\Re e$	real part of a complex

method was introduced into seismology by Tarantola (1988). Based on the Spectral-Element method (SEM) or Finite-Difference solvers, Tromp et al. (2005a); Sieminski et al. (2007); Liu & Tromp (2006) and Fichtner et al. (2006a,b) further validated the possibility of the adjoint theory in seismology. A detailed comparison between the scattering integral and adjoint method for full waveform inversion is given in Chen et al. (2007a).

Following the development of the numerical solutions of elastic equation and theory of full waveform inversion (FWI), FWI including scattering integral and adjoint method have been successfully applied to image the seismic structure at different scales, for example, Gao & Shen (2014) took advantage of the scattering integral method and successfully imaged the upper mantle structure of the Cascades using ambient noise cross-correlation waveforms. Meanwhile, adjoint FWI has been applied more extensively for the crust and upper mantle based on passive earthquake data (e.g. Fichtner et al., 2010; Zhu et al., 2015; Tao et al., 2018) and ambient noise cross-correlation functions (e.g. Chen et al., 2014; Wang et al., 2018; Lu et al., 2020; Sager et al., 2020).

This chapter is organized as follows: in subsection 2, we present the elastic wave equation and numerical methods including Finite-Difference and Spectral-Element methods; in subsection 3, we present the adjoint theory, misfit functionals and optimization methods.

Since the following subsections involve many equations, table 3.1 gives notational conventions for the equations.

3.2 Seismic Wave Equation with Numerical Methods

This thesis involves the brief development and application of adjoint methods to the seismic tomography inverse problem. The success of an inverse problem depends primarily on the data coverage and quality and the necessary precise forward modeling tools within the inverse problem framework. Our forward simulation modeling tools include P-SV plane 2D Finite-Difference Python code modified from Seismolive project (Krischer et al., 2018a), Spectral-Element codes including Specfem2D (Tromp et al., 2008) and Salvus (Afanasiev et al., 2019), which has been applied over many aspects ranging from medical imaging to global seismic wave propagation on Earth and other extra planets.

3.2.1 Seismic Wave Equation

The equation of motion for an anelastic Earth is given by:

$$\rho(\mathbf{x}) \frac{\partial^2 \mathbf{s}(\mathbf{x}, t)}{\partial t^2} = \nabla \cdot \mathbf{T}(\mathbf{x}, t) + \mathbf{f}(\mathbf{x}, t) \tag{3.1}$$

$$\mathbf{x} \in G \subset \mathbb{R}^3 \tag{3.2}$$

where ρ denotes the density distribution, $\mathbf{s}(\mathbf{x},t)$ the seismic wavefield (displacement), $\mathbf{T}(\mathbf{x},t)$ the stress tensor and $\mathbf{f}(\mathbf{x},t)$ the external force density. $\mathbf{x}$ indicates the position within the Earth's interior G

If the medium is elastic, then Hooke's law applies:

$$\mathbf{T} = \mathbf{C} : \nabla \mathbf{s} \tag{3.3}$$

which states the stress is linearly related to the displacement gradient $\nabla \mathbf{s}$ (strain) through the fourth-order elastic tensor $\mathbf{C}(\mathbf{x})$. Thus in a more explicit expression:

$$T_{ij} = c_{ijkl} e_{kl} = \Sigma_{k=1}^{3} \Sigma_{l=1}^{3} c_{ijkl} e_{kl} (i,j,k,l = x,y,z) \tag{3.4}$$

where

$$e_{kl} = \frac{1}{2}(\frac{\partial s_k}{\partial x_l} + \frac{\partial s_l}{\partial x_k}) \tag{3.5}$$

At the surface of the Earth ∂G, the normal components (vertical to the surface of the earth) of the stress tensor $\mathbf{T}$ vanish:

$$\mathbf{T} \cdot \mathbf{n}|_{\mathbf{x} \in \partial G} = 0 \tag{3.6}$$

where $\mathbf{n}$ is the unit normal on ∂G. Thus equation 3.6 is the free surface boundary condition. Meanwhile, the displacement field ($\mathbf{s}$) and velocity field ($\mathbf{v} = \dot{\mathbf{s}} = \frac{\partial \mathbf{s}}{\partial t}$) should be zero prior to the initial time t=t0 when the external force $\mathbf{f}$ starts to act:

$$\mathbf{s}|_{t \leq t0} = \mathbf{v}|_{t \leq t0} = 0 \tag{3.7}$$

3.2.2 Numerical Methods

A large number of numerical techniques have been developed for the simulation of wave propagation in 2D or 3D elastic media for waveform inversion in the area of exploration seismic and seismology including the mostly used Finite-Difference, Pseudo-Spectral methods, Finite-Element methods, Spectral-Element methods and Discontinuous Galerkin methods. A more detailed introduction and derivation have been reviewed in Fichtner (2010); Igel (2017). In this chapter, we mainly introduce basic concepts of the Finite-Difference and Spectral-Element method.

Finite-Difference method with simple tests

Finite-Difference is one of the most widely used numerical methods for all physical sciences, for example, seismic wave propagation simulation (e.g. Igel et al., 1995; Zhang et al., 2012a) and thermo-mechanical modeling for geodynamic problems (e.g. Sobolev et al., 2005; Gerya, 2019).

Based on the approximation of an exact derivative $\partial_x f(xi)$ at a grid position xi, the function f is evaluated at a finite number of neighboring grid points. Staggered-grid approach (Virieux, 1984, 1986) marks a milestone in the finite-difference modeling which reduces the grid space compared to the conventional approach. The staggered-grid approach requires field variables defined at different grid positions (Figure 3.1).

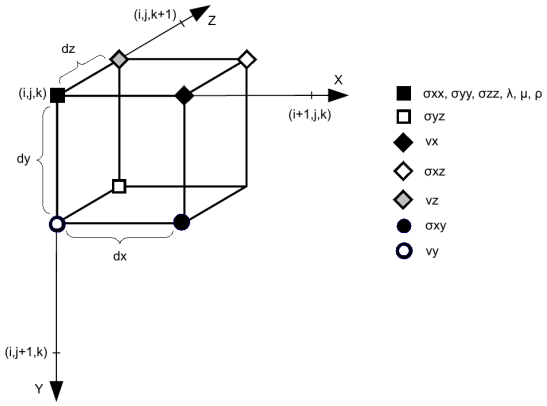

Fig. 3.1: Grid geometry for a standard stagggered grid(SSG), extracted from Bohlen (2002)

Thus Finite-Difference allows the seismic wave equation to be solved directly (in principle) for arbitrarily heterogeneous media. However, the resulting space-time discretization possibly leads to numerical dispersion that can only be reduced by sampling with more points per wavelength (Virieux, 1986). The accuracy of finite-difference operators can also be improved by using information from more grid points (i.e., higher-order approximation operators). The weights for the grid points can be obtained using the Taylor series (or other approaches). Classic plane-wave analysis of the approximative scheme leads to a stability criterion that restricts the choice of the space-time discretization. The implementation of boundary conditions in the case of Finite Differences needs special care, such as free surface and model edges for higher-order schemes problematic at interfaces. The Finite-Difference method - despite the usually low-order implementations - remains an attractive numerical scheme for many applications in seismology even for problems that require accurate surface waves provided that the free surface gets special treatment (Zang et al., 2021). In principle, Finite-Difference type operators are possible on unstructured grids but only with low-order accuracy. Finite-difference approximations to the wave equation in cylindrical or spherical coordinates is possible with restrictions due to the intrinsic singularities. More detailed derivations and discussions could be found in Moczo et al. (2007); Fichtner (2010); Igel (2017).

To avoid textbook-style duplicates, we don't provide derivations for the Finite-Difference method. Instead, a simple tutorial for 2D P-SV plane isotropic seismic wave simulation based on staggered-grid is presented in `https://github.com/yjgao-gfz/PSV-FD-SEISMOLIVE` which is modified from acoustic wave equation version based on the Seismo-live project (Krischer et al., 2018a). In this simple code, we use the Numba python module (jit based on C) to accelerate the simulation and Gaussian tampering to achieve the absorbing boundary. More technical details can be found in the code. In this tutorial, we implement a single force as the source and incorporate a west-dipping 'Slab' with a 10 km thick oceanic crust atop 50 km thick oceanic lithosphere. The oceanic crust is parameterized with -8% perturbation in both P and S wave velocity. Whereas the slab is + 6% perturbation in both P and S (Figure 3.2). The model is with 1 km regular spatial grid spacing and 0.625 s dominant frequency (to avoid grid dispersion) for the simulation with a 0.05s time step (to avoid the Courant Instability, Courant et al., 1967).

Through the modeling, we could observe the seriously distorted body wave phases in both the wavefield snapshots (Figure 3.3) and waveform comparisons (Station ID : St.6, Figure 3.4-3.5). The strong perturbations relative to the homogeneous model (e.g., subducting oceanic plate with slow velocity crust) could directly introduce seriously 'circle-skip' when comparing the two waveforms (St.6-12, Figure 3.5). Meanwhile, the strong 'oceanic crust' inspired strong multiple arrivals within itself (Figure 3.3).

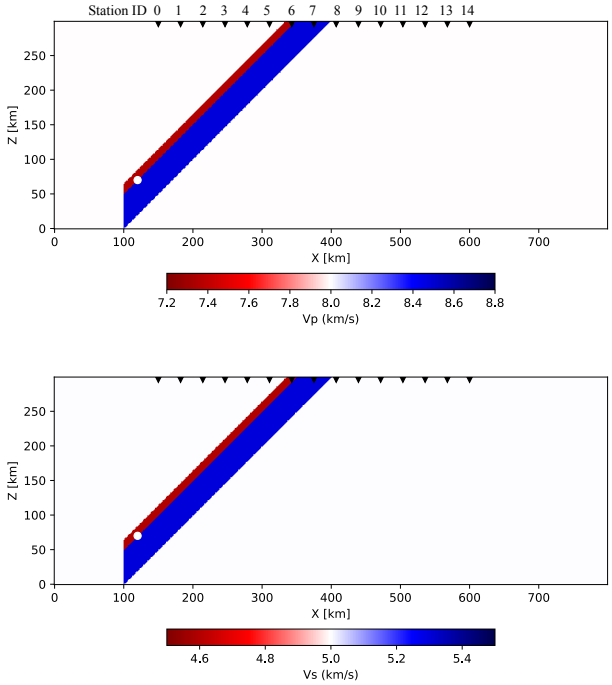

Fig. 3.2: Synthetic model for Finite-Difference: The white dot denote the source position of single force. The red and blue represent the oceanic crust and lithosphere, respectively. The inverse triangles denote the receivers at the surface.

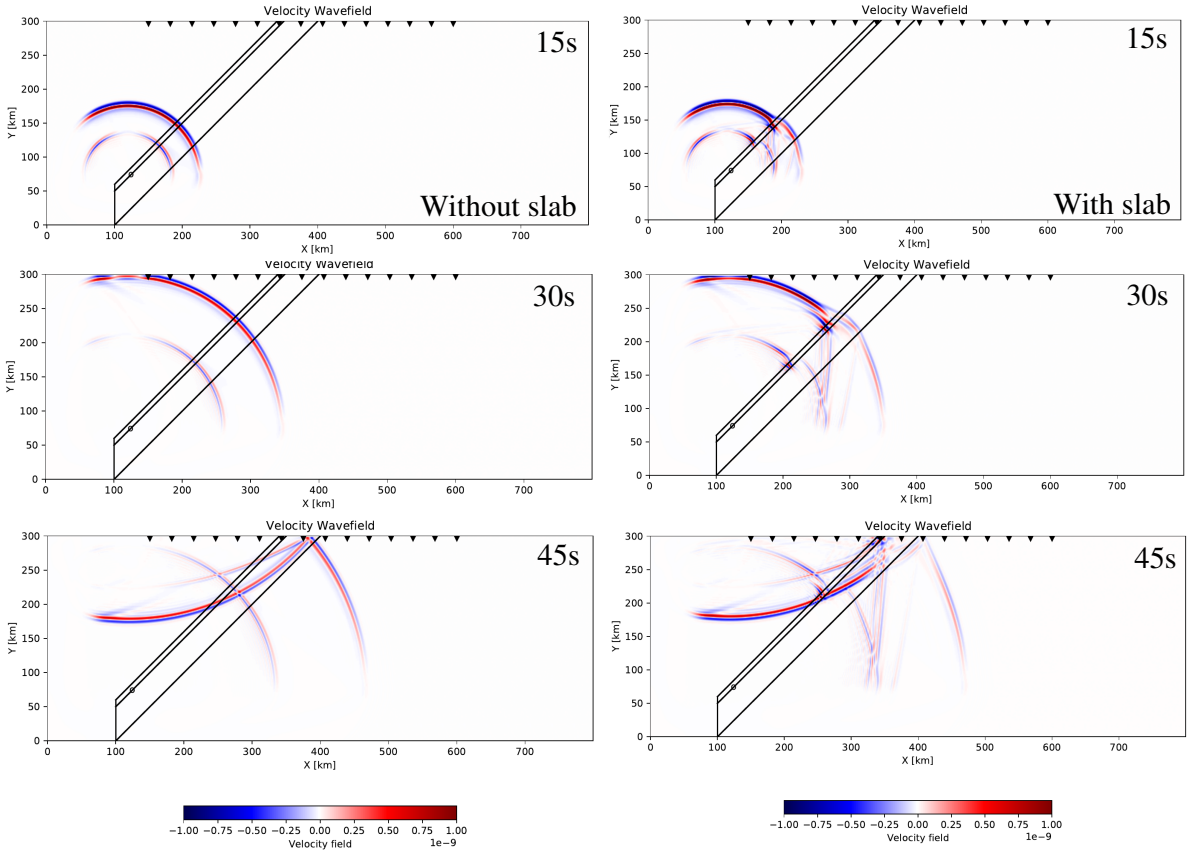

Fig. 3.3: Wavefield snapshot from 2D finite-difference seismic simulation: Left three panels denote the vertical velocity wavefield from homogeneous model with Vp= 8 km/s and Vs= 5 km/s. The slab outline here is just included for comparison with the right panels; right three panels denote the wavefield from model with west-dipping slab structure shown in Figure 3.2.

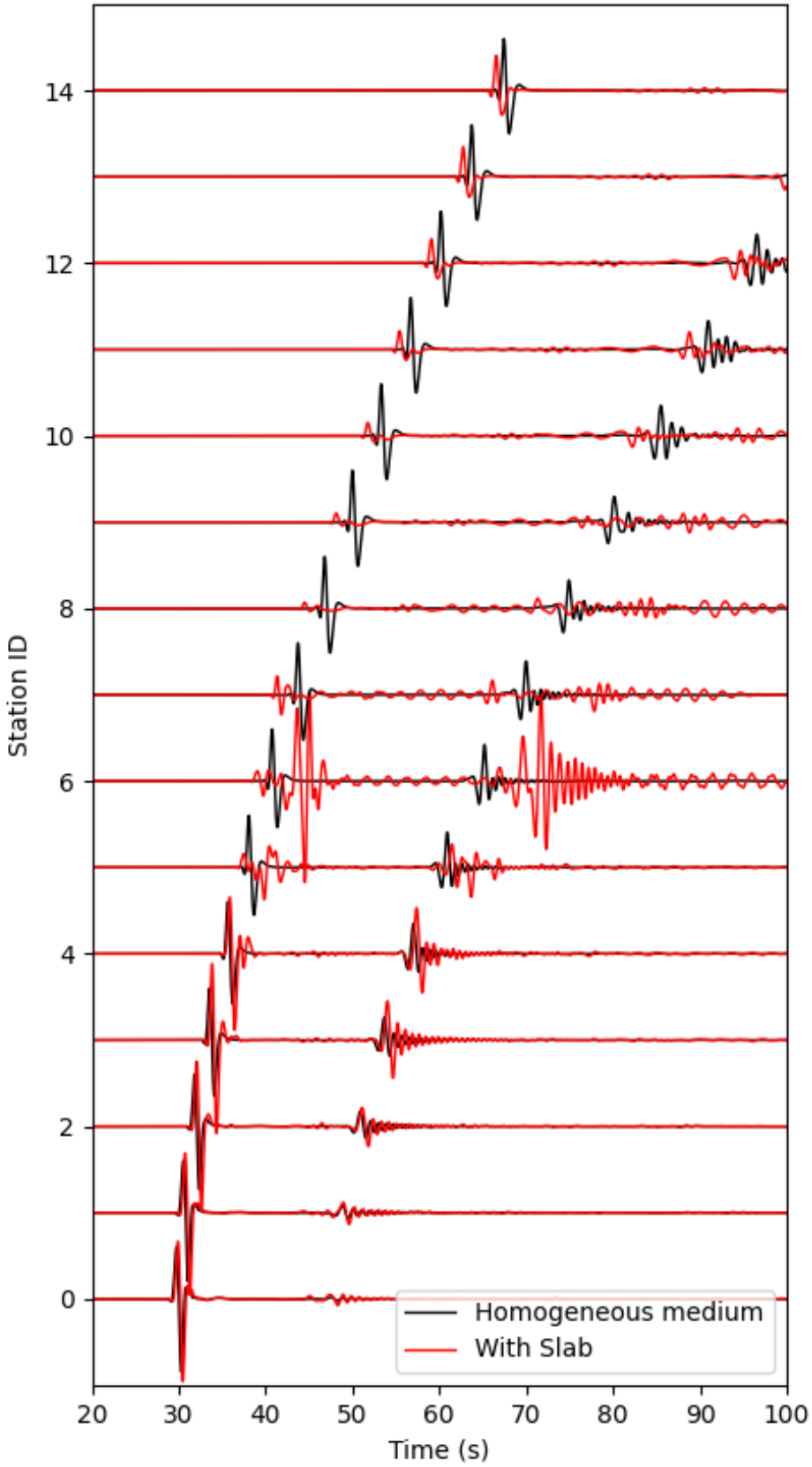

Fig. 3.4: Synthetic waveform (Z component) comparison: synthetic waveforms from homogeneous medium(black) and Slab implemented model (red). The model is illustrated in Figure 3.2.

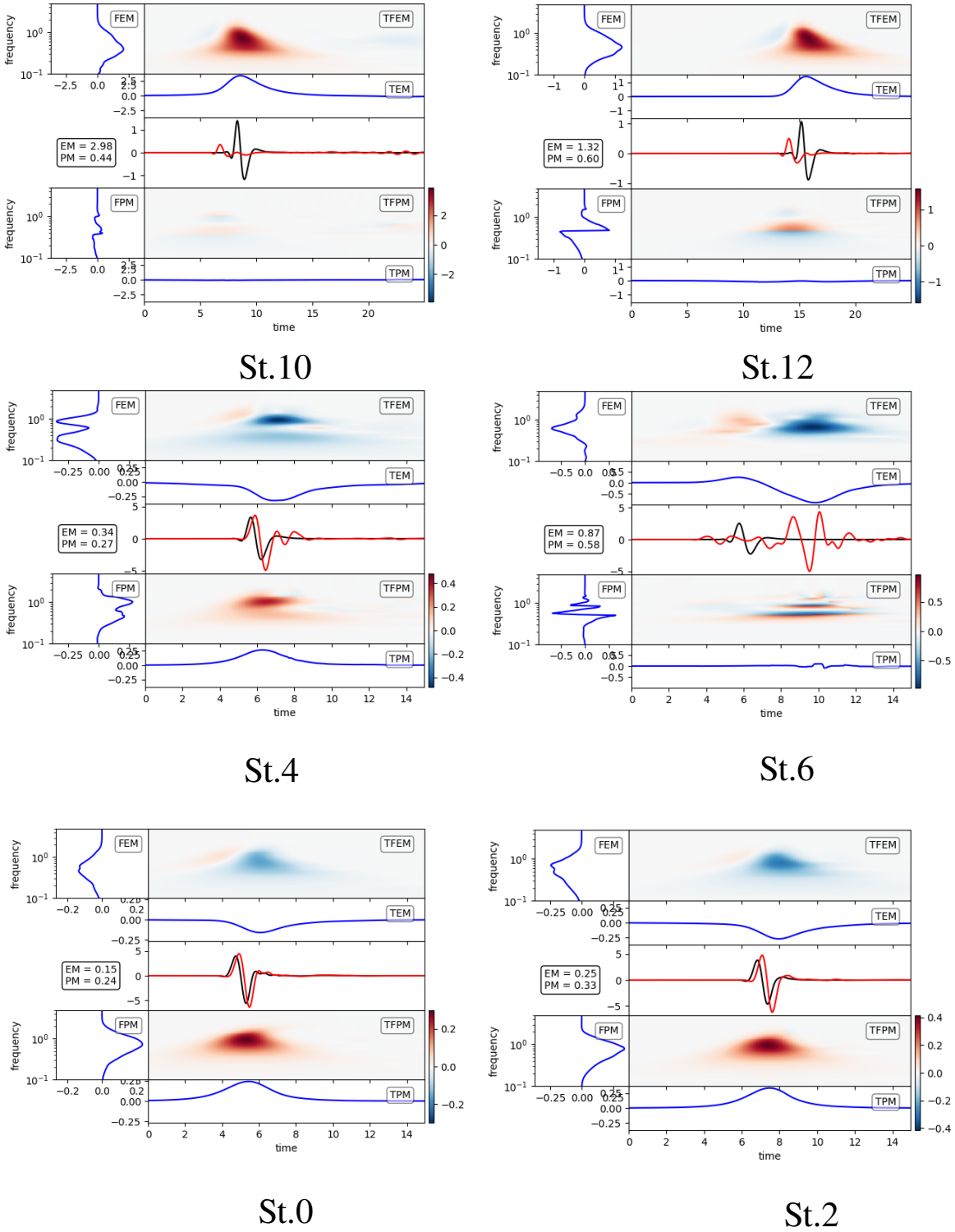

Fig. 3.5: P wave phase and envelop misfit in Time-Frequency domain. FEM: Frequency Envelope Misfit, FPM:Frequency Phase Misfit, TEM: Time Envelope Misfit, TPM: Time Phase Misfit, TFPM: Time-Frequency Phase Misfit, TFEM: Time-Frequency Envelope Misfit. Time-Frequency misfits are calculated from Obspy (Krischer et al., 2015b)

Spectral-Element method with simple tests using Specfem2D

The spectral-element method is a high-order numerical method solving the seismic wave equation in a 2D or 3D heterogeneous Earth model. The main advantage of the Spectral-Element method over Finite-Differences lie in the adaption of the mesh to the complicated surface topography and the variable wavelengths inside the Earth. The accurate topography implementation leads to accurate solution for surface waves. Applications of spectral-element have been achieved in seismology (Komatitsch & Tromp, 1999) through the popular SEM code family including Specfem2D, Specfem3D and Specfem3d_Global (Komatitsch & Tromp, 2002a,b), code SES3D (Gokhberg & Fichtner, 2016) and Salvus (Afanasiev et al., 2019).

Different from Finite-Difference which requires space-time discretization on the wave-equation (Equation 3.1), Spectral-element adopts the weak form of the equation through multiplying the wave-equation with a smooth test function ω, which gives any t $\in$ (o,T]:

$$\int_G \rho\omega \cdot \partial_t^2 \mathbf{s} d^n\mathbf{x} = \int_G \omega \cdot (\nabla \cdot \mathbf{T}) d^n\mathbf{x} + \int_G \omega \cdot \mathbf{f} d^n\mathbf{x} \tag{3.8}$$

Applying the divergence theorem to the first term on the right and integration by parts in Equation 3.8 gives

$$\int_G \rho\omega \cdot \partial_t^2 \mathbf{s} d^n\mathbf{x} = \int_{\partial G} \omega \cdot (\mathbf{T} \cdot \mathbf{n}) d^{n-1}\mathbf{x} - \int_G \nabla\omega : \mathbf{T} d^n\mathbf{x} + \int_G \omega \cdot \mathbf{f} d^n\mathbf{x} \tag{3.9}$$

The term involving the boundary integral in Equation 3.9 vanishes if the free-surface boundary condition applied (Equation 3.6). Thus the weak form of wave equation coud be reduced to

$$\int_G \rho\omega \cdot \partial_t^2 \mathbf{s} d^n\mathbf{x} = -\int_G \nabla\omega : \mathbf{T} d^n\mathbf{x} + \int_G \omega \cdot \mathbf{f} d^n\mathbf{x} \tag{3.10}$$

The free-surface condition is now implicitly included and represents a major advantage over finite difference methods, especially when modeling wave propagation through regions with strong topography. More specific and further derivation and theory of this method including spatial discretization, basis functions through Galerkin approximation and finite-element style Gauss-Lobatto-Legendre points (GLL) within the individual element are given in many classic papers and textbooks (e.g. Komatitsch & Tromp, 1999; Fichtner, 2010; Igel, 2017; Afanasiev et al., 2019) which is beyond the scope of this thesis. Instead, we present a 2D P-SV simple case using Specfem2D (Tromp et al., 2008) for a model with high velocity anomaly atop 660 km discontinuity (Figure 3.6) which could run on a regular desktop with GPU acceleration through the 1080 Nvidia Graphical Card. More specifically, we use Cubit to build the external mesh (Figure 3.7) which enables users to build complex meshes. In this test, we use a rectangular structural mesh scheme with 12 km spatial grid space (element size) to fit 10s dominant frequency wavefield (assuming minimum speed for the whole model with 2.5 km/s thus 25 km wavelength could be sampled by 2 elements, thus 35028 elements are used with NGLLX = 5, degree N = 4). Meanwhile, we implement 250 km absorbing boundary to tamper the reflections from the boundary (Stacey absorbing boundary).

In the simulation with anomaly, we could observe earlier arrival of P, pP, S and sS than the model without high velocity anomaly (Figure 3.8 and 3.9).

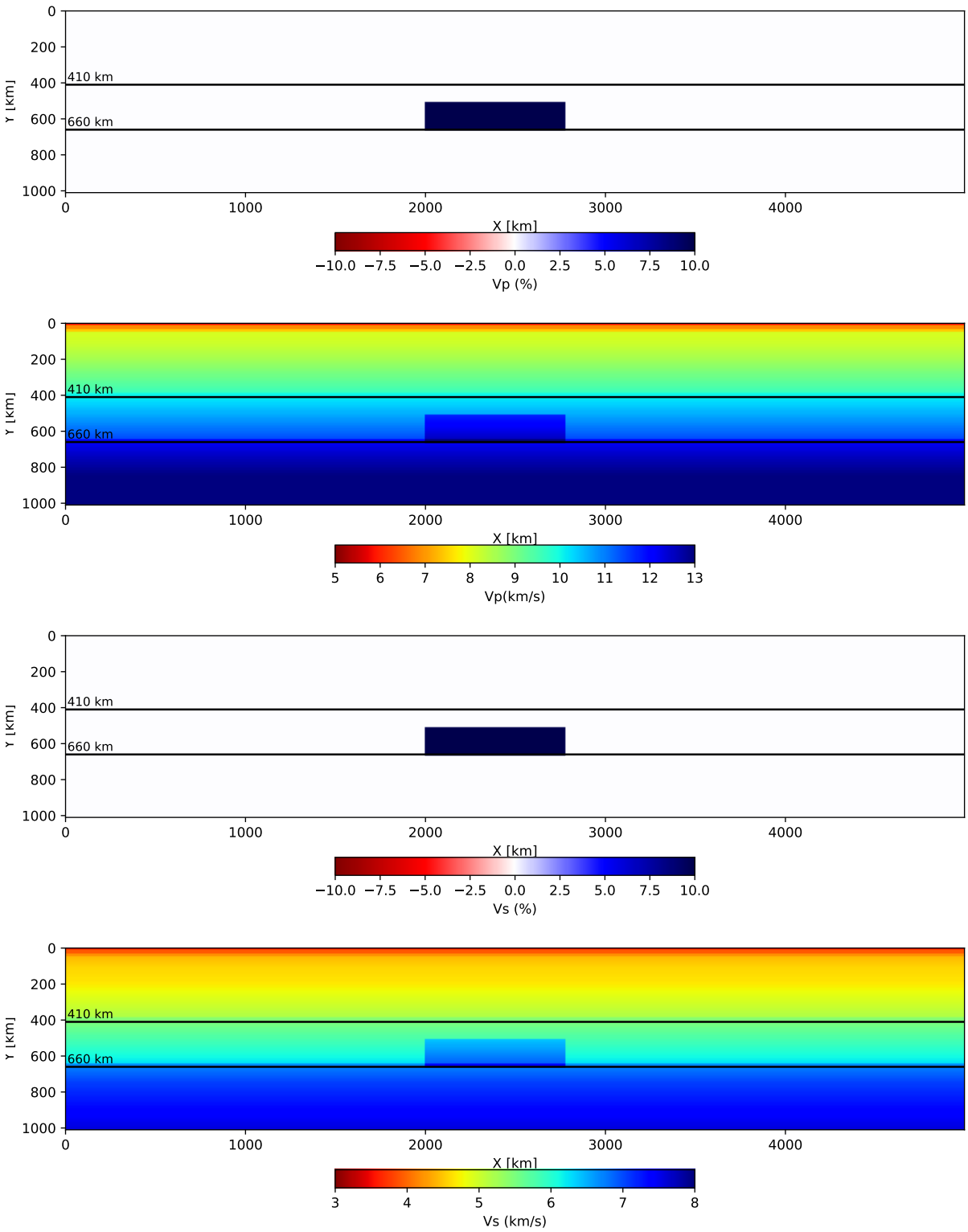

Fig. 3.6: Synthetic model through 2D P-SV plane for spectral-element (Specfem2D). The velocity and depth have been adapted to the Cartesian system through the Earth flattening transformation.

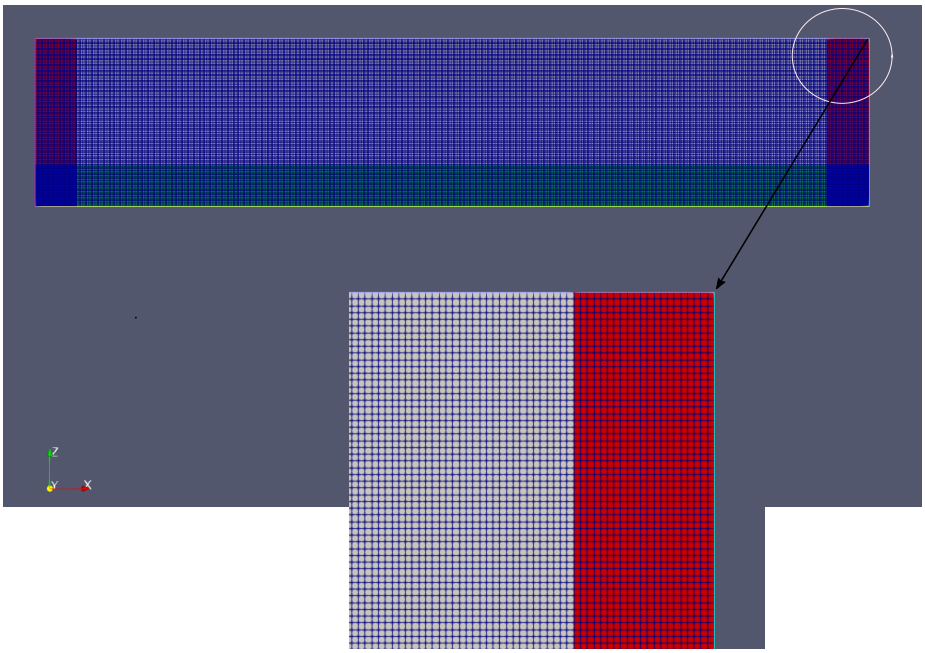

Fig. 3.7: 2D finite-element mesh built through Cubit to fit in the model in 3.6. The red blue and green block represent the absorbing areas.

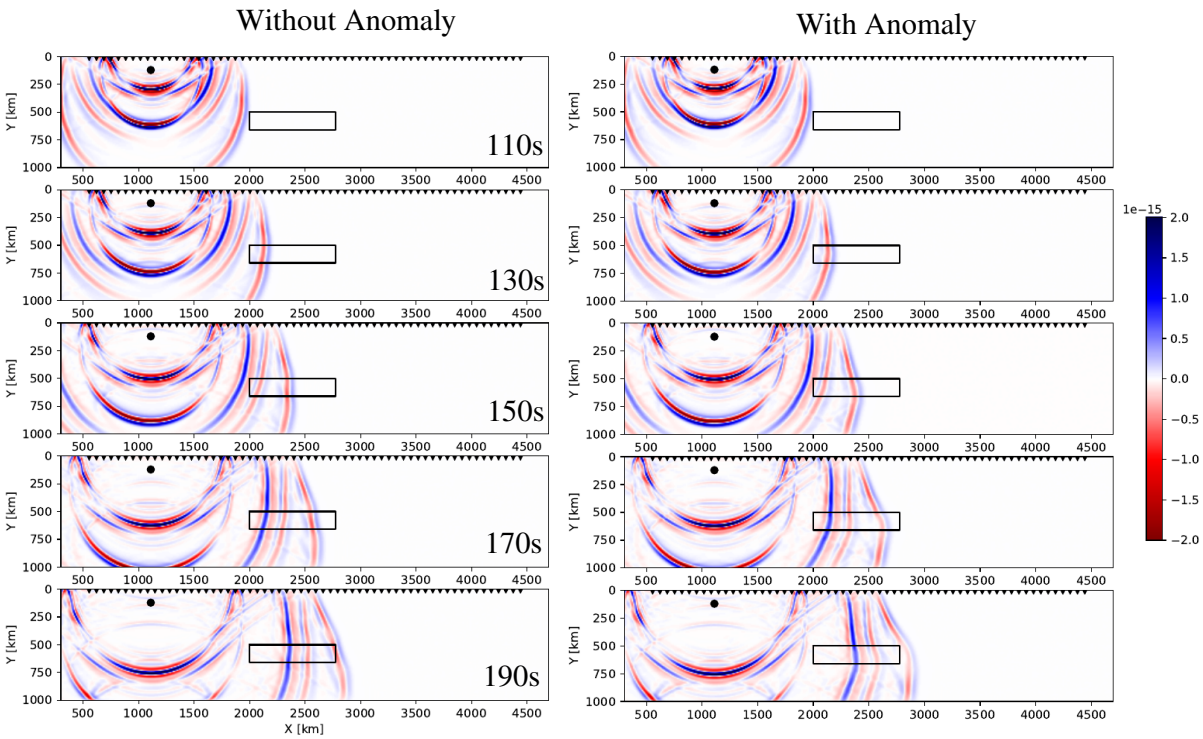

Fig. 3.8: Synthetic velocity wavefield snapshot: Right three panels: through the model with high speed anomaly atop 660 km discontinuity in Figure 3.6. Left three panels: without anomaly. The black dot denotes the location of the source, inverse triangles denote the receivers. Black rectangles mark the position of the high velocity anomaly in Figure 3.6

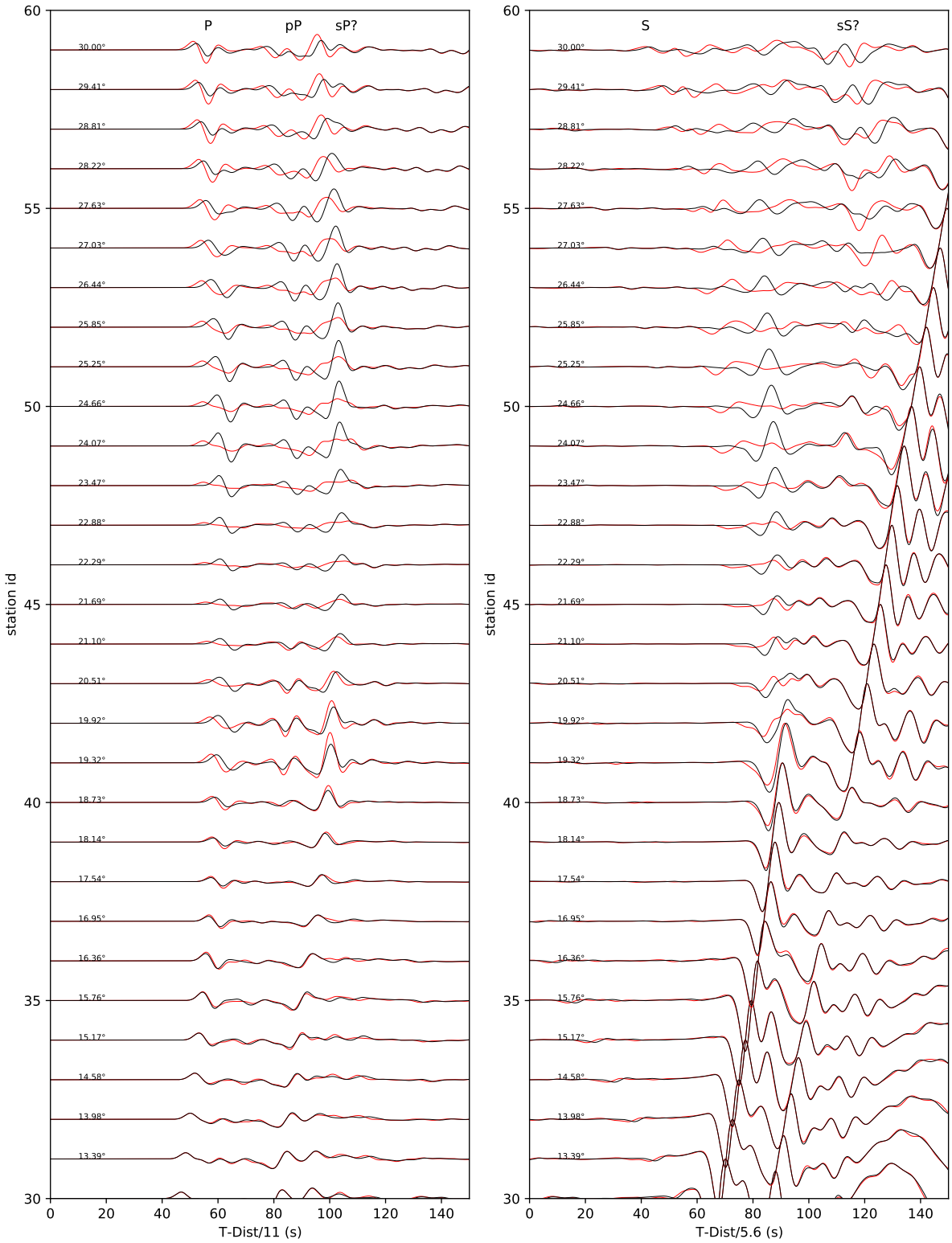

Fig. 3.9: Synthetic waveform comparison: The left panel is P wave-windowed waveforms whereas the right panel represent S wave-windowed waveforms. The red is the synthetics from the model with anomaly in Figure 3.6. The black is calculated from model without anomaly.

3.3 Adjoint Method FWI

3.3.1 Adjoint Theory

For the classic derivation of the adjoint method in the seismological applications, Tarantola (1988) gave a general formulation, which was followed by the advent of high-performance computation and development of finite-frequency theory (Tromp et al., 2005a; Fichtner et al., 2006a,b; Liu & Tromp, 2006) based on adjoint theory which could be derived through Born scattering theory or Lagrange multiplier. In this thesis, we briefly revisit simplified adjoint equation based on Lagrange multiplier and Fréchet kernels following Fichtner (2010).

For a more general physical theory symbolised by an operator $\mathbf{L}$ as the forward problem:

$$\mathbf{L}(\mathbf{s}, \mathbf{m}) = \mathbf{f} \tag{3.11}$$

The objective functional would be

$$\chi(\mathbf{m}) = \int_T \int_G \chi_1[\mathbf{s}(\mathbf{m}; \mathbf{x}, t)] dt d^3\mathbf{x} =< \chi_1 > \tag{3.12}$$

The adjoint equation:

$$\nabla_s \mathbf{L}^\dagger \mathbf{s}^\dagger = -\nabla_s \chi_1^\dagger \tag{3.13}$$

which can be simplified due to its linearity:

$$\mathbf{L}^\dagger(\mathbf{s}^\dagger) = -\nabla_s \chi_1^\dagger \tag{3.14}$$

$-\nabla_s \chi_1^\dagger$ acts as the force for the equation, namely the adjoint source $f^\dagger$.

The derivative of the objective functional is expressed:

$$\nabla_m \chi \delta\mathbf{m} =< \mathbf{s}^\dagger \cdot \nabla_m \mathbf{L} \delta\mathbf{m} >= \int_G \mathbf{K}_m \delta\mathbf{m} d^3\mathbf{x} \tag{3.15}$$

then the Fréchet kernel is:

$$\mathbf{K}_m = \int_T \mathbf{s}^\dagger \cdot \nabla_m \mathbf{L} dt \tag{3.16}$$

Application to Seismic wave equation

The Hooke's law (constitutive relation, equation 3.3) under the assumption of a linear viso-elastic rheology, the stress tensor $\mathbf{T}$ is related to the displacement gradient $\nabla\mathbf{s}$ via the constitute relation

$$\mathbf{T}(\mathbf{x}, t) = \int_{\tau=t0}^{t} \mathbf{C}(\mathbf{x}, t-\tau) : \nabla\mathbf{s}(\mathbf{x}, \tau) d\tau \tag{3.17}$$

Thus insert equation 3.17 into equation 3.1 we could derive the linear expression of the seismic wave equation through the operator $\mathbf{L}$

$$\mathbf{L}(\mathbf{s}, \rho, \mathbf{C}) = \mathbf{f} \tag{3.18}$$

$$\mathbf{L}(\mathbf{s}, \rho, \mathbf{C}) = \rho(\mathbf{x})\ddot{s}(\mathbf{x}, t) - \nabla \cdot \int_{\tau=t0}^{t} \dot{\mathbf{C}}(\mathbf{x}, t-\tau) : \nabla\mathbf{s}(\mathbf{x}, \tau) d\tau \tag{3.19}$$

Thus the adjoint equation would be

$$\rho\ddot{\mathbf{s}}^{\dagger} - \nabla \cdot \mathbf{T}^{\dagger} = -\nabla\chi_1^{\dagger} \tag{3.20}$$

The terminal and boundary conditions would be

$$\mathbf{s}^{\dagger}|_{t\geq t1} = \dot{\mathbf{s}}^{\dagger}|_{t\geq t1} = 0, \mathbf{n}\cdot\mathbf{T}^{\dagger}|_{\mathbf{x}\in\partial G} = 0 \tag{3.21}$$

Thus Equation 3.20 could be solved through the same method as for the solution of the regular wave equation, with $-\nabla\chi_1^{\dagger}$ as source term. t1 represents the end time of observation and forward simulation.

Substituting the wave equation defined in Equation 3.19 into equation 3.15, we could obtain

$$\nabla_m\chi\delta\mathbf{m} = \int_T\int_G \mathbf{s}^{\dagger}(t)\cdot[\delta\rho\ddot{\mathbf{s}}(t) - \nabla\cdot\int_{\tau=t0}^{t}\delta\dot{\mathbf{C}}(t-\tau):\nabla\mathbf{s}(\tau)d\tau]dtd^3\mathbf{x} \tag{3.22}$$

Integrating by parts we could derive:

$$\nabla_m\chi\delta\mathbf{m} = -\int_T\int_G \delta\rho\dot{\mathbf{s}}^{\dagger}(t)\cdot\dot{\mathbf{s}}(t)dtd^3\mathbf{x} + \int_T\int_G[\int_{\tau=t0}^{t}\nabla\mathbf{s}^{\dagger}(t):\delta\dot{\mathbf{C}}(t-\tau):\nabla\mathbf{s}(\tau)d\tau]dtd^3\mathbf{x} \tag{3.23}$$

Thus the Fréchet kernels related to density and elastic parameters could be derived as below

$$\mathbf{K}_{\rho} = -\int_T \dot{s}^{\dagger}(t)\cdot\dot{\mathbf{s}}dt \tag{3.24}$$

$$\mathbf{K}_{\mathbf{C}}(\tau) = \int_T \nabla s^{\dagger}(t)\otimes\nabla\mathbf{s}(t+\tau)dt \tag{3.25}$$

where $\otimes$ denote the tensor or dyadic products.

Considering the perfectly elastic medium, for which $\mathbf{C}$ keeps constant with time

$$\nabla_m\chi\delta\mathbf{m} = -\int_T\int_G \delta\rho\dot{\mathbf{s}}^{\dagger}(t)\cdot\dot{\mathbf{s}}(t)dtd^3\mathbf{x} + \int_T\int_G \nabla\mathbf{s}^{\dagger}(t):\delta\mathbf{C}:\nabla\mathbf{s}(t)dtd^3\mathbf{x} \tag{3.26}$$

Isotropic medium sensitivity kernels

For the isotropic medium, the components of $\mathbf{C}$ are given by

$$\mathbf{C}_{ijkl} = \lambda\delta_{ij}\delta_{kl} + \mu\delta_{ik}\delta_{jl} + \mu\delta_{il}\delta_{jk} \tag{3.27}$$

λ and μ denote the Lamé parameters. Thus, the complete derivative of χ is composed of three terms:

$$\nabla_m\chi\delta\mathbf{m} = \nabla_{\rho}\chi\delta\rho + \nabla_{\lambda}\chi\delta\lambda + \nabla_{\mu}\chi\delta\mu \tag{3.28}$$

with

$$\nabla_{\rho}\chi\delta\rho = -\int_T\int_G \delta\rho\dot{\mathbf{s}}^{\dagger}(t)\cdot\dot{\mathbf{s}}(t)dtd^3\mathbf{x} \tag{3.29}$$

$$\nabla_{\lambda}\chi\delta\lambda = \int_T\int_G \delta\lambda(\nabla\cdot\mathbf{s})(\nabla\cdot\mathbf{s}^{\dagger})dtd^3\mathbf{x} \tag{3.30}$$

$$\nabla_{\mu}\chi\delta\mu = \int_T\int_G \delta\mu[(\nabla\mathbf{s}^{\dagger}):(\nabla\mathbf{s}) + (\nabla\mathbf{s}^{\dagger}):(\nabla\mathbf{s})^T]dtd^3\mathbf{x} \tag{3.31}$$

The corresponding sensitivity kernels are:

$$\mathbf{K}_{\rho}^{0} = -\int_{T} \dot{\mathbf{s}}^{\dagger}(t) \cdot \dot{\mathbf{s}}(t) dt \tag{3.32}$$

$$\mathbf{K}_{\lambda}^{0} = \int_{T} (\nabla \cdot \mathbf{s})(\nabla \cdot \mathbf{s}^{\dagger}) dt = \int_{T} (tr\epsilon)(tr\epsilon^{\dagger}) dt \tag{3.33}$$

$$\mathbf{K}_{\mu}^{0} = \int_{T} [(\nabla \mathbf{s}^{\dagger}) : (\nabla \mathbf{s}) + (\nabla \mathbf{s}^{\dagger}) : (\nabla \mathbf{s})^{T}] dt = \int_{T} 2\epsilon^{\dagger} : \epsilon dt \tag{3.34}$$

where

$$\epsilon = \frac{1}{2}[(\nabla \mathbf{s}) + (\nabla \mathbf{s})^{T}] \tag{3.35}$$

With ρ v_p and v_s as independent parameters we have:

$$\mathbf{K}_{\rho} = \mathbf{K}_{\rho}^{0} + (v_p^2 - 2v_s^2)\mathbf{K}_{\lambda}^{0} + v_s^2 \mathbf{K}_{\mu}^{0} \tag{3.36}$$

$$\mathbf{K}_{v_s} = 2\rho v_s \mathbf{K}_{\mu}^{0} - 4\rho v_s \mathbf{K}_{\lambda}^{0} \tag{3.37}$$

$$\mathbf{K}_{v_p} = 2\rho v_p \mathbf{K}_{\lambda}^{0} \tag{3.38}$$

Radial anisotropic medium sensitivity kernels

The elastic tensor for radial anisotropic medium could be described by 5 independent components. Thus the full elastic tensor could be simplified as:

$$\begin{pmatrix} C_{rrrr} & C_{rr\phi\phi} & C_{rr\theta\theta} \\ C_{\phi\phi rr} & C_{\phi\phi\phi} & C_{\phi\phi\theta\theta} \\ C_{\phi\phi\theta\theta} & C_{\theta\theta\phi\phi} & C_{\theta\theta\theta\theta} \end{pmatrix} = \begin{pmatrix} \lambda+2\mu & \lambda+c & \lambda+c \\ \lambda+c & \lambda+c+2\mu & \lambda+a \\ \lambda+c & \lambda+a & \lambda+2\mu+a \end{pmatrix}$$

$$\begin{pmatrix} C_{\phi\theta\phi\theta} & C_{\phi\theta r\theta} & C_{\phi\theta\ r\phi} \\ C_{r\theta\phi\theta} & C_{r\theta r\theta} & C_{r\theta r\phi} \\ C_{r\phi\phi\theta} & C_{r\phi r\theta} & C_{r\phi r\phi} \end{pmatrix} = \begin{pmatrix} \mu & 0 & 0 \\ 0 & \mu+b & 0 \\ 0 & 0 & \mu+b \end{pmatrix}$$

Where **a** relates to the P anisotropy and **b** to S anisotropy, **c** can only be determined from P waves that do not travel in radial or horizontal directions. Meanwhile, a new parameter η is introduced by:

$$\eta = \frac{\lambda + c}{\lambda + a} \tag{3.39}$$

Thus the shear wave velocity could be expressed as:

$$v_{sv} = \sqrt{\frac{\mu + b}{\rho}} \tag{3.40}$$

$$v_{sh} = \sqrt{\frac{\mu}{\rho}} \tag{3.41}$$

The former represents the vertically polarised S wave whereas the latter horizontally polarised S wave for the horizontally propagating S wave.

Similarly,

$$v_{pv} = \sqrt{\frac{\lambda + 2\mu}{\rho}} \tag{3.42}$$

$$v_{ph} = \sqrt{\frac{\lambda + 2\mu + a}{\rho}} \tag{3.43}$$

The former is the vertically propagating P wave and the latter is horizontally propagating P wave.

Thus following Fichtner (2010), we briefly revisit the expression of sensitivity kernels with respect to physical parameters including ρ λ μ a b and c as below:

$$\mathbf{K}_\rho^0 = -\int_T \dot{\mathbf{s}}^\dagger(t) \cdot \dot{\mathbf{s}}(t) dt \tag{3.44}$$

$$\mathbf{K}_\lambda^0 = \int_T (tr\epsilon)(tr\epsilon^\dagger) dt \tag{3.45}$$

$$\mathbf{K}_\mu^0 = 2\int_T \epsilon^\dagger : \epsilon dt \tag{3.46}$$

$$\mathbf{K}_a^0 = \int_T (\epsilon_{\phi\phi}^\dagger + \epsilon_{\theta\theta}^\dagger)(\epsilon_{\phi\phi} + \epsilon_{\theta\theta}) dt \tag{3.47}$$

$$\mathbf{K}_b^0 = \int_T (\epsilon_{r\theta}^\dagger \epsilon_{r\theta} + \epsilon_{r\phi}^\dagger \epsilon_{r\phi}) dt \tag{3.48}$$

$$\mathbf{K}_c^0 = \int_T [\epsilon_{rr}(\epsilon_{\phi\phi}^\dagger + \epsilon_{\theta\theta}^\dagger) + \epsilon_{rr}^\dagger(\epsilon_{\phi\phi} + \epsilon_{\theta\theta})] dt \tag{3.49}$$

Thus for the seismological parameters

$$\begin{aligned} \mathbf{K}_\rho &= \mathbf{K}_\rho^0 + v_{SH}^2 \mathbf{K}_\mu^0 + (v_{PV}^2 - v_{SH}^2)\mathbf{K}_\lambda^0 + (v_{PH}^2 - v_{PV}^2)\mathbf{K}_\alpha^0 \\ &\quad + (v_{SV}^2 - v_{SH}^2)\mathbf{K}_b^0 + [2(1-\eta)v_{SH}^2 + \eta v_{PH}^2 - v_{PV}^2]\mathbf{K}_c^0 \\ &= \mathbf{K}_\rho^0 + \rho^{-1}(\mu\mathbf{K}_\mu^0 + \lambda\mathbf{K}_\lambda^0 + a\mathbf{K}_a^0 + b\mathbf{K}_b^0 + c\mathbf{K}_c^0) \end{aligned} \tag{3.50}$$

$$\mathbf{K}_{v_{SH}} = 2\rho v_{SH}[\mathbf{K}_\mu^0 - 2\mathbf{K}_\lambda^0 - \mathbf{K}_b^0 + 2(1-\eta)\mathbf{K}_c^0] \tag{3.51}$$

$$\mathbf{K}_{v_{SV}} = 2\rho v_{SV}\mathbf{K}_b^0 \tag{3.52}$$

$$\mathbf{K}_{v_{PH}} = 2\rho v_{PH}(\mathbf{K}_a^0 + \eta\mathbf{K}_c^0) \tag{3.53}$$

$$\mathbf{K}_{v_{PV}} = 2\rho v_{PV}(\mathbf{K}_\lambda^0 - \mathbf{K}_a^0 - \mathbf{K}_c^0) \tag{3.54}$$

3.3.2 Misfit and Adjoint Sources

Inverting surface seismic displacements to estimate subsurface seismic properties is a highly non-linear inverse problem. Two general approaches to the problem are direct search algorithms and linearization techniques based on the gradient of specific misfit functions. The direct search method samples the model parameter space in a stochastic way and tries to find acceptable models that produce misfits to the data below a certain threshold. The gradient method starts from an initial model and updates the model along a direction based on the model gradient of the misfit function. Since this approach involves an approximate linearization of a non-linear problem, model updates are made iteratively using techniques such as the non-linear conjugate gradient method (Fletcher & Reeves, 1964) or quasi-Newton methods, such as limited-memory BFGS (Liu & Nocedal, 1989). The definition of misfit function is crucial for defining the information we wish to extract. In seismology, there are several classic definitions of misfit functions including L^2, Cross-Correlation-Time-Shift, Time-Frequency Phase Shift, Cross-Correlation-Coefficient, Multitaper-Time-Shift. In this chapter, the definitions and corresponding adjoint sources for the functions are given as follow:

$\mathbf{L}^2$ Waveform Misfit

This is the simplest of all misfits and is defined as the squared difference between observed and synthetic data (Tromp et al., 2005a). The misfit $\chi(\mathbf{m})$ for a given Earth model $\mathbf{m}$ and a single receiver and component is given by

$$\chi(\mathbf{m}) = \frac{1}{2}\int_0^T \left|\mathbf{d}(t) - \mathbf{s}(t,\mathbf{m})\right|^2 dt \tag{3.55}$$

$\mathbf{d}(t)$ is the observed displacement data and $\mathbf{s}(t,\mathbf{m})$ the synthetic data.

The adjoint source for the same receiver and component is given by

$$f^\dagger(t) = -\left[\mathbf{d}(T-t) - \mathbf{s}(T-t,\mathbf{m})\right] \tag{3.56}$$

Cross Correlation Time Shift

Traveltime misfits simply measure the squared traveltime difference and a single receiver and component is given by

$$\chi(\mathbf{m}) = \frac{1}{2}\left[\tau^{\mathbf{d}} - \tau^{\mathbf{s}}(\mathbf{m})\right]^2 \tag{3.57}$$

$\tau^{\mathbf{d}}$ is the observed traveltime, and $\tau^{\mathbf{d}}$ the predicted traveltime in Earth model $\mathbf{m}$.

In practice, traveltime difference $\triangle\tau(\mathbf{m}) = \tau^{\mathbf{d}} - \tau^{\mathbf{s}}(\mathbf{m})$ is measured by cross correlating observed and predicted waveforms (Chen et al., 2007a).

The adjoint source for the same receiver and component is then given by

$$f^\dagger(t) = -\triangle\tau(\mathbf{m})\ \frac{1}{N}\ \dot{\mathbf{s}}(T-t,\mathbf{m}) \tag{3.58}$$

N is a normalization factor given by

$$N = \int_0^T \mathbf{s}(t,\mathbf{m})\ \ddot{\mathbf{s}}(t,\mathbf{m})dt \tag{3.59}$$

which plays the role in balancing (normalizing) the absolute amplitudes of the synthetics in adjoint sources.

Multitaper Time Shift

The misfit $\chi_P(\mathbf{m})$ measures frequency-dependent phase differences estimated with multitaper approach (Zhou et al., 2004; Tape, 2009). For a single receiver, the misfit is defined by:

$$\chi_P(\mathbf{m}) = \frac{1}{2}\int_0^W W_P(w)\left|\frac{\tau^{\mathbf{d}}(w) - \tau^{\mathbf{s}}(w,\mathbf{m})}{\sigma_P(w)}\right|^2 dw \tag{3.60}$$

$\tau^{\mathbf{d}}(w)$ is the frequency-dependent phase travel time of the observed data; $\tau^{\mathbf{s}}(w,\mathbf{m})$ the frequency-dependent phase travel time of the synthetic data. The function $W_P(w)$ denotes frequency-domain taper corresponding to the frequency range over which the measurements are assumed reliable. $\sigma_P(w)$ is associated with the traveltime uncertainty introduced in making measurements, which can be estimated with cross-correlation method, or Jackknife multitaper approach. Thus the travel time difference would be $\triangle\tau(\omega,\mathbf{m}) = \tau^{\mathbf{d}}(\omega) - \tau^{\mathbf{s}}(\omega,\mathbf{m})$ for a particular phase.

The tapered version of observed and synthetic waveforms could be represented by:

$$\mathbf{d}_j(t) = \mathbf{d}(t)\mathbf{h}_j(t) \tag{3.61}$$

$$\mathbf{s}_j(t,m) = \mathbf{s}(t)\mathbf{h}_j(t) \tag{3.62}$$

where $\mathbf{h}_j(t)$ is the taper which could be prolate spheroidal eigentapers (Tape, 2009).

Each windowed pulse on an individual seismogram is characterized by a (complex) transfer function from the modeled synthetics to the observed data

$$\mathbf{d}(\omega) = \mathbf{T}(\omega) * \mathbf{s}(\omega) \tag{3.63}$$

Then the transfer function could be expressed as:

$$\mathbf{T}(\omega) = \frac{\sum_j \mathbf{d}_j(\omega)\mathbf{s}_j^*(\omega)}{\sum_j \mathbf{s}_j(\omega)\mathbf{s}_j^*(\omega)} = \exp[-i\omega\Delta\tau(\omega)][1 + \Delta ln\mathbf{A}(\omega)] \tag{3.64}$$

the asterisk atop $s(\omega)$ denoting complex conjugation

Thus the time shift would be expressed:

$$\Delta\tau(\omega,\mathbf{m}) = \frac{-1}{\omega}\tan^{-1}(\frac{\Im m[\mathbf{T}(\omega)]}{\Re e[\mathbf{T}(\omega)]}) \tag{3.65}$$

$$\Delta \ln \mathbf{A}(\omega) = |\mathbf{T}(\omega)| - 1 \tag{3.66}$$

The adjoint source for a receiver is given by

$$f_P^\dagger(\omega) = \sum_j h_j(\omega)P_j(\omega) \tag{3.67}$$

in which $h_j(t)$ is one (the jth) of multi-tapers.

$$P_j(t) = 2\pi W_p(t) * \Delta\tau(t) * p_j(t) \tag{3.68}$$

$$P_j(w) = 2\pi W_p(w)\Delta\tau(w)p_j(w); \tag{3.69}$$

$$p_j(w) = \frac{iws_j(\omega)}{\sum_k (iws_k(\omega))(iws_k(\omega))^*}; \tag{3.70}$$

Time-Frequency Phase Shift

The time Frequency Phase Misfit was suggested by Fichtner et al. (2008); Fichtner (2010) and Kristeková et al. (2009). It measures a misfit in phase between synthetic seismograms ($\mathbf{s}(t,\mathbf{m})$) and recorded seismograms ($\mathbf{d}(t)$). In order to analyse the frequency content of the data with time by calculating the Fourier transform of $\mathbf{d}(t)$ by multiplication with a sliding time window function h(t-$\tau(t)$), centered around $\tau(t)$:

$$\tilde{\mathbf{d}(t)} = \mathbf{F}_h[\mathbf{d}](t,\omega) = \frac{1}{\sqrt{2\pi}}\int_\infty^{-\infty} \mathbf{d}(\tau)h^*(\tau - t)e^{-i\omega\tau}d\tau \tag{3.71}$$

Equivalent definition for synthetic $\mathbf{s}(t,\mathbf{m})$. Thus it is based on the time-frequency transform of both data and synthetics. Thus the $\mathbf{F}_h$ is then referred to as the Gabor transform. The phase misfit is defined by:

$$\chi_P(\mathbf{m}) = \int_{R^2} W_p^2(t,\omega)[\phi_i^s(t,\omega,\mathbf{m}) - \phi_i^d(t,\omega)]^2 dtd\omega \tag{3.72}$$

where $\tilde{\mathbf{d}}(t,\omega) = |\mathbf{d}(t,\omega)|e^{\mathbf{i}\phi^{\mathbf{d}}(t,\omega)}$ and $\tilde{\mathbf{s}}(t,\omega) = |\mathbf{s}(t,\omega)|e^{\mathbf{i}\phi^{\mathbf{s}}(t,\omega)}$

The weighting function is expressed and used for excluding phase discontinuities, selecting and weighing particular waveforms (improving low amplitude signals) and reducing the influence of seismic noise:

$$W_p = W_T(t)W_F(\omega)log(1+|\tilde{u}|)/max(log(1+|\tilde{u}|)) \tag{3.73}$$

Where $W_T(t)$,W_F denote Gaussian time and frequency windows.

The adjoint source for displacement seismograms:

$$f_P^{\dagger}(t) = \chi_p^{-1}\Im m \int_{\mathbf{R}^2} W_p^2(t,\omega,\mathbf{m})[\phi_i^s(t,\omega) - \phi_i^d(t,\omega)][\frac{\tilde{u}_i(t,\omega)}{|\tilde{u}_i(t,\omega)|^2}h(\tau-t)e^{i\omega\tau}]dtd\omega \tag{3.74}$$

Where $h(\tau - t)$ is a sliding window function (e.g. a gaussian).

An advantage of the time frequency phase misfit over the cross correlation time shift (which also measures phase/time shift) is that this gives a measurement of misfit as a function of time and frequency while the cross correlation only gives a single valued estimate for each window.

Cross Correlation Coefficient Misfit

This misfit function measure is as simple as the L^2 waveform misfit (Matzel & Grand, 2004; Tao et al., 2017) and is defined as the vector product between observed and synthetic data. The misfit $\chi(\mathbf{m})$ for a given Earth model $\mathbf{m}$ and a single receiver and component is given by

$$\chi(\mathbf{m}) = 1 - \frac{\int_0^T \mathbf{d}(t)\cdot\mathbf{s}(t,\mathbf{m})dt}{\sqrt{\int_0^T |\mathbf{d}(t)|^2dt \cdot \int_0^T |\mathbf{s}(t,\mathbf{m})|^2dt}} \tag{3.75}$$

The corresponding adjoint source is

$$f^{\dagger}(t) = -W^{-1}(\mathbf{d}(T-t) - A\mathbf{s}(T-t,\mathbf{m})) \tag{3.76}$$

where $W = \sqrt{\int |\mathbf{d}(t)|^2dt \cdot \int |\mathbf{s}(t,\mathbf{m})|^2dt}$ is a normalization factor.

$A = \int \mathbf{d}(t)\cdot\mathbf{s}(t,\mathbf{m})dt / \int |\mathbf{s}(t,\mathbf{m})|^2dt$ is the amplitude ratio factor.

This adjoint source is different from the adjoint sources of the waveform difference because of the additional magnitude normalization and amplitude ratio terms. The magnitude normalization term leads to equal weights for each time window, regardless of their amplitudes. The amplitude ratio term also removes the absolute amplitude ratio between data and synthetics from the misfit function. This feature is desirable because the absolute amplitude can be hard to model as it can be affected by many factors difficult to incorporate in simulations, as discussed above. However,the relative amplitudes within a time window still contain important information that constrains the velocity structure and is less affected by uncertainties in the source parameters or receiver site effects.

3.3.3 Comparison tests for different adjoint sources

Single earthquake benchmark tests for P wave

Different misfit functions are sensitive to different target structures and aspects of the waveform differences. In this part, I continue from above to compare different misfit functions and adjoint sources with misfit kernels. Different from the model configuration from subsection 3.2.2, here I decrease the model scale down to 400 km in depth and 25° in horizontal direction with a 6 km grid spacing to avoid the interference from mantle transition zone discontinuities. The minimum wavelength in the simulation is around 12 km (dominant time-period is 5 s). The earthquake source location and receiver spacing is summarized in Figure 3.10. The target model incorporates a high velocity anomaly in the upper mantle

as perturbation of the modified 1D PREM model (Dziewonski & Anderson, 1981), meanwhile, we also consider a 'halfway' model which is a smoothed version (Gaussian smoothing with σ=24 km) of the target model (Figure 3.10). Compared to the 1D initial model (PREM), the smeared 'halfway' model often plays the role of the final results for almost all traditional raytracing tomography and travel-time FWI due to many reasons, for example, the data coverage, the application of regularization and smoothing operation. The identification of sharp interfaces through the FWI is still on the horizon for seismology. In the following, we will test and present the performances of different misfit functions for body wave 'travel-time' phase shift identification (from 1D model to 'halfway') and sharp velocity edges ('halfway' to target model) to test the capabilities of identifying the sharpness of velocity anomalies.

Simulated wavefields for the horizontal component X direction based on the initial 1D model, halfway model and target model are illustrated in Figure 3.11-3.13. With the smoothed high velocity anomaly (halfway model, Figure 3.10), the direct P phase arrives earlier than in the 1D model (Figure 3.11-Figure 3.12). Figure 3.14 compares the P wave waveforms between the 1D model and halfway model. Clear earlier arrivals could be observed from receiver 38 to 60. In contrast, the target model with strong interfaces excites secondary arrival behind the main accelerated P phase (Figure 3.13). From the comparison between the target model and halfway model, we could clearly observe the time shift is very weak for the main P wave phase, however, the secondary arrival appears since Receiver 45 (Station ID 45, Figure 3.16).

In the following I will briefly introduce benchmark tests for different misfits and adjoint sources based on the theory presented in last subsection. For simplicity, I illustrate the waveform differences and adjoint sources for P wave phase from Receiver 37, 44 and 54 (Figure 3.17-3.18, 3.21-3.22 and 3.25-3.26). The misfit kernels are calculated for Receiver 54 (Figure 3.19, 3.23 and 3.27) and all receivers (Figure 3.20, 3.24 and 3.28) specifically. Comparing the halfway model with the initial 1D model, the waveform difference is mainly dominated by travel time difference (Figure 3.17 - 3.18) which is also reflected in the misfit kernel for Receiver 54 (Figure 3.19) and all receivers (Figure 3.20).

The comparison between the initial model and the target model displays a significant time shift of P wave phase, the secondary arrival of P from the target model seems fitting the first arrival of P from the initial model for receiver 54 (Figure 3.21-3.22), which should be avoided in full waveform inversion since such 'cycle skipping' could easily cause local minimum. In such case, the misfit kernel is almost the same for all misfit functions (Figure 3.23-3.24). In contrast, the comparison between the halfway model and the target model displays weak time shifts of P wave phase, thus the secondary arrival of P dominates the adjoint sources and waveform misfits, as a consequence, the adjoint sources from different definitions show very different features for Receiver 54 (Figure 3.25-3.26). Back to the difference between the target model and the halfway model in Figure 3.10, the velocity inside the box should be increased while decreased outside the box from the halfway model to the target model, thus how to recover the significant velocity contrast becomes the goal from the halfway model to the target model.

In Figure 3.27-3.28, different definitions of misfit function and adjoint sources present very different kernels reflecting the capacity to recover the strong interface. The misfit kernel of multitaper time shift and CC time shift could reflect the high velocity anomaly (blue) atop and below the box, which represent the negative direction to reduce the velocity from the half way model but failed to reflect the velocity anomaly inside the box and even give a wrong direction. For the TF phase shift function, the high velocity atop the box could be reflected while the low velocity (red) inside the box is only reflected weakly. The L2 and CCC misfit could better reflect the strong contrast across the box (Figure 3.27-3.28).

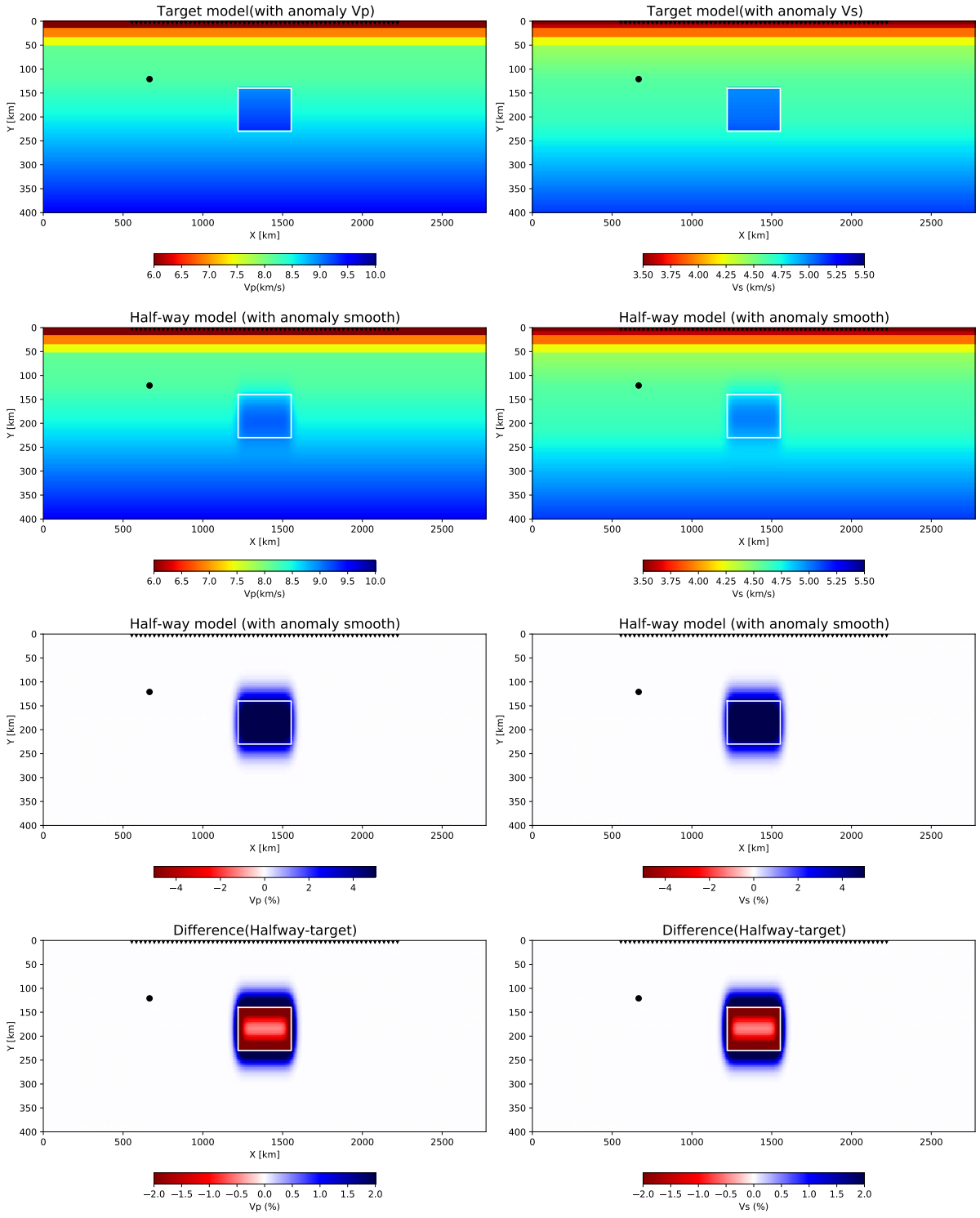

Fig. 3.10: Synthetic model through 2D P-SV plane for Specfem2D calculation. The velocity and depth have been adapted to the cartesian system through Earth flattening transformation. The left four panels denote the Vp and right four panels are Vs. The bottom two models denote the model difference between the target model (with strong and sharp high velocity anomaly) and the 'half-way' model (smoothed version). The black dots denote the location of the source, inverse triangles denote the receivers.

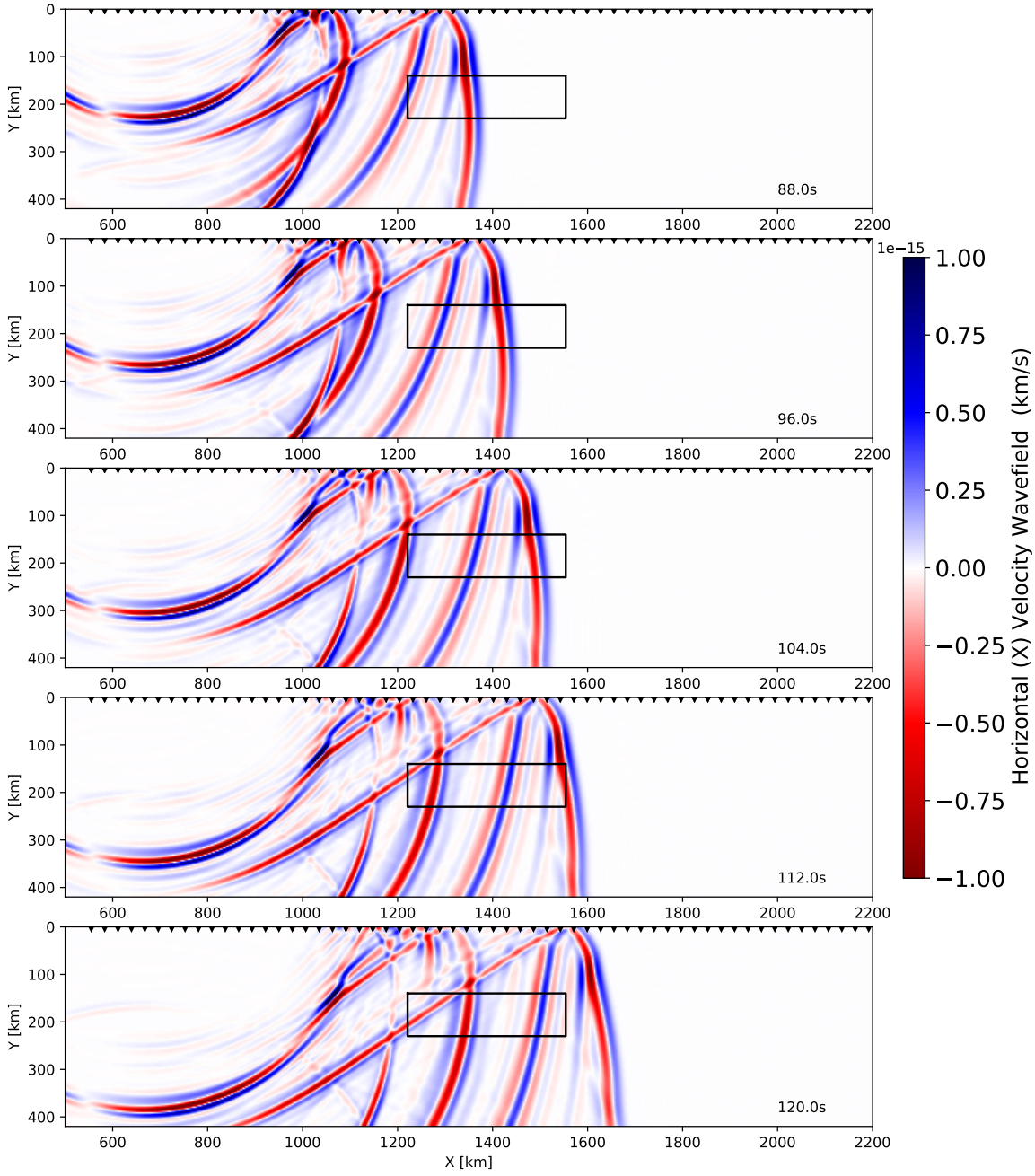

Fig. 3.11: Synthetic velocity wavefield snapshot for horizontal X component based on 1D initial model, inverse triangles denote the receivers. Black rectangular box marks the position of the high velocity anomaly in Figure 3.10 for comparison with Figure 3.12 and 3.13.

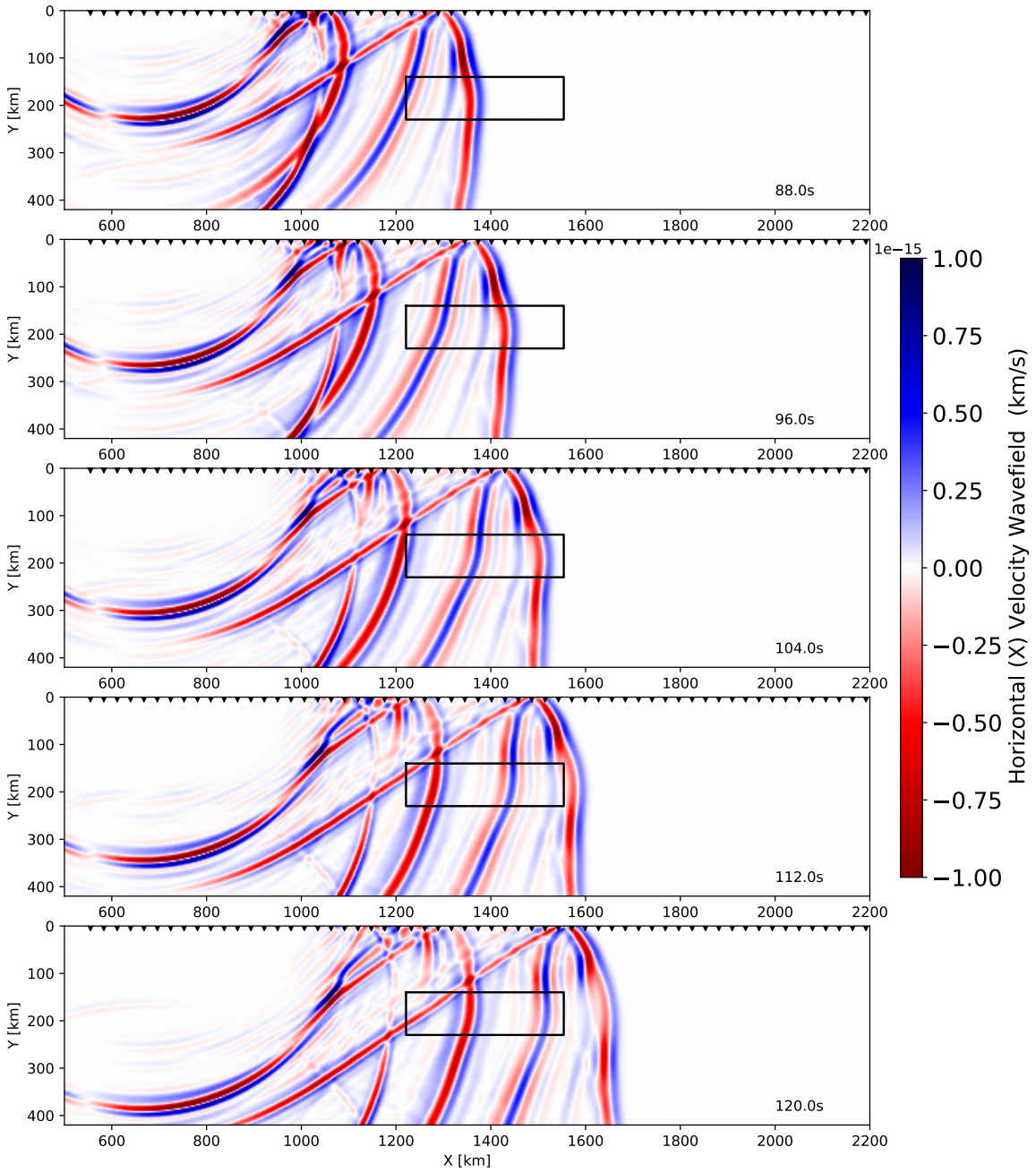

Fig. 3.12: Synthetic velocity wavefield snapshot for horizontal X component based on halfway model, inverse triangles denote the receivers. Black rectangular box marks the position of the high velocity anomaly in Figure 3.10

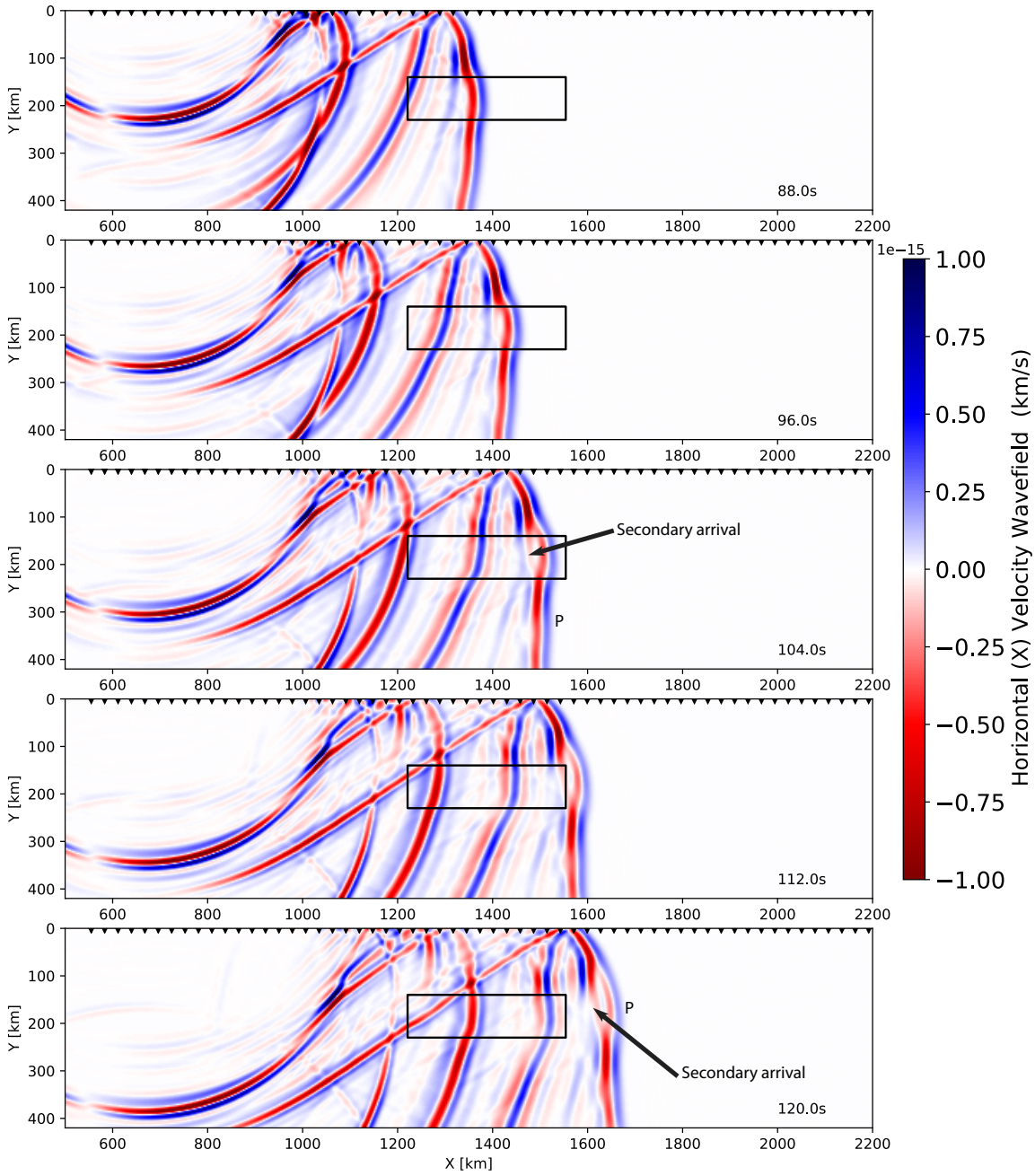

Fig. 3.13: Synthetic velocity wavefield snapshot for horizontal X component based on target model, inverse triangles denote the receivers. Black rectangular box mark the position of the high velocity anomaly in Figure 3.10. Black arrows denote the position of the 'secondary arrival' caused by sharp interface of the high velocity anomaly.

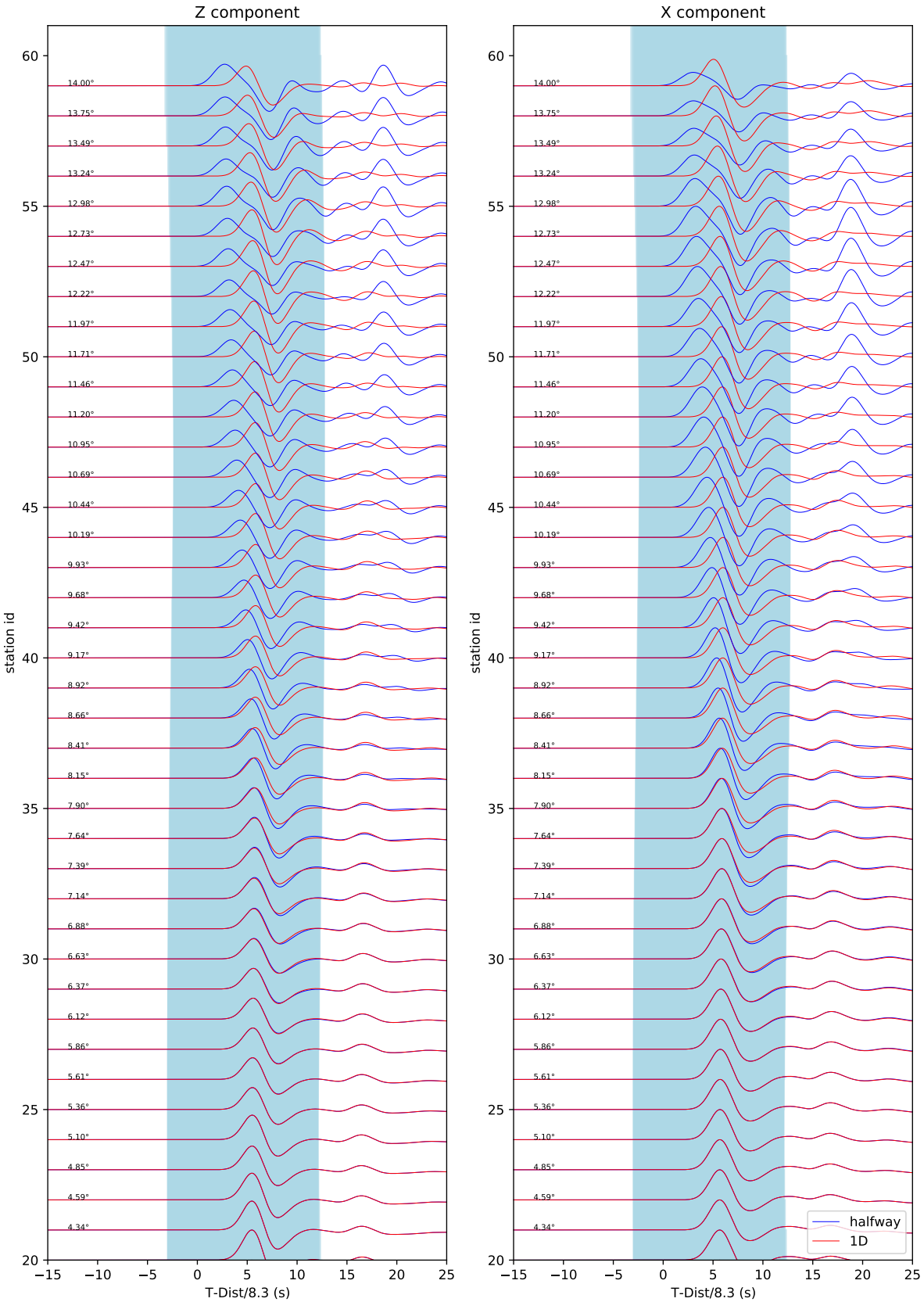

Fig. 3.14: Synthetic waveform comparison: The blue is the synthetics from the halfway model in Figure 3.6. The red are calculated from initial 1D model. The left panel is vertical Z component while the right is horizontal X component. The light blue shaded area denotes the time window for the P phase.

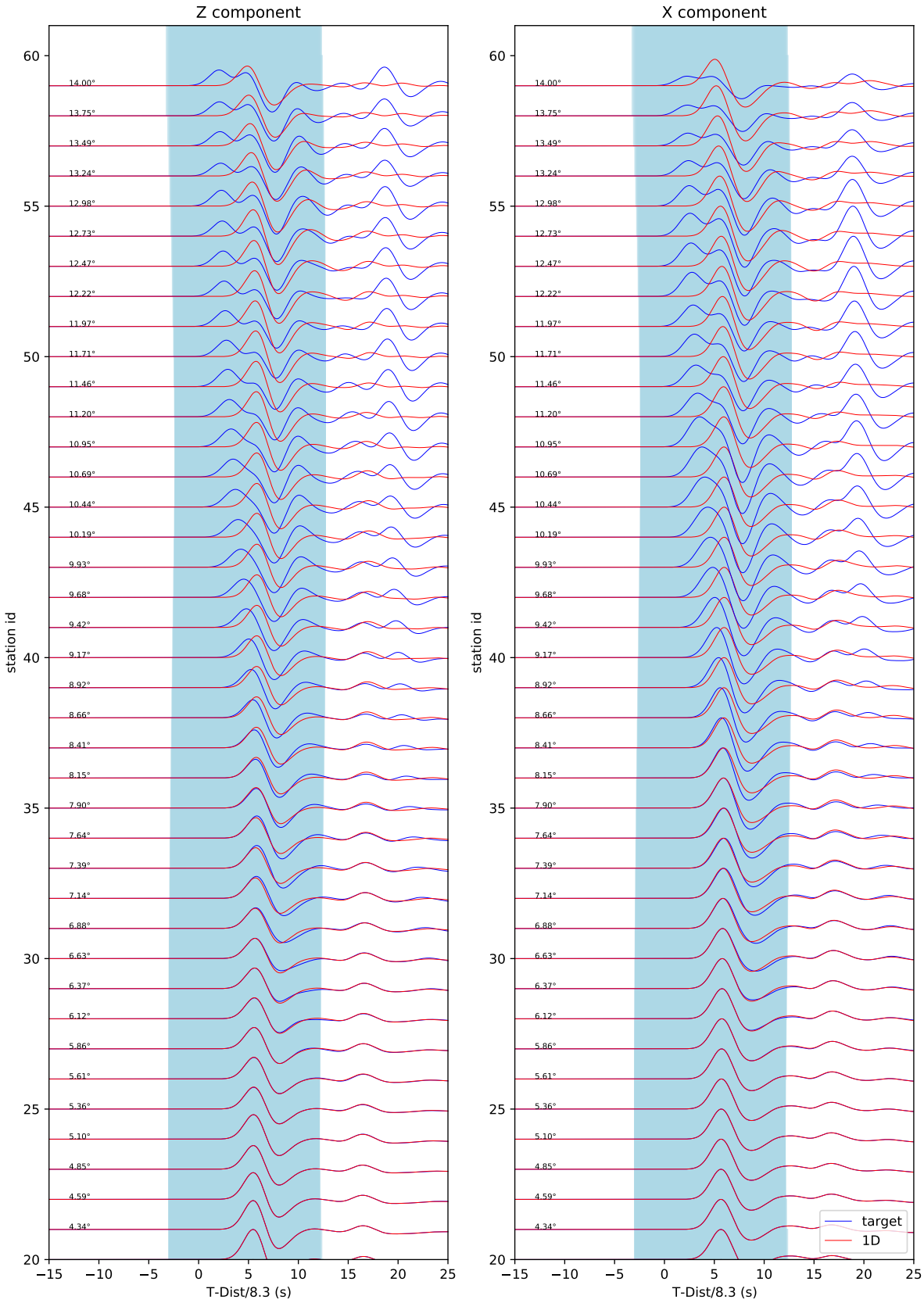

Fig. 3.15: Synthetic waveform comparison: The blue are the synthetics from the target model in Figure 3.6. The red are calculated from initial 1D model. The left panel is vertical Z component while the right is horizontal X component. The light blue shaded area denotes the time window for the P phase.

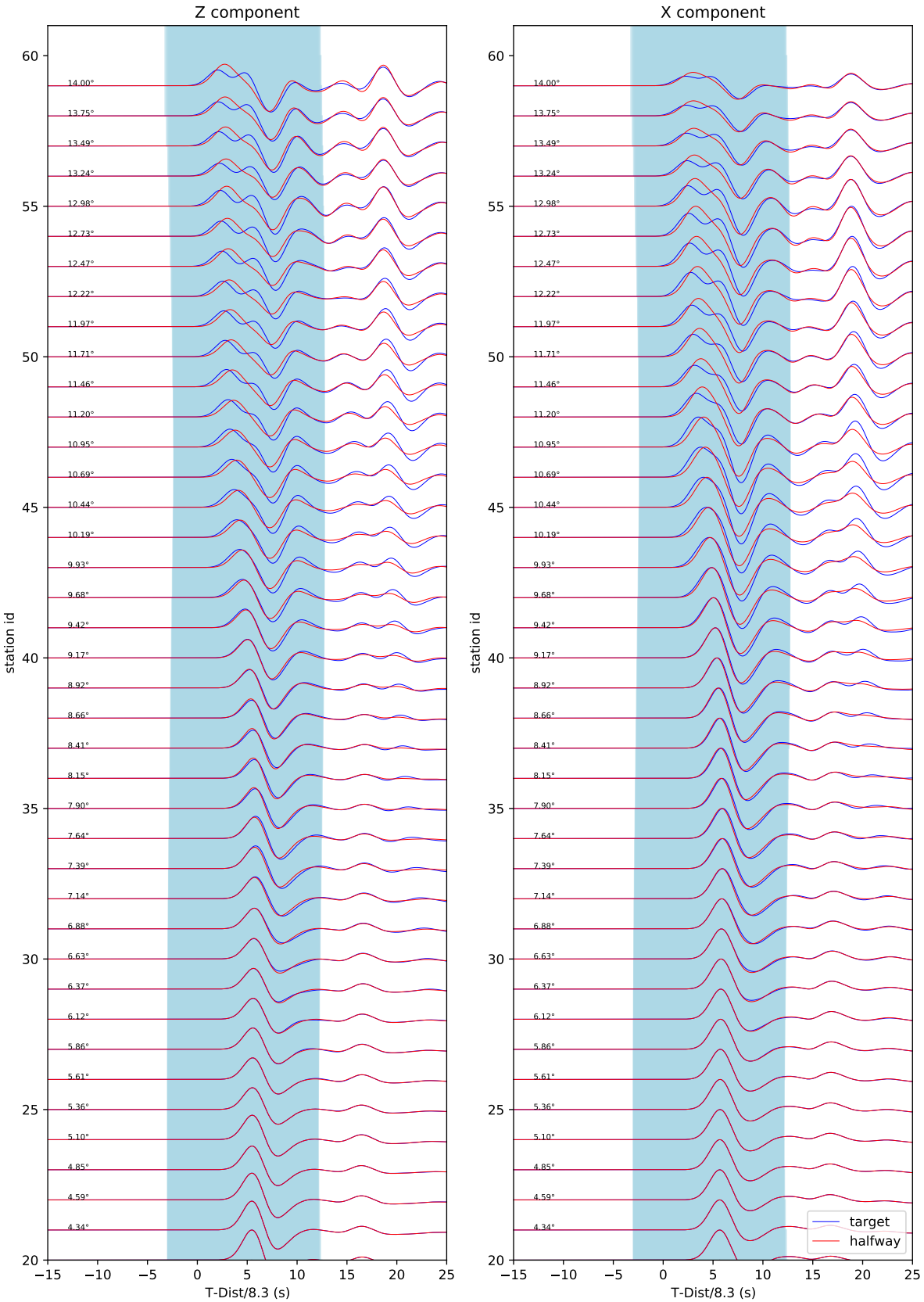

Fig. 3.16: Synthetic waveform comparison: The blue are the synthetics from the target model in Figure 3.6. The red are calculated from halfway model. The left panel is vertical Z component while the right is horizontal X component. The light blue shaded area denotes the time window for the P phase.

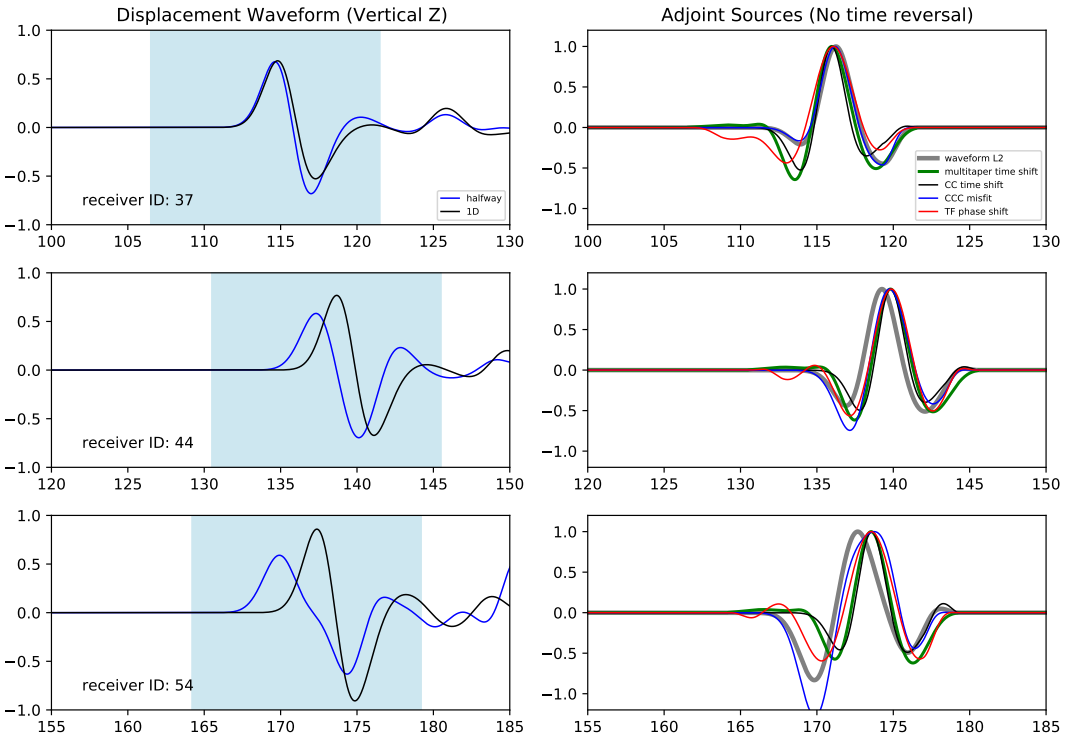

Fig. 3.17: Left: Z component Waveform comparison between the 1D initial model and halfway model for three receivers. Right: corresponding adjoint sources for three receivers. The light blue shaded area denotes the time window for the P phase.

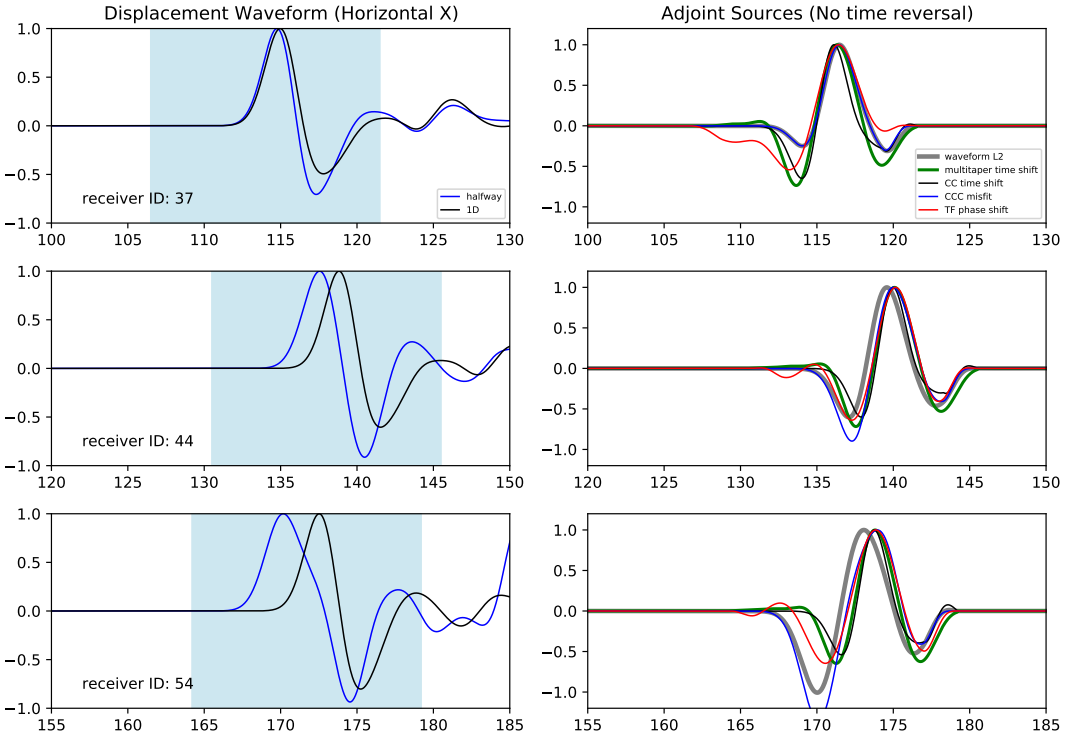

Fig. 3.18: Left: X component Waveform comparison between the 1D initial model and halfway model for three receivers. Right: corresponding adjoint sources for three receivers. The light blue shaded area denotes the time window for the P phase.

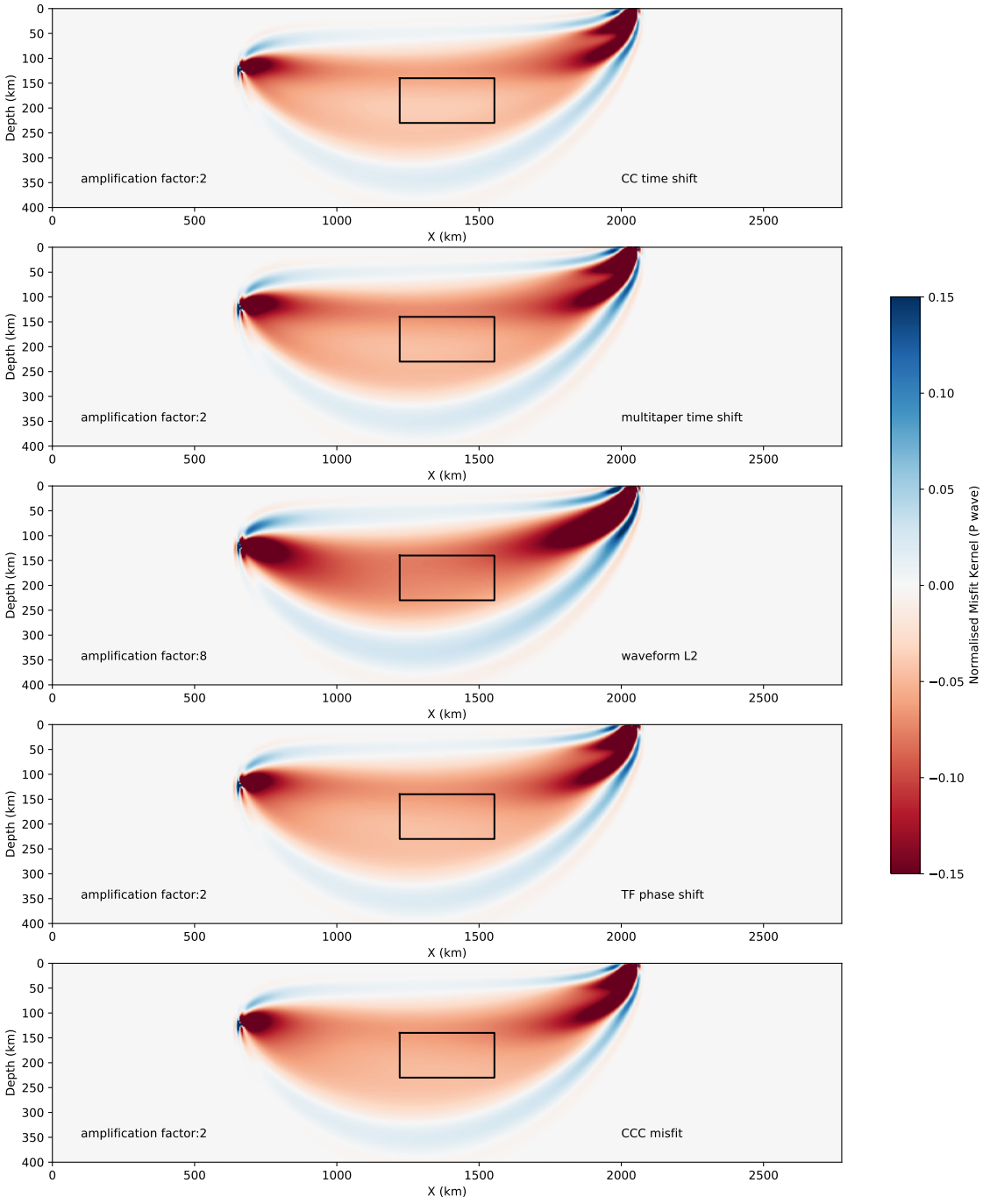

Fig. 3.19: Misfit kernels (P) of five misfit functions defined in subsection 3.3.2 for Receiver 54 (Figure 3.17-3.18). The misfits are calculated from initial model to the halfway model (initial-halfway)

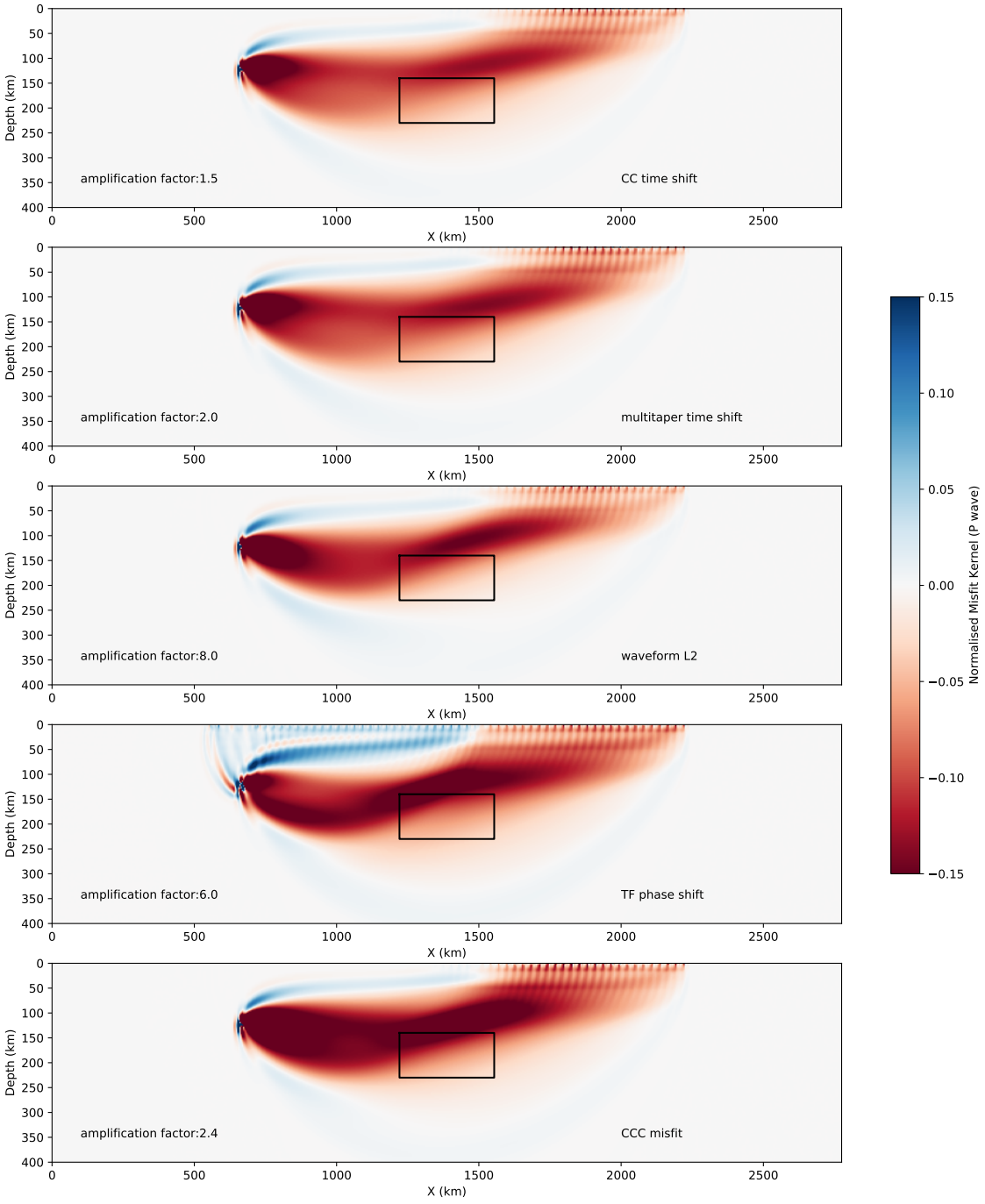

Fig. 3.20: Misfit kernels (P) of five misfit functions defined in subsection 3.3.2 for all receivers. The misfits are calculated from initial model to the halfway model (initial-halfway)

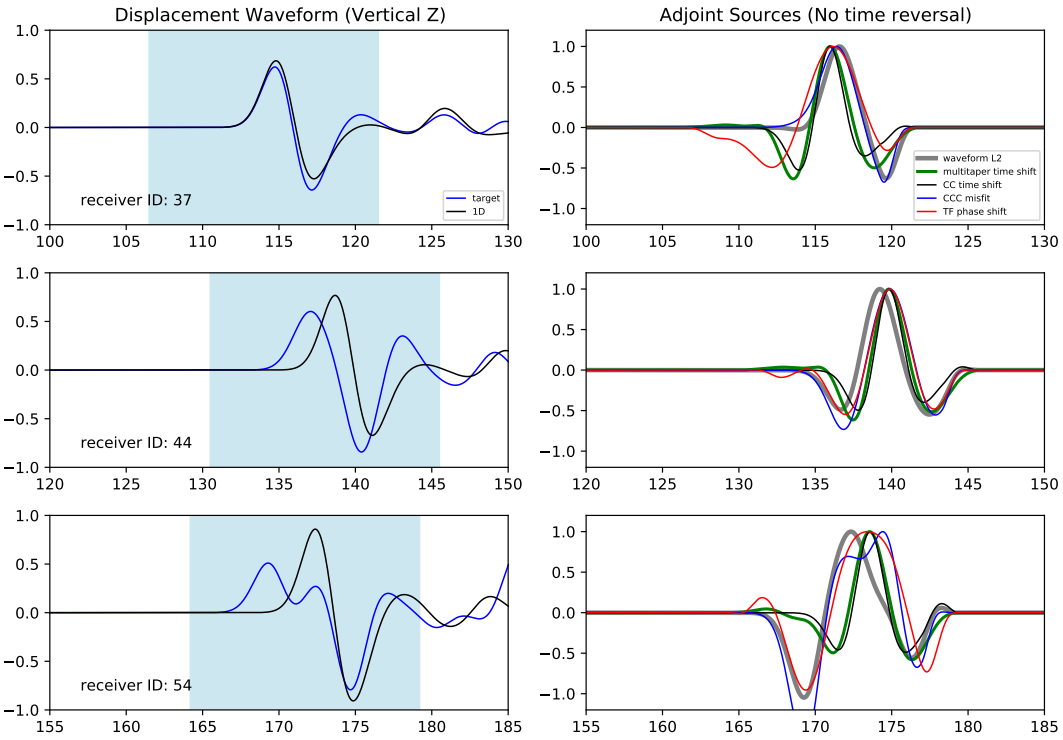

Fig. 3.21: Left: Z component Waveform comparison between the 1D initial model and target model for three receivers. Right: adjoint sources for three receivers. The light blue shaded area denotes the time window for the P phase.

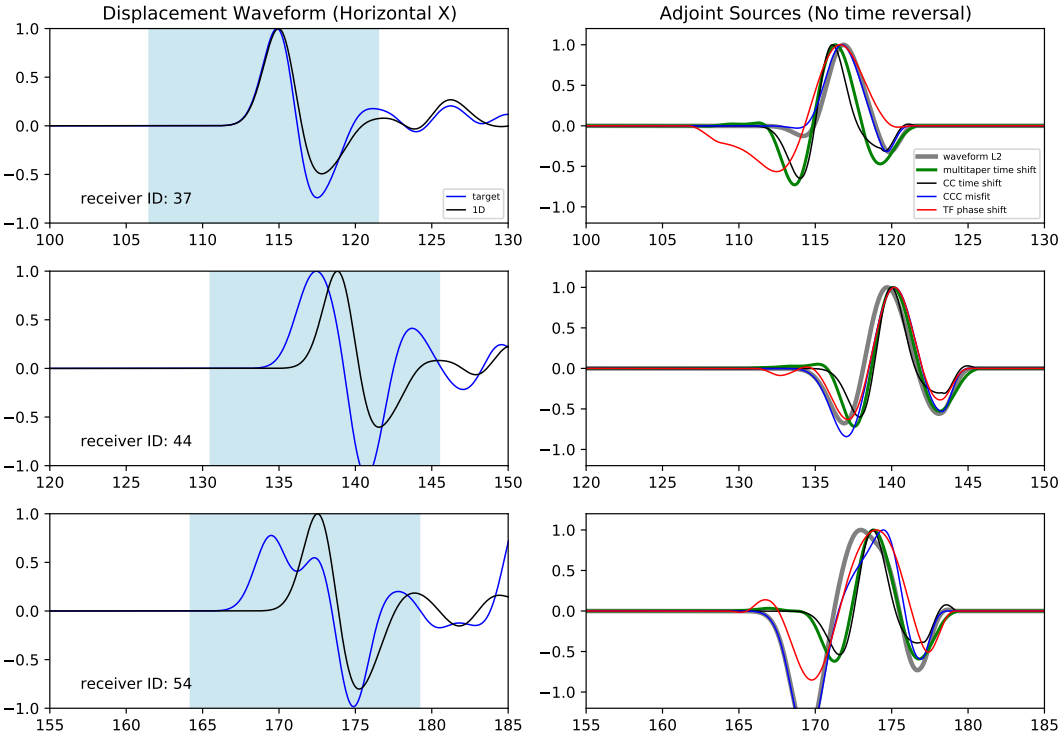

Fig. 3.22: Left: X component Waveform comparison between the 1D initial model and target model for three receivers. Right: adjoint sources for three receivers. The light blue shaded area denotes the time window for the P phase.

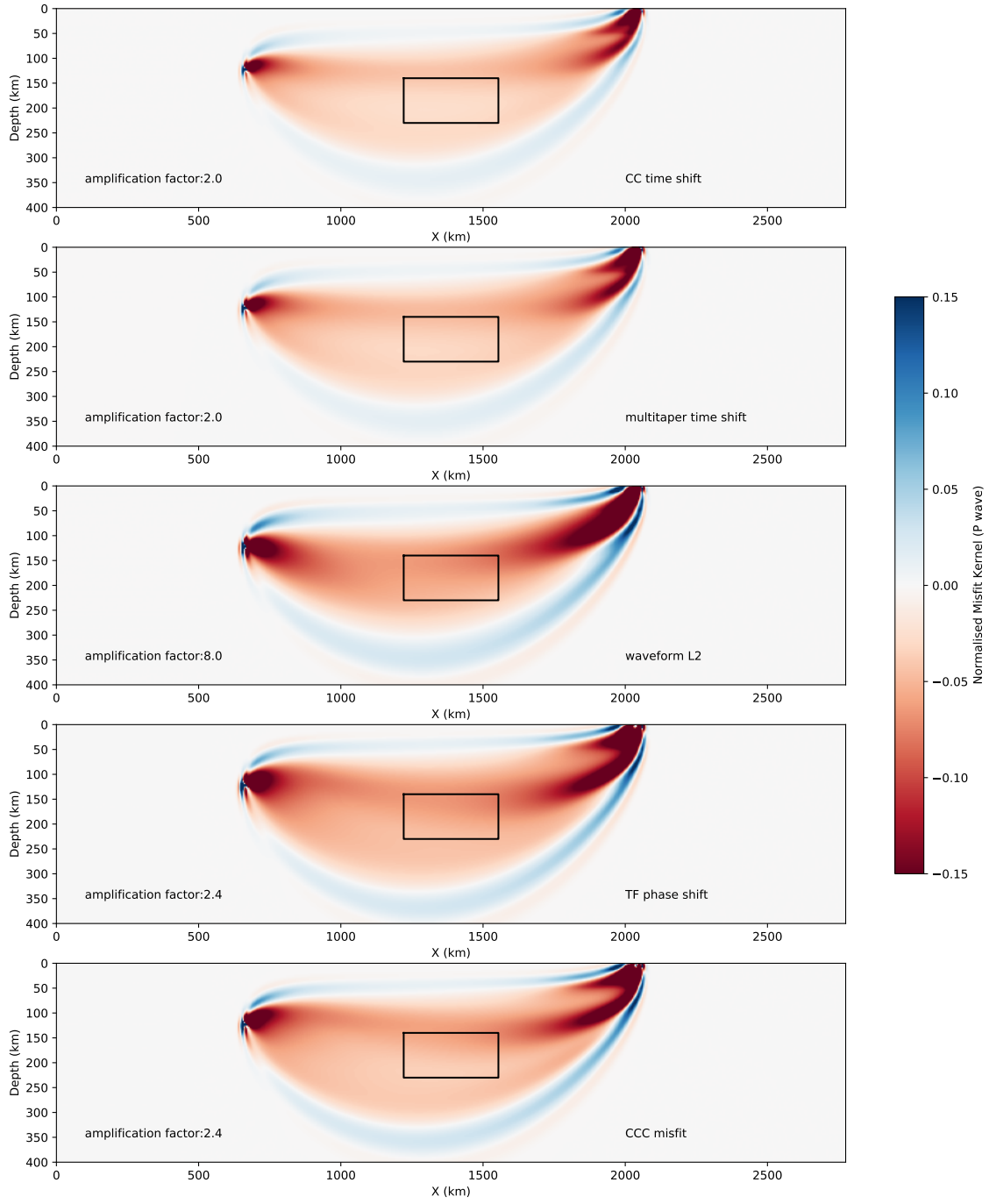

Fig. 3.23: Misfit kernels (P) of five misfit functions defined in subsection 3.3.2 for Receiver 54 (Figure 3.21-3.22). The misfits are calculated from initial model to the target model (initial-target)

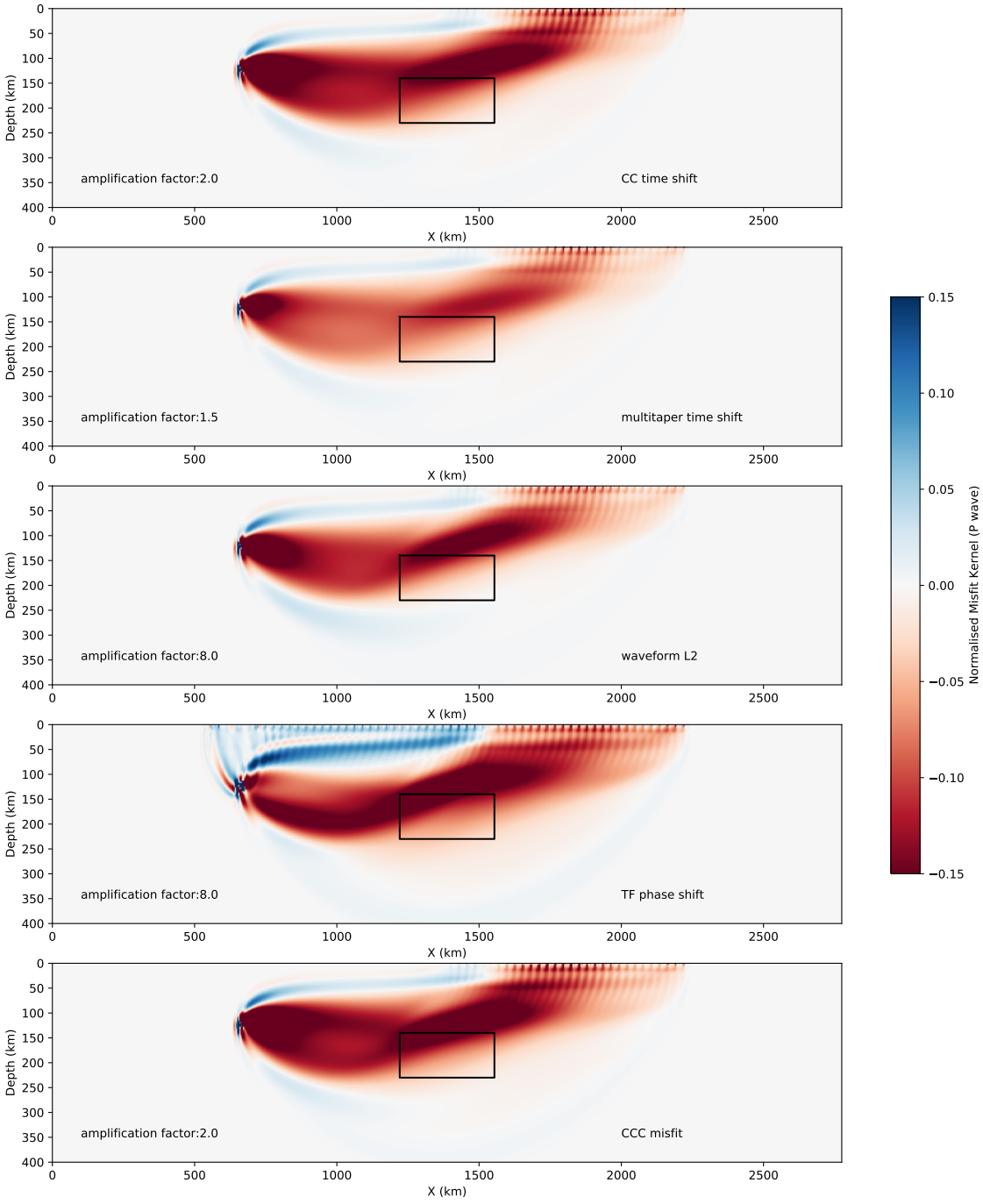

Fig. 3.24: Misfit kernels (P) of five misfit functions defined in subsection 3.3.2 for all receivers. The misfits are calculated from initial model to the target model (initial-target)

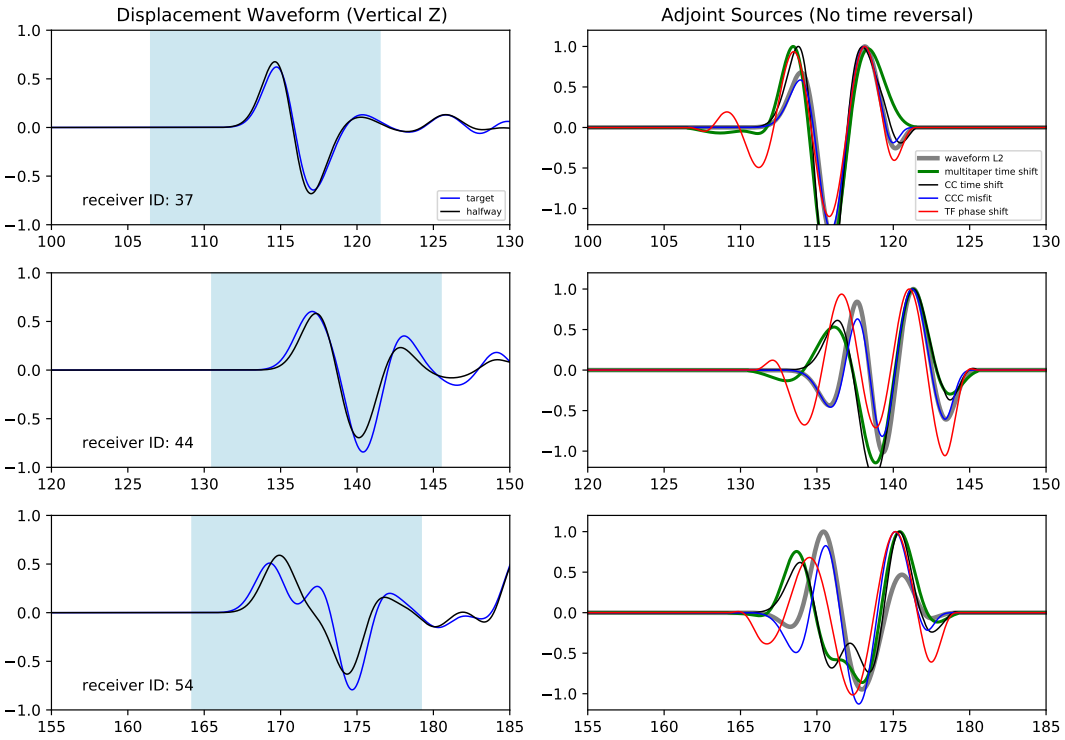

Fig. 3.25: Left: Z component Waveform comparison between the halfway model and target model for three receivers. Right: adjoint sources for three receivers. The light blue shaded area denotes the time window for the P phase.

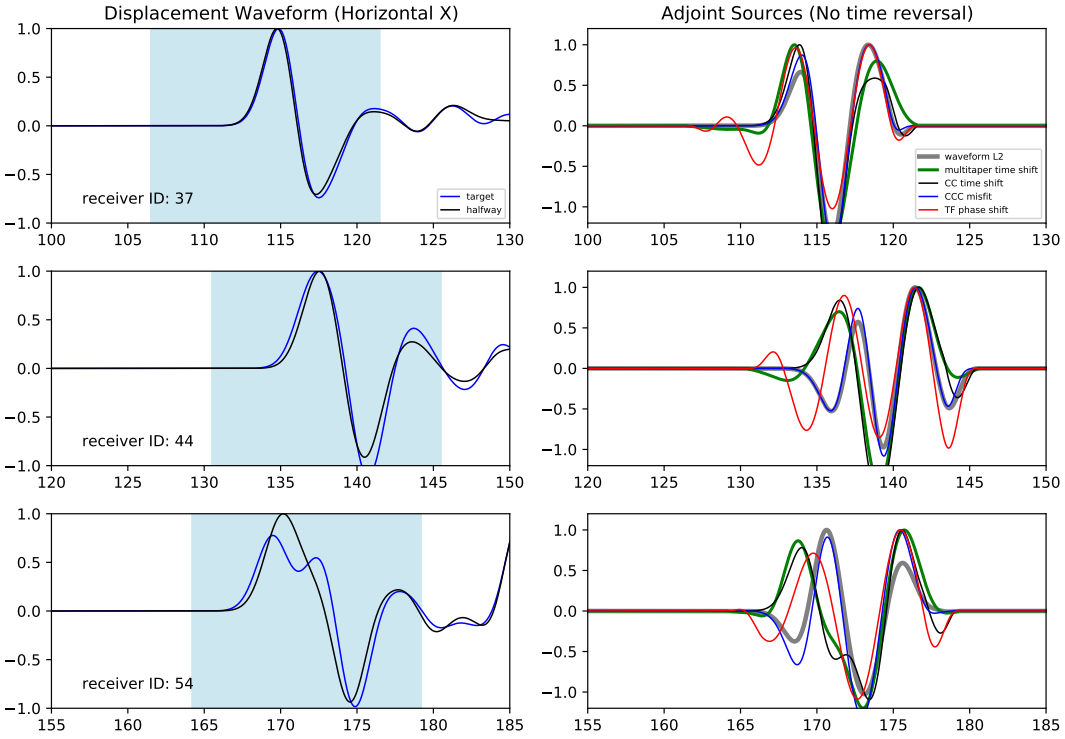

Fig. 3.26: Left: Z component Waveform comparison between the halfway model and target model for three receivers. Right: adjoint sources for three receivers. The light blue shaded area denotes the time window for the P phase.

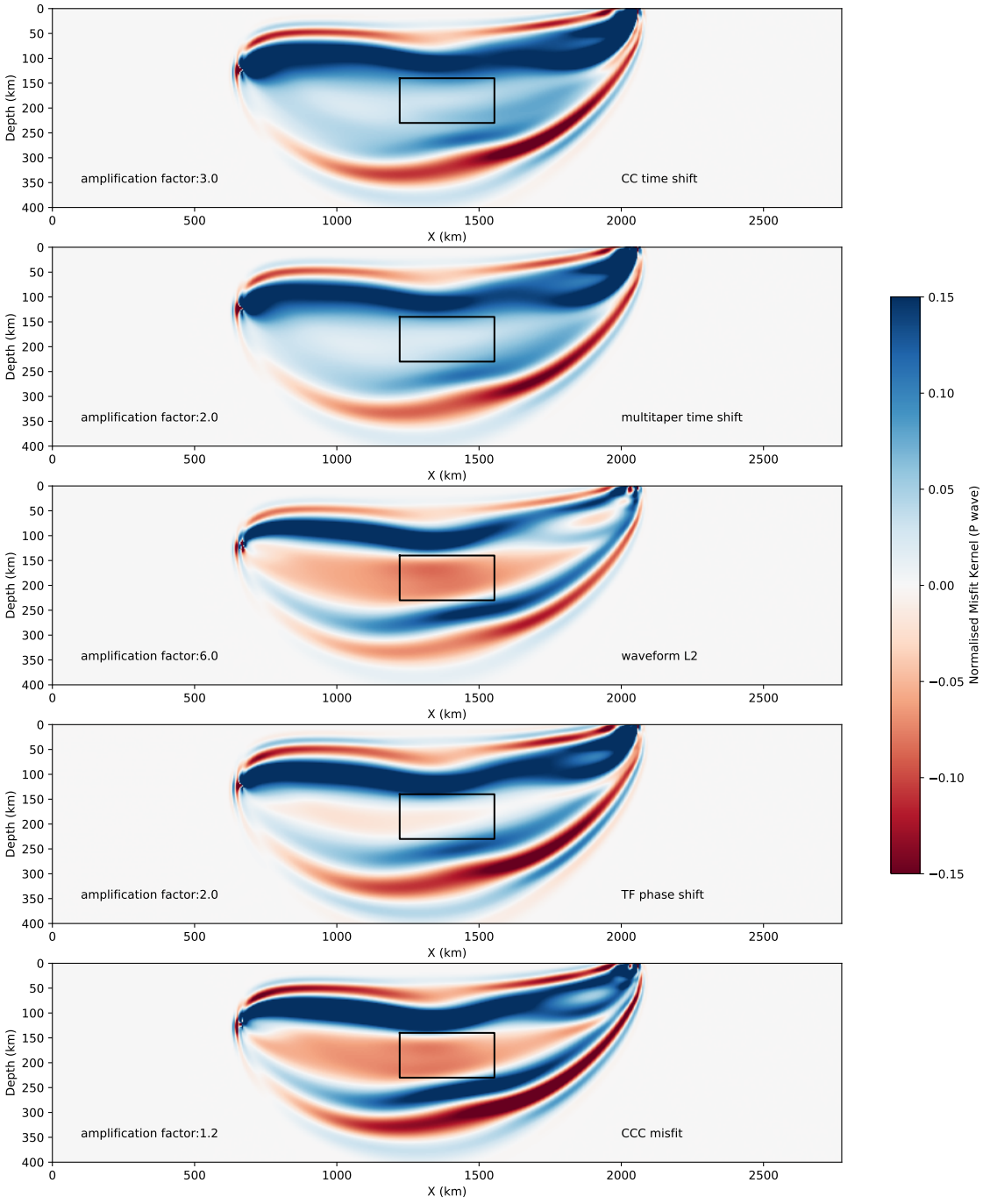

Fig. 3.27: Misfit kernels (P) of five misfit functions defined in subsection 3.3.2 for Receiver 54 (Figure 3.17-3.18). The misfits are calculated from halfway model to the target model (halfway-target)

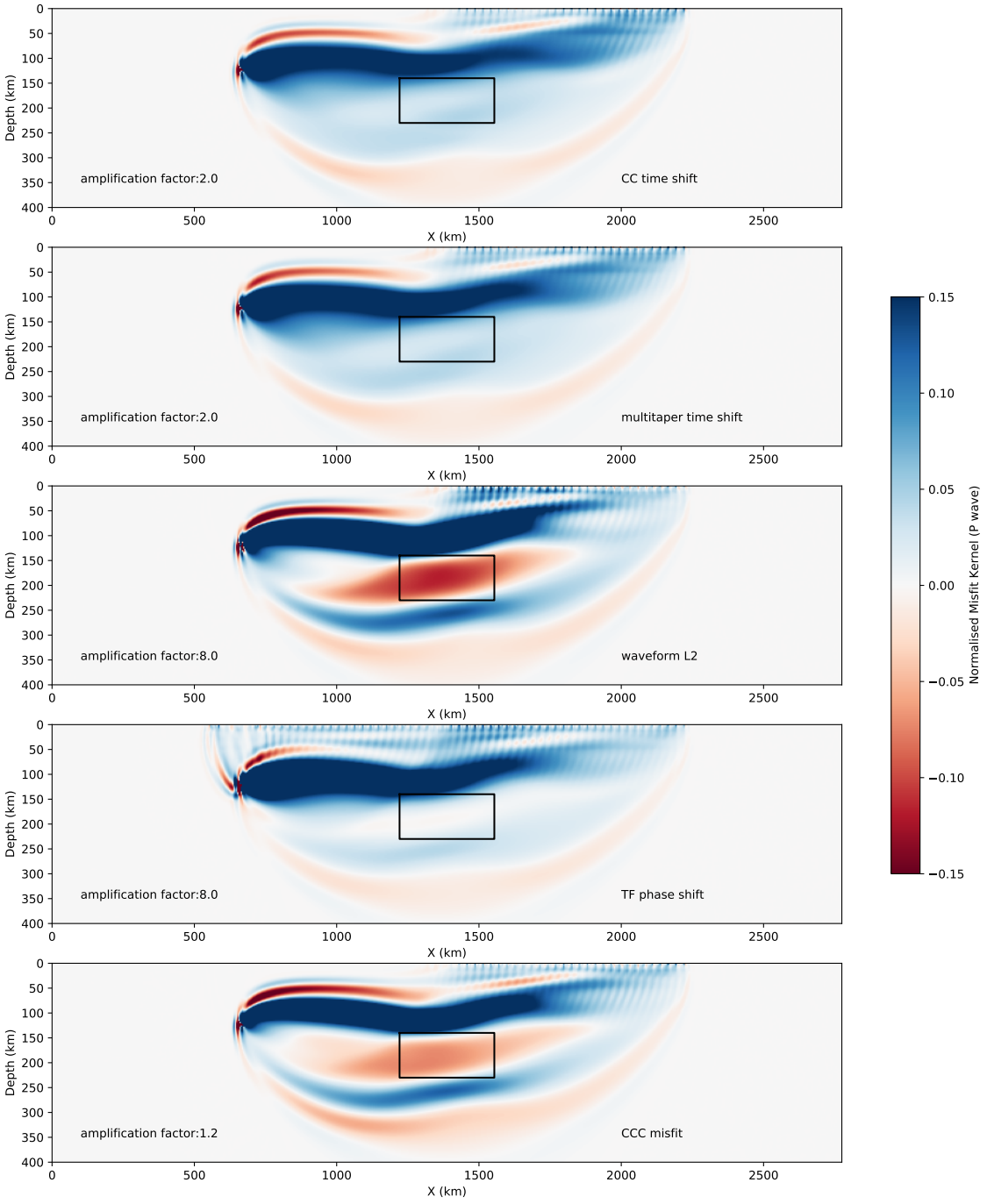

Fig. 3.28: Misfit kernels (P) of five misfit functions defined in subsection 3.3.2 for all receivers (Figure 3.17-3.18). The misfits are calculated from halfway model to the target model (halfway-target)

Multiple earthquakes benchmark tests for body wave

If we consider more earthquakes (13) for better data coverage, all five summed misfit kernels (Figure 3.29) could reflect the anomaly outside and inside the box as illustrated in Figure 3.10. However, CCC and L2 have clearer edges for the anomaly across the box and much weaker influences on the shallow depth and the areas that are far away from the anomaly (Figure 3.29). In other words, the TF phase shift, CC time shift and Multitaper time shift have stronger 'along-raypath' smearing. From the profiles along depth and horizontal X direction (Figure 3.30), we could observe the strongest constraints from CCC on the shape of the velocity difference (Figure 3.10). Thus from the halfway model approaching to the target model, CCC has more potentials to reflect the strong velocity contrasts. However, from the initial 1D model to the target model or to the halfway model, all of the misfits displayed very weak differences for the body wave, but requiring the multi-scale scheme to avoid potential local minimum (code: (`https://github.com/yjgao-gfz/specfem2dbodywave`)).

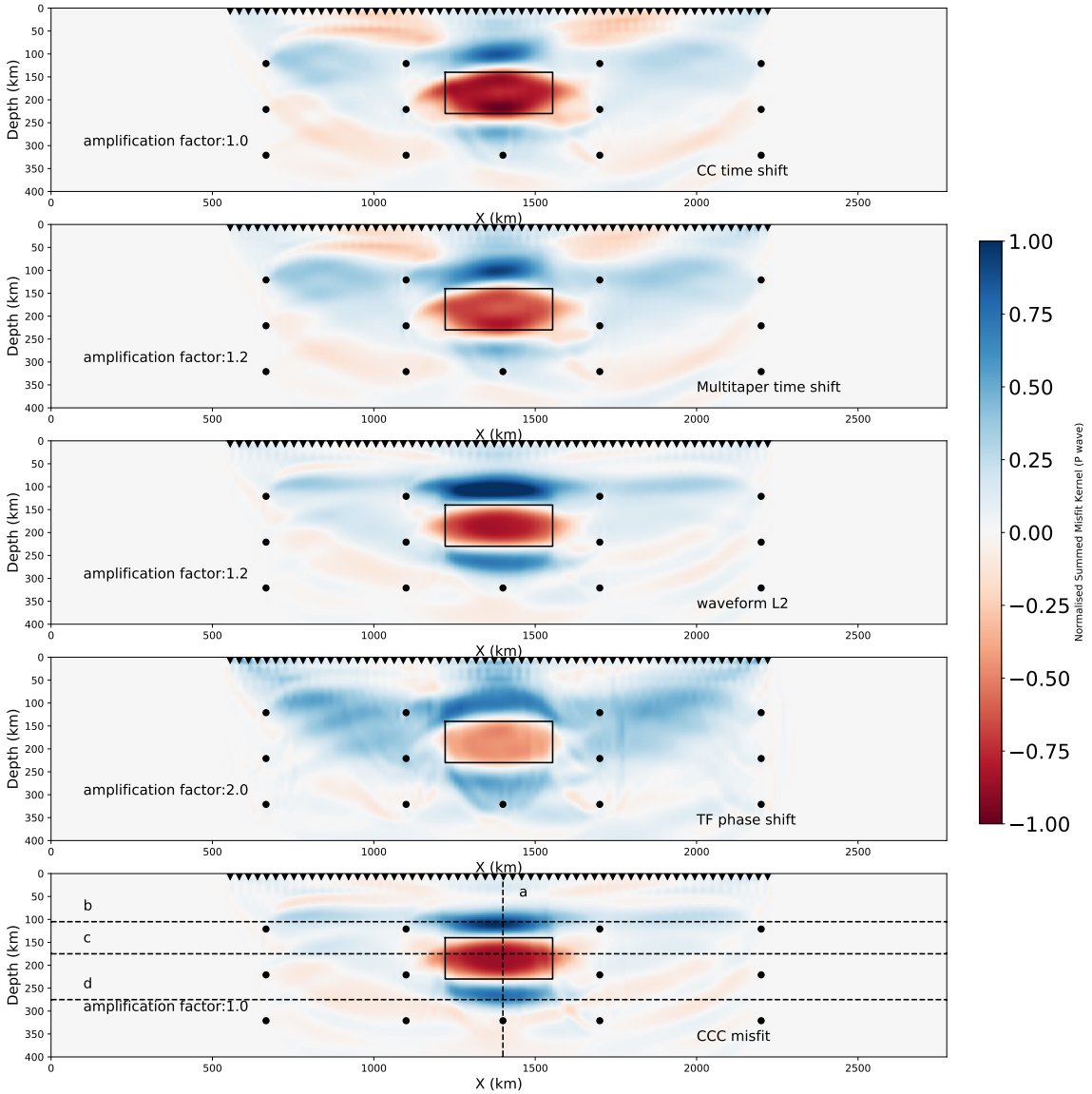

Fig. 3.29: Summed misfit kernels (P) of five misfit functions defined in subsection 3.3.2 for all receivers from 13 earthquakes (black dots). The misfits are calculated from halfway model to the target model (halfway-target). Black dashed lines denote the profile locations for Figure 3.30.

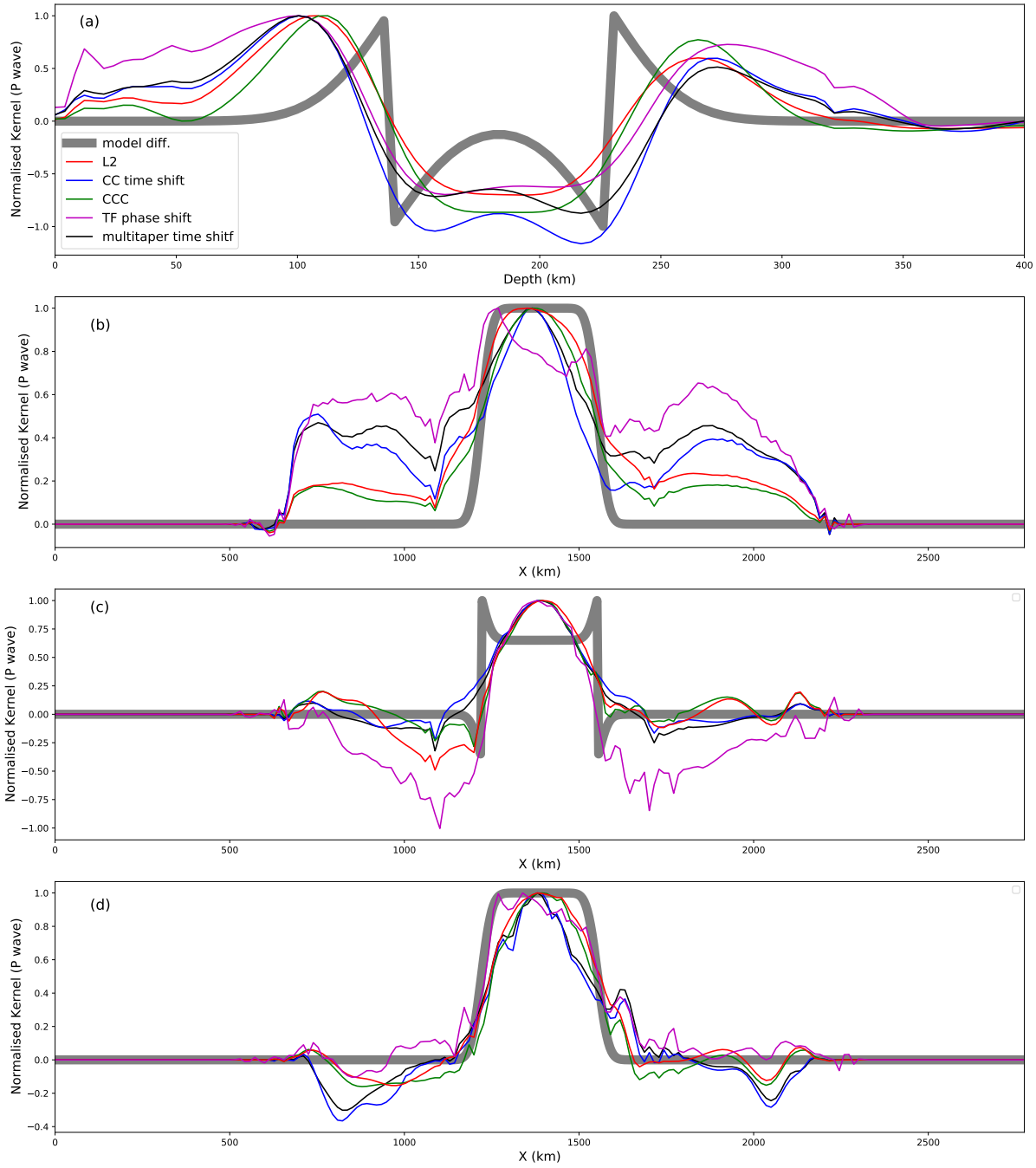

Fig. 3.30: Four profiles for the misfit kernel in Figure 3.29, thick grey line denotes the velocity variation from the halfway model to the target model defined in Figure 3.10

Single earthquake benchmark tests for S wave with Surface wave

For the S wave and surface wave trains, Fichtner et al. (2008) has already given a detailed derivation of Time-Frequency Phase shift misfit and shown its capacity and advantage over cross-correlation time shift and L2, especially for the high dispersion surface waves. Thus in this chapter, we try a more complicated case: a low velocity structure within the middle crust and high velocity anomaly structure in the lower crust (Figure 3.31) to test the responses of different misfit functions. We give relatively broad time-windows to test the capabilities of these misfit functionals.

In this test, we also consider the a smoothed model (halfway model, Gaussian smoothing with σ=20 km) for consistency. We also adjust the Centroid depth to 21 km to generate surface wave trains (Figure

3.31)

Based on the initial Modified PREM model, halfway model and target model, we calculate the synthetic wavefields and waveforms for 60 stations (Figure 3.32-3.37).

From the waveform comparisons, we could observe clear phase delay of surface wave trains from 1D initial model to halfway model or target model mainly due to the low velocity structure (Figure 3.31) and some weak advanced phases for receivers IDs over 50 (Figure 3.36). Thus, how to distinguish the high velocity structure from different misfit functionals is the target for this test.

Following a similar process, we calculate adjoint sources and adjoint simulations for initial-halfway and initial-target model waveform pairs (light blue shaded waveform trains in Figure 3.35-3.36). From Figure 3.39 and 3.38, we could observe advantages of Time-Frequency Phase shift over the other four misfit functions in the identification of the high velocity in the lower crust (red misfit kernel) for both the halfway model and target model.

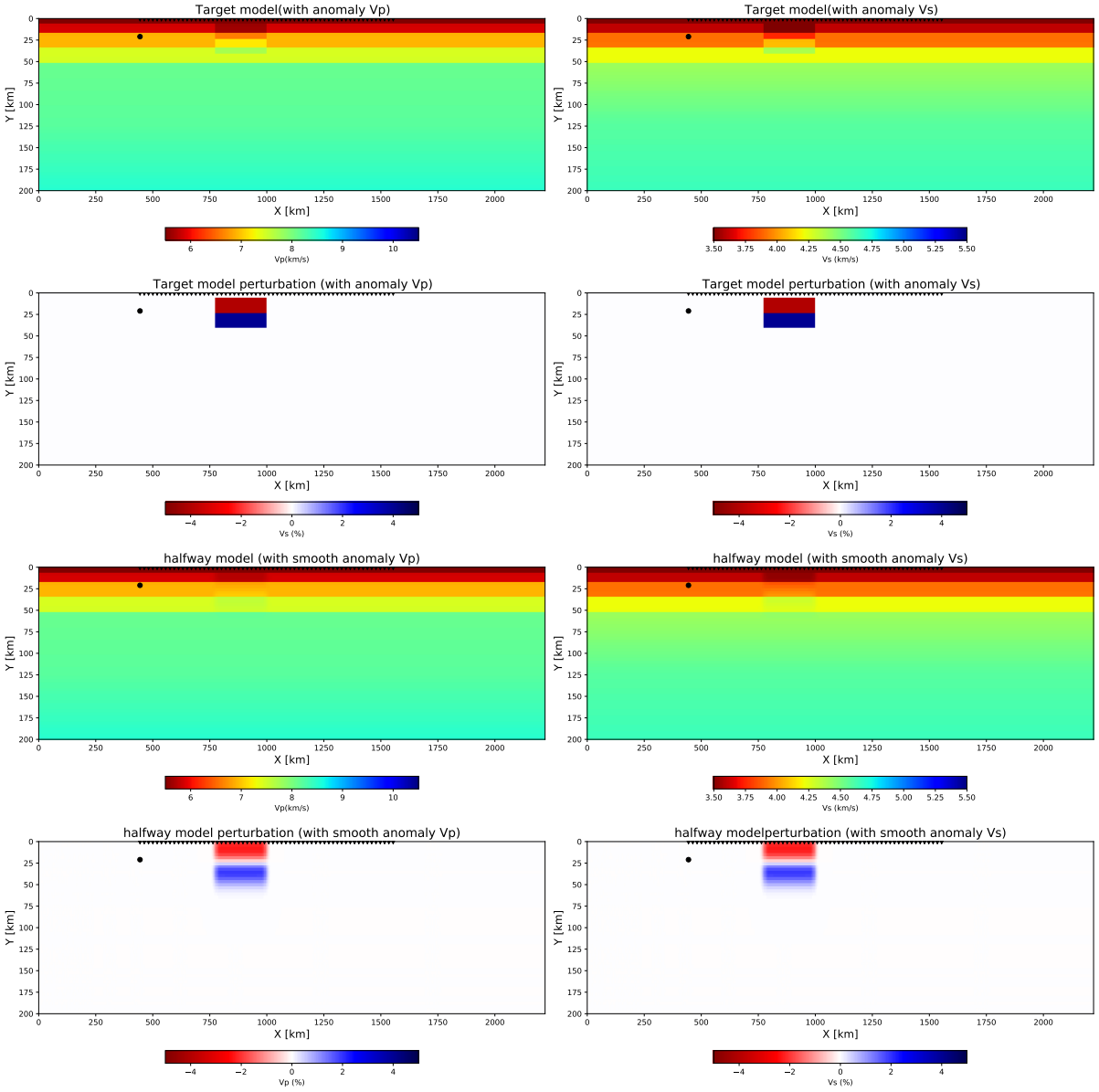

Fig. 3.31: Synthetic model through 2D P-SV plane spectral-element (Specfem2D). The velocity and depth have been adapted to the cartesian system through the Earth flattening transformation. The left four panels denote the Vp model and right four panels are Vs model. Top four panels denote the target model while lower four panels denote the halfway model.

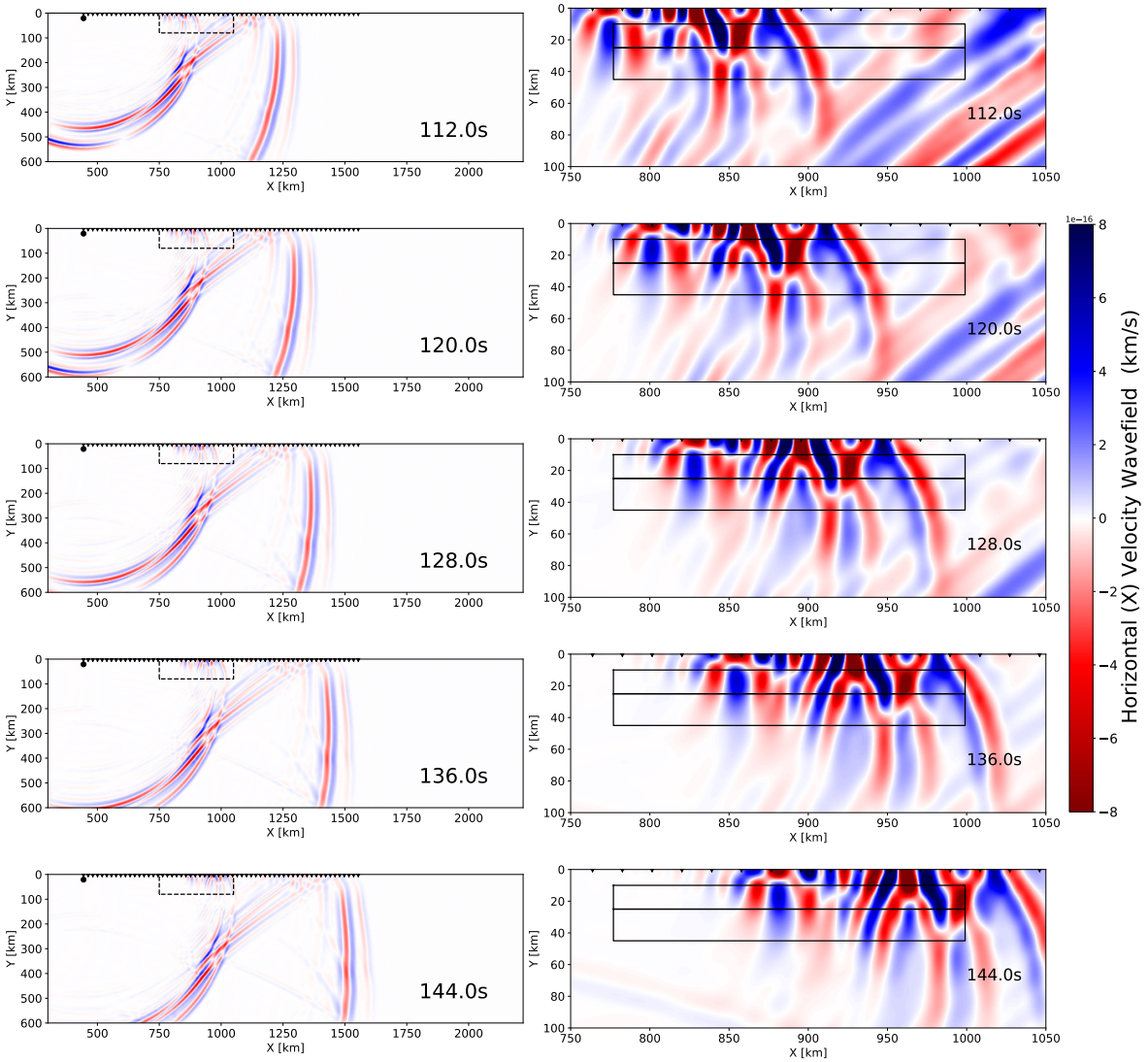

Fig. 3.32: Synthetic velocity wavefield snapshot for horizontal X component based on 1D initial model: The black dot denotes the location of the source, inverse triangles denote the receivers. Black rectangular mark the position of the low and high velocity anomaly in Figure 3.31. Left 5 panels denote the wavefield for the whole domain while right 5 panels denote the zoomed-in wavefield within the dashed box in left panels.

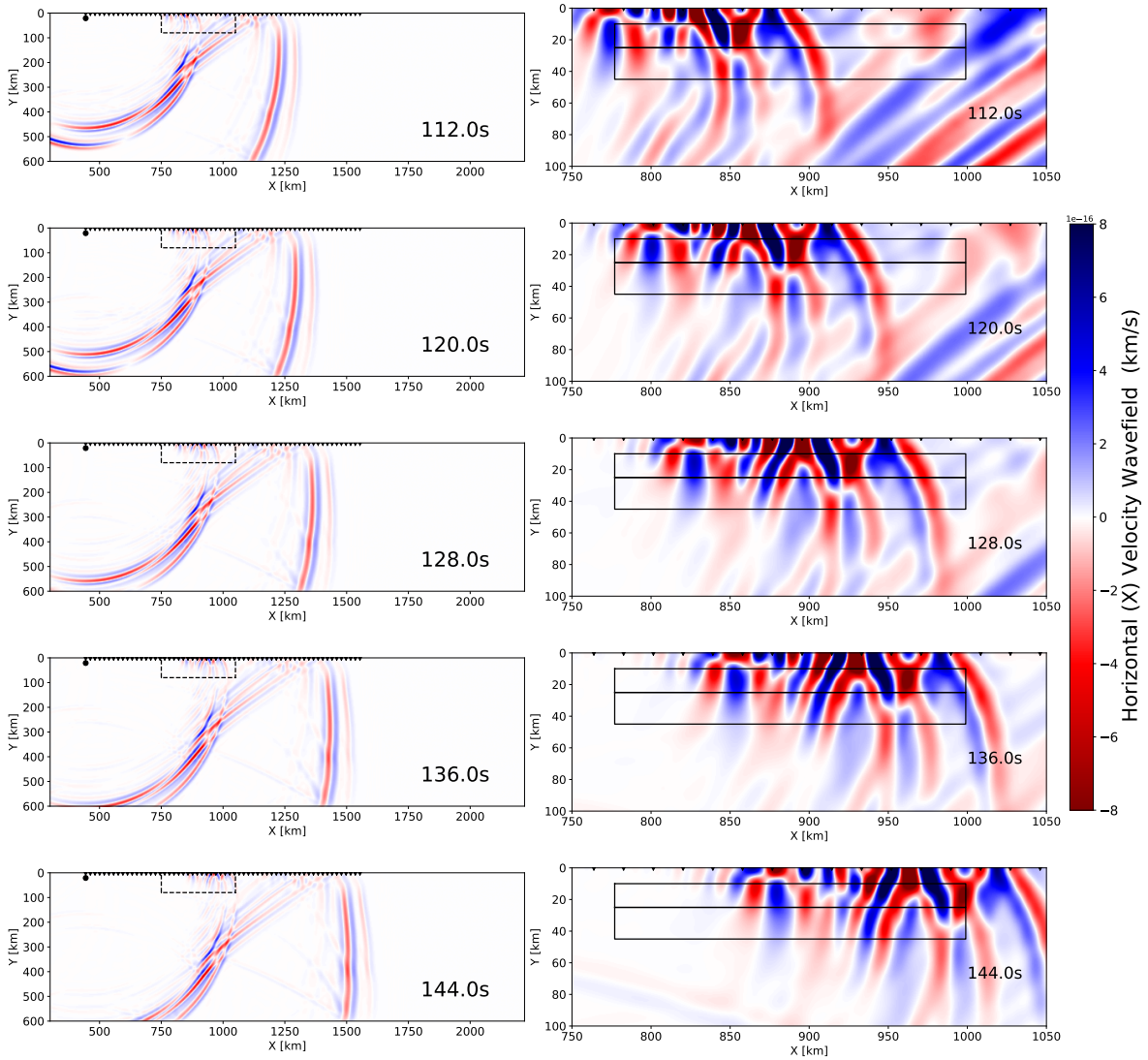

Fig. 3.33: Synthetic velocity wavefield snapshot for horizontal X component based on halfway model: The black dot denotes the location of the source, inverse triangles denote the receivers. Black rectangular mark the position of the low and high velocity anomaly in Figure 3.31. Left 5 panels denote the wavefield for the whole domain while right 5 panels denote the zoomed-in wavefield within the dashed box in left panels.

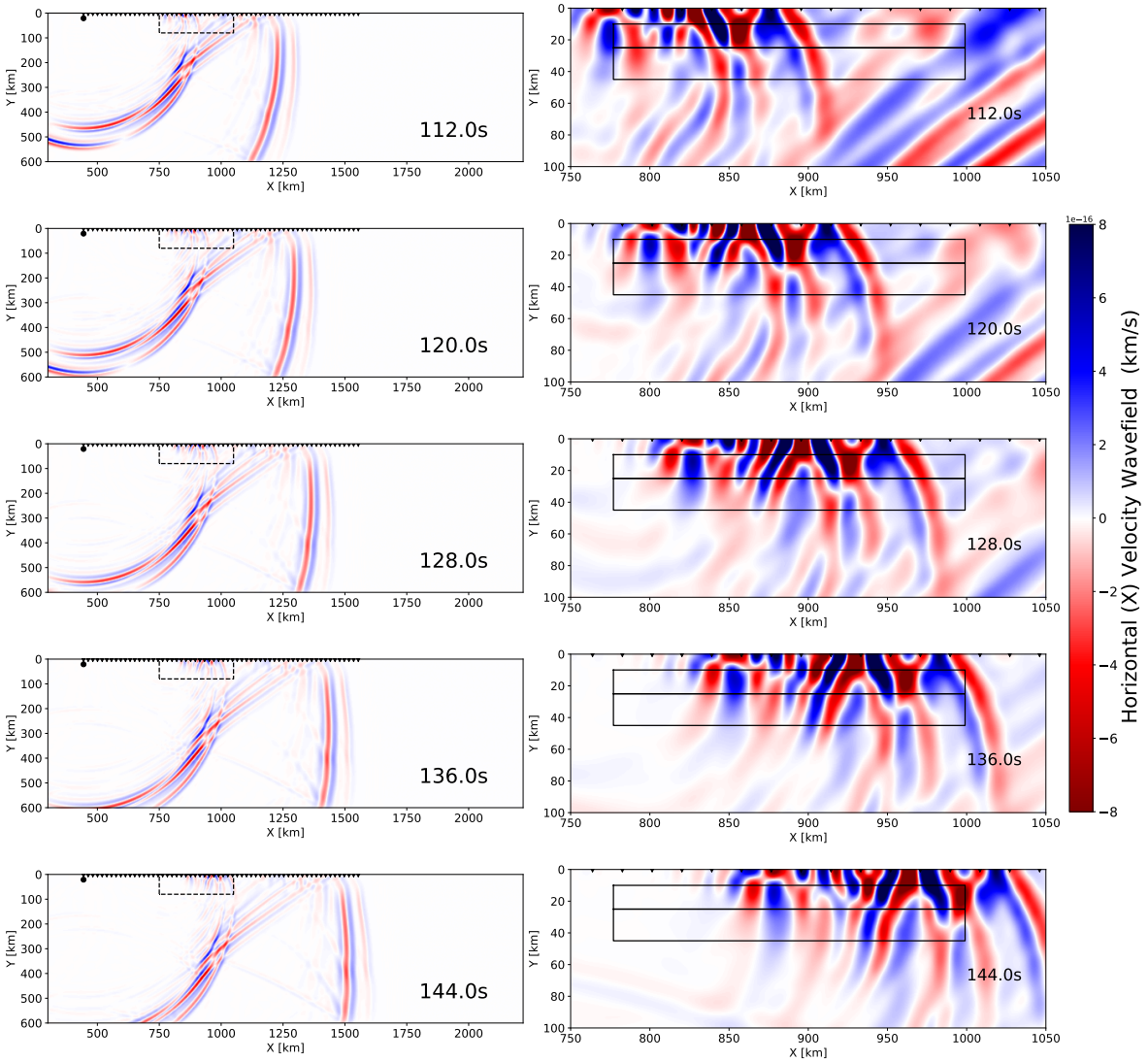

Fig. 3.34: Synthetic velocity wavefield snapshot for horizontal X component based on target model: The black dot denotes the location of the source, inverse triangles denote the receivers. Black rectangular mark the position of the low and high velocity anomaly in Figure 3.31. Left 5 panels denote the wavefield for the whole domain while right 5 panels denote the zoomed-in wavefield within the dashed box in left panels.

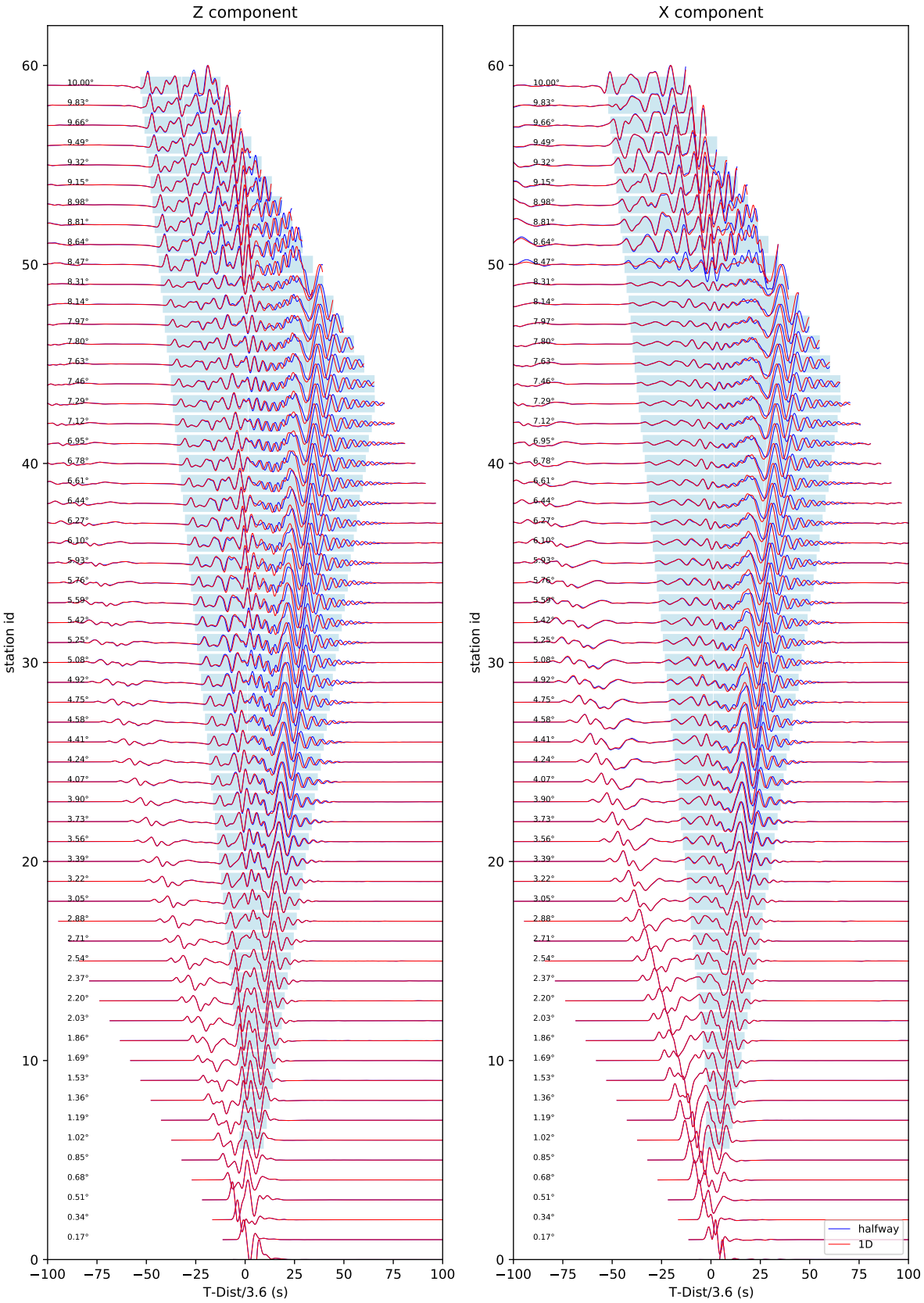

Fig. 3.35: Synthetic waveform comparison: the blue waveforms represent the synthetic waveforms from halfway model while red represent the synthetics from 1D initial model. The left panels denote vertical Z component while right denote the horizontal X component. The light blue shaded area denotes the time windows for the S wave and surface wave phases. The numbers atop waveforms denote the epicentral distances

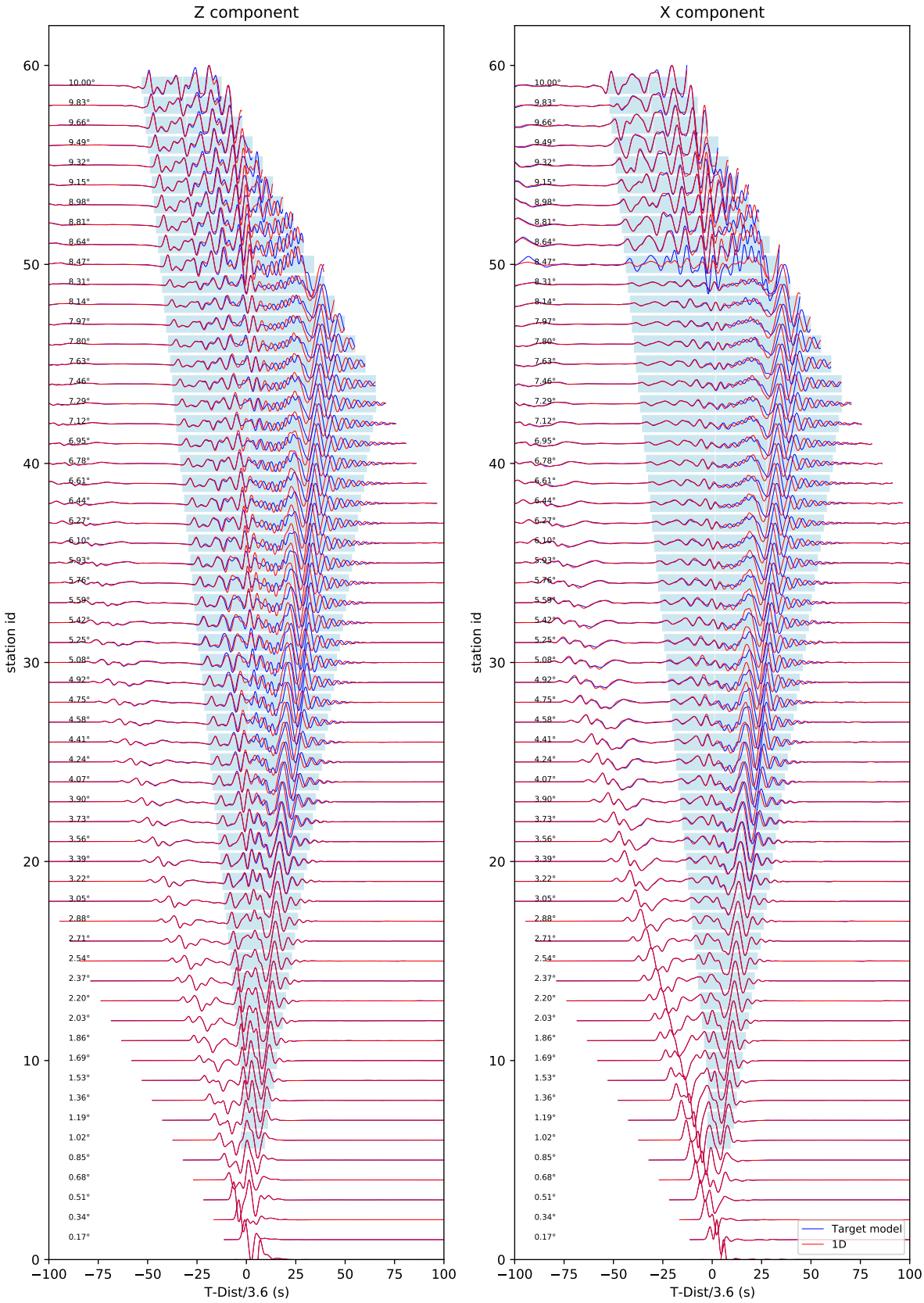

Fig. 3.36: Synthetic waveform comparison: the blue waveforms represent the synthetic waveforms from the target model while red represent the synthetics from the 1D initial model. The left panels denote the vertical Z component while the right denotes the horizontal X component. The light blue shaded area denotes the time windows for the S wave and surface wave phases.

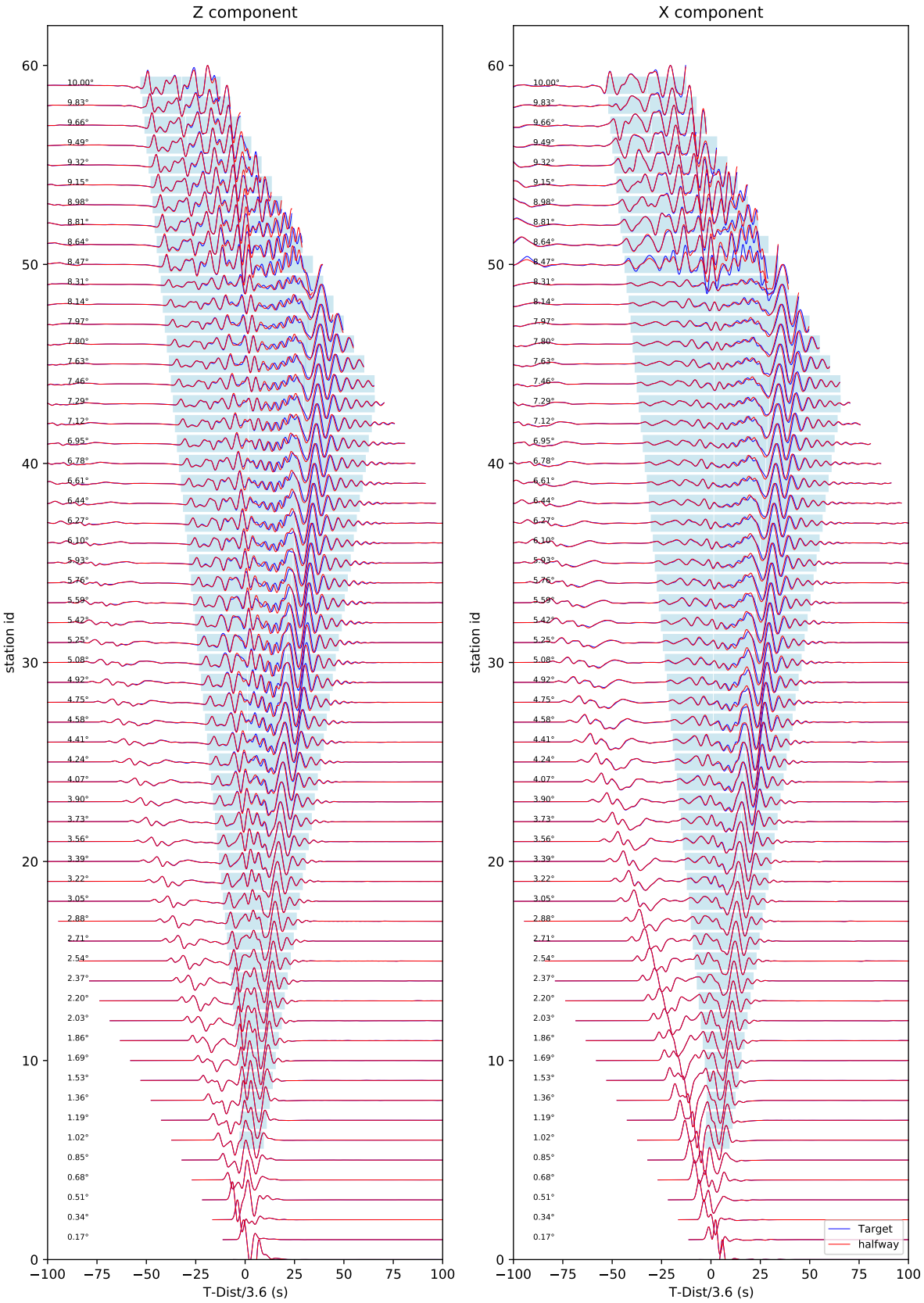

Fig. 3.37: Synthetic waveform comparison: the blue waveforms represent the synthetic waveforms from target model while red represent the synthetics from halfway model. The left panels denote vertical Z component while right denote the horizontal X component. The light blue shaded area denotes the time windows for the S wave and surface wave phases.

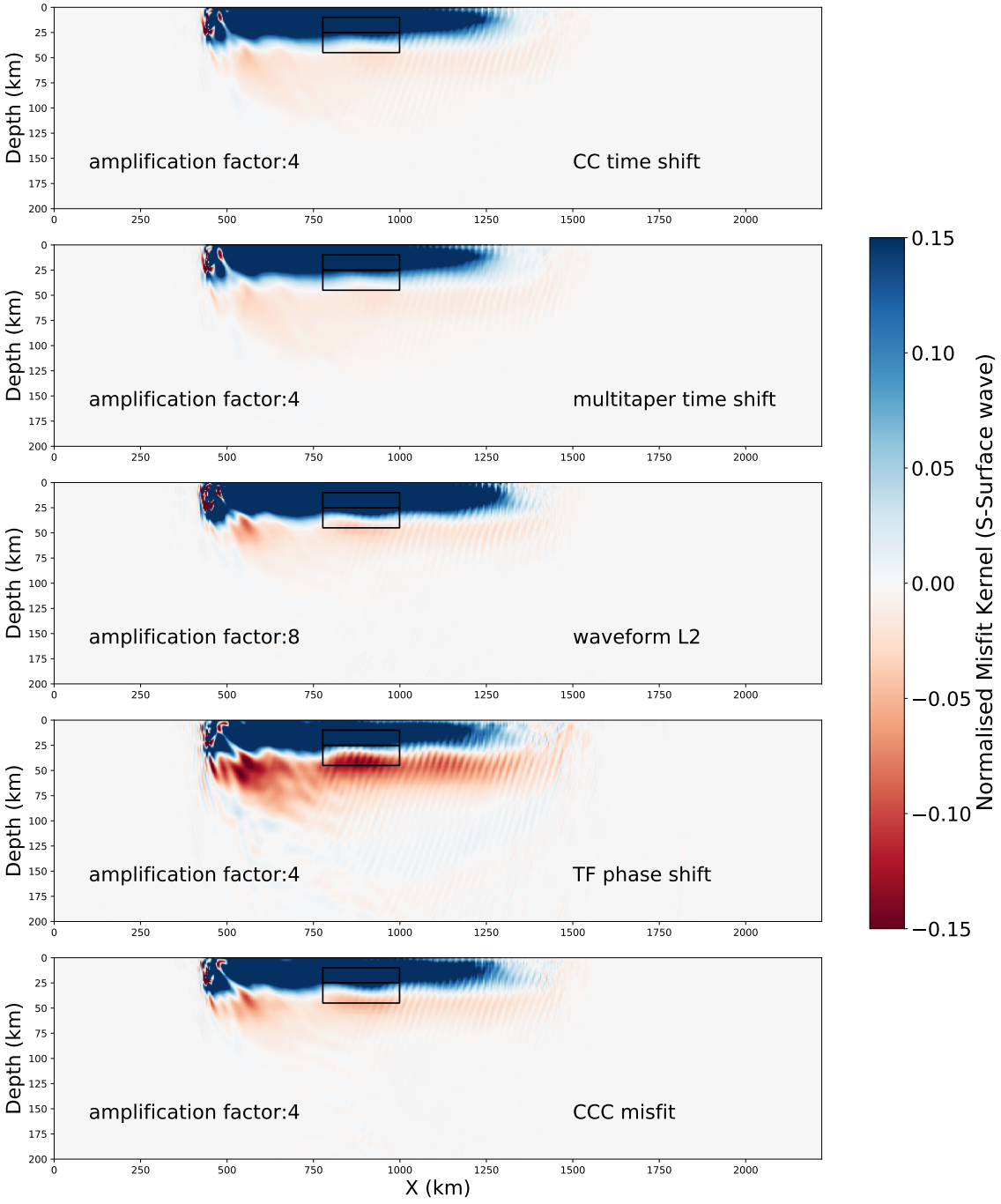

Fig. 3.38: Misfit kernels (S and Surface wave) of five misfit functions defined in subsection 3.3.2 for all receivers. The misfits are calculated from initial model to the halfway model (initial-halfway)

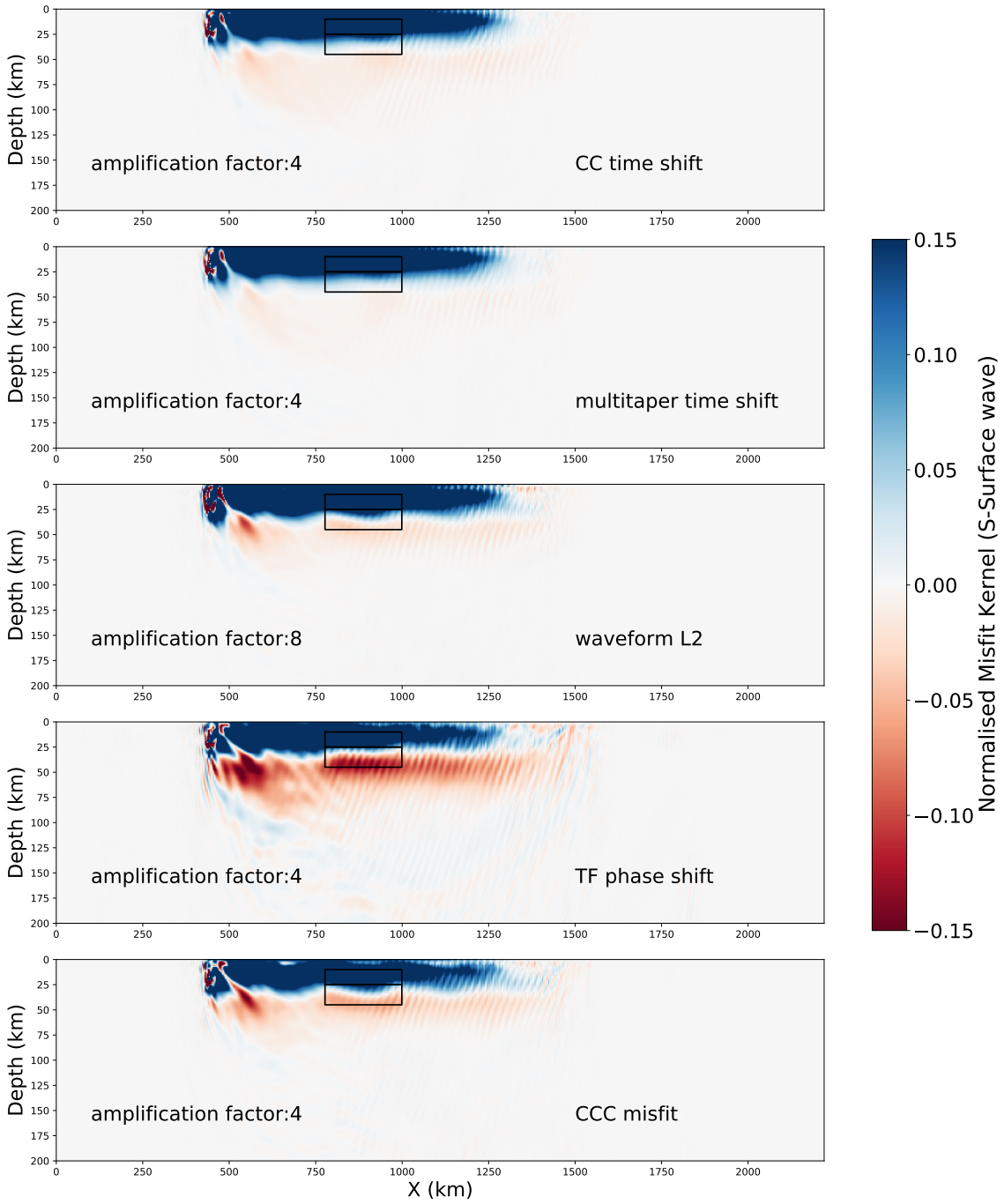

Fig. 3.39: Misfit kernels (S and Surface wave) of five misfit functions defined in subsection 3.3.2 for all receivers. The misfits are calculated from initial model to the target model (initial-target)

Multiple earthquakes benchmark tests for S wave with Surface wave

If we further consider 5 more events based on the same model configuration and same event depth (21 km). We could find the Time-Frequency Phase Shift has better capacity to identify the layered anomaly structure than other 4 misfit functions. Meanwhile, CCC could also give some identification of this feature. (code: `https://github.com/yjgao-gfz/specfem2Dsurfacewave`)

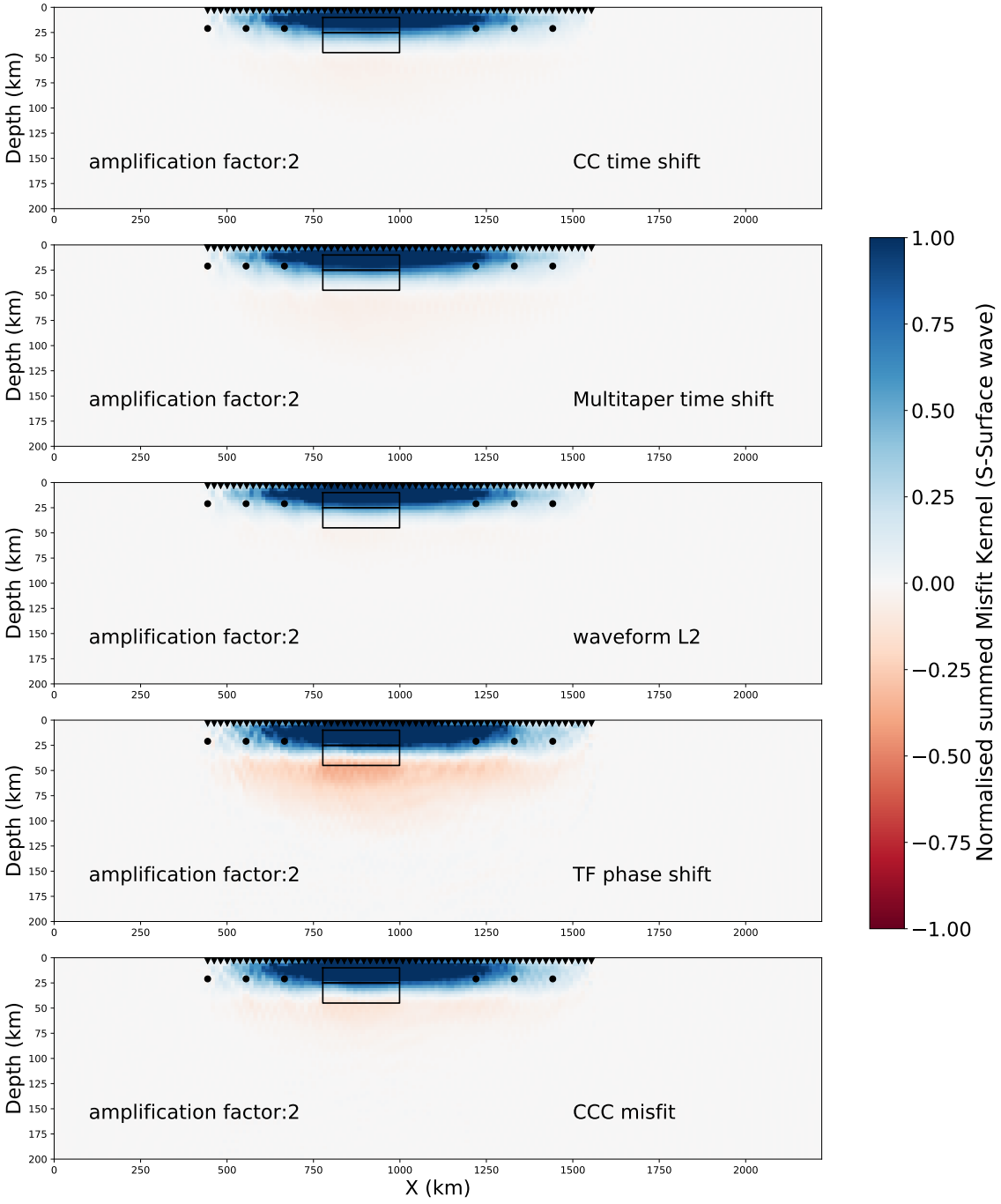

Fig. 3.40: Summed misfit kernels (S-surface wave) of five misfit functions defined in subsection 3.3.2 for all receivers from 6 shallow earthquakes (black dots). The misfits are calculated from initial model to the halfway model (initial-halfway).

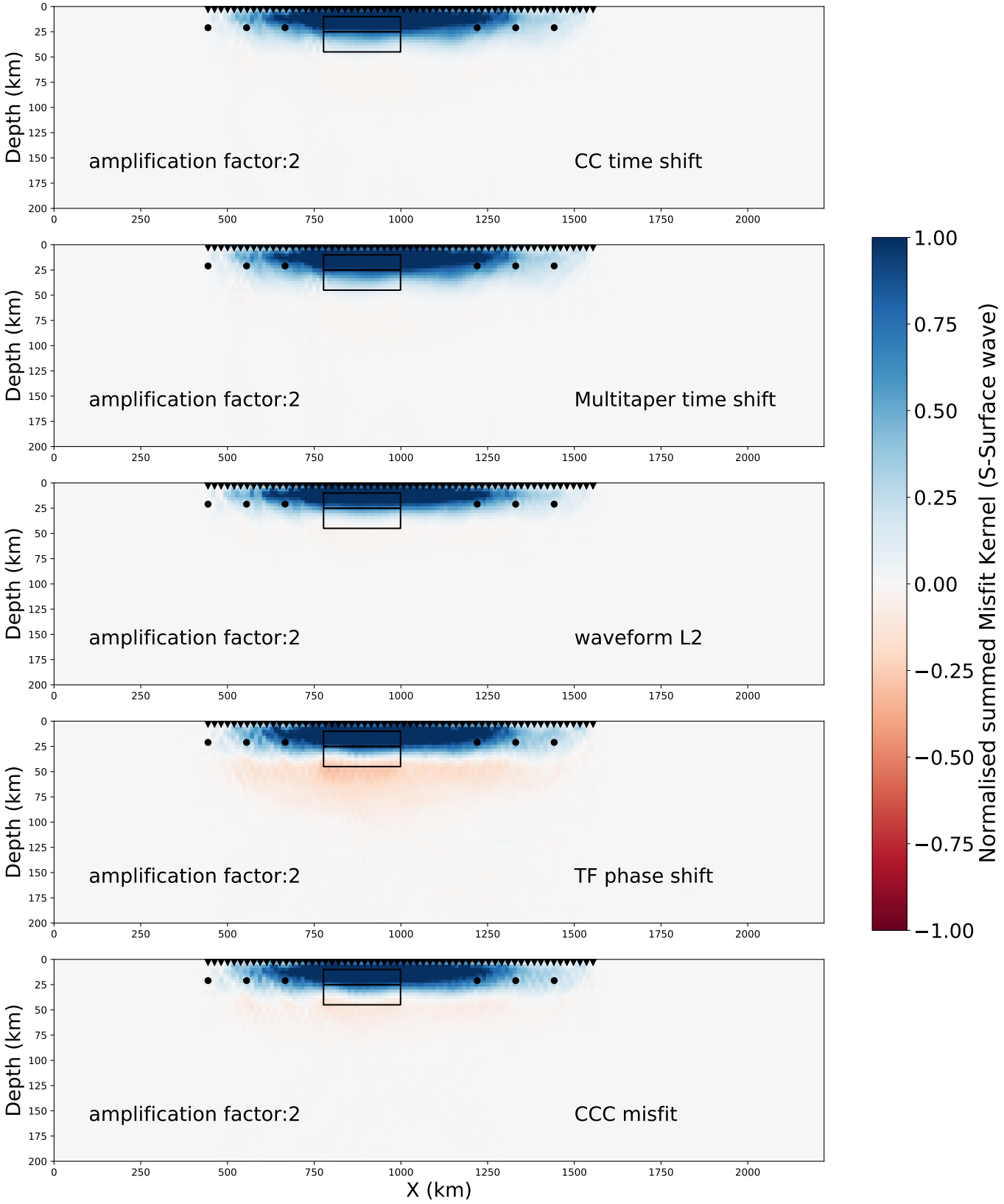

Fig. 3.41: Summed misfit kernels (S-surface wave) of five misfit functions defined in subsection 3.3.2 for all receivers from 6 shallow earthquakes (black dots). The misfits are calculated from initial model to the target model (initial-target).

Remarks

Various misfit functionals have been defined and applied in previous FWI studies (Liu & Tromp, 2008; Kristeková et al., 2009; Fichtner, 2010; Tao et al., 2017; Yuan et al., 2020). A reasonable and robust design for the misfit functional with its corresponding adjoint sources plays a crucial role in the convergence and final outcome of the inversion (Fichtner, 2010). The main effect of the long-wavelength Earth structure is to speed up or delay the arrival times of the seismic phases, but applying the classical L^2 misfit directly on the waveforms would introduce local minima, as the absolute amplitude recordings are less reliable than the phase measurements and the misfit is prone to be dominated by the outliers, thus placing strong demands on the quality of measurements. In addition, amplitudes are highly sensitive to the focal mechanism at some azimuths. At the other extreme, the cross-correlation time shift is probably the most widely used misfit measure in finite-frequency inversions. Its popularity results from the robustness of the measurement for the specific seismic phase shifts and its quasi-linear relation to the Earth structure that facilitates the solution for tomographic inverse problems and overcomes the excessive non-linearity introduced by the L^2 (Luo & Schuster, 1991; Chen et al., 2015; Zhu et al., 2015; Liu et al., 2017). However this method cannot fully exploit the distortion of the observed data due to the small scale heterogeneities or the interference of multiple phases (Fichtner, 2010; Tao et al., 2017). Although the L^2 waveform fit and cross-correlation time shift have been applied successfully in FWI, their applicability is limited to the cases where the seismic phases are clearly separable (cross-correlation time shift) or where the observed and the synthetic waveforms are very similar (L^2 waveform fit). For the highly-dispersive surface wave trains, we prefer to use Time-Frequency Phase shift as misfit functional. It is based on the transformation of both the observed and synthetic data into the time-frequency domain where the frequency-dependent phase shift misfits are measured and thus more waveform details are included than in the single cross-correlation time shift misfits. A significant advantage of this functional is the freedom of the time window selection, where it is no longer required to isolate particular seismic phases. The disadvantage of this approach is that additional care needs to be taken to avoid cycle skipping, especially for the higher frequency signals used in the final iteration stages. For more derivation of this misfit functional and corresponding adjoint sources, the reader is referred to Fichtner (2010).

Just as the benchmark tests demonstrated, the Cross Correlation Coefficient (CCC) misfit could provide another measurement of the discrepancy of synthetic and observed data, where the relative amplitudes of different arrivals are taken into account and which is nevertheless little affected by the source or receiver properties (Tao et al., 2018). CCC could give more constraints on the sharpness of the seismic anomalies when the current smooth model is very near the 'real model', or in other words, when the secondary phases dominate the waveform misfits and the time-shift is very weak for the main phases. However, additional care should be taken for bad quality data to avoid introducing artifacts due to outliers.

Like Yuan et al. (2020) pointed out, a hybrid approach combining different misfit functions has great potential for FWI. Thus in our production research for Central Andes, we adopted Time-Frequency phase shift for the long period surface wave iterations and CCC for the final higher frequency data iterations. More details are presented in Chapter 4 and Chapter 5.

3.3.4 Optimization Methods and Model Updates

As most of the textbooks of inverse theory and full waveform inversion have given detailed introduction about the conception of iterative non-linear minimisation (Tarantola, 2005; Fichtner, 2010), here I only describe the Conjugate-Gradients (Fletcher & Reeves, 1964) and L-BFGS (Liu & Nocedal, 1989) which are used for our productive inversion work for Central Andes in Chapter 4 and Chapter 5.

Conjugate-Gradients (CG)

We take advantage of the CG variant introduced by Fletcher & Reeves (1964), which has previously been applied to FWI by Tao et al. (2018). The specific formulation of F-R CG in our study follows as below:

$$\mathbf{z}_i = -\mathbf{G}\mathbf{g}_i + \gamma \mathbf{z}_{i-1} \tag{3.77}$$

where $\mathbf{z}_i$ and $\mathbf{z}_{i-1}$ denote the search directions in the ith and $i-1$th iterations, respectively. $\mathbf{g}_i$ is the gradient from the adjoint simulations based on the misfit functions in the ith iteration, $\mathbf{G}$ denotes the smoothing function which contains local (smoothing around the earthquake sources) and global Gaussian smoothing to suppress the local artifacts and stabilize the inversion process. Practically and specifically, for the individual gradient from every event, we use a limited width for the Gaussian smoothing (around 80 km) to damp out artifacts around the sources before summation over all events; we then clip extreme values of the summed gradients in the shallow crust in order to reduce the artefacts beneath the receivers. The summed gradient is then smoothed again, where the Gaussian smoothing width σ is decreased systematically with each stage of the multi-frequency inversion. Specifically, we set σ equal to one third to one half of the minimum wavelength in the current period. Meanwhile, $\gamma = \frac{(\mathbf{G}\mathbf{g}_i - \mathbf{G}\mathbf{g}_{i-1})^T \mathbf{G}\mathbf{g}_i}{(\mathbf{G}\mathbf{g}_i - \mathbf{G}\mathbf{g}_{i-1})^T \mathbf{z}_{i-1}}$ is the CG update parameter, which is reset to zero when it becomes negative Tao et al. (2018). The step length for the model updates is determined using a quadratic interpolation among the three test models, which are updated from the current model with step lengths with 5%, 10% and 15% of the maximum absolute amplitude of the search direction $\mathbf{z}_i$.

L-BFGS

L-BFGS is a quasi-Newton algorithm that contains the curvature information based on the inverse Hessian approximations derived from the gradients and models of the previous iterations and therefore can accelerate convergence. L-BFGS avoids the storage of the very large Hessian matrix and only requires a few vector products. We adopt the methodology from Krischer et al. (2018b), which is different from the classical algorithm dating back to Liu & Nocedal (1989) by incorporating the Gaussian smoothing operator directly into L-BFGS.

Based on the changes of the gradients defined by $\mathbf{r}_k = \mathbf{G}_{1/2}\mathbf{g}_{k+1} - \mathbf{G}_{1/2}\mathbf{g}_k$ and the model variations $\mathbf{s}_k = \mathbf{m}_{k+1} - \mathbf{m}_k$, the L-BFGS is formulated and driven as an iterative algorithm without forming the inverse Hessian approximation directly. The specific algorithm is shown as Algorithm 1.

Algorithm 1 L-BFGS algorithm

$\mathbf{q} \leftarrow \mathbf{G}_{1/2}\mathbf{g}_k$
for $i = k-1, ..., k-m$ **do**
  $\gamma_i \leftarrow \frac{1}{\mathbf{r}_i^T \mathbf{s}_i}$; $\alpha_i \leftarrow \gamma_i \mathbf{s}_i^T \mathbf{q}$; $\mathbf{q} \leftarrow \mathbf{q} - \alpha_i \mathbf{r}_i$
end for
$\eta_k \leftarrow (\mathbf{s}_{k-1}^T \mathbf{r}_{k-1}) / (\mathbf{r}_{k-1}^T \mathbf{r}_{k-1})$
$\mathbf{z} \leftarrow \eta_k \mathbf{q}$
for $i = k-m, ..., k-1$ **do**
  $\beta_i \leftarrow \gamma_i \mathbf{r}_i^T \mathbf{z}$; $\mathbf{z} \leftarrow \mathbf{z} + \mathbf{s}_i(\alpha_i - \beta_i)$
end for

m in the L-BFGS algorithm indicates the number of past model updates stored. The negative direction for the model updates would turn to be $\mathbf{G}_{1/2}\mathbf{z} = \mathbf{G}_{1/2}\mathbf{H}_k^{-1}\mathbf{G}_{1/2}\mathbf{g}_k$, where $\mathbf{G}$ is still the smoothing function which is split into $\mathbf{G} = \mathbf{G}_{1/2}\mathbf{G}_{1/2}^T$. So the model update would be:

$$\mathbf{m}_{k+1} = \mathbf{m}_k - \varphi \mathbf{G}_{1/2}\mathbf{z} \tag{3.78}$$

where φ represents the suitable step length. In our implementation, we estimate the optimal step length through the quadratic interpolation based on the waveform misfits of three updated test models with φ=20%, 50% and 80%. In practice, instead of calculating the full misfits for the step length tests, we extract 6 - 10 events with the gradient angle smaller than $1/3\pi$ between the individual event gradient and the summed gradient (van Herwaarden et al., 2020) from the current model. The number of the seismic stations for these events should be larger than the average (40 stations) to be representative of the summed gradient. Through this way, we could substantially lower the computational burden for the step length tests and thus improve the efficiency of the inversion.

Iterative Model Updates

Thus the misfit kernel (gradient) from adjoint theory drives the iterative model updates through L-BFGS or Conjugate Gradient method (Figure 3.42). More information about Gradient smoothing and data pre-processing could be found in Chapter 4.

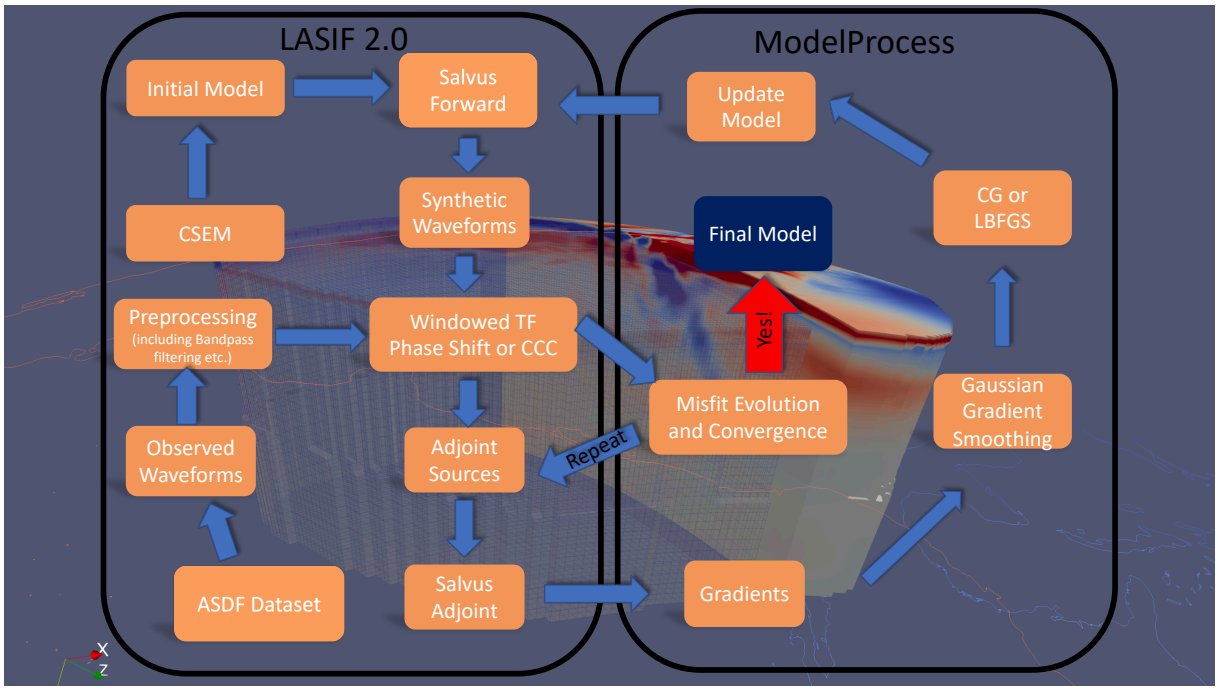

Fig. 3.42: Inversion workflow in this study with Conjugate-Gradient (CG) and L-BFGS implemented. The background is the 3D view of the final V_S velocity model.

Chapter 4

Seismic structure of North Central Andes

4.1 Abstract

We present a new seismic tomography model for the crust and upper-mantle beneath the Central Andes based on multi-scale full seismic waveform inversion, proceeding from long periods (40–80 s) over several steps down to 12–60 s. The spatial resolution and trade-offs among parameters are estimated through the multi-parameter point-spread functions. P and S wave velocity structures with spatial resolution of 30–40 km for the upper mantle and 20 km for the crust could be resolved in the central study region.

In our study, the subducting Nazca slab is clearly imaged in the upper mantle, with dip-angle variations from the north to the south. Bands of low velocities in the crust and mantle wedge indicate intense crustal partial melting and hydration of the mantle wedge beneath the frontal volcanic arc, respectively and they are linked to the vigorous dehydration from the subducting Nazca plate and intermediate depth seismicity within the slab. These low velocity bands are interrupted at 19.8°–21°S, both in the crust and uppermost mantle, hinting at the lower extent of crustal partial melting and hydration of the mantle wedge.

The variation of lithospheric high velocity anomalies below the backarc from North to South allows insight into the evolutionary foundering stages of the Central Andean margin. A high velocity layer beneath the southern Altiplano suggests underthrusting of the leading edge of the Brazilian Shield. In contrast, a steeply westward dipping high velocity block and low velocity lithospheric uppermost mantle beneath the southern Puna plateau hint at the ongoing lithospheric delamination.

4.2 Introduction

The Andes is a long mountain belt across the entire western margin of the South American continent, extending for more than 6000 km (Figure 4.1). The subduction of the Nazca plate below South America along the Central Andes has resulted in drastic crustal shortening (Oncken et al., 2006) and thickening (Yuan et al., 2000; Heit et al., 2007a, 2008a), magmatism (Wörner et al., 1992; Kay et al., 1994; Wörner et al., 2000; Kay & Mpodozis, 2002; Kay & Coira, 2009) and lithospheric delamination (Kay & Kay, 1993; Whitman et al., 1996; Allmendinger et al., 1997; Beck & Zandt, 2002; Schurr et al., 2006; Bianchi et al., 2013; Beck et al., 2015; Scire et al., 2015a; Garzione et al., 2017; Chen et al., 2020). The age of the subducting Nazca plate is ∼45–50 Ma at the trench (Müller et al., 2008) as it enters the subduction zone with a convergence rate of 61–65 mm/yr (Norabuena et al., 1999; Angermann et al., 1999). The subduction of the Nazca plate initiated around 70-80 Ma and it is thought to have reached the lower mantle beneath the Central Andes ∼50 Ma ago, according to a recent plate reconstruction based on slab unfolding (Chen et al., 2019).

The widest part of the Andean orogen is between 15° and 27°S, where the subduction angle is 20° - 30°, flanked southwards and northwards by the flat subduction segments, where the subducted Nazca plate flattens out to become nearly horizontal. The Altiplano and Puna plateaus together constitute the

second largest high plateau in the world, the Central Andean Plateau (Figure 4.1), which is also the only one that formed under a subduction regime. The Altiplano plateau (AP), in the northern part of the Central Andean Plateau, is characterised by a single internally drained basin with an average rather uniform elevation around 3800 m, whereas the southern part of the Central Andean Plateau is the Puna plateau (PN), which exhibits a higher altitude around 4500 m with more rugged relief, enclosing a series of internal drained basins. The Central Andean Plateau is flanked to the west by the Western Cordillera (WC) and to the east by the Eastern Cordillera (EC), followed by the Subandean Ranges (SA), Santa Barbara System (SB) and the Sierras Pampeanas (SP) from the north to the south (Figure 4.1).

The formation of the Central Andean Plateau is thought to be linked to lithospheric foundering beneath the Central Andes (e.g. Kay & Kay, 1993; Kay et al., 1994; Beck & Zandt, 2002; McQuarrie et al., 2005; Garzione et al., 2006; DeCelles et al., 2015). Although many researchers agree on the existence of lithospheric foundering in the Central Andes, there remain vigorous debates on its mechanisms, scale, pattern, timing and surface expression. The tectonic history of the eastern margin of the Central Andes exhibits north-south variations, which might provide an insight into the lithospheric processes. North of 24°S, deformation in the EC is occurred between ∼40 and 15 Ma (McQuarrie et al., 2005; Oncken et al., 2006) before migrating to the SA after 10 Ma, forming a thin-skinned fold and thrust belt (Allmendinger & Gubbels, 1996; Allmendinger et al., 1997; Sobolev & Babeyko, 2005; Garzione et al., 2017; Ibarra et al., 2019). In contrast, south of 24°S, the back-arc deformation becomes thick-skinned in the SB and finally changes to the basement-cored uplift in the SP (Allmendinger & Gubbels, 1996; Allmendinger et al., 1997; Sobolev & Babeyko, 2005; Oncken et al., 2006; Garzione et al., 2017). The relations between Nazca plate subduction, foundering of the continental lithosphere and the latitudinal variations of deformation style within the back-arc are still poorly understood; further progress depends on a good understanding of the lithospheric structure.

The seismic structure of the crust and upper mantle beneath the Central Andes has been investigated by many tomographic studies, including regional body wave tomography (e.g. Husen et al., 2000; Schurr & Rietbrock, 2004; Schurr et al., 2006; Koulakov et al., 2006; Comte et al., 2016; Huang et al., 2019), teleseismic tomography (Heit et al., 2008a; Bianchi et al., 2013; Scire et al., 2015a,b, 2017; Portner et al., 2020; Rodríguez et al., 2021) and surface wave and ambient noise tomography (Porter et al., 2012; Calixto et al., 2013; Ward et al., 2013, 2014; Delph et al., 2017; Antonijevic et al., 2016; Ward et al., 2016, 2017). Previous teleseismic and global tomography results revealed a continuous subducted Nazca slab from the uppermost mantle down to the lower mantle (Heit et al., 2008a; Ritsema et al., 2011; Scire et al., 2015a; Lei et al., 2020; Portner et al., 2020; Rodríguez et al., 2021) with a potential slab tear at the southeastern edge of the Pampean flat subduction zone (Portner & Hayes, 2018; Portner et al., 2020). However, teleseismic tomography cannot easily separate anomalies in the crust and uppermost mantle due to smearing along steep ray-paths, such that the starting model and crustal corrections can exert a strong influence on the final results in this depth range. In contrast, local and regional earthquake tomography can provide more details for the crust and upper mantle in the selected regions but lacks resolution at larger depths. In some of these aforementioned regional tomographic studies, the upper part of the Nazca slab is visible as a relatively continuous high velocity anomaly beneath the Central Andes and various back-arc seismic structures were also imaged (e.g. Schurr et al., 2006; Bianchi et al., 2013; Chen et al., 2020). However, these studies were limited to small specific regions according to the footprints of the temporary seismic arrays, typically differing among each others in many methodological details, which makes margin-wide comparisons difficult. In order to obtain a large scale model for a wider part of the margin without losing details in the crust, we collect seismic waveform data from the previous temporary and permanent network stations deployed between 1988 and 2018 and integrate them into a multi-scale three-dimensional full waveform inversion (FWI) (e.g. Simutė et al., 2016; Krischer et al., 2018b; Blom et al., 2020) to infer the seismic structure within the crust and upper mantle. Accurate

simulations of seismic wave propagation through laterally heterogeneous models allow the calculation of accurate finite-frequency kernels with the adjoint method. (e.g. Chen et al., 2007b; Fichtner et al., 2010; Tape et al., 2010; Chen et al., 2015; Simutė et al., 2016; Tao et al., 2018; Krischer et al., 2018b; Blom et al., 2020; Xiao et al., 2020; Lei et al., 2020; van Herwaarden et al., 2021). Advances in the computational power make it feasible to invert the full waveform to image the seismic structure at regional scales down to relatively short periods, here 12 s.

In this study, we invert for the long-wavelength seismic velocity structures from the low frequency data first and progressively move to higher frequency waveforms, thereby avoiding strong dependence on the starting model. We present a new model of the seismic velocities in the crust and upper mantle beneath the Andean orogen between 14° and 30° S, from the coast until well into the backarc, in the southern part of the study region even reaching the Andean foreland, with depth resolution down to ∼250 km.

4.3 Data

We retrieved centroid hypocenters, origin times and moment tensors for over 600 events with magnitudes between M_W 5.0 and 7.0 within our study region from the Global Centroid-Moment-Tensor (GCMT) catalog (Ekström et al., 2012). Seismic waveforms were recorded by 26 permanent and temporary networks deployed at various periods between 1994 and 2018 (Figure 4.2b and Table 4.1). We packed the waveforms and meta data into one Adaptable Seismic Data Format (ASDF, Krischer et al. (2016)) file for every event. Every complete ASDF container includes the seismic waveforms, the event information in QuakeML format (Schorlemmer et al., 2011) and the station information in StationXML format. As the computational cost for FWI scales with the number of the events, a practical approach is to maximize the amount of seismic waveform data for every event used in the study (Krischer et al., 2018b). Thus, we exclude events with only few receivers or recorded only by short-period instruments. For each stage of the inversion, as it extends to shorter periods, we make a visual check of the remaining events, and remove some waveforms, which are noisy or which show obvious signs of cycle skipping compared to synthetics computed with the current model. Events that failed to provide enough reliable measurements after visual inspection were also deleted. Each event in the final dataset has been recorded by 20–100 stations. During pre-processing, the instrument responses were removed from the raw seismic data to obtain the ground displacement. Zero-phase third order Butterworth band pass filters with varying passbands were applied during the different stages of the inversion (see section 4.4).

4.4 Methods

Our waveform modeling and inversion are mainly based on the full waveform adjoint methodology (Tromp et al., 2005b; Fichtner et al., 2009). Solutions of the visco-elastic wave equation in a radially anisotropic earth media are obtained from Salvus (Afanasiev et al., 2019), which is a suite of highly parallelised software performing full waveform modeling and inversion, which makes use of GPU acceleration and offers wavefield adapted meshes (van Driel et al., 2020; Thrastarson et al., 2020). Compared to earlier works, we introduce some technical modifications of the inversion workflow and misfit functionals, with details presented below.

Table 4.1: Seismic Network information

Code	Data Center	start	end	reference
C	IRISDMC	2007	2009	Chilean National Seismic Network
*C*1	IRISDMC	2012	-	Universidad De Chile (2013)
CX	GEOFON	2006	-	GFZ & CNRS-INSU (2006)
GE	GEOFON	1993	-	GEOFON Data Centre (1993)
GT	IRISDMC	1993	-	Albuquerque Seismological Laboratory (ASL)/USGS (1993)
IQ	GEOFON	2009	-	Cesca et al. (2009)
IU	IRISDMC	1988	-	Albuquerque Seismological Laboratory (ASL)/USGS (1988)
WA	IRISDMC	2011	-	West Central Argentina Network
2*B*	GEOFON	2007	2009	Heit et al. (2007b)
3*D*	GEOFON	2014	2016	Asch et al. (2014)
5*E*	GEOFON	2011	2013	Asch et al. (2011)
8*F*	GEOFON	2005	2012	Wigger et al. (2016)
8*G*	GEOFON	2013	2015	Salazar et al. (2013)
*X*6	IRISDMC	2007	2009	Sandvol & Brown (2007)
XE	IRISDMC	1994	1995	Silver et al. (1994)
XH	IRISDMC	1996	1997	Zandt (1996)
XP	IRISDMC	2010	2013	West & Christensen (2010)
XS	RESIF	2010	2013	Vilotte & RESIF (2011)
*Y*9	GEOFON	2007	2008	Sobiesiak & Schurr (2007)
YS	IRISDMC	2009	2013	Pritchard (2009)
ZA	GEOFON	2002	2004	Asch et al. (2002)
ZA	GEOFON	1994	1994	PISCO94
ZB	GEOFON	1997	1997	Schurr et al. (1997)
ZD	IRISDMC	2010	2013	Wagner et al. (2010)
ZG	IRISDMC	2010	2012	Beck et al. (2010)
ZL	IRISDMC	2007	2009	Beck & Zandt (2007)

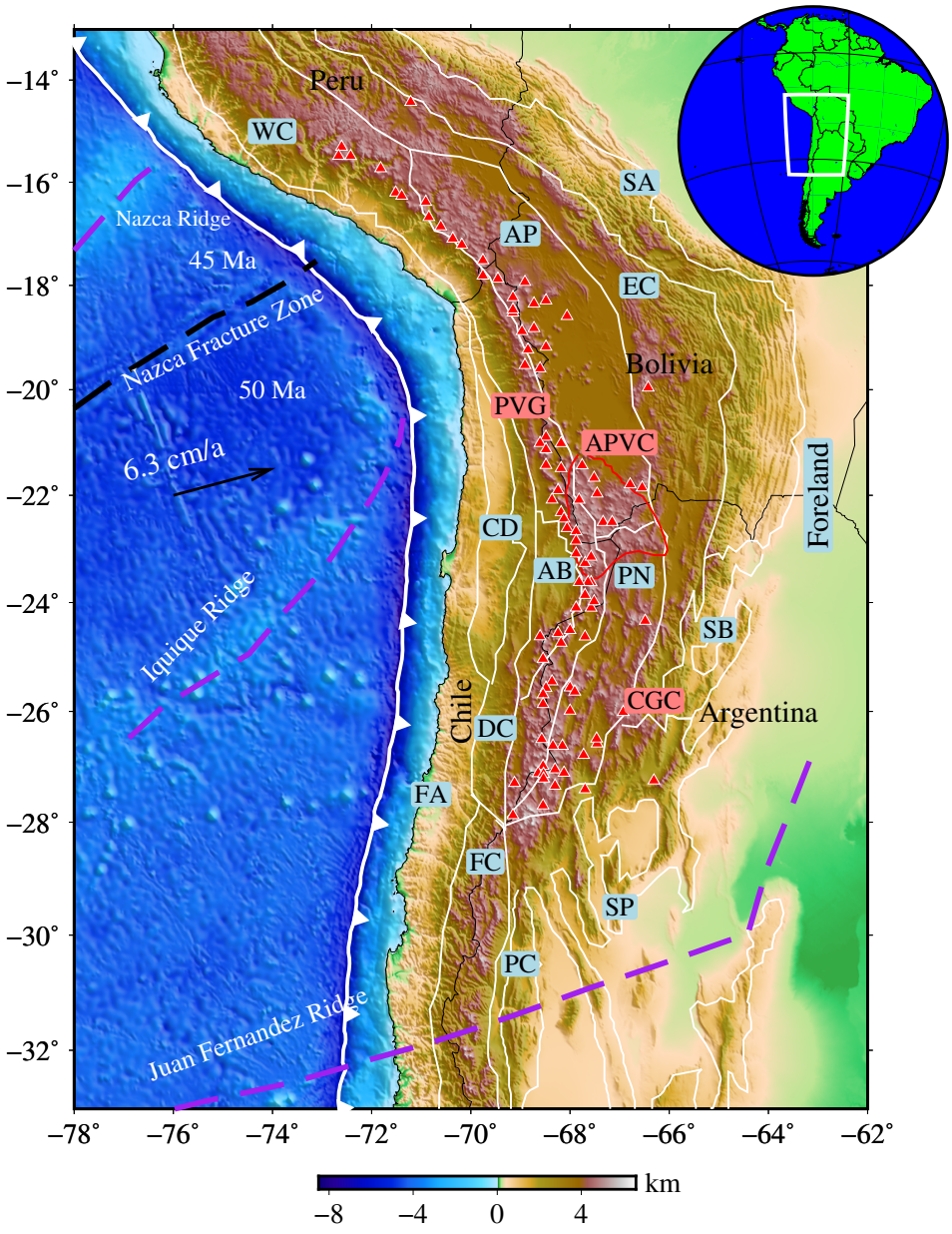

Fig. 4.1: Map of major morphotectonic provinces and volcanism centers (modified from Tassara (2005)) in the Central Andes, including the forearc (FA), Central Depression (CD), Domeyko Cordillera (DC), Atacama Basin(AB), Frontal Cordillera (FC), Western Cordillera (WC), Altiplano (AP), Eastern Cordillera (EC), Puna (PN), Precordillera (PC), Subandean Ranges (SA), Santa Barbara system (SB), Sierras Pampeanas (SP); Altiplano-Puna Volcanic Complex (APVC, enclosed by the red line). Cerro Galan Caldera (CGC); Pica Volcanic Gap (PVG). The purple dashed lines represent three major oceanic Ridges, including the Nazca Ridge, Iquique Ridge and Juan Fernandez Ridge. The reconstruction of the trace of the subducted Juan Fernandez Ridge has been taken from Yáñez et al. (2001). Red triangles denote volcanoes (retrieved from Global Volcanism Program, Smithsonian Institution, Venzke, 2013). Topography data has been retrieved from the ETOPO1 Global Relief Model Amante & Eakins (2009); the white saw-tooth line denotes the position of the Trench. Inset marks the position of our study region in South America.

4.4.1 Parameterization and starting model

The model is parameterized into velocities for vertically and horizontally propagating P waves (V_{PV} and V_{PH}) and vertically and horizontally polarised S waves (V_{SV} and V_{SH}), density ρ and shear

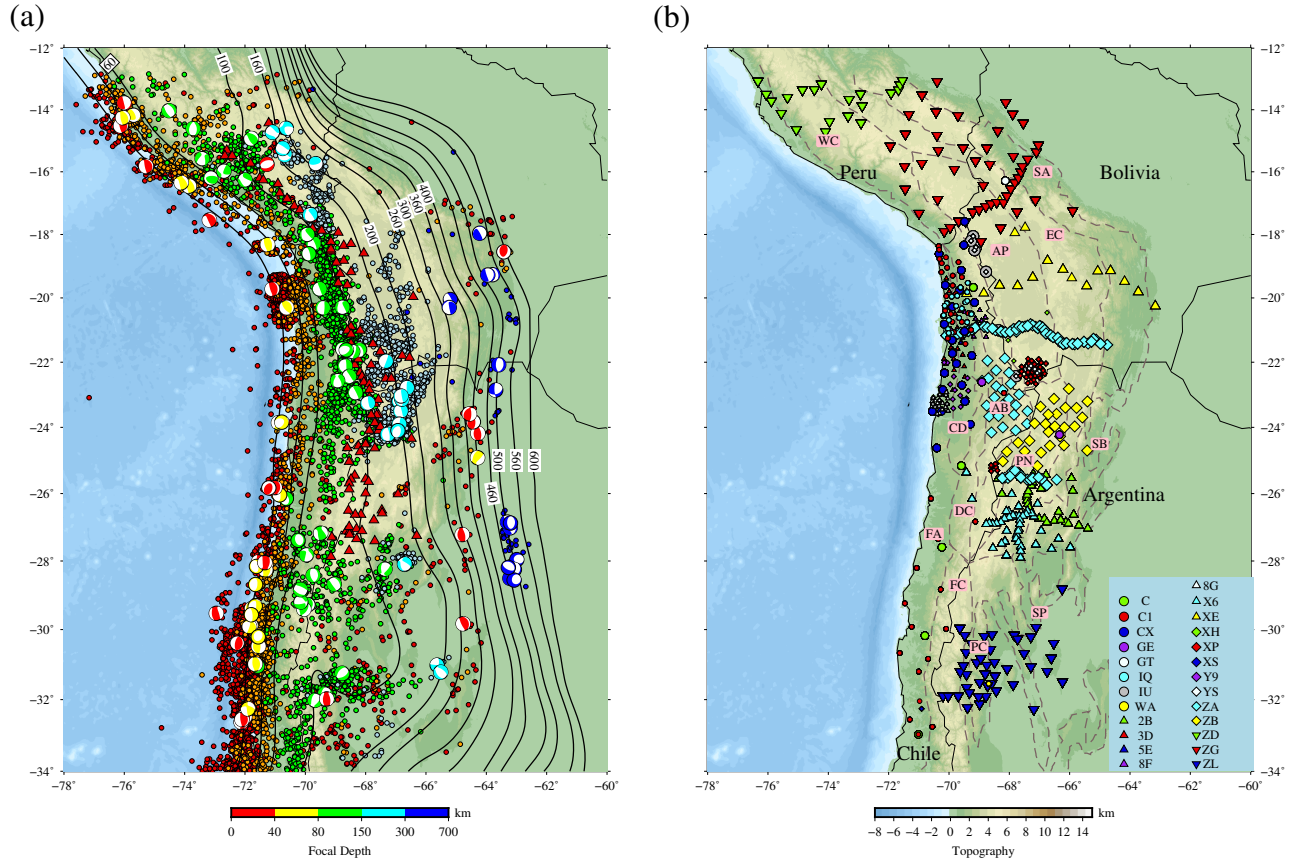

Fig. 4.2: (a) Map showing seismicity (magnitude > Mw 2.5) and Nazca slab depth contours. Black lines represent the slab contours, retrieved from the Slab2.0 global subduction zone model (Hayes et al., 2018), seismicity from 1991 to 2019 was extracted from the U.S. Geological Survey-National Earthquake Information Center (NEIC) catalog (https://earthquake.usgs.gov/earthquakes/search/). The beach balls indicate the focal mechanisms of the earthquakes used for the FWI in this study. (b) Map showing seismic stations of individual networks used in the study with circles marking the permanent stations. Detailed information about the networks is given in Table 4.1.

attenuation Q_μ (Figure 4.3). We extract an initial model from the second generation of the Collaborative Seismic Earth Model (CSEM, Fichtner et al., 2018). Specifically, the initial model consists of a global 1-D background model based on a modified Preliminary Reference Earth Model (PREM, Dziewonski & Anderson, 1981) including attenuation, where the 220-km discontinuity is replaced by a linear gradient. In the mantle, the 3-D S velocity perturbations from S20RTS (Ritsema et al., 1999) are superimposed on this model. Perturbations of the P velocity are scaled to S velocity using the relation proposed by Ritsema & van Heijst (2002). The crust is derived from the model of Meier et al. (2007). CSEM and thus our initial model also incorporate constraints from a previous large scale FWI work (Colli et al., 2013). Voigt averaged (Panning & Romanowicz, 2006) isotropic V_P and V_S of the initial model and their comparisons with the final model are illustrated within the supplementary material (Figure A.1-A.2 and A.4-A.9).

Although the parameterization specifies six parameters at each point not all can be resolved independently. In order to reduce the possible bias from a fixed density (Płonka et al., 2016; Blom et al., 2017), we update the density through the iterations but abstain from the interpretations due to the inferior resolution relative to the seismic velocity parameters. The number and type of velocity parameters being inverted for are varied through the stages of the multi-scale inversion (see section 4.4.3). Attenuation is fixed through the whole inversion. In this paper, we will focus on the

interpretation of isotropic V_S, as this is the most robustly resolved parameter (see section 4.4.4). However, V_P is also fairly well resolved and is presented in the supplementary material without interpretation.

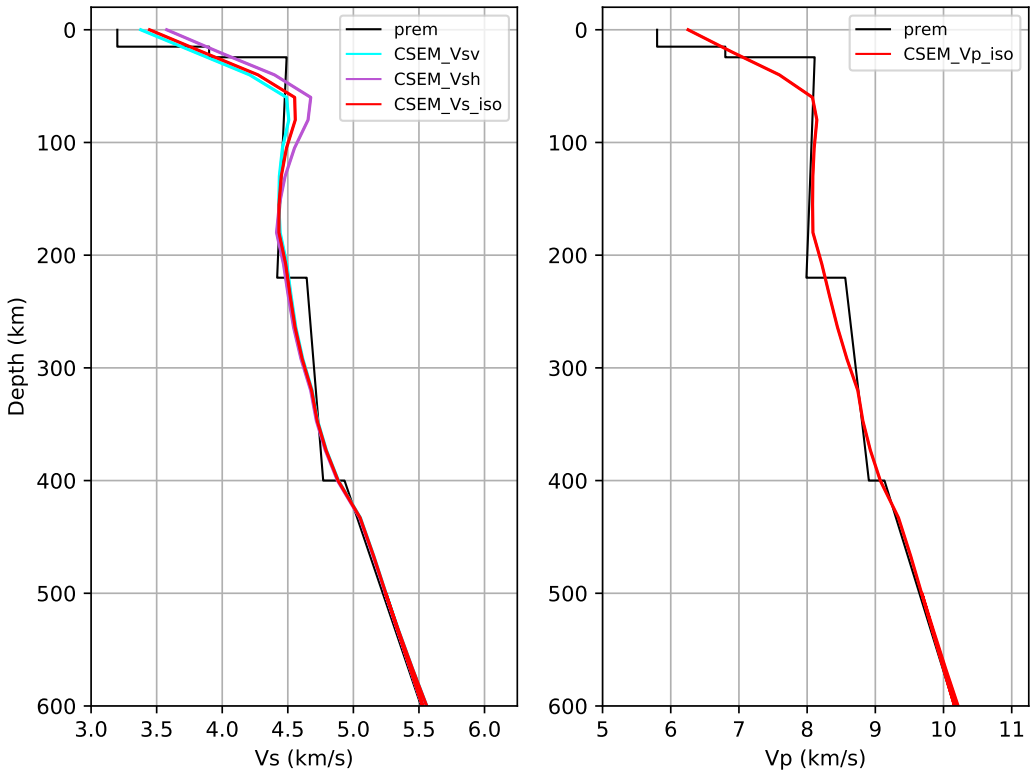

Fig. 4.3: The reference 1D model derived from the depth-averaged initial CSEM model (Fichtner et al., 2018), compared with isotropic PREM (Dziewonski & Anderson, 1981).

4.4.2 Misfit Functional

Various misfit functionals have been defined and applied in previous FWI studies (Liu & Tromp, 2008; Kristeková et al., 2009; Fichtner, 2010; Tao et al., 2017; Yuan et al., 2020). A reasonable and robust design for the misfit functional with its corresponding adjoint sources plays a crucial role in the convergence and final outcome of the inversion (Fichtner, 2010). The main effect of the long-wavelength earth structure is to speed up or delay the arrival times of the seismic phases, but applying the classical L^2 misfit directly on the waveforms would introduce local minima, as the absolute amplitude recordings are less reliable than the phase measurements and the misfit is prone to be dominated by the outliers, thus placing strong demands on the quality of measurements. In addition, amplitudes are highly sensitive to the focal mechanism at some azimuths. At the other extreme, the cross correlation time shift is probably the most widely used misfit measure in finite-frequency inversions. Its popularity results from the robustness of the measurement for the specific seismic phase shifts and its quasi-linear relation to the earth structure that facilitates the solution for tomographic inverse problems and overcomes the excessive non-linearity introduced by the L^2 (e.g. Luo & Schuster, 1991; Chen et al., 2015; Zhu et al., 2015; Liu et al., 2017). However this method cannot fully exploit the distortion of the observed data due to the small scale heterogeneities or the interference of multiple phases (Fichtner, 2010; Tao et al., 2017). Although the L^2

waveform fit and cross correlation time shift have been applied successfully in FWI, their applicability is limited to the cases where the seismic phases are clearly separable (cross correlation time shift) or where the observed and the synthetic waveforms are very similar (L^2 waveform fit). Our work takes advantage of Time-Frequency Phase Shift misfits (Fichtner et al., 2008; Kristeková et al., 2009) for the first five inversion stages (Table 4.2). It is based on the transformation of both the observed and synthetic data into the time-frequency domain where the frequency-dependent phase shift misfits are measured and thus more waveform details are included than in the single cross correlation time shift misfits. A significant advantage of this functional is the freedom of the time window selection, where it is no longer required to isolate particular seismic phases. The disadvantage of this approach is that additional care needs to be taken to avoid cycle skipping, especially for the higher frequency signals used in the final iteration stages. For the derivation of this misfit functional and corresponding adjoint sources, the reader is referred to Fichtner (2010).

In addition, we incorporate the cross correlation coefficient (CCC) misfit into the high frequency stage of our inversion workflow (stage VI in Table 4.2), which provides another measurement of the discrepancy of the synthetic and observed data, where the relative amplitudes of different arrivals are taken into account and which is nevertheless little affected by the source or receiver properties (Tao et al., 2018). This method was introduced and used for 1-D waveform fitting by Matzel & Grand (2004) and then applied to FWI by Tao et al. (2017) and Tao et al. (2018). The window selection is achieved with a semi-automatic algorithm, where the data are cross-correlated with the current synthetics within a sliding window and certain criteria are imposed on the cross correlation coefficients and time shifts for the window acceptance (Maggi et al., 2009; Krischer et al., 2015a). Following the automatic pre-selection, we visually checked and tuned the time-windows to avoid the cycle skipping aforementioned to fully exploit the distortion of the body wave phases due to small structure. The final acceptance criterion for every time-window is the CCC misfit between the synthetic waveform and the observed ones should be less than 0.4.

4.4.3 Multi-Scale inversion

The gradients of the misfit functional with respect to the model parameters are calculated using the adjoint method. The gradients can be used in various optimization schemes such as Conjugate-Gradients (CG) or L-BFGS (Liu & Nocedal, 1989), both of which we have implemented in our inversion work flow (see supplementary material A.1 and Table 4.2).

To obtain a global optimal solution and avoid the risk of being trapped in the local minimum, we follow a common approach of multi-scale inversion scheme (Bunks et al., 1995). Multi-scale FWI implies that we begin with the inversion from the long-period data for the long-wavelength seismic structure and march into the high-frequency domain to infer the small-scale structure. Through a multi-scale scheme, we could reduce the risk of the convergence to the local minima. We divide the whole inversion procedure into six stages (Table 4.2 and Figure 4.5c). For stages I–III, we use CG to update the model and observe clear drops of the misfits relative to the initial model whereas for stages IV–VI, we introduced the L-BFGS algorithm into the inversion in order to increase the convergence rate for the higher frequency inversion. We restart the CG or (and) L-BFGS for each stage, as the frequency contents, selected events and time windows and/or misfit functionals are adapted. The 20–80 s inversion was divided into two stages (III and IV) to accommodate additional time windows that are able to meet the selection criteria after the model was improved through stage III. For stages I–V, we use the time-frequency phase shift misfits (TF). Finally, in stage VI, we adopt the CCC misfit as the misfit function to measure the relative amplitudes, which captures waveform distortions from multi-pathing or scattering after most of the phase shifts have already been eliminated through the previous iterations. For the first five inversion stages

(I–IV), isotropic V_P, V_{SV}, V_{SH} and density ρ are updated, whereas for the final two inversion stages (V and VI), we update V_{PV}, V_{PH}, V_{SV}, V_{SH} and density ρ simultaneously.

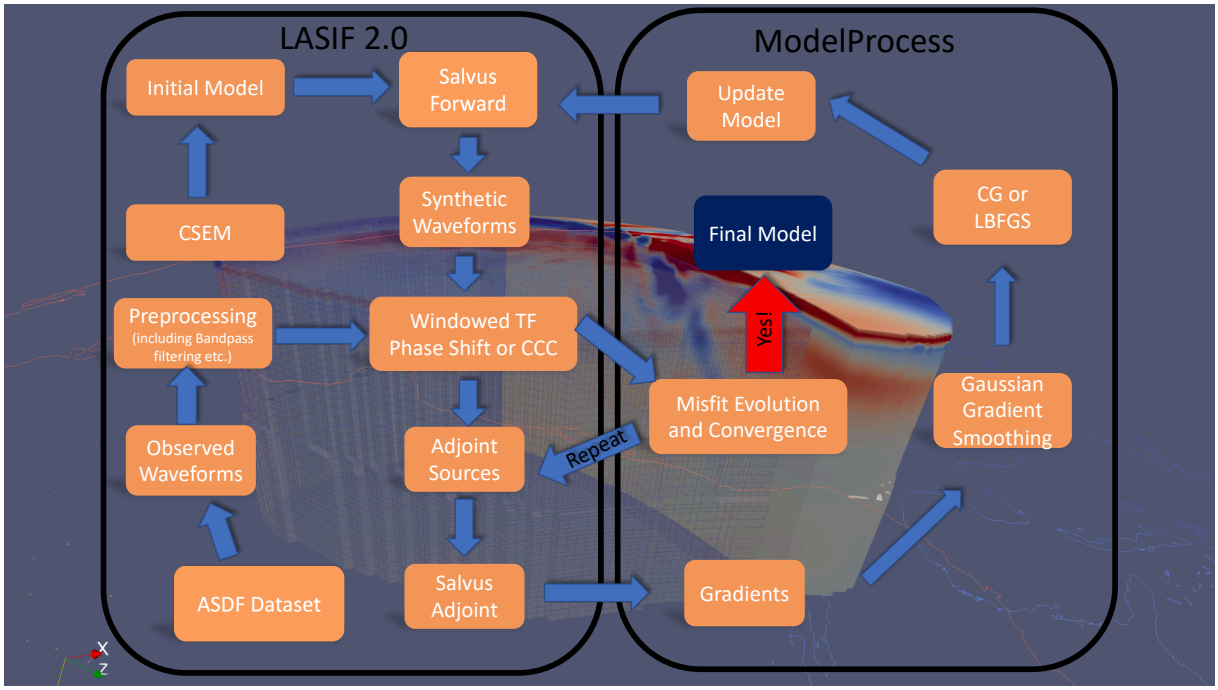

Fig. 4.4: Inversion workflow in this study with Conjugate-Gradient (CG) and L-BFGS implemented. The background is the 3D view of the final V_S velocity model.

We also build up a validation dataset to avoid the potential over-interpreting in the inversion dataset, which is independent of the inversion dataset thus not involved in the inversion procedure. The validation dataset consists in 30 events and provides 2164 unique ray-paths (Figure 4.5). Incorporation of the validation dataset could facilitate to identify the convergence due to an improved model should provide better fit to both the inversion and validation datasets (Lu et al., 2020). The evolution of the misfits within each stage is shown in Figure 4.5c. Surprisingly, during stage I and II the misfit reduction is actually slightly higher for the validation than the inversion dataset. We believe this indicates that at the long periods (and thus wave lengths), there is essentially no overfitting and the exact misfit reduction is therefore controlled by the noise levels or the earthquake-station data coverage. The fact that the validation dataset improves more is thus coincidence; the important point is that the differences in fit between both sets are minor. In every stage, the evolution of the misfits for the validation dataset has a same trend as that of the inversion dataset, which illustrates the robustness of our multi-scale inversion scheme (Lu et al., 2020; Krischer et al., 2018b).

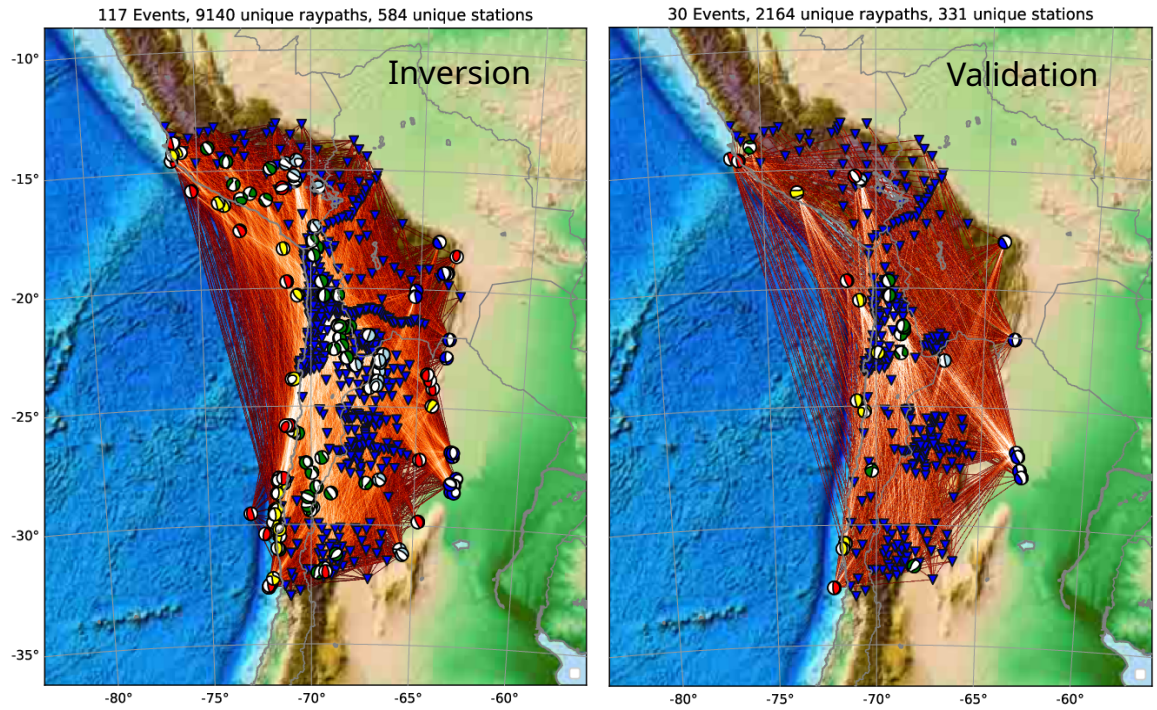

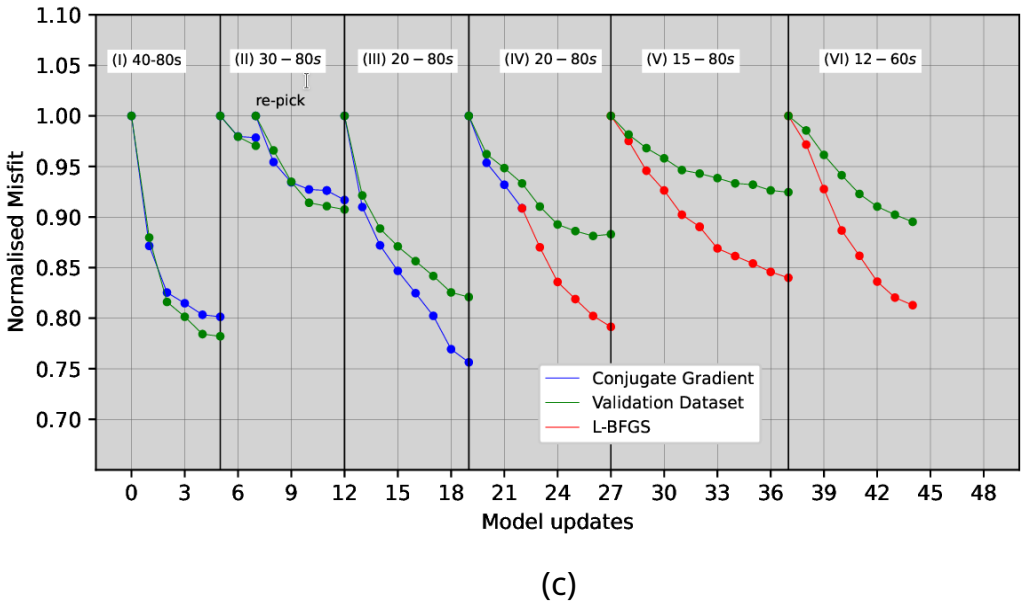

Fig. 4.5: (a) Total ray-paths used for the inversion with earthquakes and stations (b) Ray-path for the validation dataset (c) Misfit evolution over the complete inversion comprising six stages over progressively increasing frequency bands. The blue and red lines denote the misfits evolution using the Conjugate Gradient and L-BFGS method respectively. Misfits are normalized relative to each onset of the individual inversion stages. The green lines indicate the misfit evolution of the validation dataset.

Technically, in this work, we employ the Large-scale Seismic Inversion Framework 2.0 (LASIF, Krischer et al., 2015a, Thrastarson et al., 2021) for the simulation management, which is a framework and toolkit for the adjoint FWI, especially designed for Salvus. In practice, we take advantage of this package to set up iterations, generate input files for the simulation submissions, select time windows and calculate misfits and adjoint sources between the observed and synthetic data. Model updates were carried out outside LASIF based on our own implementation of the CG and L-BFGS algorithms (Figure 4.4). Furthermore,

Table 4.2: Overview of inversion stages

No.	Periods	It.	Simulation time	Events	Windows	Optimization	Misfit
I	40–80 s	5	600 s	39	8130	CG	TF
II	30–80 s	7	600 s	53	9916	CG	TF
III	20–80 s	7	600 s	77	19211	CG	TF
IV	20–80 s	8	600 s	77	32753	L-BFGS	TF
V	15–80 s	10	600 s	117	37240	L-BFGS	TF
VI	12–60 s	7	600 s	117	37242	L-BFGS	CCC

in order to lower the effects of the uneven coverage of seismic stations, we integrate the station weightings into the inversion, as implemented in LASIF (Krischer et al., 2015a; Thrastarson et al., 2021). The station weighting scheme takes fully account of the distances between neighboring stations and the number of the neighboring stations for every station. Every station weight thus is inversely proportional to the average distance with the other stations.

4.4.4 Model Assessment

In this subsection, we analyse the resolution for the inversion and the trade-offs among the parameter types. In traditional ray theory tomography, the checkerboard test is popular and relatively robust with low computational costs, but it is computationally prohibitive for FWIs. In this study, we therefore approximate the Hessian-vector product $\mathbf{H}\delta\mathbf{m}$ for a test function $\delta\mathbf{m}$ (Fichtner & Trampert, 2011; Fichtner & Leeuwen, 2015; Zhu et al., 2015, 2017; Tao et al., 2018)

$$\mathbf{H}\delta\mathbf{m} = \mathbf{g}(\mathbf{m} + \delta\mathbf{m}) - \mathbf{g}(\mathbf{m}) \tag{4.1}$$

where $\mathbf{g}(\mathbf{m})$ denotes the summed gradient from the adjoint simulations for model $\mathbf{m}$, whereas $\mathbf{g}(\mathbf{m}+\delta\mathbf{m})$ indicates the gradient from the perturbed model $\mathbf{m}+\delta\mathbf{m}$.

If the synthetics from the final model provide a good fit of the observed data and the inversion thus has reached convergence, $\mathbf{H}\delta\mathbf{m}$ can be used to estimate the model resolution. Specifically, when the $\delta\mathbf{m}$ is nearly point-localised, the $\mathbf{H}\delta\mathbf{m}$ will be a linearised point-spread function.

In order to provide a visual representation of resolution throughout the model rather than just for a single model node, we perturbed our model by adding velocity perturbations ($\delta\mathbf{m}$) in a three dimensional checkerboard pattern in the upper mantle made up of Gaussian spheres with ±1% maximum amplitude of the velocity for a specific depth and a Gaussian σ of 40 km. The horizontal and depth grid spacing of the Gaussian spheres are 2° and 100 km (Figure 4.6). We calculate $\mathbf{H}\delta\mathbf{m}$ for this anomaly pattern for V_{SV}, V_{SH} and isotropic V_P separately (Figure 4.6, 4.7, A.10 and A.11). For V_{SV} within the middle crust, we added similar Gaussian spheres but with σ=25 km at 20 km depth and a horizontal grid spacing of 1° in order to demonstrate the higher resolution at shallow depths.

Through the multi-parameter point-spread tests, we could confirm that the resolution in the crust is the highest (20-25 km). For the upper mantle, V_{SV}, V_{SH} and V_P could be resolved with 30-40 km spatial resolution, although they suffer from weak smearing and some cross-talks between parameter classes, particularly between V_{SV} and V_{SH} (Figure 4.6). Therefore, we focus our interpretation on the isotropic V_S model due to its better resolution but show the V_P model in the supplementary material (Figure A.10). To further quantitatively assess the resolution, we also present the normalised product of the perturbations $\delta\mathbf{m}$ and the resultant Hessian product $\mathbf{H}\delta\mathbf{m}$ within and between parameter classes (Figure A.12-A.14).

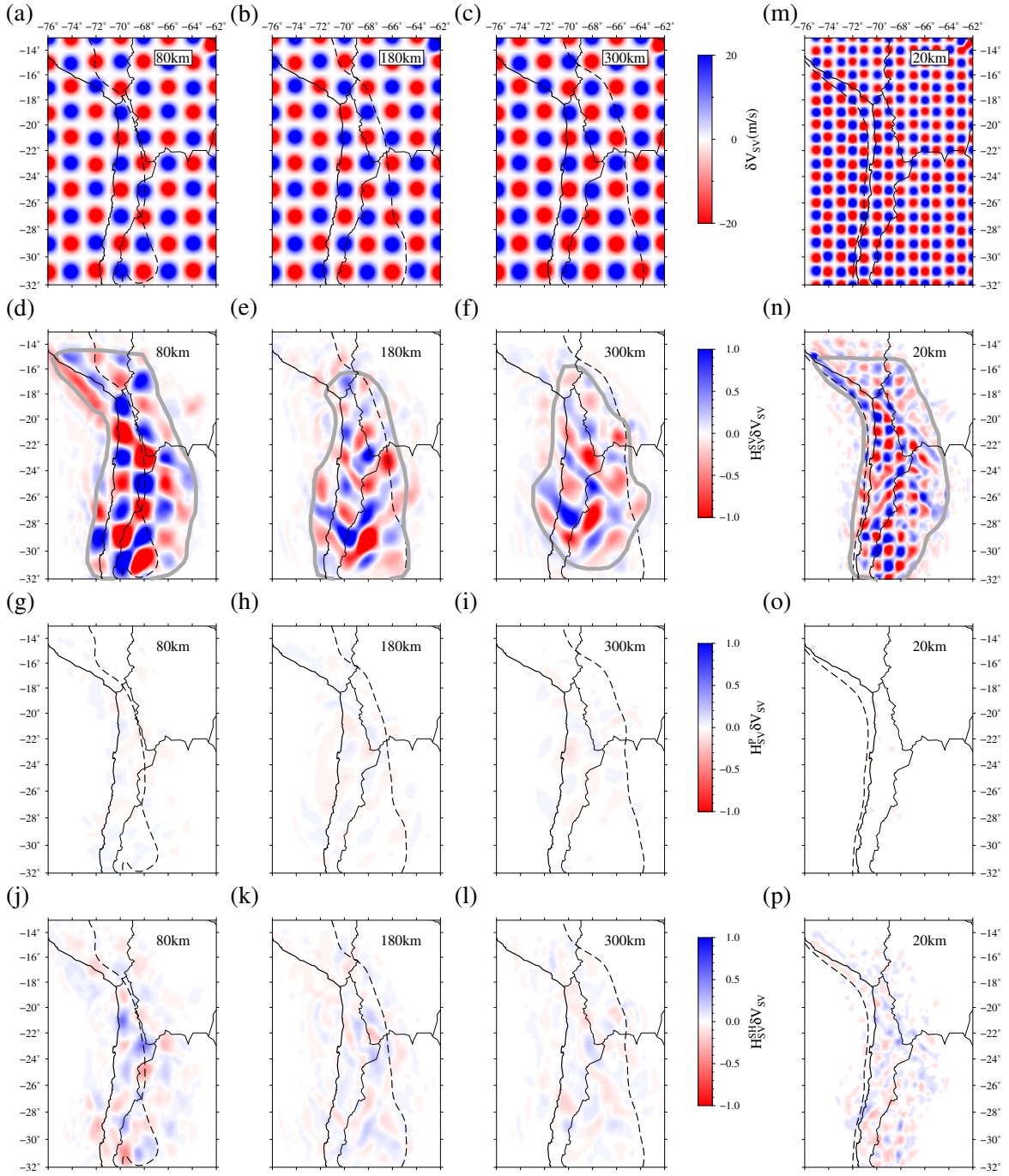

Fig. 4.6: Resolution estimates based on $\mathbf{H}\delta\mathbf{m}$, using the CCC misfit function and the same time windows and model as in the final inversion stage (VI) (see text). (a)-(c): Horizontal slices of input ($\delta\mathbf{m}$) 1% Gaussian $\mathbf{V}_{SV}$ perturbations ($\delta\mathbf{V}_{SV}$) with σ=40 km at 80 km, 180 km and 300 km depth in the upper mantle. (d)-(f): $\mathbf{H}^{SV}_{SV}\delta\mathbf{V}_{SV}$ for the upper mantle with respect to $\mathbf{V}_{SV}$ perturbations ($\delta\mathbf{V}_{SV}$); (g)-(i): $\mathbf{H}^{P}_{SV}\delta\mathbf{V}_{SV}$ for $\mathbf{V}_P$ with respect to $\delta\mathbf{V}_{SV}$, which represents the trade-offs between $\mathbf{V}_{SV}$ and $\mathbf{V}_P$; (j)-(l): Point-spread functions ($\mathbf{H}^{SH}_{SV}\delta\mathbf{V}_{SV}$) for $\mathbf{V}_{SH}$ with respect to $\delta\mathbf{V}_{SV}$, which represents the trade-offs between $\mathbf{V}_{SV}$ and $\mathbf{V}_{SH}$; (m): Independent test for the crust with input $\delta\mathbf{m}$ of 1% Gaussian V_{SV} perturbations ($\delta\mathbf{V}_{SV}$) with σ=25 km at 20 km; (n)-(p): Point-spread functions of $\mathbf{V}_{SV}$, $\mathbf{V}_P$ and $\mathbf{V}_{SH}$ in the crust with respect to the input perturbations of $\delta\mathbf{V}_{SV}$ in (m). The grey lines denote the trust region for the interpretations in Section 4.6.

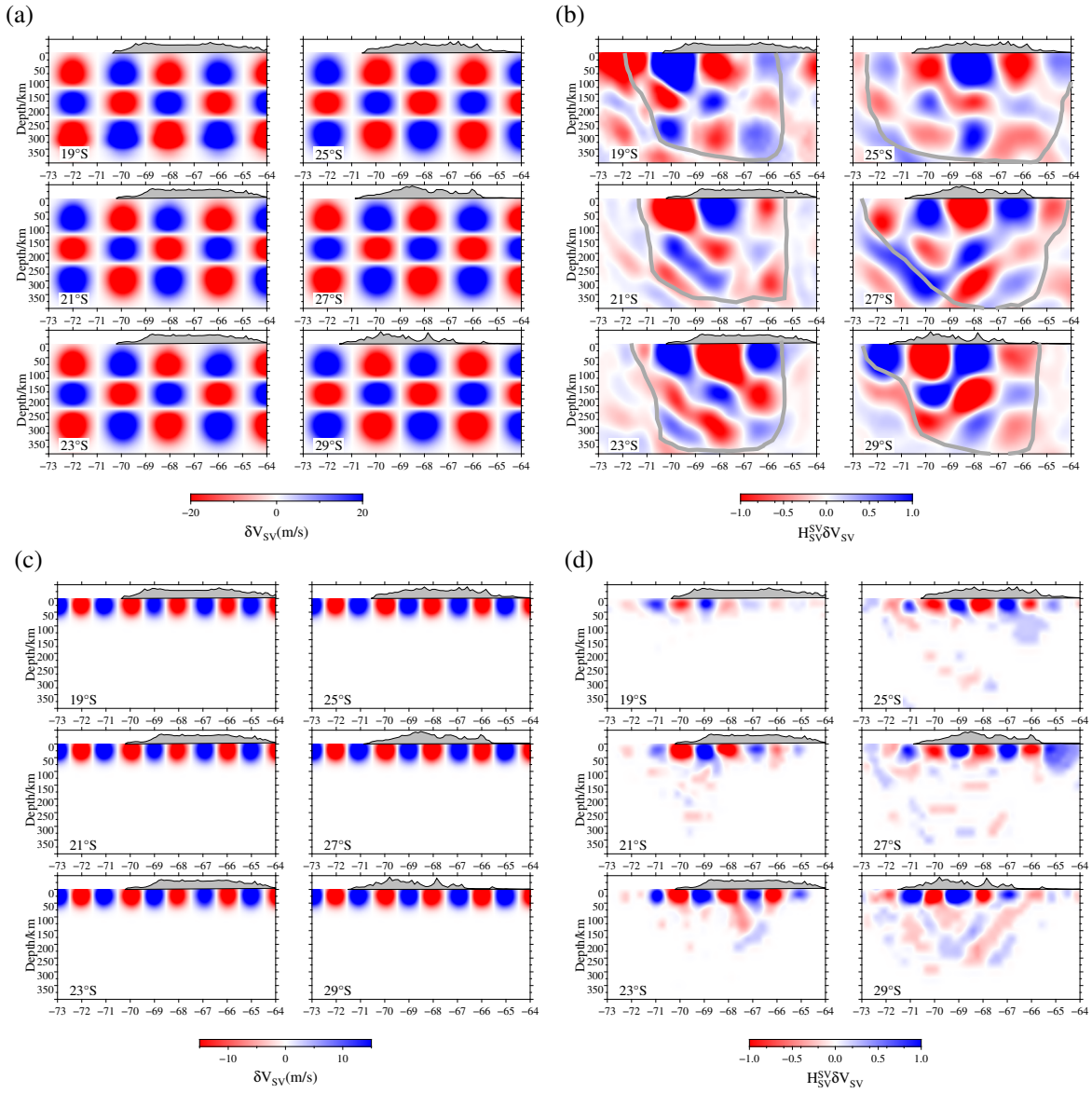

Fig. 4.7: East-west cross-sections of resolution tests for $\mathbf{V}_{SV}$ (see Fig. 4.6 and text for details) (a): Input $\delta\mathbf{m}$ for the $\mathbf{V}_{SV}$ perturbations ($\delta\mathbf{V}_{SV}$) in the mantle; (b): $\mathbf{H}_{SV}^{SV}\delta\mathbf{V}_{SV}$ in the upper mantle; (c): Input $\delta\mathbf{m}$ of V_{SV} perturbations ($\delta\mathbf{V}_{SV}$) in the crust; (d): $\mathbf{H}_{SV}^{SV}\delta\mathbf{V}_{SV}$ for V_{SV} in the crust.

4.4.5 Limitations

In this study, we do not invert for the earthquake sources but assume the centroid moment tensor solutions from the GCMT catalog to be correct. The reason is that our inversion domain is regional and many of our events are at the edge or outside the region covered by stations, implying a poor azimuthal coverage for the source inversion. Therefore the globally determined centroid solutions are likely to be better constrained than the regional moment tensor inversion. In order to mitigate the potential bias from mislocated events, we manually check and monitor the waveform fits, paying particular attention to the waveform polarities of the stations near the extension of the nodal planes of the earthquakes.

We further note that the wave propagation simulations are carried out on a regular spherical chunk mesh without taking into account the topography, ocean layer or explicitly meshed internal discontinuities. The periods covered in this study (12–60 s) mainly reflect the structure of the middle crust to the upper mantle and the effects of topography on the near surface structures could be negligible as the amplitude

of the topography (4-6 km) for the Central Andean Plateau is much smaller than half of the minimum seismic wavelength (15 km) (Nuber et al., 2016). However, in the future work, we would add more constraints from topography and internal discontinuities into the higher frequency surface wave inversion. In addition, a more sophisticated weighting scheme could be introduced and compared to further balance and estimate the effects from the uneven data coverage (Ruan et al., 2019) to speed up the convergence.

4.5 Results

After 44 iterations, we obtain the final velocity model. The improved match between observed and synthetic waveforms for the final model are shown exemplarily for a few events and stations in Figure 4.8. Moderate and deep earthquakes in the slab below the foreland of the central Andes played a particular role in providing a diversity of ray path directions. Up-going rays from these deep events do not only illuminate the slab and mantle wedge but due to their steep ray paths reduce the effect of lateral smearing in the crust and particularly upper mantle (Figure 4.8b).

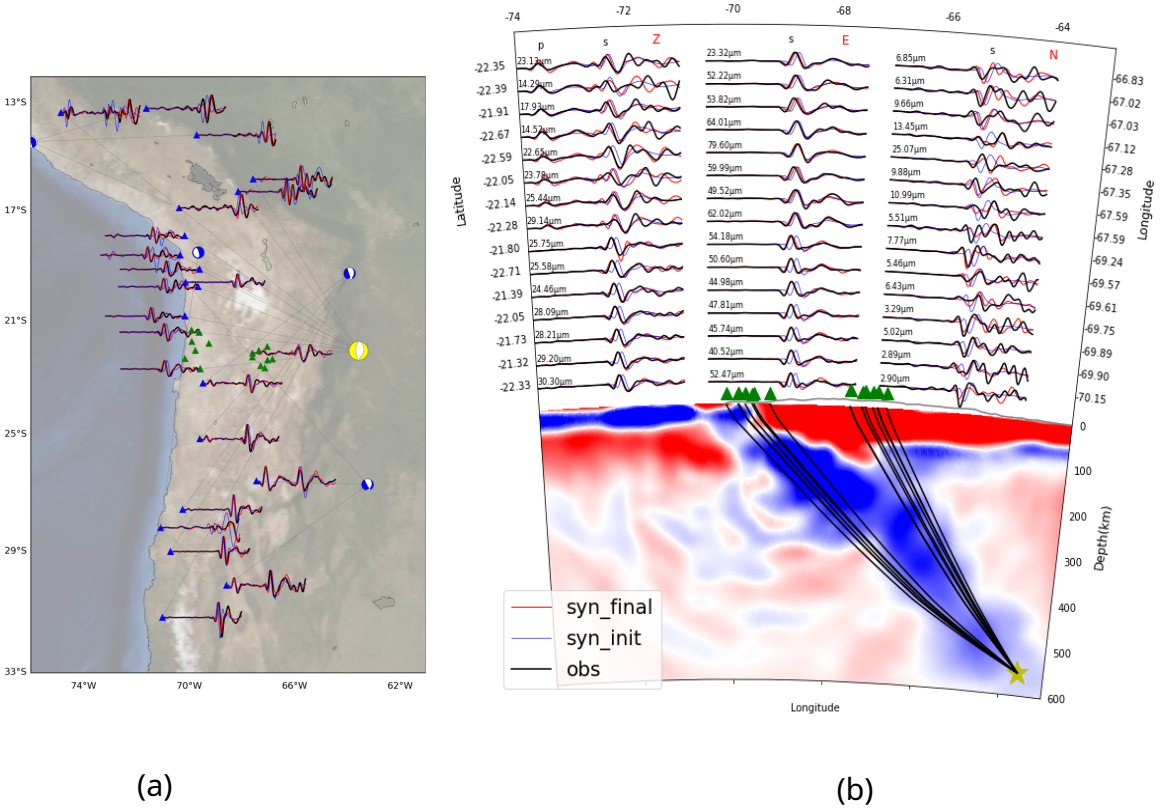

Fig. 4.8: (a): Waveform fits for Z component from the sample events beneath the Central Andes. Blue and red seismograms denote the synthetics from the initial and final models, respectively. Black seismograms represent the observed waveforms. Earthquakes and seismic stations are denoted by beach balls and triangles, respectively; (b): A cross section of the tomography model along 22°S. Black solid lines depict indicative up-going S wave ray paths, calculated based on the 1D PREM Model with the Taup module in Obspy. Three component waveforms in the top panel are arranged by longitude. Yellow star marks the position of the deep event. The locations in the map of this event and stations are denoted by the yellow beach ball and green triangles in (a). Note that amplitudes are normalized, with the normalization factor noted next to the traces. Due to the radiation pattern, the amplitude of the direct S phase on the N-S componet is comparatively small, such that low amplitude secondary arrivals become more visible.

Table 4.3: Overview of tectonic abbreviations

abbreviations	full name	abbreviations	full name
FA	Forearc	CD	Central Depression
DC	Domeyko Cordillera	AB	Atacama Basin
FC	Frontal Cordillera	WC	Western Cordillera
AP	Altiplano	PN	Puna
PC	Precordillera	SA	Subandean Ranges
SB	Santa Barbara system	SP	Sierras Pampeanas
CGC	Cerro Galan Caldera	PVG	Pica Volcanic Gap
APVC	Altiplano-Puna Volcanic Complex	APMB	Altiplano-Puna Magma Body
LMB	Lazufre Magma Body	IMB	Incahuasi Magma Body
IBMB	Incapillo-Bonete Magma Body	CGMB	Cerro Galan Magma Body
WF	West Fissure	QBBS	Quebrada Blanca Bright Spot
FAP	Fluid Ascent Path	WAZ	Weak Amplitude Zone

Because of the upper limit (12 s) of the frequency bands and the inclusion of surface waves, the resolution of V_S is better than V_P, so we focus the presentation and discussion on the V_S model. Nevertheless, the V_P model is also valid and therefore the isotropic V_P model is presented in the supplementary material. Although both V_{SV} and V_{SH} were resolved separately and contain information on the radial anisotropic structure, we prefer to translate the V_{SV} and V_{SH} into isotropic V_S through the Voigt average (Panning & Romanowicz, 2006) to avoid bias from unevenly distributed ray paths. The model is displayed in Figures 4.9–4.14. Figures 4.9 and 4.10 show the horizontal sections at crustal and mantle depths, respectively. Absolute velocities are plotted for the crust but velocity perturbations relative to the isotropic 1D CSEM model (Figure 4.3) are used for the mantle to amplify the velocity variations. Figures 4.11–4.13 show detailed horizontal and vertical sections across the whole Central Andes including Southern Peru, Northern and Central Chile, respectively; Figure 4.14 shows three along-strike cross sections (Q,R,S). Locations for all cross-sections are shown in Figure 4.9b. Meanwhile, in order to navigate the study area and facilitate the discussion, all the geological and geographical abbreviations are listed in Table 4.3.

4.5.1 Seismic velocity structure of the crust

Crustal structure of the arc and backarc

The striking feature in the crust (Figure 4.9) is a long band of low velocity anomalies extending from 16°S to 28°S, which closely follows the active volcanic arc. North of 23°S, this low velocity anomaly follows the boundary between the Altiplano (AP) and Western Cordillera (WC) and then extends southwest around the eastern boundary of the Atacama Basin (AB) into the southern tip of the WC. To facilitate the discussion, we divide this low velocity band into seven parts (low velocity anomaly C1-C7 in Figure 4.9a). C1 (from 16°S to 19.8°S) straddles the boundary of the AP and the WC, parallel to the coastline and the trench. South of 19.8°S, the amplitude of this low velocity anomaly decreases (marked as WAZ, Weak Amplitude Zone in Figure 4.9a), which coincides with a gap in the volcanic arc, the Pica Volcanic Gap (PVG), where no volcanic activity occurred since the Middle Pleistocene (Wörner et al., 1992, 2000). V_S within the WAZ ranges from 3.0 to 3.2 km/s, significantly higher than C1 and C2 where V_S=2.6–2.8 km/s (Figure 4.9, 4.12 and 4.14). South of the PVG (WAZ), the low velocity anomaly reappears as anomaly C2, coinciding with the reappearance of the active volcanoes. Anomaly C2 has previously been observed with regional body wave tomography (Koulakov et al., 2006; Schurr et al., 2006; Ward et al., 2013) and caused the appearance of a negative crustal converter in receiver function profiles across the Altiplano (Yuan et al., 2000; Wölbern et al., 2009).

From 21.5°S to 23°S (Figure 4.9 and Profile HH' in Figure 4.12), the amplitude of the crustal low velocity anomaly attains its maximum value along the whole volcanic arc in both width and amplitude beneath the Altiplano-Puna Volcanic Complex (APVC) (anomaly C3). The APVC is a late Cenozoic large-volume silicic volcanic zone (de Silva, S. L., 1989) located at the transition between the AP and the higher and more rugged Puna plateau (PN). Parts of C3 have previously been observed in a joint inversion of surface waves and receiver functions (Ward et al., 2017), where also a very low V_S of ∼2.0 km/s was inferred. The frontal volcanic arc coincides with the western edge of C3 and both deviate from the overall trend of the arc and low velocity band, so that they appear to be shifted nearly 100 km landward at 23°S (Figure 4.9 and Profile II' in Figure 4.12). The area to the west is filled by the Atacama Basin (AB), which is characterised by fast crustal V_S of ∼3.2–3.6 km/s (Figure 4.13). South of 24°S, low velocity anomaly C4 (Figure 4.9 and profile JJ' in Figure 4.13) beneath the frontal volcanic arc is much weaker than its north counterparts (C1-C3) and strikes southwestward along the eastern boundary of the AB. Further south from 26°S to 27.5°S, the low velocity anomalies labelled with C5 and C6 display further decreased strength beneath the main volcanic arc. Beneath the southern PN along 25°S and 26°S (Profile KK'–LL' in Figure 4.13), we detect one isolated low velocity anomaly (C7, V_S=2.8–3.2 km/s) beneath a back-arc volcanic center, the Cerro Galan Caldera (CGC, Kay et al., 1994; Kay & Mpodozis, 2002; Delph et al., 2017).

Crustal structure of the Forearc (FA)

Along the coast, a high velocity band marked as B is shown beneath the forearc from 19°S to 28°S, paralleling the trench and coastline (Figure 4.9) with V_S=3.6–4 km/s at 20–30 km depth (Figure 4.12). In the 40 km slice (Figure 4.9c), anomaly B presumably corresponds to the Nazca mantle lithosphere; as expected, its eastern edge approximately coincides with the top of the slab surface in Slab2.0 (Hayes et al., 2018), giving additional confidence in the resolving power of the inversion even slightly offshore. If we assume the V_S = 4.2 km/s contour as indicator of the Mohorovičić (Moho), we infer a forearc crustal thickness of 25-40 km, much thinner than the main arc beneath the WC, agreeing well with the Moho depth estimates from receiver functions (Yuan et al., 2002; Wölbern et al., 2009; Heit et al., 2014) and the density model with seismic constraints (Tassara & Echaurren, 2012).

In the cross-section along 21°S (profile GG', Figure 4.12), we can observe strong lateral gradients or sub-vertical interfaces where the velocity drops in two steps from the forearc to the volcanic arc (70.5° W to 68° W). The first sub-vertical interface separates the Central Depression (CD) from the forearc with the 4 km/s V_S contour, where the Moho depth increases from 30 km to 50 km (Yuan et al., 2002; Wölbern et al., 2009; Tassara & Echaurren, 2012), whereas the second delimits the CD and the WC by the 3.6 km/s contour, accompanied by a further drop in the Moho from 50 km to 70 km. These interfaces are also characterized by a seismically active upper crust (Bloch et al., 2014; Sippl et al., 2018). The eastern interface also marks the position of the West Fissure (WF), a sub-vertical strike-slip faults system (Victor et al., 2004; Yoon et al., 2009), which connects with the eastern end of the Quebrada Blanca Bright Spot (QBBS), a thin and distinct strong west-dipping reflector at 20–30 km depth visible in the ANCORP reflection profile (Oncken et al., 2003; Yoon et al., 2009; Storch et al., 2016). In our model this reflector follows the -10 % perturbation contour in the crust beneath the CD (Figure 4.12e). Additionally, Yoon et al. (2009) and Storch et al. (2016) identified a nearly vertical reflector connecting the western edge of the QBBS with the upper interface of the Nazca slab, which was interpreted as the Fluid Ascent Path (FAP, Figure 4.12f). In our image, the FAP is surrounded by a 'nose' of low velocities in the mantle wedge, consistent with the earlier interpretation.

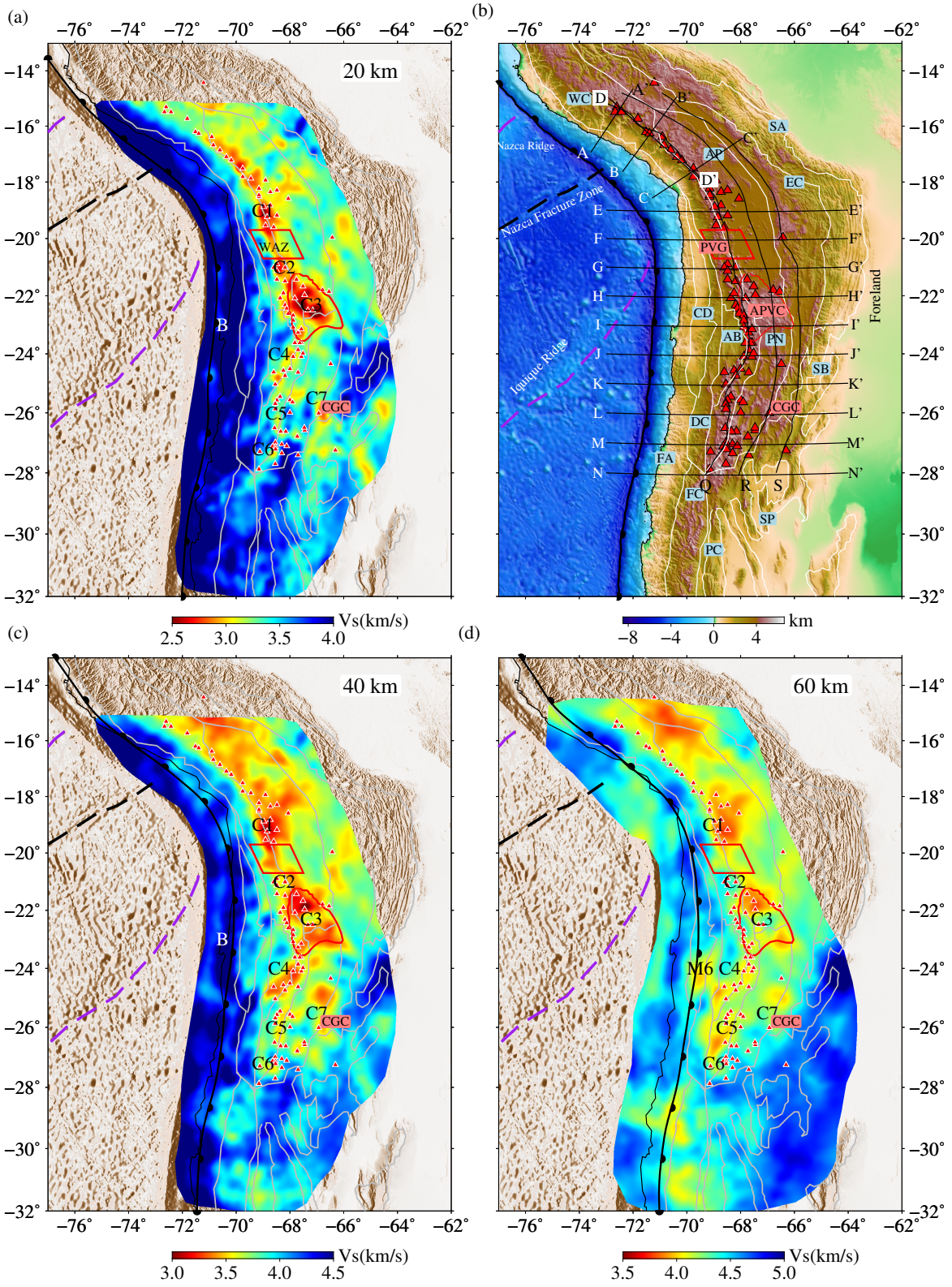

Fig. 4.9: Horizontal slices for the isotropic V_S in the crust at depths of 20 km (a), 40 km (c) and 60 km (d). Thick black lines with tooth denote the slab contours from Slab2.0. (b): Topographic map with the locations of the cross-sections (solid black lines with labels) shown in Figure 4.11–4.14 including 4 oblique cross-sections (AA'-DD') across southern Peru, 10 EW cross sections (EE'-NN') across the central Andes and 3 curved NS cross-sections (Q R and S) across the volcanic arc and backarc. Red box and circle denote the locations of the PVG (WAZ) and APVC, respectively. C1-C7 and B denote the crustal velocity anomalies discussed in the text. Please note that different color scales are used for the different depth levels.

4.5.2 Seismic velocity structure in the upper mantle

In the upper mantle, the most conspicuous feature is the strong positive velocity perturbation (anomaly H1 in Figure 4.10–4.13), which can be associated with the subducting Nazca plate. Its geometry varies from the southern edge of the flat subduction beneath South Peru (Figure 4.11c) to the normal dip subduction beneath Northern Chile (Figures 4.12 – 4.13) and then again the onset of the Pampean flat subduction at 28°S beneath Western Argentina (Profile NN' in Figure 4.13). These transitions are visible in a single along-strike cross-section, profile Q (Figure 4.14). In addition to the dominant slab anomaly H1, we detect several other anomalies in the mantle above the Nazca slab: beneath the back-arc region, we imaged high velocity anomalies located beneath the back-arc (H2 to H6) and low velocity anomalies from M1 to M9 (all visible in the map view in Figure 4.10 and back-arc profiles along R and S in Figure 4.14). In the following, we present these anomalies in detail and compare them with earlier studies.

Subducted Nazca plate and Mantle wedge beneath Southern Peru

The transition from flat to normal-dip subduction of the Nazca slab occurs below Southern Peru and Bolivia (Figure 4.11). Due to limited ray coverage for South Peru, the resolution beneath this area is restricted to around 150 km depth (Figure 4.6). Beneath the Moho along Profile BB' (Figure 4.11), a large volume low velocity region extends from the off-shore into the back-arc beneath the AP. We separate this low velocity zone into three parts, M7 to M9 (Figure 4.11); although they appear to be connected, they show noticeable differences in depth extent and spatial distribution. M7 extends from 50 to 100 km depth within the upper part of the Nazca plate, forming a necking feature in the slab (Ward et al., 2016) beneath the forearc. M9 beneath the frontal arc covers only a small depth range from 70 to 80 km and extends along the active volcanic arc in Southern Peru (Figure 4.11). In contrast, M8 spreads mainly beneath the back-arc, spanning the transition between the flat subduction and normal subduction regimes. M7 to M9 beneath South Peru share a high degree of similarity with the previous tomography results (Ma & Clayton, 2014; Ward et al., 2016; Antonijevic et al., 2015; Lim et al., 2018). South of M8, the uppermost mantle beneath the back-arc is instead dominated by a strong high velocity layer H4 at 80-120 km depth below the flat plateau of the northern AP (Ward et al., 2016). The transition from the flat to the normal-dip subduction is visible in Profile DD' (Figure 4.11) and appears to be accompanied by the increment of the velocities in the slab and decrease of the velocity within the crust beneath the volcanic arc (crustal low velocity anomaly C1 as illustrated in section 4.5.1).

Subducted Nazca plate and Mantle wedge beneath Chile

For the seismic structure beneath Northern Chile from 19°S–23°S (Profile EE'- II', Figure 4.12), a continuous and normal-dip subducting Nazca slab is clearly imaged in our model (Anomaly H1). Although the first order features are almost the same for these five profiles, there are two differences we would like to highlight. In profile EE' and FF', the seismic velocity of the Nazca slab is less pronounced than in the other three profiles (GG'-II') and accompanied by a weaker lower plane of the double seismic zone (DSZ) (Sippl et al., 2018) and absence of intermediate depth seismicity cluster compared to profiles GG'-HH' (Figure 4.12 and 4.14a). The second difference is the variation of the strength of the low velocity anomalies within the mantle wedge. From the 80 km and 105 km slices and profile F-F'(Figures 4.10 and 4.12), there is a gap between low-velocity anomalies M1 and M2 from 19.8°S to 21°S under the PVG. The velocity range for the mantle wedge beneath the PVG is 4.4–4.6 km/s, while it is 4.2-4.3 km/s for M1 and M2. We remind that a similar gap in the low velocity anomalies appears in the middle crust (the WAZ) in this area, as discussed in section 4.5.1. South of 24°S, along profiles JJ'-NN' (Figure 4.13), the Nazca slab begins to flatten slightly southwards above 200 km. Large scale

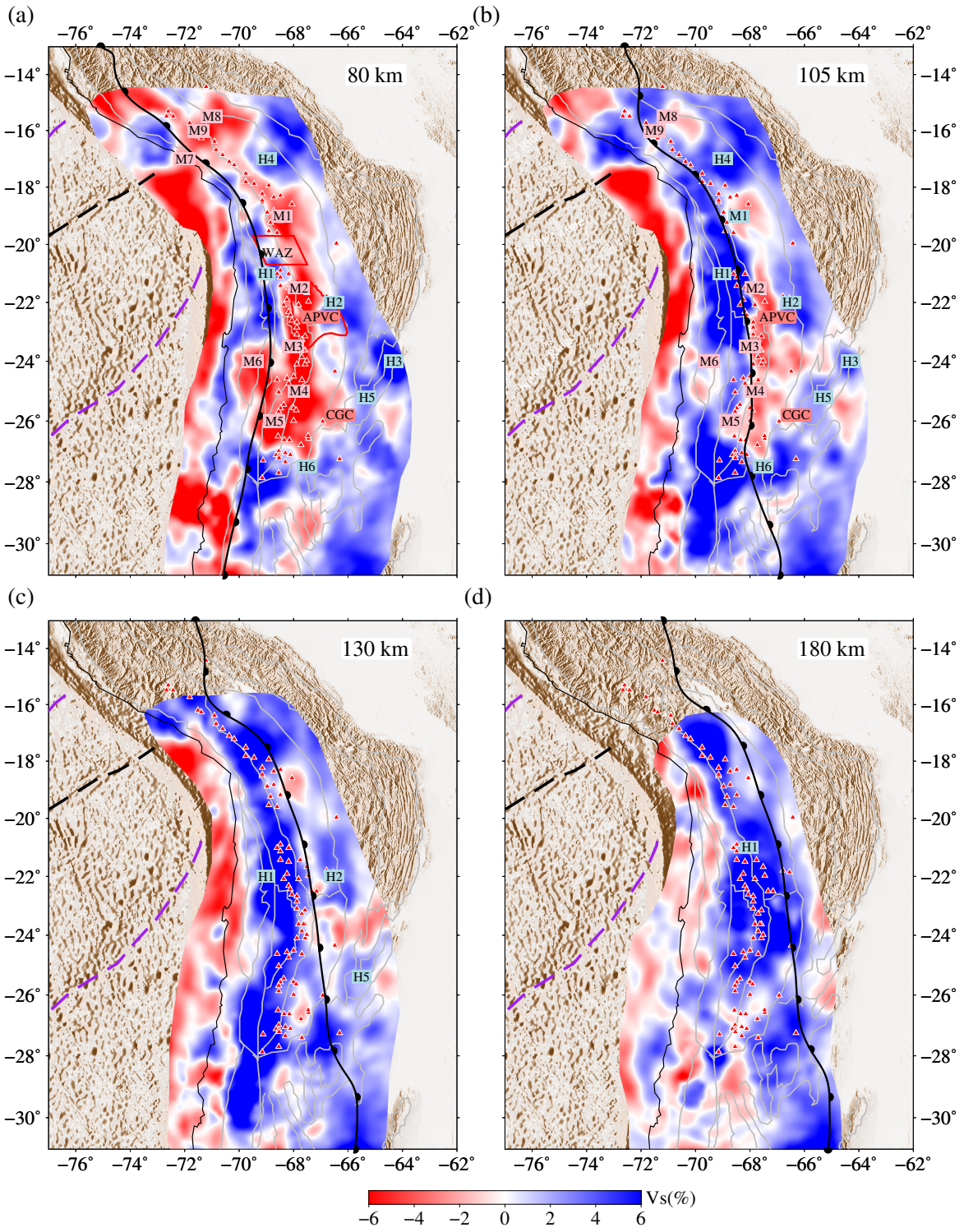

Fig. 4.10: Horizontal slices for the isotropic V_S perturbations for the upper mantle at depths of 80 km (a), 105 km (b), 130 km(c) and 180 km (d). The reference model is the 1D isotropic V_S from the CSEM shown in Figure 4.3. H1-H6 and M1-M9 indicate the high and low velocity anomalies within the slab and the continental mantle which are used for discussion.

low velocity anomalies (M3–M5) are still present above the slab (Figure 4.10) but are replaced by higher velocities south of 27°S. Separate from these, a low velocity body M6 to the west of M3 (and north of ∼24°S) extends from 25 km down to 100 km depth, spanning from the lower crust of the overriding plate to the upper part of the Nazca slab, beneath the Coastal Depression (CD) and Domeyko Cordillera (DC) (Figure 4.13). The lower limit of M6 approximately follows the oceanic Moho revealed by receiver functions (Yuan et al., 2000), which also indicated a slightly thicker-than-normal subducting oceanic crust. Therefore, the M6 appears to be confined to the oceanic crust and the fore-arc mantle wedge, possibly indicating a locally thicker and more hydrated oceanic crust (Ranero & Sallarès, 2004). Along profiles MM'-NN' (Figure 4.13), the Nazca plate reaches the northern edge of the Pampean flat subduction zone and the low velocity anomalies within the mantle wedge and middle crust are both much weaker than in the north. South of 28°S, there is a Holocene volcanic gap, where the frontal volcanic arc has been quiescent since 5 Ma (Kay & Mpodozis, 2002). Also, the amplitude of the high velocity Nazca slab decreases and the slab is less well confined compared to the North. However, this area is close to the boundary of our study domain, where the resolution is starting to diminish.

Continental lithosphere beneath the backarc Altiplano (AP) and Puna (PN)

Discrete high speed anomalies are observed beneath the back-arc area including the AP and PN, which we mark as H2, H3, H5 and H6 (see Figure 4.10, Figure 4.12–4.14). Anomaly H2 beneath the eastern AP and EC extends from 19°S to 23°S (Figure 4.12) and is still visible at 130 km depth (Figure 4.10). It reaches a maximum thickness of 50 km at 22° S and thins rapidly south of 23°S, while it weakens gradually through its full depth extent to the north (Figure 4.14). H2 was also identified by regional tomography studies although only confined from 22.5°S to 24°S and interpreted as a delaminated block (Schurr et al., 2006; Koulakov et al., 2006). Teleseismic tomography with a linear array (Heit et al., 2008a) along 21°S revealed a similar high speed anomaly under the depressed Moho beneath the AP and EC, validating the existence of high speed north of 22.5°S but without being able to constrain its along-strike extent. Using receiver functions and waveform modeling of deep eathquakes (Beck & Zandt, 2002) inferred a sub-Moho V_P of 8 km/s, which indicates lithosphere material.

An isolated cylindrical high velocity body H3 with velocity over 4.6 km/s is visible in the upper mantle down to ∼150 km below the northern edge of the Santa Barabara System (SB), connecting to a high velocity zone in the crust (Figures 4.10 and 4.13). Although this anomaly is situated close to the edge of the resolution domain and the resolution test indicates some smearing (Figure 4.6), H3 is better resolved than in previous works (Schurr et al., 2006; Ward et al., 2013; Scire et al., 2015a). We tentatively attribute this high speed anomaly from the crust to the upper mantle as part of the Brazilian shield (Scire et al., 2015a). More seismic observations are required for a precisely detailed interpretation for this strong anomaly. Another high speed anomaly H5 beneath the EC thrusts westwards down to 150–200 km in depth beneath the southern PN (Figures 4.13 and 4.14) which has also been observed with teleseismic Scire et al. (2015a) and local tomography studies (Bianchi et al., 2013; Liang et al., 2014; Chen et al., 2020) but the inferred shapes differed between those studies. H5 is accompanied by westward thickening of the crust from the EC to PN (Tassara & Echaurren, 2012). Further south, high speed anomaly H6 locates beneath the northern Sierras Pampeanas (SP), occupying the entire lithosphere and merged with the flat Nazca slab along 27°S (Figure 4.10 and 4.13).

4.6 Discussion

4.6.1 Transition zone from the flat to the normal dip subduction beneath southern Peru

Although the study domain does not fully cover the flat subduction zone beneath Peru and Bolivia, the southeast tip of the flat subduction and the transition from the flat to the normal dip subduction zone are imaged clearly (Figure 4.11). The southeastern portion of the flat subducting Nazca slab is visible along profile AA' as a continuous high-velocity body down to the bottom of the resolved region (i.e., 150 km) but becomes low velocity and discontinuous in its upper part along BB' (M7) showing a necking feature. The slab necking was also reported by other tomography studies (Ma & Clayton, 2014; Ward et al., 2016) and with a high V_P/V_S ratio (Lim et al., 2018). The inland trace of the Nazca Fracture Zone seems delineating the northern boundary of M7, which is a narrow (25-50 km) oceanic fracture zone, marking the transition of the oceanic floor age from 45 Ma to 50 Ma. This fracture zone possibly introduces more fluids into the Nazca crust and mantle lithosphere than in the adjacent regions (Figure 4.11a). Thus, low-velocity anomaly M7 may represent oceanic crust that has not yet metamorphosed into eclogite facies and possibly includes part of the hydrated Nazca mantle lithosphere (Kim & Clayton, 2015; Ward et al., 2016). Additionally, two low velocity anomalies M9 and M8 (Figure 4.11a), beneath the frontal arc and back-arc, respectively, span a broad depth range from the continental Moho to the upper interface of the slab. M9 beneath the frontal arc extends down to over 80 km, deeper than could be resolved in previous surface wave tomography (Ward et al., 2016). M9 presumably represents a more strongly serpentinized mantle wedge (Ward et al., 2016); enhanced dehydration from the oceanic crust and lithosphere within the subducted Nazca fracture zone (M7) would be expected to introduce more fluids into the mantle wedge, causing not only serpentinization but also enhanced partial melting, thus explaining also the low velocity anomalies in the continental crust (Figure 4.9). M8 beneath the backarc is a horizontal low velocity layer below the Moho, extending ∼100 km along strike, hinting at the absence of the continental lithophere of the upper plate. Ward et al. (2016) tentatively interpreted this anomaly as the concentration of fluids coming off the distorted slab. Based on our model, we do not preclude the possibility of the removal of the lithosphere due to the delamination, which would also explain the observed surface uplift since 9 Ma (Garzione et al., 2017).

Interestingly, in cross section CC' (Figure 4.11e), fast anomaly H4 has a similar depth extent (up to ∼ 100 km) as low velocity anomaly M8 in BB' (Figure 4.11g), when considering the velocity perturbations. We note the anti-correlation between the velocity within the uppermost mantle and topography, i.e., H4 is accompanied by the (relatively) lower topography in the AP and EC, while M8 is associated with the on average 4000 m high topography along BB', as qualitatively expected if the mantle lithosphere contributes to the isostatic balance (Ward et al., 2016). Two hypotheses were proposed to explain the presence of lithospheric material (anomaly H4) here. Either, it is the original mantle lithosphere of the AP (Ward et al., 2016), or it corresponds to the Brazilian Shield underthrusting from the East (Beck & Zandt, 2002; Ma & Clayton, 2015). Though coming up to the edge of the resolved region, H4 does seem to be connected with the lithosphere from the east beneath EC and Subandean Ranges (SA), so that our results favour the latter hypothesis.

4.6.2 Normal dip subduction zone and the dehydration of the Nazca Plate beneath the Northern Chile

We first review the key seismological observations related to the normal-dip subduction as we illustrated in the last section: (1) A weak low velocity zone within the uppermost mantle and middle crust (WAZ) from

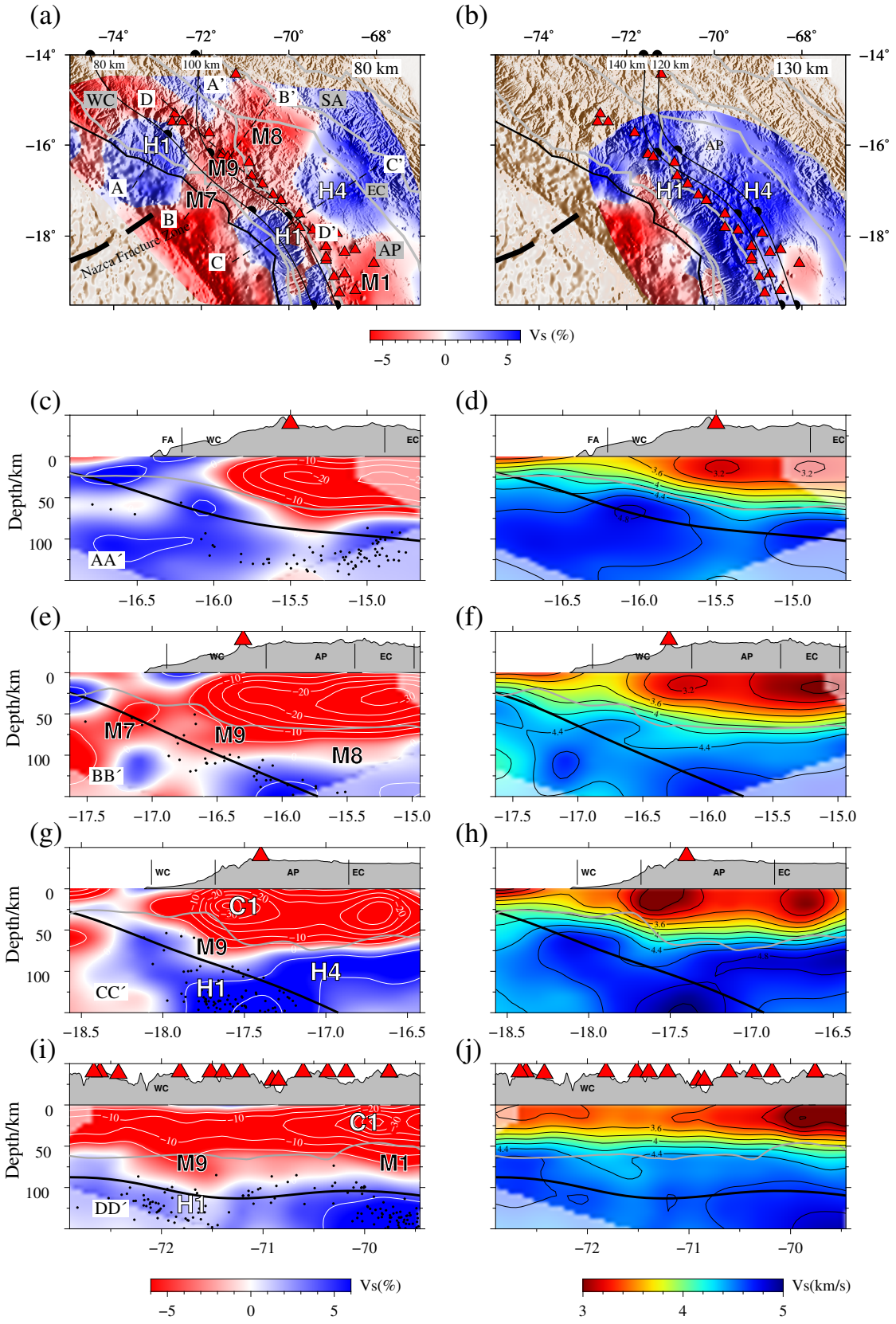

Fig. 4.11: (a) and (b) are zoomed-in horizontal slices for V_S perturbations at depths of 80 and 130 km beneath the southern Peru. Black dashed lines in (a) mark the positions of profile AA' – DD'. (c), (e), (g) and (i) are cross sections of V_S perturbations. Thin white lines mark 5% perturbation contours. (d), (f), (h) and (j) are absolute V_S velocity model. Thin black lines mark 0.2 km/s velocity contours. Solid black lines denote the slab contours from Slab 2.0 and the solid dark grey lines indicate the Moho depth extracted from (Bishop et al., 2017). The black dots are seismicity retrieved from (Kumar et al., 2016).

19.8°S-21°S, coincides with the Pica Volcanic Gap (PVG): north and south to this gap, large amplitude low velocity anomalies emerge within the middle crust (anomalies C1 and C2) and the uppermost mantle (anomalies M1 and M2) beneath the active volcanoes (Figures 4.12 and 4.14); (2) The positive velocity anomalies within the slab at depth of 80-120 km are stronger and accompanied by a more vigorous DSZ and prominent intermediate depth seismicity cluster south of 21°S than further north (Figure 4.12) (Sippl et al., 2018).

In receiver functions images a strong oceanic Moho converter has been observed (Yuan et al., 2000, 2002). Sippl et al. (2018) compared the locations of the upper plane of the DSZ with this converter and thus demonstrated that the upper plane DSZ seismicity locates within the oceanic crust. Both DSZ and converter disappear down-dip at the same position and the DSZ is replaced with a dense intermediate-depth seismic cluster which was interpreted as indicating the completion of eclogitization of the oceanic crust (Sobolev & Babeyko, 1994; Bjørnerud et al., 2002; Hacker et al., 2003; Okazaki & Hirth, 2016; Sippl et al., 2018; Wagner et al., 2020). At 21°S (Figure 4.12), M2 locates above the intermediate-depth seismic cluster, so we interpret M2 as the hydrated and hot mantle wedge (Wada & Wang, 2009). The dehydration of the oceanic lithosphere due to antigorite breakdown provides a plausible source of fluids. Here, the subducted mantle lithosphere probably contributes more fluids than the oceanic crust to the mantle wedge south of 21°S (Sippl et al., 2018; Cabrera et al., 2021), causing hydration and partial melting in the mantle wedge (Wada & Wang, 2009) and continental crust (Schilling & Partzsch, 2001; Schilling et al., 2006; Kay & Coira, 2009; Ward et al., 2013) beneath the volcanic arc and triggering the dense cluster of intermediate and deep seismicity within the oceanic lithosphere; even the deeper, the slab is dried up and intermediate depth seismicity shuts off quickly downdip (Peacock, 2001; Ferrand et al., 2017; Sippl et al., 2018; Wagner et al., 2020).

A recent magnetotelluric study (Araya Vargas et al., 2019) inferred the crust and mantle wedge beneath the PVG to have higher electric resistivity, whereas from 21°S to 23°S, a large volume low resistivity body exists within the mantle wedge, extending from 70 km down to 100 km above the intermediate-depth seismicity cluster, confirming its hydrated and thermal state. Further supporting evidence comes from attenuation tomography, which revealed a high attenuation feature within the crust and uppermost mantle from 21°S to 23°S beneath the volcanic arc (Schurr et al., 2003). Combining the different extents of the partial melts within the crust, the hydration of the mantle wedge, the activity of the intermediate depth seismicity cluster and the electrical resistivity, we infer that the dehydration from the subducted Nazca lithosphere appears to be much more vigorous from 21°S to 23°S than beneath the PVG.

The PVG extends from 19.8°S to 21°S, corresponding to a segment where the volcanic activity is absent since Middle Pleistocene (Wörner et al., 1992). Araya Vargas et al. (2019) proposed that the crust beneath the PVG represents a block with anomalously low permeability, which precludes circulation of magmas or fluids within the continental crust. Some authors have argued that the subducted Iquique Ridge (Figure 4.1), composed of several seamounts (Madella et al., 2018), is associated with enhanced hydration of the Nazca plate prior to entering the trench from 20°S to 21°S (Comte et al., 2016; Araya Vargas et al., 2019). However, there is no clear evidence that this is the case for the Iquique ridge, and in fact some clues indicate reduced water input into the subduction zone. Geersen et al. (2018) observed bending-related outer rise faulting only at 18°S-20°S, north of the projection of the Iquique ridge. These faults are often thought to provide pathways for fluids into the mantle (Ranero & Sallarès, 2004), so the absence of faulting from 20∘S to 21∘S hints at reduced hydration of the oceanic lithosphere. In addition, no evidence for fluid seepage in the marine forearc was found in this area (Geersen et al., 2018).

In our model, higher velocities than the north and south in the crust and mantle wedge beneath the PVG indicate that mantle wedge is drier and (or) colder than north and south of this gap. This

observation may suggest a much reduced slab dehydration (and wedge hydration) beneath the PVG. From an anisotropic P wave tomography (Huang et al., 2019), the uppermost mantle at 60 km from 21° S to 23° S is characterised by trench-normal fast directions, while below the PVG trench-parallel fast directions are found, presumably indicating the disruption of the flow pattern in the mantle wedge. The Iquique Ridge has been subducting since ∼2 Ma in this region (Rosenbaum et al., 2005) and its arrival is probably coeval with the formation of the PVG during the Holocene (Wörner et al., 1992). We therefore agree with previous studies that attribute the development of the PVG to the subduction of the Iquique ridge (Wörner et al., 2000), but argue that this has diminished hydration of the mantle wedge due to the decreased dehydration from the oceanic lithosphere. (Wagner et al., 2020) suggests a possible reason for this by showing that thicker oceanic crust due to the seamounts and underplating would impede fluid infiltration reaching the oceanic mantle lithosphere. There is therefore no need to invoke permeability variations in the lower crust to explain the absence of volcanism there. Interestingly, unlike the Nazca Ridge beneath southern Peru and Juan Fernandez Ridge (Figure 4.1) beneath Pampean Chile, which are accompanied by prominent flat subductions of the Nazca plate, the subduction of the Iquique Ridge does not seem to influence the subduction angle or at least has not yet initiated a large scale flat subduction possibly due to the short subduction history of the Iquique Ridge (Ramos & Folguera, 2009; Manea et al., 2017).

A wedge-like cluster of crustal seismicity (Sippl et al., 2018; Bloch et al., 2014) appears to overlap with the high velocity forearc crust and the shallow part of the Nazca slab (anomaly B, Figure 4.12c-j, profiles F-I). The eastern boundary of this seismicity cluster (equivalent to the 4 km/s V_S contour) is at or slightly east of the transition from the forearc to the CD. This fast crustal forearc is characterized by high electrical resistivity (Araya Vargas et al., 2019) and low attenuation (Schurr et al., 2006, 2003). The obervations thus indicate cold temperatures beneath the forearc and low interconnectivity of the interstitial fluids. The second lateral transition mentioned in section 4.5, the boundary between the CD and WC, is characterized by intense upper crustal seismicity (Figure 4.12c-h, profiles F-H). At the surface this location coincides with the West Fissure (WF) faulting and the western edge of the AP. Here, the electrical resisitivity is low all the way from the crust to the fore-arc mantle (Araya Vargas et al., 2019), where the low resistivity region connects to the slab at the onset of intermediate depth intra-slab seismicity. We further conclude that this sub-vertical transition might be related to upward migrating fluids from the forearc mantle wedge to the overriding plate crust, where it modifies the rheological properties of the forearc crust from brittle in the west to ductile in the east (Bloch et al., 2014).

To summarize, from 18° S to 27° S, five low velocity anomalies M1 - M5 enclose the hydrated mantle wedge within the uppermost mantle beneath the frontal volcanic arc and cause the partial melting within the mantle wedge and crust (C1-C5, Figure 4.14a). In order to further quantify the fraction of partial melts within the crust and mantle wedge, we provide a brief estimation of partial melts in Figure A.15 and discuss the assumptions and methods for estimation of partial melts in supplementary material A.2 (Chu et al., 2010; Delph et al., 2017; Ward et al., 2014). The partial melt fraction within the middle crust beneath the Pica Volcanic Gap is around 5 %, whereas south of 21°S it is over 10 %.

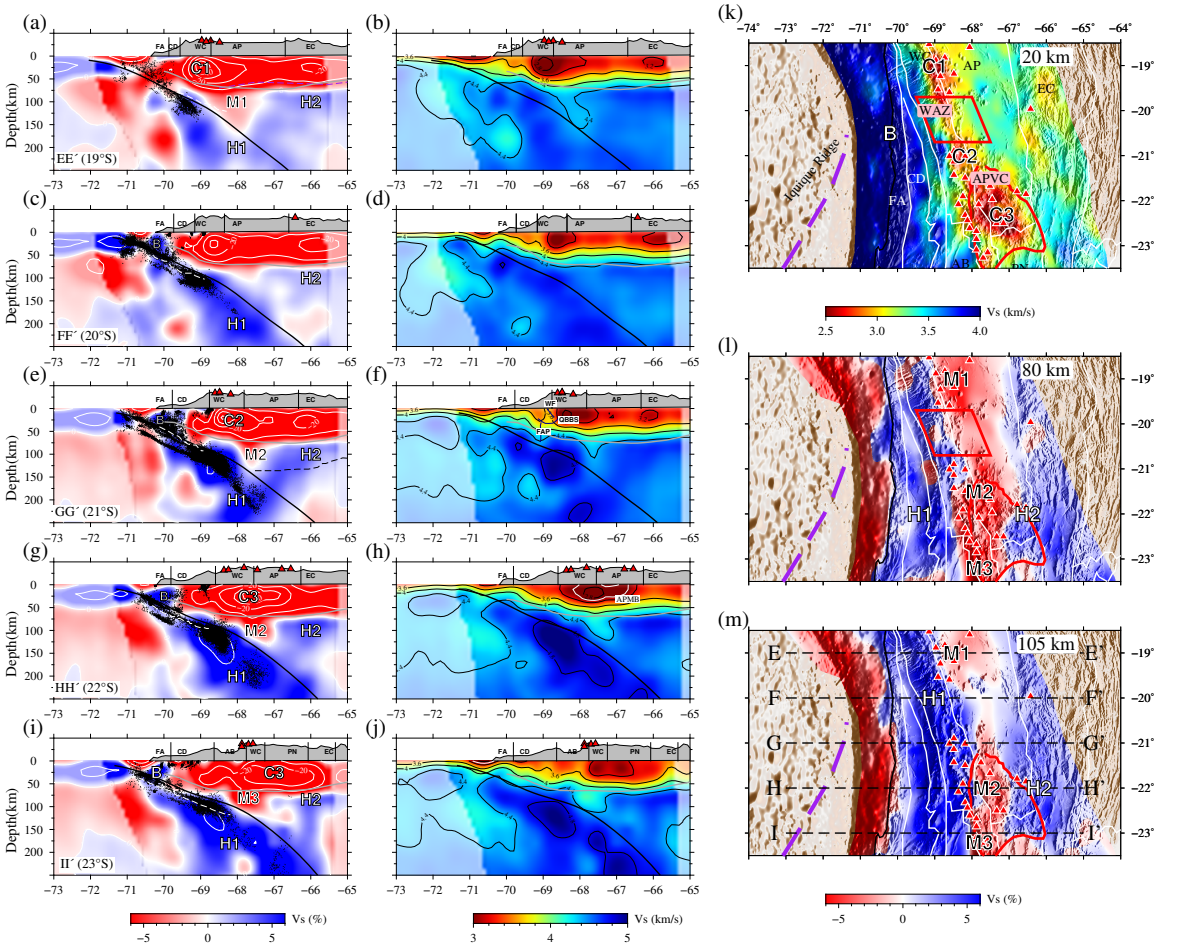

Fig. 4.12: (a), (c), (e), (g) and (i) are cross sections of the V_S perturbations for profiles EE' – II'. (b), (d), (f), (h) and (j) are cross sections of the absolute V_S. Black dots denote the seismicity from Sippl et al. (2018). The Moho is extracted from Tassara & Echaurren (2012), denoted by grey lines. Thin black dashed lines beneath anomaly H2 in (e) is the LAB depth contour extracted from Heit et al. (2007a). Solid blue lines within the crust beneath the CD mark the positions of West Fissure, QBBS and Fluid Ascent Path (FAP) Bloch et al. (2014); Yoon et al. (2009) along GG' in (f) and the white dashed lines in (c)-(i) are oceanic Moho retrieved from (Yuan et al., 2000). Solid black lines denote the slab contour from Slab2.0. (k),(l) and (m) are zoomed-in horizontal slices for the crust and upper mantle. Other elements as in Fig. 4.11.

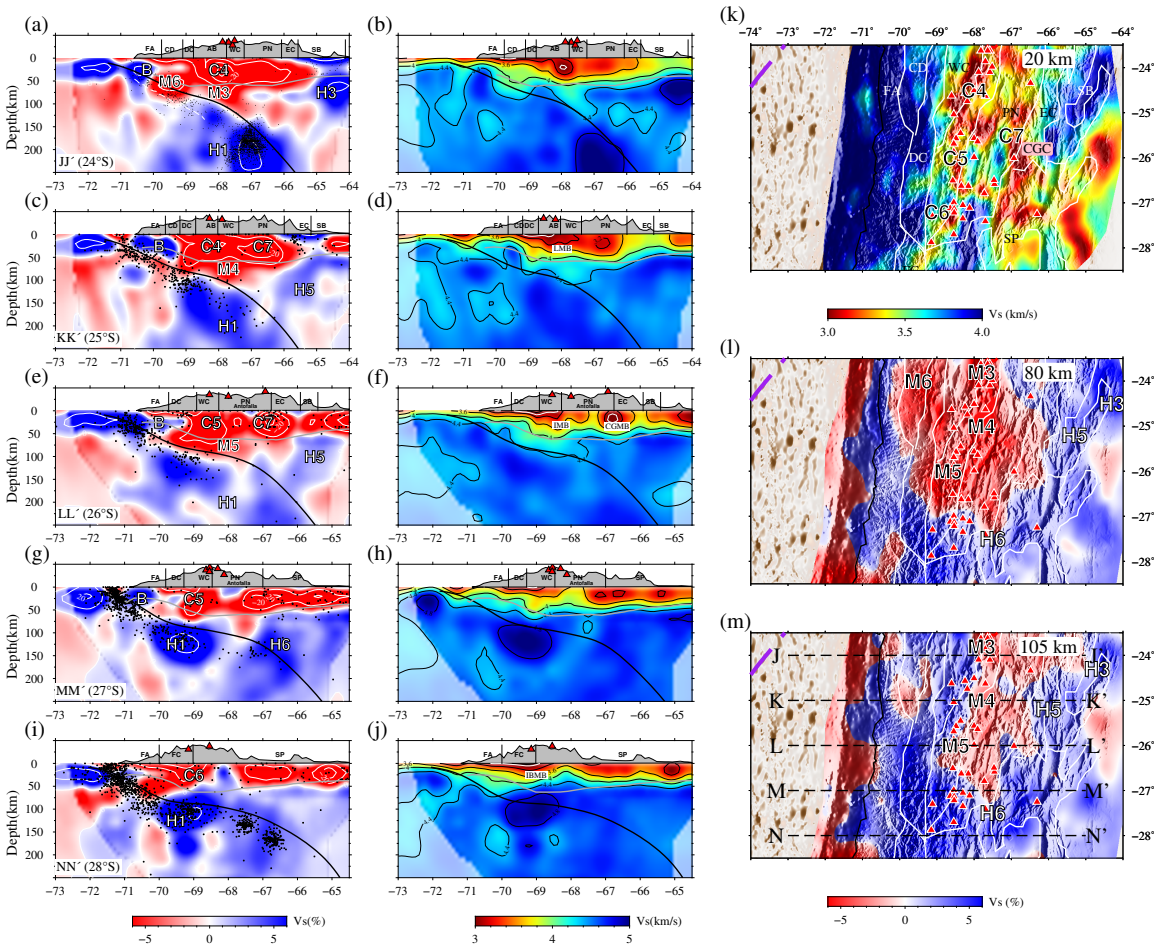

Fig. 4.13: (a), (c), (e), (g) and (i) are cross sections of V_S perturbations for profiles JJ'–NN'. (b), (d), (f), (h) and (j) are cross-sections of the absolute V_S. Black dots denote the seismicity retrieved from ISC-EHB catalogue `http://www.isc.ac.uk/isc-ehb/`. Grey solid lines denote the Moho depth retrieved from Tassara & Echaurren (2012). Solid black lines denote the slab contour from Slab2.0. The white dashed line in (a) is the oceanic Moho retrieved from Yuan et al. (2000). (k), (l) and (m) Zoomed-in horizontal slices for the crust and upper mantle. Other elements as in Fig. 4.11.

4.6.3 Multi-stage continental lithospheric foundering and the evolution of the crustal magma chambers

High velocity anomaly H2, extending between 20.5°S and 23°S and down to 130 km in depth, represents a thin mantle lithosphere with a thickness of ∼50 km beneath the southern AP and northern PN. Receiver function images of the lithosphere-asthenosphere boundary (LAB) along 21°S (Heit et al., 2007a) confirm this thickness estimate (black dashed line in Profile GG', Figure 4.12). We interpret this high velocity layer as the westward leading edge of the Brazilian shield that fills in the room left by the removal of the autochthonous lithosphere of the EC. Therefore, the Brazilian shield has reached beneath the EC and the east part of the southern AP (Beck & Zandt, 2002; McQuarrie et al., 2005; Scire et al., 2015a). Meanwhile, the extent of the large scale Altiplano-Puna Magma Body (APMB, Ward2017, anomaly C3 in the crust from our nomenclature) beneath the APVC implies large scale partial melting, resulting in the largest magma reservoir on Earth (Ward et al., 2013, 2014, 2017) with over 22 % partial melt fraction (Figure A.15). The thin lithosphere and additional fluid flux from enhanced hydration melting in the mantle wedge (see section 5.2) contribute to the flare-up of large volume ignimbrites and the overlying higher topographic dome (Perkins et al., 2016).

South of 24°S, the thinned lithosphere H2 finally disappears beneath the southern PN and is replaced by the low velocity uppermost mantle (Figure 4.13), possibly representing the upwelling asthenosphere and connected with the mantle wedge (M3-M5) beneath the frontal volcanic arc (Bianchi et al., 2013; Scire et al., 2015a; Wang & Currie, 2015; Chen et al., 2020). However, in the deeper part of the upper mantle atop of the subducting Nazca plate, a high velocity anomaly H5 (Profile KK'–LL' in Figure 4.13) is dipping westwards from the boundary of the EC and SB, with its leading edge to the southern PN. Low attenuation was inferred for this anomaly previously (Liang et al., 2014). Bianchi et al. (2013) detected a smaller-sized high speed block extending from 67°W to 66°W at 100 km depth beneath the CGC and C7, which could be a part of H5 in our image. We interpret this high speed anomaly H5 as delaminated continental lithosphere, which agrees well with the predicted shape of delaminated blocks in the geodynamic modelling studies (Sobolev & Babeyko, 2005; Sobolev et al., 2006; Currie et al., 2015). Those models predict that delamination initiates at the lateral boundary between weak and strong crust (Krystopowicz & Currie, 2013; Currie et al., 2015; Beck et al., 2015) and the delaminated lithosphere block then sinks into the deep upper mantle (Sobolev et al., 2006), causing the upwelling of asthenosphere. In this interpretation, H5 therefore represents an intermediate stage in the delamination process when the lithospheric block has detached but not yet sunken into the deeper mantle. Back-arc low velocity anomaly C7 (Figure 4.13) atop of H5 is separated from the volcanic arc by a normal to high speed barrier beneath Antofalla (Götze & Krause, 2002) along 26° S (Figure 4.13f). Low velocities at this location were previously interpreted as Cerro Galan Magma Body (Delph et al., 2017; Ward et al., 2017). The removal of the lithosphere by delamination supports the formation of the 'MASH' zone (melting, assimilation, storage and homogenization) near the crust-mantle boundary (Hildreth & Moorbath, 1988; Delph et al., 2017; de Silva, S. L. and Kay, Suzanne M., 2018), which might have led to the formation of the Cerro Galan magma chamber (i.e., C7). South of ∼26.5°S, the high velocity zone reaches much further west (anomaly H6, Figure 4.13), so we prefer to interpret it as the continental lithosphere of the SP (Bianchi et al., 2013; Beck et al., 2015; Scire et al., 2015a). There is no clear break between H6 and the Nazca slab, implying the absence of an actively convecting mantle wedge. There is therefore no indication of ongoing or past delamination near the southern limit of the study region.

The difference of the back-arc lithospheric depth structure from the southern AP to the southern PN reveals a cold to warm transition of the backarc lithospheric upper mantle. However, the frontal arc and back-arc low velocity anomalies within the middle crust both in our work and previous work Ward et al. (2017) reveals a reversed pattern: The crustal magma chambers including APMB (Altiplano-Puna Magma Body, C3), LMB (Lazufre Magma Body, C4), IMB (Incahuasi Magma Body, C5), IBMB (Incapillo-Bonete Magma Body C6) and CGMB (Cerro Galan Magma Body, C7) are associated with silicic volcanics. From north to south they diminish in size and maximum anomaly strength (Ward et al., 2013, 2014, 2017), indicating a reduction of temperature and magma supply in the crust (Allmendinger & Gubbels, 1996; Kay & Coira, 2009; Beck et al., 2015; Ward et al., 2017).

From the history of the deformation and shortening for the Central Andes, north of 24°S, tectonic shortening initiated around 50 Ma but the most intensive phase started at 30-25 Ma (Allmendinger & Gubbels, 1996; Sobolev & Babeyko, 2005; Oncken et al., 2006; Garzione et al., 2017) and terminated around 10 Ma (Allmendinger et al., 1997; Oncken et al., 2006). In contrast, beneath the southern PN, tectonic shortening started around 20-15 Ma but continued until 1-2 Ma (Allmendinger & Gubbels, 1996; Allmendinger et al., 1997; Oncken et al., 2006; Sobolev et al., 2006; Kay & Coira, 2009). The intense stages of shortening in the AP and PN are perhaps coeval with the passage of the Juan Fernandez Ridge and flat subduction of the Nazca plate (Yáñez et al., 2001; Kay & Coira, 2009; Bello-González et al., 2018). The southward sweep of the Juan Fernandez Ridge and the transition to a flat Nazca slab progressively initiates or at least facilitates Kay & Coira (2009); Liang et al. (2014); Beck et al. (2015) the crustal shortening and thickening, which activates the eclogitization of the lower crust and the

weakening of the continental lithosphere from the north to the south. The following re-steepening of the Nazca plate beneath the southern AP around 16-11 Ma, 10-6 Ma for the northern PN and 6-3 Ma for the southern PN (Kay & Coira, 2009) progressively facilitate the injection of the hot astheosphere beneath the weakened continental lithosphere, thus triggering extensive delamination through fulfilling the critical conditions, such as the presence of thick crust (over 45 km) in the back-arc (Sobolev & Babeyko, 2005; Oncken et al., 2006; Sobolev et al., 2006; Krystopowicz & Currie, 2013; de Silva, S. L. and Kay, Suzanne M., 2018; Ibarra et al., 2019), just as we are observing beneath the southern PN now. The delamination process would be followed by the thickening, heating and partial melting of the felsic part of the crust generating a large topography gradient, which would be then evened out by the following crustal flow (Sobolev et al., 2006; DeCelles et al., 2015; Ibarra et al., 2019), like the flat topography of AP. Finally, thin skinned and simple shear deformation pattern developed in the SA (Allmendinger & Gubbels, 1996; Allmendinger et al., 1997; Sobolev & Babeyko, 2005; Ibarra et al., 2019; Garzione et al., 2017) with the underthrusting of the Brazilian shield beneath the AP during the final stage of the shortening after the delamination, just as the high velocity layer H2 we detected in this work.

The initial time for the delamination beneath southern AP is around 20-12 Ma (Sobolev et al., 2006; Beck et al., 2015), while beneath southern PN is inferred at 6-3 Ma (Kay et al., 1994; Kay & Coira, 2009; Beck et al., 2015; de Silva, S. L. and Kay, Suzanne M., 2018), near the time of the eruption of the CGC (CGMB, C7). So for the southern PN, the delamination is probably still in progress with asthenosphere warming the base of the crust and possibly accompanied by the steepening process of the Nazca slab. Additionally, de Silva, S. L. and Kay, Suzanne M. (2018) proposed that the southward migration of Juan Fernandez Ridge on the Nazca plate results in a switch in the styles of the volcanism: from a steady state (possibly andesite-dacite) to the flare-up mode (dominantly large-scale ignimbrites and caldera complexes).

To summarise, we could infer a hotter crust but rather colder back-arc lithosphere beneath the southern AP and northern PN with possible underthrusting of the Brazilian shield from our image. In contrast, the relatively cold crust and hot asthenosphere are accompanied by the delaminated lithospheric block sinking beneath the southern PN. The AP has undergone tectonic shortening for a few tens of millions of years and created a gravitationally unstable, overthickened mantle lithosphere, finally resulting in the delamination of the lithosphere 15 million years ago (Sobolev et al., 2006), thus acting as a current 'waning' stage for the lithospheric foundering, while the crust of the southern PN is still being heated or has not been fully warmed up by the upwelling asthenosphere during the delamination (Oncken et al., 2006; Beck et al., 2015; Ward et al., 2017), marking the possible 'waxing' stage of the foundering.

4.7 Conclusions

In this study, we applied full waveform inversion to investigate the seismic velocity structure beneath the Central Andes from 16°S to 30°S and from the Chilean and Peruvian forearc into the Eastern foreland in Brazil and Argentina. We used 117 earthquakes recorded at 584 stations, which provided 9150 unique ray-paths. The new velocity model reveals a high resolution seismic structure including the crust and upper mantle (the spatial resolution is around 20 km in the crust and 30-40 km in the upper mantle), which allows a better understanding of the variation of dehydration in the mantle wedge and subsequent size of crustal magma bodies. The main features are highlighted in Figure 4.15 with selected volume contours.

(1) The subducting Nazca slab and the transitions between flat and normal-dip subduction are fully imaged in the onshore region.

(2) Large scale crustal partial melting and the hydrated mantle wedge beneath the volcanic arc are

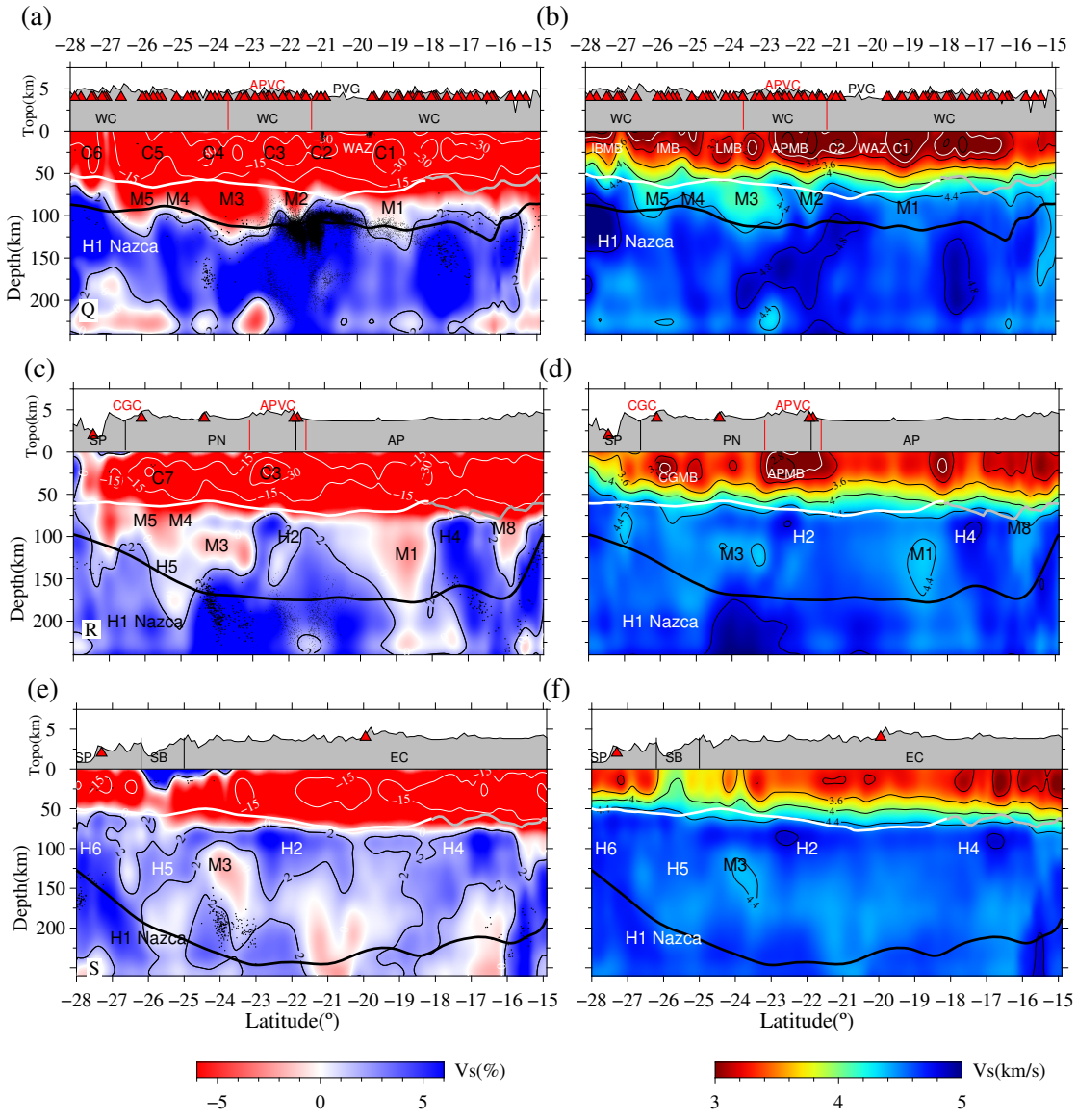

Fig. 4.14: Three curved NS cross sections in the frontal arc and back-arc area (Q, R and S) from west to the east; locations are defined in Figure 4.9b. (a), (c) and (e) are cross-sections of V_S perturbations. (b),(d) and (f) are absolute velocity models. White solid lines denote the Moho depth derived from Tassara & Echaurren (2012) while grey lines are Moho from Bishop et al. (2017) for southern Peru, north of 18°S. Black lines are Nazca slab contours extracted from Slab2.0. The seismicity denoted by black dots are retrieved from Kumar et al. (2016) north of 18°S, Sippl et al. (2018) for 18°S–23°S and ISC-EHB catalog south of 23°S. The seismicity plotted along each profile has a half-width of 0.8° around the central longitude.

also clearly imaged as low velocity zones. There is a general trend, from north to south, for the magnitude of these anomalies to become smaller, demonstrating a spatial variation from the north to the south but there are local variations on top of this trend.

(2a) Hints for higher hydration of the incoming oceanic crust and lithosphere are identified in offshore low velocity anomalies. These are followed by higher inferred degree of serpentinization in the mantle wedge beneath the south Peru, possibly associated with the subduction of the Nazca Fracture Zone.

(2b) Weaker crustal partial melting and a lower degree of hydration within the mantle wedge beneath the Pica Volcanic Gap from 19.8°S to 21°S are observed just where also intraslab seismicity is reduced compared to the south of this anomalous region. At this latitude, the Iquique ridge is subducting and seems to reduce (rather than enhance) fluid input into the mantle wedge and crust.

(3) Underthrusting of the leading edge from the Brazilian Shield beneath the southern Altiplano and the westward sinking of the delaminated lithosphere beneath the southern Puna are clearly imaged, while the autochthonous lithosphere still appears to be present in the south of the study region below the Sierras Pampeanas. The southward weakening of the crustal magma reservoirs and the variable shapes of the back-arc lithosphere can be interpreted as delineating different stages of the lithospheric evolution. The transition from the 'waning' to the 'waxing' stages of the lithospheric foundering from the north to the south is confirmed and associated with the southward sweeping of the Juan Fernandez Ridge and the flat subduction.

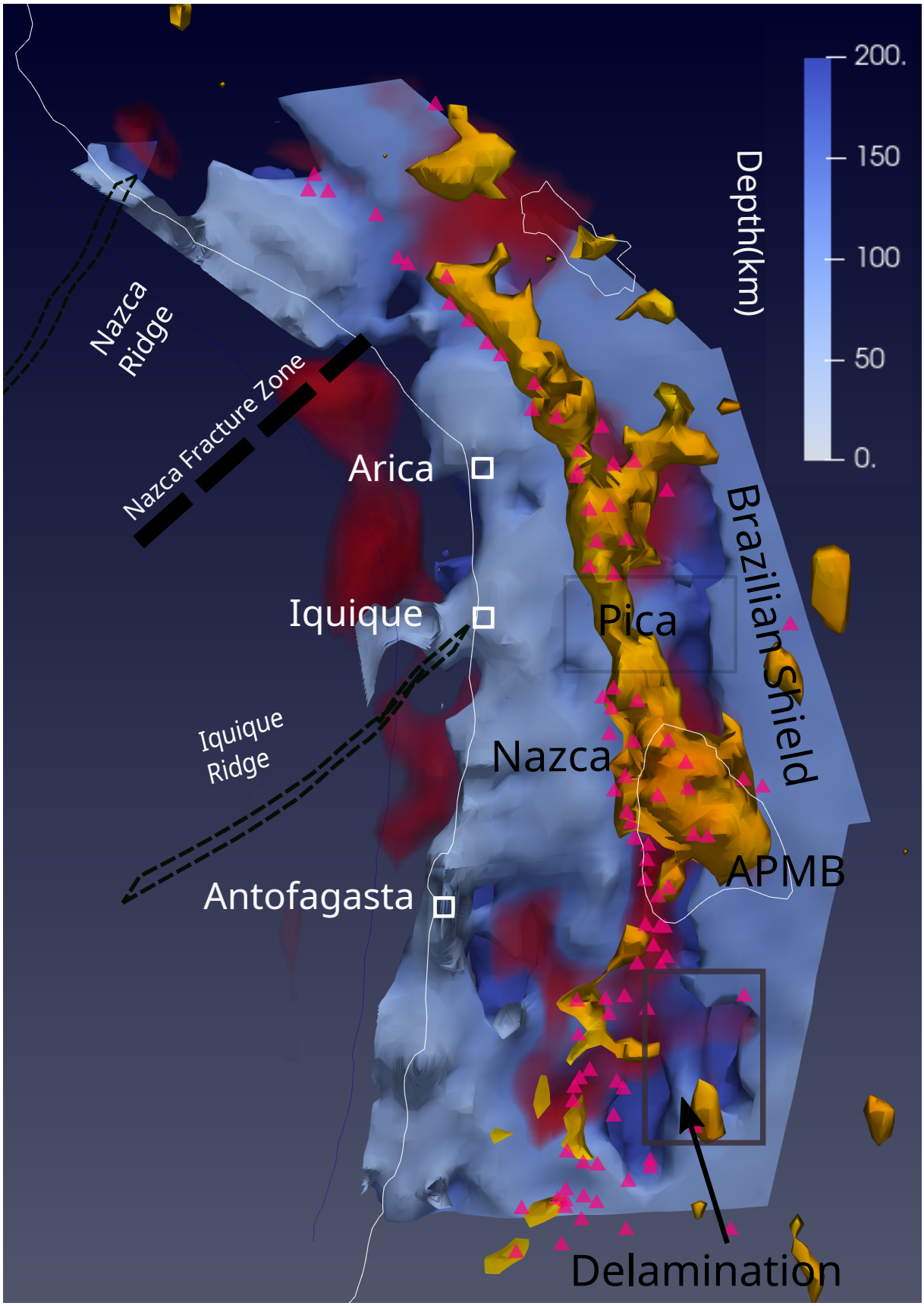

Fig. 4.15: Conceptual model illustrated with volume contours retrieved from isotropic V_S. The regions enclosed by dark yellow surfaces represent low velocity anomalies (partial melting) within the crust and red denotes low velocity anomalies within the uppermost mantle, representing the mantle wedge and subslab asthenosphere; blue marks high velocity regions interpreted as Nazca and continental lithosphere, color-scaled by depth. Volcanoes are denoted by magenta triangles. White rectangles indicate main cities in the Chile.

Chapter 5

Seismic structure of South Central Andes

5.1 Abstract

A new seismic model for crust and upper mantle of the south Central Andes is derived from full waveform inversion, covering the Pampean flat and adjacent Payenia steep subduction segments. Focused crustal low-velocity anomalies indicate partial melts in the Payenia segment along the volcanic arc, whereas weaker low-velocity anomalies covering a wide zone in the Pampean segment are interpreted as remnant partial melts. Thinning and tearing of the flat Nazca slab is inferred from gaps in the slab along the inland projection of the Juan-Fernandez-Ridge. A high-velocity anomaly in the mantle below the flat slab is interpreted as relic Nazca slab segment, which indicates an earlier slab break-off triggered by the buoyancy of the Juan-Fernandez-Ridge during the flattening process. In Payenia, large-scale low-velocity anomalies atop and below the re-steepened Nazca slab are associated with the re-opening of the mantle wedge and sub-slab asthenospheric flow, respectively.

5.2 Introduction

The temporal and spatial appearances of flat subduction segments along the South American western margin have been extensively debated (e.g. Gutscher et al., 2000; Ramos & Folguera, 2009; Marot et al., 2014; Antonijevic et al., 2015). Two prominent on-going flat subduction segments beneath the Andes are the Peruvian and Pampean flat subduction zones, north and south of the conspicuous kink in the South American coastline, respectively. They have been documented based on seismology (e.g. Wagner et al., 2005; Pesicek et al., 2012), volcanism (e.g. Kay & Abbruzzi, 1996; Kay & Mpodozis, 2002), gravity modeling (e.g. Sánchez et al., 2019) and electrical conductivity measurements (e.g. Burd et al., 2013, 2014). In this study we focus on the Pampean flat subduction and Payenia steep subduction to the south, from 28°–38°S (Fig. 5.1). Here, the Nazca slab is subducting beneath central Chile and western Argentina with a convergence rate of ∼6.7 cm a^{-1} in the N78°E direction (Kendrick et al., 2003). In the Pampean flat subduction zone (Ramos et al., 2002; Kay & Mpodozis, 2002), the Nazca slab propagates horizontally for 200-300 km beneath the southern Central Andes (Figure 5.1a) whereas the Payenia segment was dominated by flat subduction period from 15-5 Ma but has been re-steepening since 4-5 Ma (Ramos & Folguera, 2009, 2011).

The current Pampean flat subduction zone is widely believed to be associated with the subduction of the Juan Fernandez seamount ridge (JFR, Figure 5.1) (e.g. Gutscher et al., 2000; Kay & Mpodozis, 2002; Ramos et al., 2002). Plate reconstructions (Yáñez et al., 2001; Bello-González et al., 2018) indicate that the ridge has been moving southward along the western margin of South America. It was subducting beneath the Altiplano and Puna plateaus (20°-26°S) at ∼40-20 Ma, inducing temporary flat subduction and inland migration of volcanism and a temporary lull between 20-12 Ma (Yáñez et al., 2001; Kay & Coira, 2009; Beck et al., 2015). The JFR arrived at the current position beneath the Sierras Pampeanas

around 12 Ma (Figure 5.1) and the related flat subduction of the Nazca slab has again triggered inland migration and cessation of the subduction-related volcanism (Kay & Mpodozis, 2002), uplift of the main Andes, thick-skinned deformation, crustal thickening and basement uplift over a broad zone in the overriding plate (Cristallini & Ramos, 2000; Ramos et al., 2002). However, the mechanisms and consequences of the flat subduction are still under debate (Hu & Liu, 2016; Liu & Currie, 2019; Manea et al., 2012). In contrast, the sudden re-steepening of the Nazca plate beneath the Payenia segment is associated with the roll-back of the trench (Ramos et al., 2014); thus, the Payenia segment has undergone a complete cycle from crustal thickening, mountain uplift and inland migration of volcanism (Kay et al., 2005; Ramos & Folguera, 2009) during flat subduction to extensional collapse and trenchward migration of volcanism during the re-steepening period (5 Ma to now) (Folguera et al., 2008; Ramos & Folguera, 2009; Ramos et al., 2014).

The geological timing of the slab angle variations is constrained by the deformation (e.g. Ramos & Folguera, 2009) and volcanism (e.g. Kay & Kay, 2002; Spagnuolo et al., 2012) history in both areas. However, existing seismic images still give an incomplete picture. Teleseismic tomography provides a good larger-scale view of the upper mantle but has low vertical resolution, particularly at shallow depths, making it hard to distinguish velocity variations in the crust and uppermost mantle, while local travel time tomography studies can give insight into local structures and processes, e.g. magma pathways feeding individual volcanic systems, but usually fail to image the full width of the subducting slab due to their small study scale; the small scale also hampers an understanding of the regional variations. Here, we employ seismic full waveform inversion (FWI) to better constrain the seismic structure in the crust and upper mantle beneath the south Central Andes, which would facilitate to further investigate the slab configuration and the crustal melt distributions in response to the subduction of the JFR in the Pampean and the mantle wedge evolution in response to the slab re-steepening in the Payenia.

5.3 Data and Method

Following the same workflow as (Gao et al., 2021a), we collected 139 earthquakes from the Global Centroid-Moment-Tensor (GCMT) catalog (Ekström et al., 2012), which were recorded by 19 seismic networks (Figure 5.1 and Figure B.1) operating between 1996 to 2019 and magnitudes between M_W 5.0 to 7.0. Detailed network information and ray-path coverage are presented in the supplementary material (Figures B.1–B.2 and TableB.1). Our seismic velocity model is the result of the multi-scale FWI based on the adjoint methodology (e.g. Fichtner et al., 2010; Tape et al., 2010) and started from the initial 3D V_P and V_S model *SP12RTS* (Koelemeijer et al., 2015). Solutions of the visco-elastic wave equation in a radially anisotropic Earth model are obtained from *Salvus* (Afanasiev et al., 2019). The inversion starts by inverting periods 60–120 s using a time-frequency phase shift misfit and proceeds progressively to shorter periods, with waveforms between 12–100 s being inverted for in the final iterations, using a cross-correlation coefficient based misfit function. More information about the inversion workflow is provided in the supplementary material (Text B.1, Figure B.4 and Table B.2).

In order to analyse the resolution of the inversion and trade-offs between the parameters, we calculated the Hessian-vector product Hδm as point-spread functions to assess possible smearing and distortion (e.g. Fichtner & Trampert, 2011; Tao et al., 2018). We find that the isotropic V_S and V_P models are robustly determined in the resolved region with a spatial resolution of 30-40 km in the upper mantle and 25-30 km in the crust, both horizontally and vertically. Detailed resolution tests are described in Text B.1 and Figure B.22-B.32.

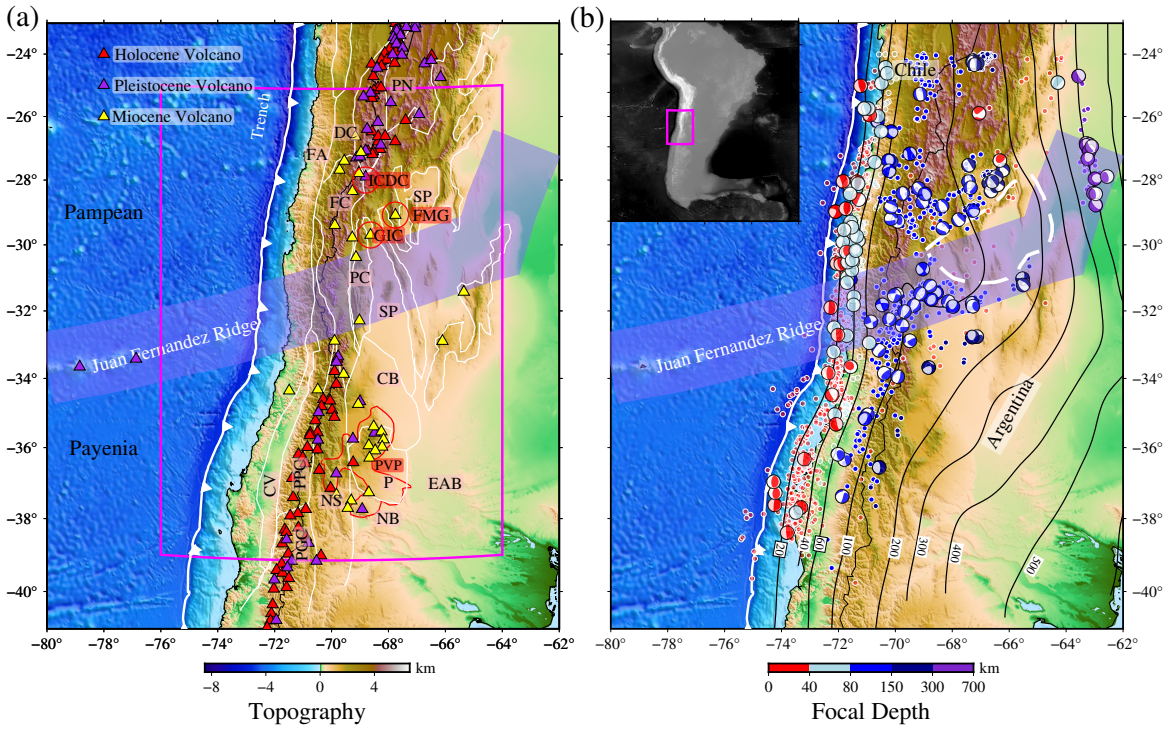

Fig. 5.1: Tectonic setting of the South Central Andes, with the Nazca plate subducting to the east beneath the South America plate. (a) Major morphotectonic provinces are modified from (Tassara et al., 2006; Piceda et al., 2020)). Fore-Arc (FA), Domeyko Cordillera (DC), Frontal Cordillera (FC), Puna (PN), Precordillera (PC), Subandean Ranges (SA), SierrasPampeanas (SP), Patagonian Cordillera (PGC), Principal Cordillera (PPC), Central Valley (CV), Neuquen Basin (NB), Payenia Craton (P), Payenia Volcanic Province (PVP), Incapillo Caldera and Dome Complex (ICDC), Famatina Mogotes Group (FMG), Gualcamayo Igneous Complex (GIC). Black solid line denotes the Payenia Volcanic Province Ramos & Folguera (2011). White saw-tooth line denotes the trench. (b) Map showing focal mechanisms of the earthquakes used for FWI. Color-coded circles represent the seismicity (magnitude > Mw 4.0) retrieved from the ISC-EHB catalog Engdahl et al. (2020). Black solid lines denote the Nazca slab contours from Slab 2.0 Hayes et al. (2018). Inset map marks the position of our study region. Topography data is retrieved from ETOPO1 Global Relief Model Amante & Eakins (2009).

5.4 Results and discussion

After 53 iterations of FWI, the crust and upper mantle structure beneath central Chile and western Argentina has been clearly imaged. We display the isotropic V_S model with some key depth and cross-sections. Further images and the isotropic V_P model are shown in the supplementary material (Figures B.5-B.20).

5.4.1 Multi-stage crustal partial melting and mantle wedge evolution

In contrast to the vigorous partial melting represented by strong low-velocity anomalies in the middle-crust beneath the Altiplano-Puna Volcanic Complex and volcanic arc for the northern Chile steep subduction zone (Yuan et al., 2000; Ward et al., 2014; Gao et al., 2021a), the middle crust in the Pampean flat subduction zone (28°–33° S) exhibits only moderately low to normal velocities along the volcanic arc (Figure 5.2a).

Low-velocity anomaly C1 (Figure 5.2a and B.21) is located beneath the Frontal Cordillera (FC) and has been reported by several earlier studies (e.g. Ward et al., 2013, 2017; Gao et al., 2021a). In agreement with these earlier studies, we interpret C1 to mark the waning partial melting (Ward et al., 2017; Gao et al., 2021a) beneath the Incapillo Caldera and Dome Complex (ICDC, Figure 5.1a), which

is the southernmost ignimbritic caldera of the Central Andes during the Pleistocene (Goss et al., 2009, 2011). Meanwhile, weak and isolated low-velocity anomalies (C2 and C3, Figure 5.2a) beneath the Sierras Pampeanas (SP) are accompanied by middle to late Miocene adakitic volcanoes including the Famatina Mogotes Group (FMG, Kay & Mpodozis (2002)) and Gualcamayo Igneous Complex (GIC, D´Annunzio et al. (2018)), hinting at the relic and waning slab melting origin (Kay & Abbruzzi, 1996; Kay & Kay, 2002; Gutscher et al., 2000; Hu & Liu, 2016) during the flattening process around 6-3 Ma (Hu & Liu, 2016).

A striking low-velocity anomaly C5 (Figure 5.2b and Profile (a) in Figure 5.3) at approximate Moho depth (60 km) extends from the Frontal Cordillera to the Sierras Pampeanas (SP), forming a thin layer above the Pampean flat slab. As the mantle wedge must have been thinned to a sliver or completely closed during the flattening of the Nazca slab (Gutscher et al., 2000; Manea et al., 2017), this low-velocity anomaly could be attributed to the hydrated continental lithosphere due to the accumulation of fluids released from the current flat slab (Hildreth & Moorbath, 1988).The flat slab has the potential to significantly modify the overriding lithosphere for a long distance from the trench due to the dehydration (Marot et al., 2014; Li, 2020; Hiett et al., 2021) or scraping-off of the base of the continental mantle lithosphere, as has been suggested for the Laramide orogeny (Axen et al., 2018) and the North China Craton (Li, 2020) from numerical modelling.

In contrast, south of 33°S, C4 may mark the restoration of partial melt accumulation in the middle crust during the re-steepening process of the Nazca slab beneath the Payenia (Marot et al., 2014; Ramos & Folguera, 2009). The late Miocene volcanic activity in the back-arc and Pleistocene-Holocene volcanic activity in the frontal arc (including large-scale Payenia Volcanic Province, Figure 5.1a) indicate a trench-ward migration of the volcanism. Following the re-steepening of the slab since 4-5 Ma, the mantle wedge has re-opened, leading to the re-injection of hot asthenosphere and renewed melt formation in the wedge induced by slab-derived fluids dehydration, in turn inducing trench-ward migration of the volcanism (Gutscher et al., 2000; Kay & Mpodozis, 2002; Ramos & Folguera, 2009, 2011; Marot et al., 2014). The re-opened mantle wedge is clearly imaged in our model as low-velocity anomaly M3 and represents the present situation after the slab re-steepening (Figure 5.2c and profile (d) and (e) in Figure 5.3).

5.4.2 Slab thinning and tearing along the Juan Fernandez Ridge

In the central part of the Pampean flat slab, two low-velocity anomalies (M1 and M2) span a slab window along the inland projection of the JFR (Figure 5.2c and Profile (b) in Figure 5.3) and are surrounded by two high-velocity limbs of the flat slab (H2). Though many prior works detected the Pampean flat slab with strong heterogeneities, most of seismological studies focused on the seismic structure south of 29°S (e.g. Wagner et al., 2005; Porter et al., 2012; Marot et al., 2014; Linkimer et al., 2020), leaving an observational gap from 27°–29°S. In this study, events and stations north of 27°S are included in the inversion, allowing us to resolve M1 and M2.

The inland projection of the JFR is not well constrained from previous plate reconstruction studies (Yáñez et al., 2001; Bello-González et al., 2018) due to its relatively long subduction and migration history (12 Ma) beneath the Pampean area. Hence, the extent of the region affected by the JFR is not known precisely, nor are details of the seismic structure associated with the JFR (Gutscher et al., 2000; Wagner et al., 2005; Gans et al., 2011; Marot et al., 2014; Haddon & Porter, 2018). Following Kay & Mpodozis (2002), we assume the uncertainty width of the influence zone of the JFR within the oceanic lithosphere is 200 km, which also takes into account the region of underplating and possible hydration of the oceanic lithosphere (Kopp et al., 2004), which extends beyond the seamount chain itself. Thus, the low-velocity anomalies M1 and M2 are located within the JFR influence range. Similar to predictions from numerical modelling (Hu & Liu, 2016), the slab thinning and tearing zone develops within the central part of the

current flat slab. In Hu & Liu's model, slab thinning and tearing initiates from the inboard tip of the flat slab before re-steepening downdip and propagates trench-wards, parallel to the track of the JFR and consistent our direct observation. In addition to the enhanced buoyancy of the JFR, its hydration state and inherited normal faults (Kopp et al., 2004) might have caused zones of weakness along which the thinning and tearing could progress.

Conspicuously, the slab tearing zone (M1 and M2) is characterized by the absence of intra-slab seismicity, in contrast to the slab limbs to the north and south (Fig. 5.2c). The focal mechanisms show a clear asymmetric pattern across the JFR track: the north branch of H2 is characterized by predominantly NE-SW oriented T axes, which are subparallel to the track of the JFR, whereas the T axes for events in the southern branch of H2 are oriented mainly NW-SE, sub-normal to the JFR trend, implying a $\sim 90°$ rotation of T axes across the aseismic zone (Figure 5.2c) at 120-160 km at depth. The northeast extension in the northern slab limb parallel to the JFR is superimposed on dominant slab pull (downdip extension), which is also reflected in the velocity field (Hu & Liu, 2016) and azimuthal anisotropy (Hu et al., 2017; Lynner et al., 2017). The south branch is coincident with the track of the JFR and attributed to the reactivation of the preexisting normal faults, causing vigorous intra-slab seismicity Ranero et al. (2005); Anderson et al. (2007); Gans et al. (2011); Ammirati et al. (2015); Wagner et al. (2020).

Along 30° S, Heit et al. (2008b) detected a strong oceanic LAB signal west of 69°W that suddenly disappears and even changes polarity further east below the slab tearing zone (Figure 5.3(b)). Recent magnetic and gravity modeling work (Sánchez et al., 2019) also inferred hot asthenospheric flow beneath the flat slab and local slab thinning. These observations further validate our interpretation of M1 and M2 as evidence for thinning and tearing of the slab (Figure 5.4).

M1 and M2 are spatially associated with weak crustal low-velocity anomalies C3 and C2 below the late Miocene adakitic volcanism including the GIC (D´Annunzio et al., 2018) and FMG (Kay & Mpodozis, 2002), respectively (Figure 5.2a). As adakitic volcanism is attributed to melting of the oceanic slab (Kay & Mpodozis, 2002; Gutscher et al., 2000; Hu & Liu, 2016), which would be expected at the onset of thinning and tearing when the flat slab was being heated up. This indicates a slab tearing at this position might have initiated in the late Miocene during the flattening process and since then started propagating trench-wards (Hu & Liu, 2016) until now, as new slab material is brought into the tearing zone by the ongoing subduction (Figure 5.4a).

The Pampean flat slab, after having developed in the Middle to Late Miocene, suffered from numerous instabilities, such as internal stresses induced by the increased buoyancy of the JFR relative to its two flanks, changes in hydration state, reactivation of inherited normal faults, and basal heating by asthenosphere flow (Rodríguez-González et al., 2014). These factors have induced weakening, thinning and finally tearing of the oceanic slab, accompanied by melting of the oceanic crust as predicted by the geodynamic model (Hu & Liu, 2016). The basalt input from the melted oceanic crust leads to the adakitic volcanism (Gutscher et al., 2000) during the late Miocene (Figure 5.4a). However, as Hu & Liu (2016) pointed out, the cessation of adakitic eruption possibly correlated with the waning asthenosphere upwelling after thermal equilibration has been achieved following upward flow of hot astheonspheric material through the gap and cooling-down and even complete closure of the mantle wedge due to the further flattening process after late Miocence (5-3 Ma) (Figure 5.4).

5.4.3 Slab break-off: transition from steep to flat subduction?

A prominent high-velocity anomaly (H3) is found just below the flat Nazca slab (H2), extending from 28° S to 30° S (Figure 5.2d). At depth, H3 is dipping steeply to the east from 200 km down to 350 km depth (Profile (a), Figure 5.3). This anomaly was also visible in previous global or teleseismic tomography

studies, but was so far not interpreted (e.g. Li et al., 2008; Portner et al., 2020; Mohammadzaheri et al., 2021). Recent S-wave teleseismic work (Rodríguez et al., 2021) captured a similar but larger-scale high-velocity anomaly extending from 200 km down to the lower mantle and attributed it to a part of relic Phoenix/Aluk plate, which was completely subducted by the late Cretaceous (Horton, 2018; Gianni et al., 2018). However, the resolution of the aforementioned models is limited in the upper mantle due to vertical smearing. We prefer to relate this anomaly to the more recent Nazca plate subduction as it seems unlikely that a part of the Phoenix slab could remain in the upper mantle for more than 100 million years and has not sunk into the lower mantle or thermally equilibrated with the surrounding mantle (Ramos & Folguera, 2009; Bello-González et al., 2018; Chen et al., 2019). Thus, we propose this anomaly to be a fossil fragment of the Nazca slab that was subducting steeply prior to the onset of flattening, indicating break-off from the leading edge of the current Nazca slab (Liu & Currie, 2016). Slab break-off during the slab flattening process is common in geodynamic models (e.g. Haschke et al., 2002; Liu & Currie, 2016, 2019; Dai et al., 2020). The conditions for slab break-off during the slab flattening process include fast trenchward migration of the overriding plate (high convergence rate) and a strong buoyancy contrast between either an oceanic plateau or aseismic ridge crust (here the JFR) and the normal thickness oceanic crust of an old slab (Haschke et al., 2002; Li et al., 2011; Liu & Currie, 2016, 2019). The removal of the leading dense portion would allow the positive buoyancy of the trailing edge to quickly flatten out the slab (Figure 5.4b). In many global tomography models, the Nazca slab extends to much shallower depth in the south than the north, where it is visible down to 1000 km depth (Li et al., 2008; Obayashi et al., 2013). Several teleseismic tomography models (Portner et al., 2017, 2020; Rodríguez et al., 2021) for South America seem to indicate a slab hole at 200-300 km depth around 32°S in the re-steepened portion within the upper mantle. Thus the relic slab break-off or detachment from the head of the young and buoyant Nazca slab seems a viable option.

Taking account of the initial time of the transition from the steep to the flat subduction around 12 Ma coeval with the subduction of the JFR (Yáñez et al., 2001; Kay & Mpodozis, 2002; Ramos & Folguera, 2009), this would also be the time for the high density portion ahead of the JFR to break off from the leading edge of the young Nazca slab (Figure 5.4b). Furthermore, partial eclogitization of the oceanic crust before the onset of the flat subduction may play an important role in controlling the breaking-off time (Liu & Currie, 2019) and sinking depth in the upper mantle. Thus, the tail of the broken portion would sink slowly in the upper mantle due to its relatively young age, while the head would have already sunk into the mantle transition zone or deeper, below the resolution limit of our model. After break-off, the young and buoyant Nazca slab with the JFR could lift to extend horizontally eastwards for nearly 300 km before re-steepening with a steep angle to a relatively shallower depth compared to the dip subduction zone north of 28° S (Figure 5.4b).

We note that the position of the relic slab is further westward than we expected from the geodynamic model of (Liu & Currie, 2019). While we cannot offer a fully satisfactory explanation for this, we speculate that westward directed asthenospheric flow could potentially account for this discrepancy. In order to solve this puzzle, 3D geodynamic models and future imaging extending high resolution imaging throughout the transition zone and into the uppermost part of the lower mantle will likely be required.

5.4.4 Subslab asthenospheric flow induced by sudden re-steepening of the Nazca slab beneath the Payenia?

Another striking feature in our model is the low-velocity anomaly M4 extending from 32°–36°S below the steep Nazca slab in Payenia subduction zone and from slab depths to 250–300 km depth (Figures 5.2c and 5.3, Profile. (e)-(h)). This low-velocity anomaly has also been observed by some earlier tomography studies (Feng et al., 2007; Portner et al., 2017, 2020; Celli et al., 2020; Rodríguez et al., 2021). (Portner

et al., 2017) attributed it to the asthenosphere entrainment by the JFR with the subducting Nazca slab due to the coupling between the asthenosphere and overlying oceanic lithosphere Liu & Zhou (2015). However, due to its large size and location, it may more likely be caused by hot asthenospheric flow induced by the sudden re-steepening of the Nazca slab and trench retreat (Ramos & Folguera, 2009; Lin, 2014; Hu et al., 2017; Mohammadzaheri et al., 2021) since 4 Ma beneath the Payenia subduction zone (Figure 5.4a).

5.5 Conclusions

Through multi-scale full seismic waveform inversion, we identify low velocity zones within the Pampean flat slab parallel to the inland projection of the Juan Fernandez Ridge, which we interpret as a tearing zone within the flat slab. It may be induced by the buoyancy contrast between the Pampean flat slab with Juan Fernandez Ridge attached and its surrounding steep slab portions to the north and south. Meanwhile, the buoyancy contrast between the young Nazca slab and the preceding steep Nazca slab appears to have triggered the slab break-off from the leading edge of current Nazca slab. The resulting buoyancy increase could possibly sustain the long-distance flat subduction. Flat subduction also expelled the mantle wedge and shut off partial melting, resulting in much reduced volcanic activity and presence of partial melt in the crust. Re-steepening of the Nazca slab beneath the Payenia subduction zone seems to have significantly perturbed the sub-slab asthenospheric flow and introduced large-scale mantle flow, as visible in large low-velocity zone both above and below the slab. Re-opening of the mantle wedge and injection of the asthenosphere induced by the re-steepening of the Nazca slab may have caused the re-accumulation of partial melts within the middle crust and volcanic arc trench-ward migration and reactivation in the Payenia segment.

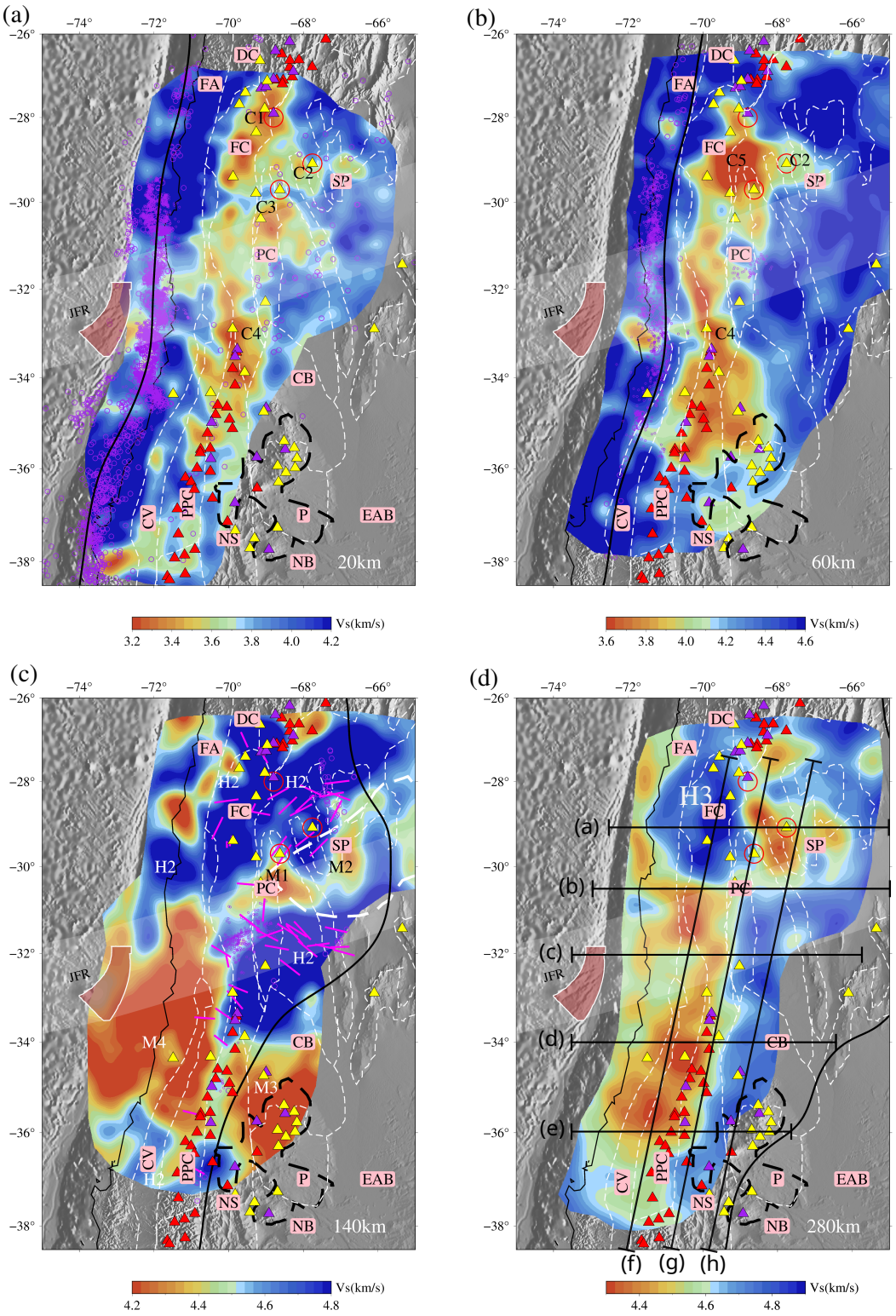

Fig. 5.2: Horizontal slices for isotropic V_S. In (c) T (tension) axes from GCMT focal mechanism solutions Ekström et al. (2012) for earthquakes between 120 and 150 km depth with magnitude M_W >5.0 are indicated by magenta bars. The large and small magenta circles are seismicity from ISC-EHB catalog and the relocated catalog from (Sippl et al., 2021), respectively, and within 10 km of the nominal depth of the slice. The pink shaded area off-shore indicates the position of the weakened oceanic lithosphere detected by (Kopp et al., 2004) along the JFR. Solid black lines denote the top of the slab according to Slab 2.0 Hayes et al. (2018) at the depth of the slice. Black straight lines in (d) denote the positions of the cross-sections in Figure 5.3. Black thick dashed line denotes the Payenia Volcanic Province, and white dashed line in (c) denotes the intraslab aseismic zone.

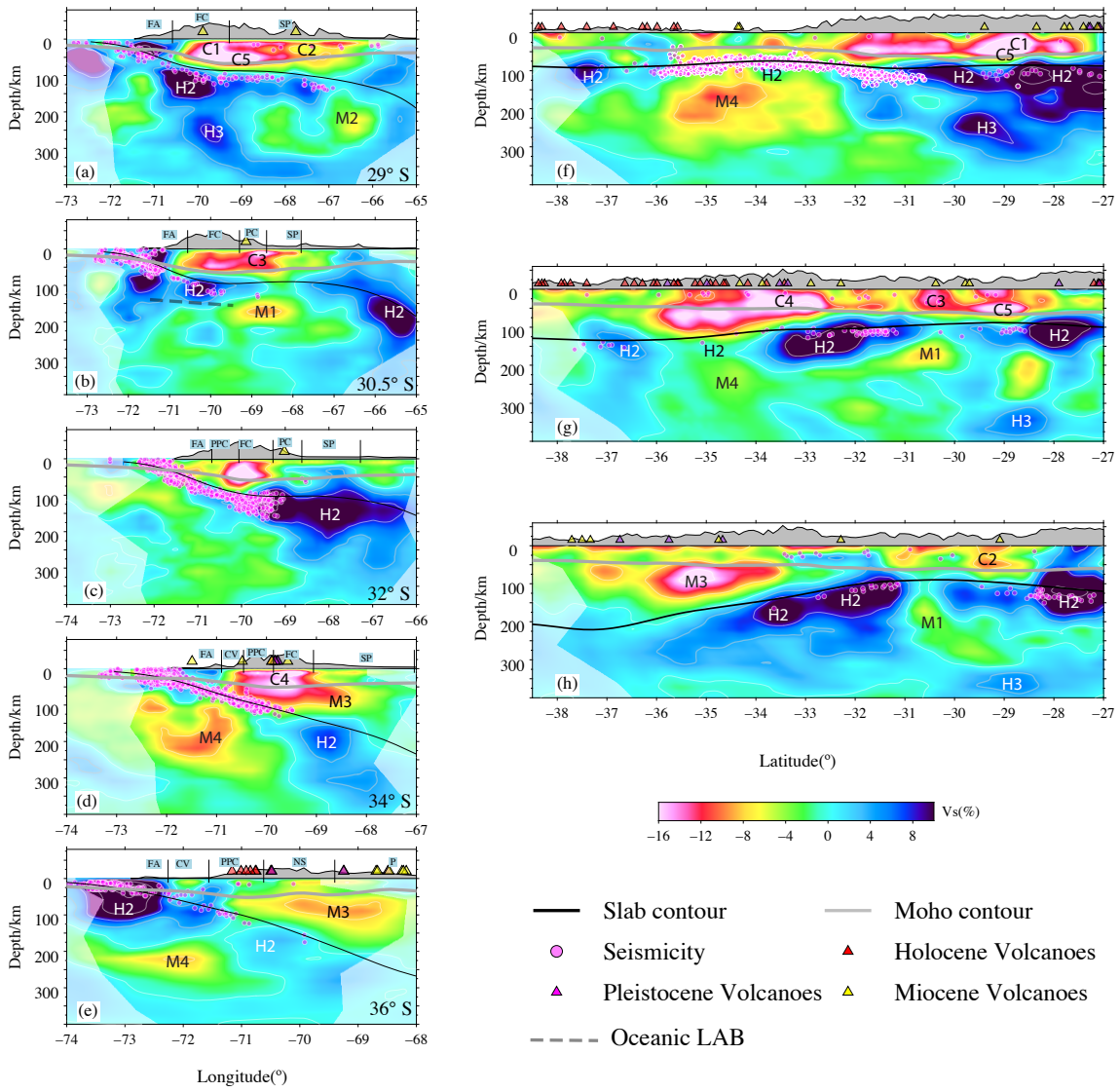

Fig. 5.3: Cross-sections of isotropic V_S perturbation relative to the reference 1D V_S defined in Figure B.3. (see Figure 5.2d for profile locations). Thick solid black lines denote the continental Moho (Rivadeneyra-Vera et al., 2019) and thin solid black lines denote the slab contour from Slab 2.0 Hayes et al. (2018). The thick white dashed line in (b) denotes the oceanic LAB from receiver function Heit et al. (2008b). Magenta dots in b-d denote the seismicity relocated by (Sippl et al., 2021) and in other profiles are retrieved from ISC-EHB catalog. All the labeled tomographic anomalies can be found in the main text. See Fig.S14 for a version of this figure without labels and seismicity.

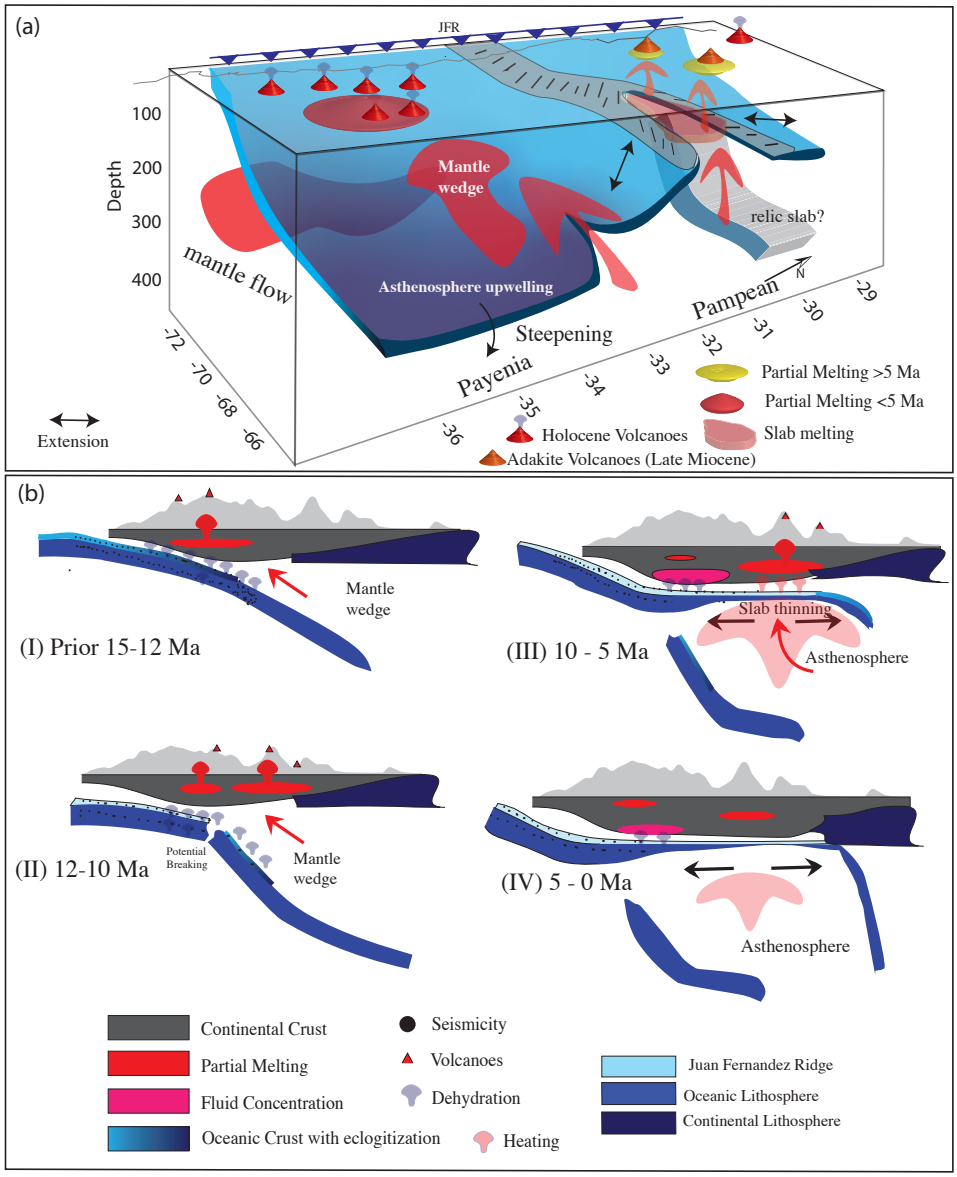

Fig. 5.4: (a) Schematic representation of the current Nazca slab configuration west of 66°W. Gray zone with short bars indicates the inland projection of the Juan Fernandez Ridge. South of 33°S the Nazca plate subducts steeply in the Payenia segment. (b) Proposed sequence of the steep to flat slab subduction evolution along 29°S since 12 Ma, which can explain the observed pattern of sub-slab anomalies.

Chapter 6

Conclusion and outlook

6.1 Summary

In my thesis, I investigate the crustal and mantle lithosphere of the entire Central Andes down to a depth of 400 km. Central Andes is charming for Earthscience scientists due to its special subduction type, the 'Andean-type', where an oceanic plate descends beneath a convergent continental margin, typically forming a coastal orogeny or cordillera. Periodical flat subduction and the following slab re-steepening process modified the overriding plate structure and impacts on the deformation and volcanism history. Frequent and pervasive moderate earthquakes within the slab, along the coast and intra-continental plate allow me to take advantage of the seismic waveforms to investigate the seismic structure within the crust and uppermost mantle which is crucial to investigate the interaction zone between the slab and the overriding plate.

With the seismic waveform modeling, we could simulate the seismic wave propagation within 3D media with radial anisotropy. A spectral-element code (Salvus) enables me to calculate accurate synthetic waveforms for the full waveform train including body wave and surface wave phases. Thus how to take advantage of the synthetic waveform to progressively fit the observed data to improve the seismic velocity structure is the theme of the method part. Here we mainly take advantage of the adjoint full waveform inversion method to conduct our research. Thus we collected seismic displacement records from over 600 moderate magnitude earthquakes recorded by over 30 permanent and temporary networks within the Central Andes, with a time spanning over 20 years.

In order to constrain the deep long-wavelength structure in the mantle, at the same time, to avoid the risk of local minimum, we incorporate and start from long-period data (40-80 s for northern Central Andes, 60-120 s for southern Central Andes) and proceed to higher frequency data (12s) through several stages. Time-Frequency Phase Shift misfit functional is used for first inversion stages to constrain the large-scale structure whereas Cross Correlation Coefficient misfit functional is applied to the final inversion stage to better constrain small-scale structure through fitting the waveforms directly.

Through two multi-scale full waveform inversion works, we successfully imaged the crustal and upper mantle seismic structure for the northern Central Andes with steep subduction and southern Central Andes with flat subdutcion beneath Pampean and steep subduction beneath Payenia. Our studies mainly targeted the interactions between the subducting oceanic slab and the overriding Andean plate, involving the fluid migration due to the dehydration of the slab, the continental lithosphere foundering processes, partial melting with magma evolution and the responses of the mantle wedge and sub-slab asthenosphere to the slab angle variations.

Specifically, for the steep subduction zone beneath the northern Central Andes including the Altiplano and Puna, the subducting Nazca slab could be clearly imaged within the upper mantle, with low-velocity mantle wedge corner located between the slab and overriding Andean plate. Meanwhile, strong low-velocity anomaly belt along the volcanic arc is detected within the middle crust, reflecting the active

partial melts which are feeding the active volcanoes. The partial melting belt is interrupted beneath the Pica Volcanic Gap where the volcanic activity is silent since the Middle Pleistocene, which is also reflected by the weak hydration of the mantle wedge corner and scarcity of intermediate-depth intra-slab seismicity. The dehydration of the oceanic mantle lithosphere possibly contributes more fluids than the oceanic crust and causes hydration within the mantle wedge corner and further promotes the magma chamber formation by lowering the conditions for partial melting. The climax of the partial melting within the crust is located beneath the Altiplano-Puna Volcanic Complex, which is known as Altiplano-Puna-Magma-Body, with the S wave velocity lower than 2 km/s. Approximate estimation for the partial melt fraction is also given in our study for this area with up to 20 % at maximum beneath the Altiplano-Puna Volcanic Complex. The backarc lithosphere foundering process across the whole Central Andes is another hotly debated topic that is related to the crustal shortening history and eclogitization process of the lower crust. In our study, we observed discrete backarc lithosphere structure: thin lithosphere exists beneath northern Puna and southern Altiplano, possibly hinting at the underthrusting of the Brazilian shield. Whereas southern Puna is dominated by the lithosphere delamination accompanied by asthenosphere upwelling and back-arc volcanic activities. A high-velocity block is westward sinking in our image, correlated with the predictions from the numerical modeling of the backarc delamination process beneath the Central Andes. The different backarc lithosphere structure and southward waning of partial melting within the middle crust are accompanied by the southward migration of the flat subduction period triggered by the subduction of Juan Fernandez Ridge since 40 Ma. Thus the the dip angle of Nazca plate displayed a southward decreasing pattern, similar to the crustal partial melting fraction feature.

For the southern Central Andes, where the Nazca plate is propagating horizontally beneath the Pampean from 28 °S to 33 °S triggered by the subduction of the Juan Fernandez Ridge since 12 Ma. Atop the flat subduction zone, the crustal low-velocity beneath the orogeny is weaker than the northern Central Andes, marking the cessation of partial melting due to the low temperature caused by the closure of the mantle wedge. However, a thin low-velocity layer is observed within the bottom of the over-thickened crust atop the current flat Nazca plate which demonstrates the ongoing dehydration of the flat slab and fluid accumulation near the interface of the flat slab and overriding plate. Meanwhile, hydration possibly weakens the strength of the overriding plate and the ongoing flattening process possibly erodes the base of the lithosphere of the overriding plate. In our image, the flat Nazca plate is clearly detected extending horizontally for 200-300 km before re-steepening. Interestingly, a slab thinning and tearing zone within the central zone of the flat slab is detected, parallel to the inland prediction of track of the Juan Fernandez Ridge. This slab tearing zone correlates well with the predictions from 3D numerical geodynamic modeling work. The thinning and even tearing effect is mainly caused by the buoyancy difference between the Juan Fernandez Ridge and its two flanks which are controlled by negative buoyancy. This phenomenon is also confirmed by the current T axis of the intraslab earthquake focal mechanism, north of the tearing zone is controlled by the northeast T axis whereas the south of the tearing zone is southeast. The subduction of buoyant Juan Fernandez Ridge since 12 Ma possibly introduced a breaking-off event between the young Nazca plate and the tail of the relic normal-dip slab. The tail of the relic Nazca slab possibly is sinking slowly within the upper mantle after the breaking-off due to its relatively young age. Thus after breaking-off, the flat slab with Juan Fernandez Ridge attached obtained more buoyancy to keep a long-distance flat subduction. South of the Pampean flat subduction, the subduction regime is characterized by steep subduction which was flat subduction before 5-4 Ma. The resteepening of the Nazca plate is accompanied by re-opening of the mantle wedge and partial melting within the crust. Thus the re-steepening process is also marked by trenchward migration of the volcanic arc and rejuvenation. The resteepening process significantly modified the deformation pattern from compression to extension. Not only the large-scale mantle wedge could be observed as low-velocity anomaly in our imaging, but sub-slab asthenosphere flow is also identified which is caused by the perturbation of the

upper mantle due to the re-steepening process. Though our two studies should be categorized into large-scale tomography works compared to regional studies based on specific networks, through multi-scale full waveform inversion scheme incorporating high-frequency body and surface wave trains, we could resolve detailed structure in the upper mantle with 30-40 km resolution length and 25 km in the crust. For most of the regional ray-tracing travel time tomography, the resolution is prone to be influenced by the footprint of the networks and mostly limited by the seismicity distribution. Damping and regularization parameters are also influencing the final inversion results. So for this area, many tomography gave small patches possibly influenced by the grid spacing during the inversion and also making it hard to view the larger scale of the subduction zone and compare features along strike. Previous studies prefer to combine different tomography studies including the crust structure from surface wave and upper mantle from the teleseismic tomography. The critical question is that teleseismic tomography usually fails to resolve the uppermost mantle due to its near-vertical smearing along the path, imposing a significant requirements on the initial model. Thus incorporating so many uncertainties from different models and methods to derive a complicated conception model is risky. Our study provided an unprecedented robust fine-scale structure for the whole Central Andes including the crust and upper mantle, making it feasible to build a new and reliable conception model to understand the interaction between the slab and overriding Anden plateau through one tomography work.

6.2 Outlook

Even though we provided an unprecedented seismic model for the crust and upper mantle beneath the whole Central Andes, where the shape of the slab and interaction zone could be clearly imaged. There are still several questions that should be addressed. For instance, in order to resolve the seismic structure along the Juan Fernandez Ridge, previous seismologists deployed instruments only along the predicted inland track of the ridge. The consequence is that the slab thinning and tearing zone is very difficult to be detected by regional tomography or along strike receiver functions. Though we have to admit the cost of deployment of instruments sometimes is high and also related to the project availability and the access to the forbidden areas. More observations within the foreland area are expected and crucial to understanding the material migration for the flat subduction zone, where the slab re-steepens. From the numerical modeling, the scratched material by the flat slab could be shifted to the foreland area, forming a 'keel' structure, but from our image, this structure is at the boundary of the best resolution area, posing a limit to understanding the geodynamic process. Thus from the observational seismology, we should be more forward planning and consider the uncertainty of the position of some expected structures. Meanwhile, a more uniform and unbiased data coverage benefits more parameters inversion, for example, the radial anisotropy.

From the technical aspects, though our current models contain radial anisotropy, an azimuthal anisotropy is expected to resolve the deformation pattern in the overriding plate and alignment of minerals within the slab, the flow direction of the asthenosphere. Our current inversion only contains data up to 12 s period. Higher frequency data should be incorporated to resolve the subducting thin oceanic crust which is important to recover the eclogitization depth of the crustal minerals which is also possibly linked to the onset depth of intermediate-depth seismicity within the oceanic lithosphere. Recent hybrid teleseismic full waveform inversion or 'Box' tomography provides new opportunities using the injected wavefronts coming from teleseismic earthquakes to better resolve the upper mantle and crust structure including anisotropy and density. Thus I suggest more flexible inversion schemes including azimuthal anisotropy, ambient noise cross correlation waveform data and teleseismic data could be incorporated to give a more clear and whole crust-mantle domain image to better understand the geodynamic process for the Central Andes or even the whole planet. All in all, a new comprehensive

understanding of the geodynamic process relies on the robust and high-resolution image of the crust and upper mantle, which is the overall mission for tomography. Improving observation coverage and improving imaging methods are two paths for improving imaging.

Bibliography

Afanasiev, M., Boehm, C., van Driel, M., Krischer, L., Rietmann, M., May, D. A., Knepley, M. G., & Fichtner, A., 2019. Modular and flexible spectral-element waveform modelling in two and three dimensions, *Geophysical Journal International*, **216**(3), 1675–1692.

Akcelik, V., Biros, G., & Ghattas, O., 2002. Parallel Multiscale Gauss-Newton-Krylov Methods for Inverse Wave Propagation, in *SC '02: Proceedings of the 2002 ACM/IEEE Conference on Supercomputing*, pp. 41–41.

Albuquerque Seismological Laboratory (ASL)/USGS, 1988. Global Seismograph Network (GSN - IRIS/USGS).

Albuquerque Seismological Laboratory (ASL)/USGS, 1993. Global Telemetered Seismograph Network (USAF/USGS).

Allmendinger, R. W. & Gubbels, T., 1996. Pure and simple shear plateau uplift, Altiplano-Puna, Argentina and Bolivia, *Tectonophysics*, **259(1)**, 1–13.

Allmendinger, R. W., Jordan, T. E., Kay, S. M., & Isacks, B. L., 1997. The evolution of the Altiplano-Puna plateau of the Central Andes, *Annual Review of Earth and Planetary Sciences*, **25**, 139–174.

Alterman, Z. & Karal, F. C., J., 1968. Propagation of elastic waves in layered media by finite difference methods, *Bulletin of the Seismological Society of America*, **58**(1), 367–398.

Amante, C. & Eakins, B. W., 2009. ETOPO1 Global Relief Model converted to PanMap layer format.

Ammirati, J. B., Alvarado, P., & Beck, S., 2015. A lithospheric velocity model for the flat slab region of Argentina from joint inversion of Rayleigh wave phase velocity dispersion and teleseismic receiver functions, *Geophysical Journal International*, **202**(1), 224–241.

Anderson, M., Alvarado, P., Zandt, G., & Beck, S., 2007. Geometry and brittle deformation of the subducting Nazca Plate, Central Chile and Argentina, *Geophysical Journal International*, **171**(1), 419–434.

Angermann, D., Klotz, J., & Reigber, C., 1999. Space-geodetic estimation of the Nazca-South America Euler vector, *Earth and Planetary Science Letters*, **171**(3), 329–334.

Antonijevic, S. K., Wagner, L. S., Kumar, A., Beck, S. L., Long, M. D., Zandt, G., Tavera, H., & Condori, C., 2015. The role of ridges in the formation and longevity of flat slabs, *Nature*, **524**(7564), 212–215.

Antonijevic, S. K., Wagner, L. S., Beck, S. L., Long, M. D., Zandt, G., & Tavera, H., 2016. Effects of change in slab geometry on the mantle flow and slab fabric in Southern Peru, *Journal of Geophysical Research: Solid Earth*, **121**(10), 7252–7270.

Araya Vargas, J., Meqbel, N., Ritter, O., Brasse, H., Weckmann, U., Yáñez, G., & Godoy, B., 2019. Fluid distribution in the Central Andes subduction zone imaged with magnetotellurics, *Journal of Geophysical Research: Solid Earth*, **124**(4), 4017–4034.

Asch, G., Heit, B., & Yuan, X., 2002. The ReFuCA project: Receiver Functions Central Andes.

Asch, G., Tilmann, F., Schurr, B., & Ryberg, T., 2011. Seismic network 5E: MINAS project (2011/2013).

Asch, G., Tilmann, F., Heit, B., & Schurr, B., 2014. HART-PISAGUA Project Chile.

Axen, G. J., van Wijk, J. W., & Currie, C. A., 2018. Basal continental mantle lithosphere displaced by flat-slab subduction, *Nature Geoscience*, **11**(12), 961–964.

Beck, Susan, L. & Terry, W., 2000. Slab Geometry in the Southern Andes.

Beck, Susan, L. & Zandt, G., 2002. The nature of orogenic crust in the central Andes, *Journal of Geophysical Research: Solid Earth*, **107**(B10), ESE–7.

Beck, Susan, L. & Zandt, G., 2007. Lithospheric Structure and Deformation of the Flat Slab Region of Argentina.

Beck, Susan, L., Zandt, G., & Wagner, L., 2010. Central Andean uplift and the geodynamics of the high topography.

Beck, Susan, L., Zandt, G., Ward, K. M., & Scire, A., 2015. Multiple styles and scales of lithospheric foundering beneath the Puna Plateau, Central Andes, in *Geodynamics of a Cordilleran Orogenic System: The Central Andes of Argentina and Northern Chile*, Geological Society of America.

Bello-González, J. P., Contreras-Reyes, E., & Arriagada, C., 2018. Predicted path for hotspot tracks off South America since Paleocene times: Tectonic implications of ridge-trench collision along the Andean margin, *Gondwana Research*, **64**, 216–234.

Bianchi, M., Heit, B., Jakovlev, A., Yuan, X., Kay, S., Sandvol, E., Alonso, R., Coira, B., Brown, L., Kind, R., & Comte, D., 2013. Teleseismic tomography of the southern Puna plateau in Argentina and adjacent regions, *Tectonophysics*, **586**, 65 – 83.

Bishop, B. T., Beck, S. L., Zandt, G., Wagner, L., Long, M., Antonijevic, S. K., Kumar, A., & Tavera, H., 2017. Causes and consequences of flat-slab subduction in southern Peru, *Geosphere*, **13**(5), 1392–1407.

Bjørnerud, M., Austrheim, H., & Lund, M., 2002. Processes leading to eclogitization (densification) of subducted and tectonically buried crust, *Journal of Geophysical Research: Solid Earth*, **107**(B10), ETG–14.

Bloch, W., Kummerow, J., Salazar, P., Wigger, P., & Shapiro, S. A., 2014. High-resolution image of the North Chilean subduction zone: seismicity, reflectivity and fluids, *Geophysical Journal International*, **197**(3), 1744–1749.

Blom, N., Boehm, C., & Fichtner, A., 2017. Synthetic inversions for density using seismic and gravity data, *Geophysical Journal International*, **209**(2), 1204–1220.

Blom, N., Gokhberg, A., & Fichtner, A., 2020. Seismic waveform tomography of the central and eastern Mediterranean upper mantle, *Solid Earth*, **11**(2), 669–690.

Bohlen, T., 2002. Parallel 3-d viscoelastic finite difference seismic modelling, *Computers & Geosciences*, **28**(8), 887–899.

Boutelier, D. A. & Cruden, A. R., 2008. Impact of regional mantle flow on subducting plate geometry and interplate stress: insights from physical modelling, *Geophysical Journal International*, **174**(2), 719–732.

Brossier, R., Operto, S., & Virieux, J., 2009. Robust elastic frequency-domain full-waveform inversion using the L1 norm, *Geophysical Research Letters*, **36**, L20310.

Bunks, C., Saleck, F. M., Zaleski, S., & Chavent, G., 1995. Multiscale seismic waveform inversion, *Geophysics*, **60**(5), 1457–1473.

Burd, A. I., Booker, J. R., Mackie, R., Pomposiello, C., & Favetto, A., 2013. Electrical conductivity of the Pampean shallow subduction region of Argentina near 33 S: Evidence for a slab window, *Geochemistry, Geophysics, Geosystems*, **14**(8), 3192–3209.

Burd, A. I., Booker, J., Mackie, R., Favetto, A., & Pomposiello, M. C., 2014. Three-dimensional electrical conductivity in the mantle beneath the payún matrú volcanic field in the andean backarc of argentina near 36.5 s: Evidence for decapitation of a mantle plume by resurgent upper mantle shear during slab steepening, *Geophysical Journal International*, **198**(2), 812–827.

Cabrera, L., Ruiz, S., Poli, P., Contreras-Reyes, E., Osses, A., & Mancini, R., 2021. Northern Chile intermediate-depth earthquakes controlled by plate hydration, *Geophysical Journal International*, **226**(1), 78–90.

Calixto, F. J., Sandvol, E., Kay, S., Mulcahy, P., Heit, B., Yuan, X., Coira, B., Comte, D., & Alvarado, P., 2013. Velocity structure beneath the southern Puna plateau: Evidence for delamination, *Geochemistry, Geophysics, Geosystems*, **14**(10), 4292–4305.

Capdeville, Y., 2005. An efficient Born normal mode method to compute sensitivity kernels and synthetic seismograms in the Earth, *Geophysical Journal International*, **163**(2), 639–646.

Celli, N. L., Lebedev, S., Schaeffer, A. J., Ravenna, M., & Gaina, C., 2020. The upper mantle beneath the South Atlantic Ocean, South America and Africa from waveform tomography with massive data sets, *Geophysical Journal International*, **221**(1), 178–204.

Cesca, S., Sobiesiak, M., Tassara, A., Olcay, M., Günther, E., Mikulla, S., & Dahm, T., 2009. The Iquique Local Network and PicArray.

Chen, J., Kufner, S. K., Yuan, X., Heit, B., Wu, H., Yang, D., Schurr, B., & Kay, S., 2020. Lithospheric Delamination Beneath the Southern Puna Plateau Resolved by Local Earthquake Tomography, *Journal of Geophysical Research: Solid Earth*, **125**(10).

Chen, M., Huang, H., Yao, H., van der Hilst, R., & Niu, F., 2014. Low wave speed zones in the crust beneath SE Tibet revealed by ambient noise adjoint tomography, *Geophysical Research Letters*, **41**(2), 334–340.

Chen, M., Niu, F., Liu, Q., Tromp, J., & Zheng, X., 2015. Multiparameter adjoint tomography of the crust and upper mantle beneath East Asia: 1. Model construction and comparisons, *Journal of Geophysical Research: Solid Earth*, **120**(3), 1762–1786.

Chen, P., Jordan, T. H., & Zhao, L., 2007a. Full three-dimensional tomography: a comparison between the scattering-integral and adjoint-wavefield methods, *Geophysical Journal International*, **170**(1), 175–181.

Chen, P., Zhao, L., & Jordan, T. H., 2007b. Full 3D tomography for the crustal structure of the Los Angeles region, *Bulletin of the Seismological Society of America*, **97**(4), 1094–1120.

Chen, Y., Wu, J., & Suppe, J., 2019. Southward propagation of Nazca subduction along the Andes, *Nature*, **565**(7740), 441–447.

Chu, R., Helmberger, D. V., Sun, D., Jackson, J. M., & Zhu, L., 2010. Mushy magma beneath Yellowstone, *Geophysical Research Letters*, **37**(1).

Colli, L., Fichtner, A., & Bunge, H.-P., 2013. Full waveform tomography of the upper mantle in the South Atlantic region: Imaging a westward fluxing shallow asthenosphere?, *Tectonophysics*, **604**, 26 – 40.

Comte, D., Carrizo, D., Roecker, S., Ortega-Culaciati, F., & Peyrat, S., 2016. Three-dimensional elastic wave speeds in the northern Chile subduction zone: variations in hydration in the supraslab mantle, *Geophysical Journal International*, **207**(2), 1080–1105.

Courant, R., Friedrichs, K., & Lewy, H., 1967. On the partial difference equations of mathematical physics, *IBM journal of Research and Development*, **11**(2), 215–234.

Cristallini, E. O. & Ramos, V. A., 2000. Thick-skinned and thin-skinned thrusting in the La Ramada fold and thrust belt: crustal evolution of the High Andes of San Juan, Argentina (32° SL), *Tectonophysics*, **317**(3-4), 205–235.

Currie, C. A., Ducea, M. N., DeCelles, P. G., & Beaumont, C., 2015. Geodynamic models of Cordilleran orogens: Gravitational instability of magmatic arc roots, *Memoir of the Geological Society of America*, **212**(01), 1–22.

Dahlen, F. A., Hung, S.-H., & Nolet, G., 2000. Fréchet kernels for finite-frequency traveltimes—I. Theory, *Geophysical Journal International*, **141**(1), 157–174.

Dai, L., Wang, L., Lou, D., Li, Z.-H., Dong, H., Ma, F., Li, F., Li, S., & Yu, S., 2020. Slab rollback versus delamination: Contrasting fates of flat-slab subduction and implications for South China evolution in the Mesozoic, *Journal of Geophysical Research: Solid Earth*, **125**(4), e2019JB019164.

de Hoop, M. V. & van Der Hilst, R. D., 2005. On sensitivity kernels for 'wave-equation' transmission tomography, *Geophysical Journal International*, **160**(2), 621–633.

de Silva, S. L., 1989. Altiplano-Puna volcanic complex of the central Andes, *Geology*, **17**(12), 1102–1106.

de Silva, S. L. and Kay, Suzanne M., 2018. Turning up the heat: High-flux magmatism in the central andes, *Elements*, **14**(4), 245–250.

DeCelles, P. G., Zandt, G., Beck, S. L., Currie, C. A., Ducea, M. N., Kapp, P., Gehrels, G. E., Carrapa, B., Quade, J., & Schoenbohm, L. M., 2015. Cyclical orogenic processes in the Cenozoic central Andes, *Memoir of the Geological Society of America*, **212**(22), 459–490.

Delph, J. R., Ward, K. M., Zandt, G., Ducea, M. N., & Beck, S. L., 2017. Imaging a magma plumbing system from MASH zone to magma reservoir, *Earth and Planetary Science Letters*, **457**, 313 – 324.

Dumbser, M., Käser, M., & De La Puente, J., 2007. Arbitrary high-order finite volume schemes for seismic wave propagation on unstructured meshes in 2D and 3D, *Geophysical Journal International*, **171**(2), 665–694.

Dziewonski, A. M. & Anderson, D. L., 1981. Preliminary reference Earth model, *Physics of the Earth and Planetary Interiors*, **25**(4), 297 – 356.

D´Annunzio, M. C., Rubinstein, N., & Rabbia, O., 2018. Petrogenesis of the Gualcamayo Igneous Complex: Regional implications of Miocene magmatism in the Precordillera over the Pampean flat-slab segment, Argentina, *Journal of South American Earth Sciences*, **88**, 16–28.

Ekström, G., Nettles, M., & Dziewoński, A., 2012. The global CMT project 2004–2010: Centroid-moment tensors for 13,017 earthquakes, *Physics of the Earth and Planetary Interiors*, **200-201**, 1 – 9.

Engdahl, E. R., Di Giacomo, D., Sakarya, B., Gkarlaouni, C. G., Harris, J., & Storchak, D. A., 2020. ISC-EHB 1964–2016, an Improved Data Set for Studies of Earth Structure and Global Seismicity, *Earth and Space Science*, **7**(1), e2019EA000897.

Feng, M., Van der Lee, S., & Assumpção, M., 2007. Upper mantle structure of South America from joint inversion of waveforms and fundamental mode group velocities of Rayleigh waves, *Journal of Geophysical Research: Solid Earth*, **112**(B4).

Ferrand, T. P., Hilairet, N., Incel, S., Deldicque, D., Labrousse, L., Gasc, J., Renner, J., Wang, Y., Green II, H. W., & Schubnel, A., 2017. Dehydration-driven stress transfer triggers intermediate-depth earthquakes, *Nature Communications*, **8**(1), 15247.

Fichtner, A., 2010. *Full seismic waveform modelling and inversion*, Springer Science & Business Media.

Fichtner, A. & Leeuwen, T. v., 2015. Resolution analysis by random probing, *Journal of Geophysical Research: Solid Earth*, **120**(8), 5549–5573.

Fichtner, A. & Trampert, J., 2011. Resolution analysis in full waveform inversion, *Geophysical Journal International*, **187**(3), 1604–1624.

Fichtner, A., Bunge, H.-P., & Igel, H., 2006a. The adjoint method in seismology: I. Theory, *Physics of the Earth and Planetary Interiors*, **157**(1), 86–104.

Fichtner, A., Bunge, H.-P., & Igel, H., 2006b. The adjoint method in seismology: II. Applications: traveltimes and sensitivity functionals, *Physics of the Earth and Planetary Interiors*, **157**(1), 105–123.

Fichtner, A., Kennett, B. L., Igel, H., & Bunge, H.-P., 2008. Theoretical background for continental and global scale full-waveform inversion in the time–frequency domain, *Geophysical Journal International*, **175**(2), 665–685.

Fichtner, A., Kennett, B. L. N., Igel, H., & Bunge, H.-P., 2009. Full seismic waveform tomography for upper-mantle structure in the Australasian region using adjoint methods, *Geophysical Journal International*, **179**(3), 1703–1725.

Fichtner, A., Kennett, B. L., Igel, H., & Bunge, H.-P., 2010. Full waveform tomography for radially anisotropic structure: new insights into present and past states of the Australasian upper mantle, *Earth and Planetary Science Letters*, **290**(3-4), 270–280.

Fichtner, A., van Herwaarden, D.-P., Afanasiev, M., Simutė, S., Krischer, L., Çubuk Sabuncu, Y., Taymaz, T., Colli, L., Saygin, E., Villaseñor, A., Trampert, J., Cupillard, P., Bunge, H.-P., & Igel, H., 2018. The collaborative seismic earth model: Generation 1, *Geophysical Research Letters*, **45**(9), 4007–4016.

Fletcher, R. & Reeves, C. M., 1964. Function minimization by conjugate gradients, *The Computer Journal*, **7**(2), 149–154.

Folguera, A., Bottesi, G., Zapata, T., & Ramos, V. A., 2008. Crustal collapse in the Andean backarc since 2 Ma: Tromen volcanic plateau, Southern Central Andes (36° 40' – 37° 30'S), *Tectonophysics*, **459**(1), 140–160, New Insights into Andean Evolution.

Folguera, A., Naranjo, J. A., Orihashi, Y., Sumino, H., Nagao, K., Polanco, E., & Ramos, V. A., 2009. Retroarc volcanism in the northern San Rafael Block (34 –35 S), southern Central Andes: Occurrence, age, and tectonic setting, *Journal of Volcanology and Geothermal Research*, **186**(3), 169–185.

Gans, C. R., Beck, S. L., Zandt, G., Gilbert, H., Alvarado, P., Anderson, M., & Linkimer, L., 2011. Continental and oceanic crustal structure of the Pampean flat slab region, western Argentina, using receiver function analysis: New high-resolution results, *Geophysical Journal International*, **186**(1), 45–58.

Gao, H. & Shen, Y., 2014. Upper mantle structure of the Cascades from full-wave ambient noise tomography: Evidence for 3D mantle upwelling in the back-arc, *Earth and Planetary Science Letters*, **390**, 222–233.

Gao, Y., Tilmann, F., van Herwaarden, D.-P., Thrastarson, S., Fichtner, A., Heit, B., Yuan, X., & Schurr, B., 2021a. Full Waveform Inversion beneath the Central Andes: Insight into the dehydration of the Nazca slab and delamination of the back-arc lithosphere, *Journal of Geophysical Research: Solid Earth*, **126**(7), e2021JB021984.

Gao, Y., Yuan, X., Heit, B., Tilmann, F., van Herwaarden, D.-P., Thrastarson, S., Fichtner, A., & Schurr, B., 2021b. Impact of the Juan Fernandez ridge on the Pampean flat subduction inferred from full waveform inversion, *Geophysical Research Letters*, **48**(21), e2021GL095509.

Garzione, C. N., Molnar, P., Libarkin, J. C., & MacFadden, B. J., 2006. Rapid late Miocene rise of the Bolivian Altiplano: Evidence for removal of mantle lithosphere, *Earth and Planetary Science Letters*, **241**(3-4), 543–556.

Garzione, C. N., McQuarrie, N., Perez, N. D., Ehlers, T. A., Beck, S. L., Kar, N., Eichelberger, N., Chapman, A. D., Ward, K. M., Ducea, M. N., et al., 2017. Tectonic evolution of the Central Andean plateau and implications for the growth of plateaus, *Annual Review of Earth and Planetary Sciences*, **45**, 529–559.

Geersen, J., Ranero, C. R., Klaucke, I., Behrmann, J. H., Kopp, H., Tréhu, A. M., Contreras-Reyes, E., Barckhausen, U., & Reichert, C., 2018. Active tectonics of the North Chilean marine forearc and adjacent oceanic Nazca Plate, *Tectonics*, **37**(11), 4194–4211.

GEOFON Data Centre, 1993. GEOFON Seismic Network.

Gerya, T., 2019. *Introduction to numerical geodynamic modelling*, Cambridge University Press.

GFZ & CNRS-INSU, 2006. IPOC Seismic Network.

Gianni, G., Pesce, A., & Soler, S., 2018. Transient plate contraction between two simultaneous slab windows: Insights from Paleogene tectonics of the Patagonian Andes, *Journal of Geodynamics*, **121**, 64–75.

Gilbert, H., 2008. Eastern Sierras Pampeanas, Lithospheric Structure above the variably dipping Nazca Slab.

Gokhberg, A. & Fichtner, A., 2016. Full-waveform inversion on heterogeneous HPC systems, *Computers & Geosciences*, **89**, 260–268.

Goss, A., Kay, S., Mpodozis, C., & Singer, B., 2009. The Incapillo Caldera and Dome Complex (28°S, central Andes): A stranded magma chamber over a dying arc, *Journal of volcanology and geothermal research*, **184**(3-4), 389–404.

Goss, A., Kay, S., & Mpodozis, C., 2011. The geochemistry of a dying continental arc: the incapillo caldera and dome complex of the southernmost central andean volcanic zone (˜28°s), *Contributions to Mineralogy and Petrology*, **161**(1), 101–128.

Gutscher, M.-A., Olivet, J.-L., Aslanian, D., Eissen, J.-P., & Maury, R., 1999. The "lost inca plateau": cause of flat subduction beneath peru?, *Earth and Planetary Science Letters*, **171**(3), 335–341.

Gutscher, M.-A., Maury, R., Eissen, J.-P., & Bourdon, E., 2000. Can slab melting be caused by flat subduction?, *Geology*, **28**(6), 535–538.

Götze, H.-J. & Krause, S., 2002. The Central Andean gravity high, a relic of an old subduction complex?, *Journal of South American Earth Sciences*, **14**(8), 799 – 811.

Hacker, B. R., Peacock, S. M., Abers, G. A., & Holloway, S. D., 2003. Subduction factory 2. Are intermediate-depth earthquakes in subducting slabs linked to metamorphic dehydration reactions?, *Journal of Geophysical Research: Solid Earth*, **108**(B1).

Haddon, A. & Porter, R., 2018. S-wave receiver function analysis of the pampean flat-slab region: Evidence for a torn slab, *Geochemistry, Geophysics, Geosystems*, **19**(10), 4021–4034.

Hampel, A., 2002. The migration history of the Nazca Ridge along the Peruvian active margin: a re-evaluation, *Earth and Planetary Science Letters*, **203**(2), 665–679.

Haschke, M., Scheuber, E., Günther, A., & Reutter, K.-J., 2002. Evolutionary cycles during the Andean orogeny: repeated slab breakoff and flat subduction?, *Terra nova*, **14**(1), 49–55.

Hayes, G. P., Moore, G. L., Portner, D. E., Hearne, M., Flamme, H., Furtney, M., & Smoczyk, G. M., 2018. Slab2, a comprehensive subduction zone geometry model, *Science*, **362**(6410), 58–61.

Heit, B., Sodoudi, F., Yuan, X., Bianchi, M., & Kind, R., 2007a. An S receiver function analysis of the lithospheric structure in South America, *Geophysical Research Letters*, **34**(14).

Heit, B., Yuan, X., Kind, R., & Asch, G., 2007b. Lithospheric dynamics in the southernmost Andean Plateau (PUDEL).

Heit, B., Koulakov, I., Asch, G., Yuan, X., Kind, R., Alcocer-Rodriguez, I., Tawackoli, S., & Wilke, H., 2008a. More constraints to determine the seismic structure beneath the Central Andes at 21°S using teleseismic tomography analysis, *Journal of South American Earth Sciences*, **25**(1), 22 – 36.

Heit, B., Yuan, X., Bianchi, M., Sodoudi, F., & Kind, R., 2008b. Crustal thickness estimation beneath the southern central Andes at 30°S and 36°S from S wave receiver function analysis, *Geophysical Journal International*, **174**(1), 249–254.

Heit, B., Bianchi, M., Yuan, X., Kay, S., Sandvol, E., Kumar, P., Kind, R., Alonso, R., Brown, L., & Comte, D., 2014. Structure of the crust and the lithosphere beneath the southern Puna plateau from teleseismic receiver functions, *Earth and Planetary Science Letters*, **385**, 1 – 11.

Hiett, C. D., Newell, D. L., & Jessup, M. J., 2021. ^{3}He evidence for fluid transfer and continental hydration above a flat slab, *Earth and Planetary Science Letters*, **556**, 116722.

Hildreth, W. & Moorbath, S., 1988. Crustal contributions to arc magmatism in the Andes of central Chile, *Contributions to mineralogy and petrology*, **98**(4), 455–489.

Hirt, C. & Rexer, M., 2015. Earth2014: 1 arc-min shape, topography, bedrock and ice-sheet models – Available as gridded data and degree-10,800 spherical harmonics, *International Journal of Applied Earth Observation and Geoinformation*, **39**, 103 – 112.

Horton, B. K., 2018. Tectonic Regimes of the Central and Southern Andes: Responses to Variations in Plate Coupling During Subduction, *Tectonics*, **37**(2), 402–429.

Hu, J. & Liu, L., 2016. Abnormal seismological and magmatic processes controlled by the tearing South American flat slabs, *Earth and Planetary Science Letters*, **450**, 40–51.

Hu, J., Liu, L., Hermosillo, A., & Zhou, Q., 2016. Simulation of late Cenozoic South American flat-slab subduction using geodynamic models with data assimilation, *Earth and Planetary Science Letters*, **438**(March), 1–13.

Hu, J., Faccenda, M., & Liu, L., 2017. Subduction-controlled mantle flow and seismic anisotropy in South America, *Earth and Planetary Science Letters*, **470**, 13–24.

Huang, Z., Tilmann, F., Comte, D., & Zhao, D., 2019. P Wave Azimuthal Anisotropic Tomography in Northern Chile: Insight Into Deformation in the Subduction Zone, *Journal of Geophysical Research: Solid Earth*, **124**(1), 742–765.

Huangfu, P., Wang, Y., Cawood, P. A., Li, Z.-H., Fan, W., & Gerya, T. V., 2016. Thermo-mechanical controls of flat subduction: Insights from numerical modeling, *Gondwana Research*, **40**, 170–183.

Husen, S., Kissling, E., & Flueh, E. R., 2000. Local earthquake tomography of shallow subduction in north Chile: A combined onshore and offshore study, *Journal of Geophysical Research: Solid Earth*, **105**(B12), 28183–28198.

Ibarra, F., Liu, S., Meeßen, C., Prezzi, C., Bott, J., Scheck-Wenderoth, M., Sobolev, S., & Strecker, M., 2019. 3D data-derived lithospheric structure of the Central Andes and its implications for deformation: Insights from gravity and geodynamic modelling, *Tectonophysics*, **766**, 453 – 468.

Igel, H., 1999. Wave propagation in three-dimensional spherical sections by the Chebyshev spectral method, *Geophysical Journal International*, **136**(3), 559–566.

Igel, H., 2017. *Computational seismology: a practical introduction*, Oxford University Press.

Igel, H., Mora, P., & Riollet, B., 1995. Anisotropic wave propagation through finite-difference grids, *Geophysics*, **60**(4), 1203–1216.

IPGP & EOST, 1982. GEOSCOPE, French Global Network of broad band seismic stations.

James, D. E. & Sacks, I. S., 1999. Cenozoic Formation of the Central Andes: A Geophysical Perspective, in *Geology and Ore Deposits of the Central Andes*, Society of Economic Geologists.

Kay, R. W. & Kay, S. M., 1993. Delamination and delamination magmatism, *Tectonophysics*, **219**(1-3), 177–189.

Kay, R. W. & Kay, S. M., 2002. Andean adakites: three ways to make them, *Acta Petrologica Sinica*, **18**(3), 303–311.

Kay, S. M. & Abbruzzi, J., 1996. Magmatic evidence for Neogene lithospheric evolution of the central Andean "flat-slab" between 30°S and 32 S, *Tectonophysics*, **259**(1-3), 15–28.

Kay, S. M. & Coira, B. L., 2009. Shallowing and steepening subduction zones, continental lithospheric loss, magmatism, and crustal flow under the Central Andean Altiplano-Puna Plateau, in *Backbone of the Americas: Shallow Subduction, Plateau Uplift, and Ridge and Terrane Collision*, Geological Society of America.

Kay, S. M. & Mpodozis, C., 2002. Magmatism as a probe to the Neogene shallowing of the Nazca plate beneath the modern Chilean flat-slab, *Journal of South American Earth Sciences*, **15**(1), 39–57.

Kay, S. M., Coira, B., & Viramonte, J., 1994. Young mafic back arc volcanic rocks as indicators of continental lithospheric delamination beneath the Argentine Puna Plateau, central Andes, *Journal of Geophysical Research: Solid Earth*, **99**(B12), 24323–24339.

Kay, S. M., Gorring, M., & Ramos, V. A., 2004. Magmatic sources, setting and causes of Eocene to recent Patagonian plateau magmatism (36 S to 52 S latitude), *Revista de la Asociacion Geologica Argentina*, **59**(4), 556–568.

Kay, S. M., Godoy, E., & Kurtz, A., 2005. Episodic arc migration, crustal thickening, subduction erosion, and magmatism in the south-central Andes, *GSA Bulletin*, **117**(1-2), 67–88.

Kendrick, E., Bevis, M., Smalley Jr, R., Brooks, B., Vargas, R. B., Laurıa, E., & Fortes, L. P. S., 2003. The Nazca–South America Euler vector and its rate of change, *Journal of South American Earth Sciences*, **16**(2), 125–131.

Kim, Y. & Clayton, R. W., 2015. Seismic properties of the Nazca oceanic crust in southern Peruvian subduction system, *Earth and Planetary Science Letters*, **429**, 110 – 121.

Koelemeijer, P., Ritsema, J., Deuss, A., & van Heijst, H.-J., 2015. SP12RTS: a degree-12 model of shear- and compressional-wave velocity for Earth's mantle, *Geophysical Journal International*, **204**(2), 1024–1039.

Komatitsch, D. & Tromp, J., 1999. Introduction to the spectral element method for three-dimensional seismic wave propagation, *Geophysical Journal International*, **139**(3), 806–822.

Komatitsch, D. & Tromp, J., 2002a. Spectral-element simulations of global seismic wave propagation-i. validation, *Geophysical Journal International*, **149**(2), 390–412.

Komatitsch, D. & Tromp, J., 2002b. Spectral-element simulations of global seismic wave propagation–ii. three-dimensional models, oceans, rotation and self-gravitation, *Geophysical Journal International*, **150**(1), 303–318.

Kopp, H., Flueh, E. R., Papenberg, C., & Klaeschen, D., 2004. Seismic investigations of the O'Higgins Seamount Group and Juan Fernández Ridge: Aseismic ridge emplacement and lithosphere hydration, *Tectonics*, **23**(2), 1–21.

Kosloff, D. D. & Baysal, E., 1982. Forward modeling by a fourier method, *GEOPHYSICS*, **47**(10), 1402–1412.

Koulakov, I., Sobolev, S. V., & Asch, G., 2006. P- and S-velocity images of the lithosphere–asthenosphere system in the Central Andes from local-source tomographic inversion, *Geophysical Journal International*, **167**(1), 106–126.

Krischer, L., Fichtner, A., Zukauskaite, S., & Igel, H., 2015a. Large-scale seismic inversion framework, *Seismological Research Letters*, **86**(4), 1198.

Krischer, L., Tobias, M., Robert, B., Moritz, B., Thomas, L., Corentin, C., & Joachim, W., 2015b. ObsPy: a bridge for seismology into the scientific Python ecosystem, *Computational Science and Discovery*, **8**(1).

Krischer, L., Smith, J., Lei, W., Lefebvre, M., Ruan, Y., de Andrade, E. S., Podhorszki, N., Bozdağ, E., & Tromp, J., 2016. An adaptable seismic data format, *Geophysical Supplements to the Monthly Notices of the Royal Astronomical Society*, **207**(2), 1003–1011.

Krischer, L., Aiman, Y. A., Bartholomaus, T., Donner, S., van Driel, M., Duru, K., Garina, K., Gessele, K., Gunawan, T., Hable, S., et al., 2018a. Seismo-live: An educational online library of jupyter notebooks for seismology, *Seismological Research Letters*, **89**(6), 2413–2419.

Krischer, L., Fichtner, A., Boehm, C., & Igel, H., 2018b. Automated Large-Scale Full Seismic Waveform Inversion for North America and the North Atlantic, *Journal of Geophysical Research: Solid Earth*, **123**(7), 5902–5928.

Kristeková, M., Kristek, J., & Moczo, P., 2009. Time-frequency misfit and goodness-of-fit criteria for quantitative comparison of time signals, *Geophysical Journal International*, **178**(2), 813–825.

Krystopowicz, N. J. & Currie, C. A., 2013. Crustal eclogitization and lithosphere delamination in orogens, *Earth and Planetary Science Letters*, **361**, 195–207.

Kumar, A., Wagner, L. S., Beck, S. L., Long, M. D., Zandt, G., Young, B., Tavera, H., & Minaya, E., 2016. Seismicity and state of stress in the central and southern Peruvian flat slab, *Earth and Planetary Science Letters*, **441**, 71 – 80.

Lange, D., Cembrano, J., & Sielfeld, G., 2019. Crustal Seismicity along for the Southern Andes Volcanic Zone (LOFS).

Laske, G., Masters, G., Ma, Z., & Pasyanos, M., 2013. Update on CRUST1. 0—A 1-degree global model of Earth's crust, in *Geophys. Res. Abstracts, 15, Abstract EGU2013-2658*.

Lei, W., Ruan, Y., Bozdağ, E., Peter, D., Lefebvre, M., Komatitsch, D., Tromp, J., Hill, J., Podhorszki, N., & Pugmire, D., 2020. Global adjoint tomography - Model GLAD-M25, *Geophysical Journal International*, **223**(1), 1–21.

Li, C., Van Der Hilst, R. D., Engdahl, E. R., & Burdick, S., 2008. A new global model for P wave speed variations in Earth's mantle, *Geochemistry, Geophysics, Geosystems*, **9**(5).

Li, Z., Xu, Z., & Gerya, T., 2011. Flat versus steep subduction: Contrasting modes for the formation and exhumation of high-to ultrahigh-pressure rocks in continental collision zones, *Earth and Planetary Science Letters*, **301**(1-2), 65–77.

Li, Z. H., 2020. Flat subduction versus big mantle wedge: contrasting modes for deep hydration and overriding craton modification, *Journal of Geophysical Research: Solid Earth*, **125**(8), e2020JB020018.

Liang, X., Sandvol, E., Kay, S., Heit, B., Yuan, X., Mulcahy, P., Chen, C., Brown, L., Comte, D., & Alvarado, P., 2014. Delamination of southern Puna lithosphere revealed by body wave attenuation tomography, *Journal of Geophysical Research: Solid Earth*, **119**(1), 549–566.

Lim, H., Kim, Y., Clayton, R. W., & Thurber, C. H., 2018. Seismicity and structure of Nazca Plate subduction zone in southern Peru, *Earth and Planetary Science Letters*, **498**, 334 – 347.

Lin, S., 2014. Three-dimensional mantle circulations and lateral slab deformation in the southern Chilean subduction zone, *Journal of Geophysical Research: Solid Earth*, **119**(4), 3879–3896.

Linkimer, L., Beck, S., Zandt, G., Alvarado, P., Anderson, M., Gilbert, H., & Zhang, H., 2020. Lithospheric structure of the Pampean flat slab region from double-difference tomography, *Journal of South American Earth Sciences*, **97**, 102417.

Liu, D. & Nocedal, J., 1989. On the limited memory BFGS method for large scale optimization, *Mathematical Programming*, **45**(1), 503–528.

Liu, K. & Zhou, Y., 2016. Global Rayleigh wave phase-velocity maps from finite-frequency tomography, *Geophysical Journal International*, **205**(1), 51–66.

Liu, L. & Zhou, Q., 2015. Deep recycling of oceanic asthenosphere material during subduction, *Geophysical Research Letters*, **42**(7), 2204–2211.

Liu, Q. & Tromp, J., 2006. Finite-Frequency Kernels Based on Adjoint Methods, *Bulletin of the Seismological Society of America*, **96**(6), 2383–2397.

Liu, Q. & Tromp, J., 2008. Finite-frequency sensitivity kernels for global seismic wave propagation based upon adjoint methods, *Geophysical Journal International*, **174**(1), 265–286.

Liu, S. & Currie, C. A., 2016. Farallon plate dynamics prior to the Laramide orogeny: Numerical models of flat subduction, *Tectonophysics*, **666**, 33–47.

Liu, X. & Currie, C. A., 2019. Influence of upper plate structure on flat-slab depth: Numerical modeling of subduction dynamics, *Journal of Geophysical Research: Solid Earth*, **124**(12), 13150–13167.

Liu, Y., Teng, J., Xu, T., Wang, Y., Liu, Q., & Badal, J., 2017. Robust time-domain full waveform inversion with normalized zero-lag cross-correlation objective function, *Geophysical Journal International*, **209**(1), 106–122.

Lu, Y., Stehly, L., Brossier, R., Paul, A., & Group, A. W., 2020. Imaging Alpine crust using ambient noise wave-equation tomography, *Geophysical Journal International*, **222**(1), 69–85.

Luo, Y. & Schuster, G. T., 1991. Wave-equation traveltime inversion, *Geophysics*, **56**(5), 645–653.

Lynner, C., Anderson, M. L., Portner, D. E., Beck, S. L., & Gilbert, H., 2017. Mantle flow through a tear in the Nazca slab inferred from shear wave splitting, *Geophysical Research Letters*, **44**(13), 6735–6742.

Lysmer, J. & Drake, L. A., 1972. *A Finite Element Method for Seismology*, vol. 11, pp. 181–216, Elsevier.

Ma, Y. & Clayton, R. W., 2014. The crust and uppermost mantle structure of Southern Peru from ambient noise and earthquake surface wave analysis, *Earth and Planetary Science Letters*, **395**, 61–70.

Ma, Y. & Clayton, R. W., 2015. Flat slab deformation caused by interplate suction force, *Geophysical Research Letters*, **42**(17), 7064–7072.

Madella, A., Delunel, R., Audin, L., & Schlunegger, F., 2018. Why is there no Coastal Cordillera at the Arica Bend (Western Central Andes)?, *Basin Research*, **30**(S1), 248–268.

Maggi, A., Tape, C., Chen, M., Chao, D., & Tromp, J., 2009. An automated time-window selection algorithm for seismic tomography, *Geophysical Journal International*, **178**(1), 257–281.

Manea, V. C., Pérez-Gussinyé, M., & Manea, M., 2012. Chilean flat slab subduction controlled by overriding plate thickness and trench rollback, *Geology*, **40**(1), 35–38.

Manea, V. C., Manea, M., Ferrari, L., Orozco-Esquivel, T., Valenzuela, R., Husker, A., & Kostoglodov, V., 2017. A review of the geodynamic evolution of flat slab subduction in Mexico, Peru, and Chile, *Tectonophysics*, **695**, 27–52.

Marot, M., Monfret, T., Gerbault, M., Nolet, G., Ranalli, G., & Pardo, M., 2014. Flat versus normal subduction zones: A comparison based on 3-D regional traveltime tomography and petrological modelling of central Chile and western Argentina (29°-35°S), *Geophysical Journal International*, **199**(3), 1633–1654.

Matzel, E. & Grand, S. P., 2004. The anisotropic seismic structure of the East European platform, *Journal of Geophysical Research: Solid Earth*, **109**(B1).

McQuarrie, N., Horton, B. K., Zandt, G., Beck, S., & DeCelles, P. G., 2005. Lithospheric evolution of the Andean fold–thrust belt, Bolivia, and the origin of the central Andean plateau, *Tectonophysics*, **399**(1), 15 – 37.

Meier, U., Curtis, A., & Trampert, J., 2007. Fully nonlinear inversion of fundamental mode surface waves for a global crustal model, *Geophysical Research Letters*, **34**(16).

Moczo, P., Kristek, J., Galis, M., Pazak, P., & Balazovjech, M., 2007. The finite-difference and finite-element modeling of seismic wave propagation and earthquake motion, *Acta physica slovaca*, **57**(2).

Mohammadzaheri, A., Sigloch, K., Hosseini, K., & Mihalynuk, M. G., 2021. Subducted Lithosphere Under South America From Multifrequency P Wave Tomography, *Journal of Geophysical Research: Solid Earth*, **126**(6), e2020JB020704.

Montelli, R., Nolet, G., Dahlen, F., Masters, G., Engdahl, E. R., & Hung, S.-H., 2004. Finite-frequency tomography reveals a variety of plumes in the mantle, *Science*, **303**(5656), 338–343.

Müller, R. D., Sdrolias, M., Gaina, C., & Roest, W. R., 2008. Age, spreading rates, and spreading asymmetry of the world's ocean crust, *Geochemistry, Geophysics, Geosystems*, **9**(4).

Norabuena, E. O., Dixon, T. H., Stein, S., & Harrison, C. G. A., 1999. Decelerating Nazca-South America and Nazca-Pacific Plate motions, *Geophysical Research Letters*, **26**(22), 3405–3408.

Nuber, A., Manukyan, E., & Maurer, H., 2016. Ground topography effects on near-surface elastic full waveform inversion, *Geophysical Journal International*, **207**(1), 67–71.

Obayashi, M., Yoshimitsu, J., Nolet, G., Fukao, Y., Shiobara, H., Sugioka, H., Miyamachi, H., & Gao, Y., 2013. Finite frequency whole mantle P wave tomography: Improvement of subducted slab images, *Geophysical Research Letters*, **40**(21), 5652–5657.

Okazaki, K. & Hirth, G., 2016. Dehydration of lawsonite could directly trigger earthquakes in subducting oceanic crust, *Nature*, **530**(7588), 81–84.

Oncken, O., Asch, G., Haberland, C., Metchie, J., Sobolev, S., Stiller, M., Yuan, X., Brasse, H., Buske, S., Giese, P., et al., 2003. Seismic imaging of a convergent continental margin and plateau in the central Andes (Andean Continental Research Project 1996 (ANCORP'96)), *Journal of Geophysical Research: Solid Earth*, **108**(B7).

Oncken, O., Hindle, D., Kley, J., Elger, K., Victor, P., & Schemmann, K., 2006. Deformation of the central Andean upper plate system—Facts, fiction, and constraints for plateau models, in *The Andes*, pp. 3–27, Springer.

Panning, M. & Romanowicz, B., 2006. A three-dimensional radially anisotropic model of shear velocity in the whole mantle, *Geophysical Journal International*, **167**(1), 361–379.

Pavlis, N. K., Holmes, S. A., Kenyon, S. C., & Factor, J. K., 2012. The development and evaluation of the Earth Gravitational Model 2008 (EGM2008), *Journal of Geophysical Research: Solid Earth*, **117**(B4).

Peacock, S. M., 2001. Are the lower planes of double seismic zones caused by serpentine dehydration in subducting oceanic mantle?, *Geology*, **29**(4), 299–302.

Perkins, J. P., Ward, K. M., De Silva, S. L., Zandt, G., Beck, S. L., & Finnegan, N. J., 2016. Surface uplift in the Central Andes driven by growth of the Altiplano Puna Magma Body, *Nature Communications*, **7**(1), 1–10.

Pesicek, J., Engdahl, E., Thurber, C., DeShon, H., & Lange, D., 2012. Mantle subducting slab structure in the region of the 2010 M 8.8 Maule earthquake (30–40 S), Chile, *Geophysical Journal International*, **191**(1), 317–324.

Piceda, C. R., Wenderoth, M. S., Dacal, M. L. G., Bott, J., Prezzi, C. B., & Strecker, M. R., 2020. Lithospheric density structure of the Southern Central Andes constrained by 3D data-integrative gravity modelling, *International Journal of Earth Sciences*, **110**(2333–2359).

Płonka, A., Blom, N., & Fichtner, A., 2016. The imprint of crustal density heterogeneities on regional seismic wave propagation, *Solid Earth*, **7**(6), 1591–1608.

Porter, R., Gilbert, H., Zandt, G., Beck, S., Warren, L., Calkins, J., Alvarado, P., & Anderson, M., 2012. Shear wave velocities in the Pampean flat-slab region from Rayleigh wave tomography: Implications for slab and upper mantle hydration, *Journal of Geophysical Research B: Solid Earth*, **117**(11), 1–21.

Portner, D. E. & Hayes, G. P., 2018. Incorporating teleseismic tomography data into models of upper mantle slab geometry, *Geophysical Journal International*, **215**(1), 325–332.

Portner, D. E., Beck, S., Zandt, G., & Scire, A., 2017. The nature of subslab slow velocity anomalies beneath South America, *Geophysical Research Letters*, **44**(10), 4747–4755.

Portner, D. E., Rodríguez, E. E., Beck, S., Zandt, G., Scire, A., Rocha, M. P., Bianchi, M. B., Ruiz, M., França, G. S., Condori, C., & Alvarado, P., 2020. Detailed Structure of the Subducted Nazca Slab into the Lower Mantle Derived From Continent-Scale Teleseismic P Wave Tomography, *Journal of Geophysical Research: Solid Earth*, **125**(5).

Pritchard, M., 2009. The life cycle of Andean volcanoes: combining space-based and field studies.

Ramos, V. A. & Folguera, A., 2009. Andean flat-slab subduction through time, *Geological Society, London, Special Publications*, **327**(1), 31–54.

Ramos, V. A. & Folguera, A., 2011. Payenia volcanic province in the Southern Andes: An appraisal of an exceptional Quaternary tectonic setting, *Journal of Volcanology and geothermal Research*, **201**(1-4), 53–64.

Ramos, V. A., Cristallini, E. O., & Pérez, D. J., 2002. The Pampean flat-slab of the Central Andes, *Journal of South American earth sciences*, **15**(1), 59–78.

Ramos, V. A., Litvak, V. D., Folguera, A., & Spagnuolo, M., 2014. An Andean tectonic cycle: From crustal thickening to extension in a thin crust (34°– 37°SL), *Geoscience Frontiers*, **5**(3), 351–367.

Ranero, C. R. & Sallarès, V., 2004. Geophysical evidence for hydration of the crust and mantle of the Nazca plate during bending at the north Chile trench, *Geology*, **32**(7), 549–552.

Ranero, C. R., Villaseñor, A., Phipps Morgan, J., & Weinrebe, W., 2005. Relationship between bend-faulting at trenches and intermediate-depth seismicity, *Geochemistry, Geophysics, Geosystems*, **6**(12).

Rietbrock, A., Haberland, C., Bataille, K., Lange, D., & Dahm, T., 2004. TIPTEQ-Temporary seismological network (North) (2004/2005).

Ritsema, J. & van Heijst, H.-J., 2002. Constraints on the correlation of P- and S-wave velocity heterogeneity in the mantle from P, PP, PPP and PKPab traveltimes, *Geophysical Journal International*, **149**(2), 482–489.

Ritsema, J., van Heijst, H. J., & Woodhouse, J. H., 1999. Complex shear wave velocity structure imaged beneath Africa and Iceland, *Science*, **286**(5446), 1925–1928.

Ritsema, J., Deuss, A., van Heijst, H. J., & Woodhouse, J. H., 2011. S40RTS: a degree-40 shear-velocity model for the mantle from new Rayleigh wave dispersion, teleseismic traveltime and normal-mode splitting function measurements, *Geophysical Journal International*, **184**(3), 1223–1236.

Rivadeneyra-Vera, C., Bianchi, M., Assumpção, M., Cedraz, V., Julià, J., Rodríguez, M., Sánchez, L., Sánchez, G., Lopez-Murua, L., Fernandez, G., et al., 2019. An updated crustal thickness map of central South America based on receiver function measurements in the region of the Chaco, Pantanal, and Paraná Basins, southwestern Brazil, *Journal of Geophysical Research: Solid Earth*, **124**(8), 8491–8505.

Rodríguez, E. E., Portner, D. E., Beck, S. L., Rocha, M. P., Bianchi, M. B., Assumpção, M., Ruiz, M., Alvarado, P., Condori, C., & Lynner, C., 2021. Mantle dynamics of the Andean Subduction Zone from continent-scale teleseismic S-wave tomography, *Geophysical Journal International*, **224**(3), 1553–1571.

Rodríguez-González, J., Negredo, A. M., & Billen, M. I., 2012. The role of the overriding plate thermal state on slab dip variability and on the occurrence of flat subduction, *Geochemistry, Geophysics, Geosystems*, **13**(1).

Rodríguez-González, J., Negredo, A. M., & Carminati, E., 2014. Slab–mantle flow interaction: influence on subduction dynamics and duration, *Terra Nova*, **26**(4), 265–272.

Roecker, S. & Russo, R., 2010. RAMP response for 2010 earthquake.

Rosenbaum, G., Giles, D., Saxon, M., Betts, P. G., Weinberg, R. F., & Duboz, C., 2005. Subduction of the Nazca Ridge and the Inca Plateau: Insights into the formation of ore deposits in Peru, *Earth and Planetary Science Letters*, **239**(1-2), 18–32.

Ruan, Y., Lei, W., Modrak, R., Örsvuran, R., Bozdağ, E., & Tromp, J., 2019. Balancing unevenly distributed data in seismic tomography: A global adjoint tomography example, *Geophysical Journal International*, **219**(2), 1225–1236.

Sager, K., Boehm, C., Ermert, L., Krischer, L., & Fichtner, A., 2020. Global-scale full-waveform ambient noise inversion, *Journal of Geophysical Research: Solid Earth*, **125**(4), e2019JB018644.

Salazar, P., Wigger, P., Bloch, W., Asch, G., Shapiro, S., & Kummerow, J., 2013. MEJIPE, GFZ Data Services, Other/Seismic Network.

Sánchez, M. A., García, H. P., Acosta, G., Gianni, G. M., Gonzalez, M. A., Ariza, J. P., Martinez, M. P., & Folguera, A., 2019. Thermal and lithospheric structure of the Chilean-Pampean flat-slab from gravity and magnetic data, in *Andean Tectonics*, pp. 487–507, Elsevier.

Sandvol, E. & Brown, L., 2007. SLIP—Seismic Lithospheric Imaging of the Puna Plateau.

Sandwell, D. T., Müller, R. D., Smith, W. H. F., Garcia, E., & Francis, R., 2014. New global marine gravity model from CryoSat-2 and Jason-1 reveals buried tectonic structure, *Science*, **346**(6205), 65–67.

Schepers, G., Van Hinsbergen, D. J., Spakman, W., Kosters, M. E., Boschman, L. M., & McQuarrie, N., 2017. South-American plate advance and forced Andean trench retreat as drivers for transient flat subduction episodes, *Nature Communications*, **8**(0316), 1–9.

Schilling, F. & Partzsch, G., 2001. Quantifying partial melt fraction in the crust beneath the central Andes and the Tibetan Plateau, *Physics and Chemistry of the Earth, Part A: Solid Earth and Geodesy*, **26**(4-5), 239–246.

Schilling, F. R., Trumbull, R. B., Brasse, H., Haberland, C., Asch, G., Bruhn, D., Mai, K., Haak, V., Giese, P., Muñoz, M., et al., 2006. Partial melting in the Central Andean crust: a review of geophysical, petrophysical, and petrologic evidence, *The Andes*, pp. 459–474.

Schorlemmer, D., Euchner, F., Kästli, P., & Saul, J., 2011. Quakeml: status of the xml-based seismological data exchange format, *Annals of Geophysics*, **54**(1), 59–65.

Schurr, B. & Rietbrock, A., 2004. Deep seismic structure of the Atacama basin, northern Chile, *Geophysical Research Letters*, **31**(12).

Schurr, B., Asch, G., & Wigger, P., 1997. PUNA Project Western Argentina.

Schurr, B., Asch, G., Rietbrock, A., Trumbull, R., & Haberland, C., 2003. Complex patterns of fluid and melt transport in the central Andean subduction zone revealed by attenuation tomography, *Earth and Planetary Science Letters*, **215**(1-2), 105–119.

Schurr, B., Rietbrock, A., Asch, G., Kind, R., & Oncken, O., 2006. Evidence for lithospheric detachment in the central Andes from local earthquake tomography, *Tectonophysics*, **415**(1), 203 – 223.

Scire, A., Biryol, C. B., Zandt, G., & Beck, S., 2015a. Imaging the Nazca slab and surrounding mantle to 700 km depth beneath the central Andes (18 S to 28 S), *Geodynamics of a Cordilleran Orogenic System: The Central Andes of Argentina and Northern Chile: Geological Society of America Memoir*, **212**, 23–41.

Scire, A., Zandt, G., Beck, S., Long, M., Wagner, L., Minaya, E., & Tavera, H., 2015b. Imaging the transition from flat to normal subduction: variations in the structure of the Nazca slab and upper mantle under southern Peru and northwestern Bolivia, *Geophysical Journal International*, **204**(1), 457–479.

Scire, A., Zandt, G., Beck, S., Long, M., & Wagner, L., 2017. The deforming Nazca slab in the mantle transition zone and lower mantle: Constraints from teleseismic tomography on the deeply subducted slab between 6°S and 32°S, *Geosphere*, **13**(3), 665–680.

Seton, M., Whittaker, J. M., Wessel, P., Müller, R. D., DeMets, C., Merkouriev, S., Cande, S., Gaina, C., Eagles, G., Granot, R., et al., 2014. Community infrastructure and repository for marine magnetic identifications, *Geochemistry, Geophysics, Geosystems*, **15**(4), 1629–1641.

Sieminski, A., Liu, Q., Trampert, J., & Tromp, J., 2007. Finite-frequency sensitivity of surface waves to anisotropy based upon adjoint methods, *Geophysical Journal International*, **168**(3), 1153–1174.

Silver, P., Beck, S., & Wallace, T., 1994. Broadband study of the Altiplano and central Andes.

Simutė, S., Steptoe, H., Cobden, L., Gokhberg, A., & Fichtner, A., 2016. Full-waveform inversion of the Japanese Islands region, *Journal of Geophysical Research: Solid Earth*, **121**(5), 3722–3741.

Sippl, C., Schurr, B., Asch, G., & Kummerow, J., 2018. Seismicity structure of the northern Chile forearc from 100,000 double-difference relocated hypocenters, *Journal of Geophysical Research: Solid Earth*, **123**(5), 4063–4087.

Sippl, C., Moreno, M., & Benavente, R., 2021. Microseismicity appears to outline highly coupled regions on the central chile megathrust, *Journal of Geophysical Research: Solid Earth*, **126**(11), e2021JB022252.

Sobiesiak, M. & Schurr, B., 2007. Taskforce Tocopilla 2007.

Sobolev, S. V. & Babeyko, A. Y., 1994. Modeling of mineralogical composition, density and elastic wave velocities in anhydrous magmatic rocks, *Surveys in geophysics*, **15**(5), 515–544.

Sobolev, S. V. & Babeyko, A. Y., 2005. What drives orogeny in the Andes?, *Geology*, **33**(8), 617–620.

Sobolev, S. V., Petrunin, A., Garfunkel, Z., Babeyko, A. Y., Group, D., et al., 2005. Thermo-mechanical model of the Dead Sea Transform, *Earth and Planetary Science Letters*, **238**(1-2), 78–95.

Sobolev, S. V., Babeyko, A. Y., Koulakov, I., & Oncken, O., 2006. *Mechanism of the Andean Orogeny: Insight from Numerical Modeling*, pp. 513–535, Springer Berlin Heidelberg.

Spagnuolo, M. G., Litvak, V. D., Folguera, A., Bottesi, G., & Ramos, V. A., 2012. Neogene magmatic expansion and mountain building processes in the southern Central Andes, 36–37°S, Argentina, *Journal of Geodynamics*, **53**, 81–94.

Storch, I., Buske, S., Schmelzbach, C., & Wigger, P., 2016. Seismic imaging of a megathrust splay fault in the North Chilean subduction zone (Central Andes), *Tectonophysics*, **689**, 157 – 166.

Tao, K., Grand, S. P., & Niu, F., 2017. Full-waveform inversion of triplicated data using a normalized-correlation-coefficient-based misfit function, *Geophysical Journal International*, **210**(3), 1517–1524.

Tao, K., Grand, S. P., & Niu, F., 2018. Seismic Structure of the Upper Mantle Beneath Eastern Asia From Full Waveform Seismic Tomography, *Geochemistry, Geophysics, Geosystems*, **19**(8), 2732–2763.

Tape, C., 2009. *Seismic tomography of southern California using adjoint methods*, Ph.D. thesis, California Institute of Technology.

Tape, C., Liu, Q., Maggi, A., & Tromp, J., 2010. Seismic tomography of the southern California crust based on spectral-element and adjoint methods, *Geophysical Journal International*, **180**(1), 433–462.

Tarantola, A., 1988. Theoretical background for the inversion of seismic waveforms, including elasticity and attenuation, in *Scattering and attenuations of seismic waves, part i*, pp. 365–399, Springer.

Tarantola, A., 2005. *Inverse problem theory and methods for model parameter estimation*, SIAM.

Tassara, A., 2005. Interaction between the Nazca and South American plates and formation of the Altiplano-Puna plateau: Review of a flexural analysis along the Andean margin (15°-34°S), *Tectonophysics*, **399**, 39–57.

Tassara, A. & Echaurren, A., 2012. Anatomy of the Andean subduction zone: three-dimensional density model upgraded and compared against global-scale models, *Geophysical Journal International*, **189**(1), 161–168.

Tassara, A., Götze, H.-J., Schmidt, S., & Hackney, R., 2006. Three-dimensional density model of the Nazca plate and the Andean continental margin, *Journal of Geophysical Research: Solid Earth*, **111**(B9).

Thrastarson, S., van Driel, M., Krischer, L., Boehm, C., Afanasiev, M., van Herwaarden, D. P., & Fichtner, A., 2020. Accelerating numerical wave propagation by wavefield adapted meshes. Part II: full-waveform inversion, *Geophysical Journal International*, **221**(3), 1591–1604.

Thrastarson, S., van Herwaarden, D. P., Krischer, L., & Fichtner, A., 2021. LASIF: Large-scale Seismic Inversion Framework, an updated version.

Thurber, C., 2015. Laguna del Maule seismic imaging.

Tromp, J., Tape, C., & Liu, Q., 2005a. Seismic tomography, adjoint methods, time reversal and banana-doughnut kernels, *Geophysical Journal International*, **160**(1), 195–216.

Tromp, J., Tape, C., & Liu, Q., 2005b. Seismic tomography, adjoint methods, time reversal and banana-doughnut kernels, *Geophysical Journal International*, **160**(1), 195–216.

Tromp, J., Komatitsch, D., & Liu, Q., 2008. Spectral-element and adjoint methods in seismology, *Communications in Computational Physics*, **3**(1), 1–32.

Tunik, M., Folguera, A., Naipauer, M., Pimentel, M., & Ramos, V. A., 2010. Early uplift and orogenic deformation in the Neuquén Basin: Constraints on the Andean uplift from U–Pb and Hf isotopic data of detrital zircons, *Tectonophysics*, **489**(1), 258–273.

Universidad De Chile, 2013. Red Sismologica Nacional.

van Driel, M., Boehm, C., Krischer, L., & Afanasiev, M., 2020. Accelerating numerical wave propagation using wavefield adapted meshes. Part I: forward and adjoint modelling, *Geophysical Journal International*, **221**(3), 1580–1590.

van Herwaarden, D. P., Afanasiev, M., Thrastarson, S., & Fichtner, A., 2021. Evolutionary full-waveform inversion, *Geophysical Journal International*, **224**(1), 306–311.

van Herwaarden, D. P., Boehm, C., Afanasiev, M., Thrastarson, S., Krischer, L., Trampert, J., & Fichtner, A., 2020. Accelerated full-waveform inversion using dynamic mini-batches, *Geophysical Journal International*, **221**(2), 1427–1438.

Venzke, E., 2013. Global volcanism program, *Volcanoes of the World*, **4**, 1.

Victor, P., Oncken, O., & Glodny, J., 2004. Uplift of the western Altiplano plateau: Evidence from the Precordillera between 20° and 21°S (northern Chile), *Tectonics*, **23**(4).

Vilotte, J. P. & RESIF, 2011. Seismic network XS: CHILE MAULE aftershock temporary experiment (RESIF-SISMOB).

Virieux, J., 1984. Sh-wave propagation in heterogeneous media: Velocity-stress finite-difference method, *Geophysics*, **49**(11), 1933–1942.

Virieux, J., 1986. P-sv wave propagation in heterogeneous media: Velocity-stress finite-difference method, *Geophysics*, **51**(4), 889–901.

Wada, I. & Wang, K., 2009. Common depth of slab-mantle decoupling: Reconciling diversity and uniformity of subduction zones, *Geochemistry, Geophysics, Geosystems*, **10**(10).

Wagner, L., Beck, S., & Long, M., 2010. Peru lithosphere and slab experiment.

Wagner, L., Caddick, M., Kumar, A., Beck, S., & Long, M., 2020. Effects of oceanic crustal thickness on intermediate depth seismicity, *Frontiers in Earth Science*, **8**(244).

Wagner, L. S., Beck, S., & Zandt, G., 2005. Upper mantle structure in the south central Chilean subduction zone (30° to 36° S), *Journal of Geophysical Research: Solid Earth*, **110**(B1).

Waite, G. P., 2010. An Integrated Analysis of Low-Frequency Seismicity at Villarrica Volcano, Chile.

Wang, H. & Currie, C. A., 2015. Magmatic expressions of continental lithosphere removal, *Journal of Geophysical Research: Solid Earth*, **120**(10), 7239–7260.

Wang, K., Yang, Y., Basini, P., Tong, P., Tape, C., & Liu, Q., 2018. Refined crustal and uppermost mantle structure of southern California by ambient noise adjoint tomography, *Geophysical Journal International*, **215**(2), 844–863.

Ward, K. M., Porter, R. C., Zandt, G., Beck, S. L., Wagner, L. S., Minaya, E., & Tavera, H., 2013. Ambient noise tomography across the Central Andes, *Geophysical Journal International*, **194**(3), 1559–1573.

Ward, K. M., Zandt, G., Beck, S. L., Christensen, D. H., & McFarlin, H., 2014. Seismic imaging of the magmatic underpinnings beneath the Altiplano-Puna volcanic complex from the joint inversion of surface wave dispersion and receiver functions, *Earth and Planetary Science Letters*, **404**, 43 – 53.

Ward, K. M., Zandt, G., Beck, S. L., Wagner, L. S., & Tavera, H., 2016. Lithospheric structure beneath the northern Central Andean Plateau from the joint inversion of ambient noise and earthquake-generated surface waves, *Journal of Geophysical Research: Solid Earth*, **121**(11), 8217–8238.

Ward, K. M., Delph, J. R., Zandt, G., Beck, S. L., & Ducea, M. N., 2017. Magmatic evolution of a Cordilleran flare-up and its role in the creation of silicic crust, *Scientific Reports*, **7**(1), 1–8.

West, M. & Christensen, D., 2010. Investigating the relationship between pluton growth and volcanism at two active intrusions in the central Andes.

Whitman, D., Isacks, B., & Kay, S., 1996. Lithospheric structure and along-strike segmentation of the Central Andean Plateau: seismic Q, magmatism, flexure, topography and tectonics, *Tectonophysics*, **259**(1), 29 – 40.

Wigger, P., Salazar, P., Kummerow, J., Bloch, W., Asch, G., & Shapiro, S., 2016. West–Fissure- and Atacama-Fault Seismic Network (2005/2012).

Wörner, G., Moorbath, S., & Harmon, R. S., 1992. Andean Cenozoic volcanic centers reflect basement isotopic domains, *Geology*, **20**(12), 1103–1106.

Wörner, G., Hammerschmidt, K., Henjes-Kunst, F., Lezaun, J., & Wilke, H., 2000. Geochronology (40Ar/39Ar, K-Ar and He-exposure ages) of Cenozoic magmatic rocks from northern Chile (18-22 S): implications for magmatism and tectonic evolution of the central Andes, *Revista geológica de Chile*, **27**(2), 205–240.

Wright, N. M., Seton, M., Williams, S. E., & Müller, R. D., 2016. The late cretaceous to recent tectonic history of the pacific ocean basin, *Earth-Science Reviews*, **154**, 138–173.

Wölbern, I., Heit, B., Yuan, X., Asch, G., Kind, R., Viramonte, J., Tawackoli, S., & Wilke, H., 2009. Receiver function images from the Moho and the slab beneath the Altiplano and Puna plateaus in the Central Andes, *Geophysical Journal International*, **177**(1), 296–308.

Xiao, Z., Fuji, N., Iidaka, T., Gao, Y., Sun, X., & Liu, Q., 2020. Seismic Structure Beneath the Tibetan Plateau From Iterative Finite-Frequency Tomography Based on ChinArray: New Insights Into the Indo-Asian Collision, *Journal of Geophysical Research: Solid Earth*, **125**(2).

Yáñez, G. A., Ranero, C. R., Von Huene, R., & Díaz, J., 2001. Magnetic anomaly interpretation across the southern central Andes (32°-34°S): The role of the Juan Fernández Ridge in the late Tertiary evolution of the margin, *Journal of Geophysical Research: Solid Earth*, **106**(B4), 6325–6345.

Yoon, M., Buske, S., Shapiro, S., & Wigger, P., 2009. Reflection Image Spectroscopy across the Andean subduction zone, *Tectonophysics*, **472**(1), 51 – 61.

Yuan, X., Sobolev, S. V., Kind, R., Oncken, O., Bock, G., Asch, G., Schurr, B., Graeber, F., Rudloff, A., Hanka, W., Wylegalla, K., Tibi, R., Haberland, C., Rietbrock, A., Giese, P., Wigger, P., Röwer, P., Zandt, G., Beck, S., Wallace, T., Pardo, M., & Comte, D., 2000. Subduction and collision processes in the Central Andes constrained by converted seismic phases, *Nature*, **408**(6815), 958–961.

Yuan, X., Sobolev, S., & Kind, R., 2002. Moho topography in the central Andes and its geodynamic implications, *Earth and Planetary Science Letters*, **199**(3), 389 – 402.

Yuan, Y. O., Bozdağ, E., Ciardelli, C., Gao, F., & Simons, F. J., 2020. The exponentiated phase measurement, and objective-function hybridization for adjoint waveform tomography, *Geophysical Journal International*, **221**(2), 1145–1164.

Yáñez, G., Cembrano, J., Pardo, M., Ranero, C., & Selles, D., 2002. The Challenger–Juan Fernández–Maipo major tectonic transition of the Nazca–Andean subduction system at 33°–34°S: geodynamic evidence and implications, *Journal of South American Earth Sciences*, **15**(1), 23–38, Flat-Slab Subduction in the Andes.

Zandt, G., 1996. Altiplano-Puna Volcanic Complex Seismic Experiment.

Zang, N., Zhang, W., & Chen, X., 2021. An overset-grid finite-difference algorithm for simulating elastic wave propagation in media with complex free-surface topography, *GEOPHYSICS*, **86**(4), T277–T292.

Zhang, W., Shen, Y., & Zhao, L., 2012a. Three-dimensional anisotropic seismic wave modelling in spherical coordinates by a collocated-grid finite-difference method, *Geophysical Journal International*, **188**(3), 1359–1381.

Zhang, W., Shen, Y., & Zhao, L., 2012b. Three-dimensional anisotropic seismic wave modelling in spherical coordinates by a collocated-grid finite-difference method, *Geophysical Journal International*, **188**(3), 1359–1381.

Zhang, Z., Shen, Y., & Zhao, L., 2007. Finite-frequency sensitivity kernels for head waves, *Geophysical Journal International*, **171**(2), 847–856.

Zhao, L. & Jordan, T. H., 2006. Structural sensitivities of finite-frequency seismic waves: a full-wave approach, *Geophysical Journal International*, **165**(3), 981–990.

Zhao, L., Jordan, T. H., & Chapman, C. H., 2000. Three-dimensional Fréchet differential kernels for seismic delay times, *Geophysical Journal International*, **141**(3), 558–576.

Zhao, L., Jordan, T. H., Olsen, K. B., & Chen, P., 2005. Fréchet kernels for imaging regional earth structure based on three-dimensional reference models, *Bulletin of the Seismological Society of America*, **95**(6), 2066–2080.

Zhou, Y., Dahlen, F. A., & Nolet, G., 2004. Three-dimensional sensitivity kernels for surface wave observables, *Geophysical Journal International*, **158**(1), 142–168.

Zhou, Y., Nolet, G., Dahlen, F. A., & Laske, G., 2006. Global upper-mantle structure from finite-frequency surface-wave tomography, *Journal of Geophysical Research: Solid Earth*, **111**(B4).

Zhu, H., Bozdăg, E., & Tromp, J., 2015. Seismic structure of the European upper mantle based on adjoint tomography, *Geophysical Journal International*, **201**(1), 18–52.

Zhu, H., Komatitsch, D., & Tromp, J., 2017. Radial anisotropy of the North American upper mantle based on adjoint tomography with USArray, *Geophysical Journal International*, **211**(1), 349–377.

Appendix A

Supplementary material for chapter 4

A.1 Optimization Scheme

A.1.1 Conjugate-Gradients (CG)

We take advantage of the CG variant introduced by Fletcher & Reeves (1964), which has previously been applied to FWI by Tao et al. (2018). The specific formulation of F-R CG in our study follows as below:

$$\mathbf{z}_i = -\mathbf{G}\mathbf{g}_i + \gamma \mathbf{z}_{i-1} \tag{A.1}$$

where $\mathbf{z}_i$ and $\mathbf{z}_{i-1}$ denote the search directions in the ith and $i-1$th iterations, respectively. $\mathbf{g}_i$ is the gradient from the adjoint simulations based on the misfit functions in the ith iteration, $\mathbf{G}$ denotes the smoothing function which contains local (smoothing around the earthquake sources) and global Gaussian smoothing to suppress the local artifacts and stabilize the inversion process. Practically and specifically, for the individual gradient from every event, we use a limited width for the Gaussian smoothing (around 80 km) to damp out artifacts around the sources before summation over all events; we then clip extreme values of the summed gradients in the shallow crust in order to reduce the artefacts beneath the receivers. The summed gradient is then smoothed again, where the Gaussian smoothing width σ is decreased systematically with each stage of the multi-frequency inversion. Specifically, we set σ equal to one third to one half of the minimum wavelength in the current period. Meanwhile, $\gamma = \frac{(\mathbf{G}\mathbf{g}_i - \mathbf{G}\mathbf{g}_{i-1})^T \mathbf{G}\mathbf{g}_i}{(\mathbf{G}\mathbf{g}_i - \mathbf{G}\mathbf{g}_{i-1})^T \mathbf{z}_{i-1}}$ is the CG update parameter, which is reset to zero when it becomes negative Tao et al. (2018). The step length for the model updates is determined using a quadratic interpolation among the three test models, which are updated from the current model with step lengths with 5%, 10% and 15% of the maximum absolute amplitude of the search direction $\mathbf{z}_i$.

A.1.2 L-BFGS

L-BFGS is a quasi-Newton algorithm that contains the curvature information based on the inverse Hessian approximations derived from the gradients and models of the previous iterations and therefore can accelerate convergence. L-BFGS avoids the storage of the very large Hessian matrix and only requires a few vector products. We adopt the methodology from Krischer et al. (2018b), which is different from the classical algorithm dating back to Liu & Nocedal (1989) by incorporating the Gaussian smoothing operator directly into L-BFGS.

Based on the changes of the gradients defined by $\mathbf{r}_k = \mathbf{G}_{1/2}\mathbf{g}_{k+1} - \mathbf{G}_{1/2}\mathbf{g}_k$ and the model variations $\mathbf{s}_k = \mathbf{m}_{k+1} - \mathbf{m}_k$, the L-BFGS is formulated and driven as an iterative algorithm without forming the inverse Hessian approximation directly. The specific algorithm is shown as Algorithm 2.

m in the L-BFGS algorithm indicates the number of past model updates stored. In practice, history of the past 6 iterations would be used for every inversion stage once m exceeds 6. The negative direction

Algorithm 2 L-BFGS algorithm

$\mathbf{q} \leftarrow \mathbf{G}_{1/2}\mathbf{g}_k$
for $i = k-1, ..., k-m$ **do**
  $\gamma_i \leftarrow \frac{1}{\mathbf{r}_i^T \mathbf{s}_i}$; $\alpha_i \leftarrow \gamma_i \mathbf{s}_i^T \mathbf{q}$; $\mathbf{q} \leftarrow \mathbf{q} - \alpha_i \mathbf{r}_i$
end for
$\eta_k \leftarrow (\mathbf{s}_{k-1}^T \mathbf{r}_{k-1})/(\mathbf{r}_{k-1}^T \mathbf{r}_{k-1})$
$\mathbf{z} \leftarrow \eta_k \mathbf{q}$
for $i = k-m, ..., k-1$ **do**
  $\beta_i \leftarrow \gamma_i \mathbf{r}_i^T \mathbf{z}$; $\mathbf{z} \leftarrow \mathbf{z} + \mathbf{s}_i(\alpha_i - \beta_i)$
end for

for the model updates would turn to be $\mathbf{G}_{1/2}\mathbf{z}$=$\mathbf{G}_{1/2}\mathbf{H}_k^{-1}\mathbf{G}_{1/2}\mathbf{g}_k$, where $\mathbf{G}$ is still the smoothing function which is split into $\mathbf{G} = \mathbf{G}_{1/2}\mathbf{G}_{1/2}^T$. So the model update would be:

$$\mathbf{m}_{k+1} = \mathbf{m}_k - \varphi \mathbf{G}_{1/2}\mathbf{z} \tag{A.2}$$

where φ represents the suitable step length. In our implementation, we estimate the optimal step length through the quadratic interpolation based on the waveform misfits of three updated test models with φ=20%, 50% and 80%. In practice, instead of calculating the full misfits for the step length tests, we extract 6 - 10 events with the gradient angle smaller than $1/3\pi$ between the individual event gradient and the summed gradient van Herwaarden et al. (2020) from the current model. The number of the seismic stations for these events should be larger than the average (40 stations) to be representative of the summed gradient. Through this way, we could substantially lower the computational burden for the step length tests and thus improve the efficiency of the inversion.

A.2 Partial melt estimation

Quantifying the fraction of partial melt within the crust and uppermost mantle from the seismic velocity is difficult due to the dependence of seismic velocities on many variables, including temperature, pressure, composition, melt fraction and fluid concentration. Thus providing a precise estimation of the partial melt fraction based on shear wave velocities alone is almost impossible. Nevertheless, we can get an idea of the along-strike variations in melt fraction by applying uniform assumptions on other needed parameters, even if absolute estimates are subject to large uncertainties. In order to compare our estimates to previous works, for the middle crust we estimate the partial melt fraction using the relationship between the melt/fluid filled porosity of a granite composition and shear velocity Chu et al. (2010); Ward et al. (2014). The maximum inferred partial melt fraction is 22 % within the APMB beneath the APVC, similar to the results (25 %) from joint inversion of receiver function and surface wave Ward et al. (2014). Meanwhile, for the CGMB beneath the Cerro Galan, the partial melt within the middle crust is around 12 %, smaller than the previous estimation Delph et al. (2017) due to the different estimation method. Figure S15a shows a map view of the inferred partial melt fraction in the middle crust. For the crust-mantle transition zone (near depressed Moho) at 60 km, we calculate two alternative estimates based on different assumption about the composition Delph et al. (2017). Hydrated quartz composition (Figure S15b) gives relatively higher melt fraction values than olivine-basalts (Figure S15c). Thus the MASH zone possibly contains 3%-10 % partial melts beneath the Cerro Galan Delph et al. (2017). For the uppermost mantle (80 km), we estimate the partial melt using the Olivine-basalt composition. Within the WAZ (beneath the Pica Volcanic Gap, PVG) low but non-zero partial melt fractions are inferred within the crust and uppermost mantle (Figure S15).

A.3 Supplementary Figures

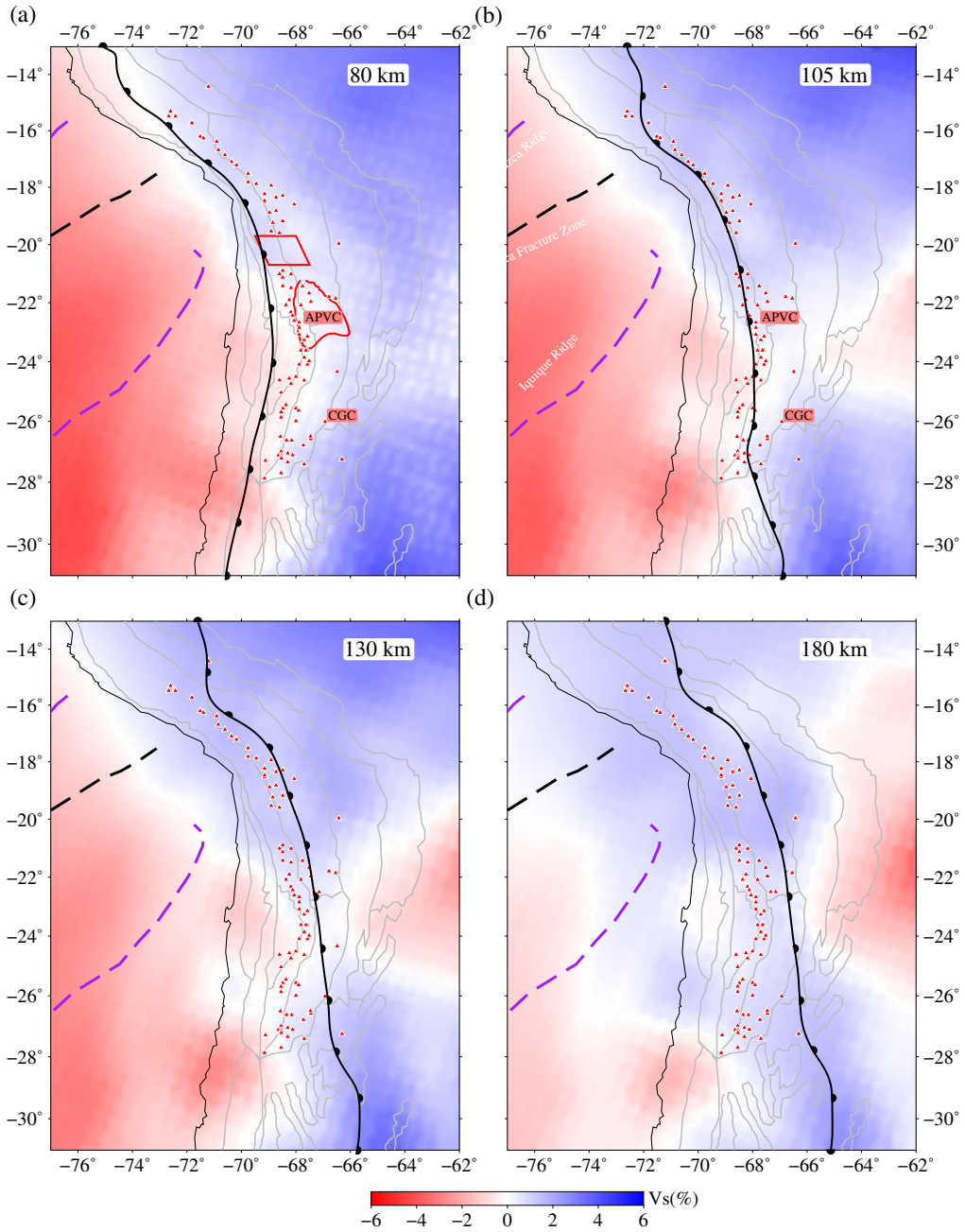

Fig. A.1: Isotropic V_S relative velocity horizontal slices for the upper mantle at 80 km (a), 105 km (b), 130 km(c) and 180 km (d) from the initial model. All velocity perturbations are relative to the depth-average 1D model of the CSEM mode (Figure 3 in main text).

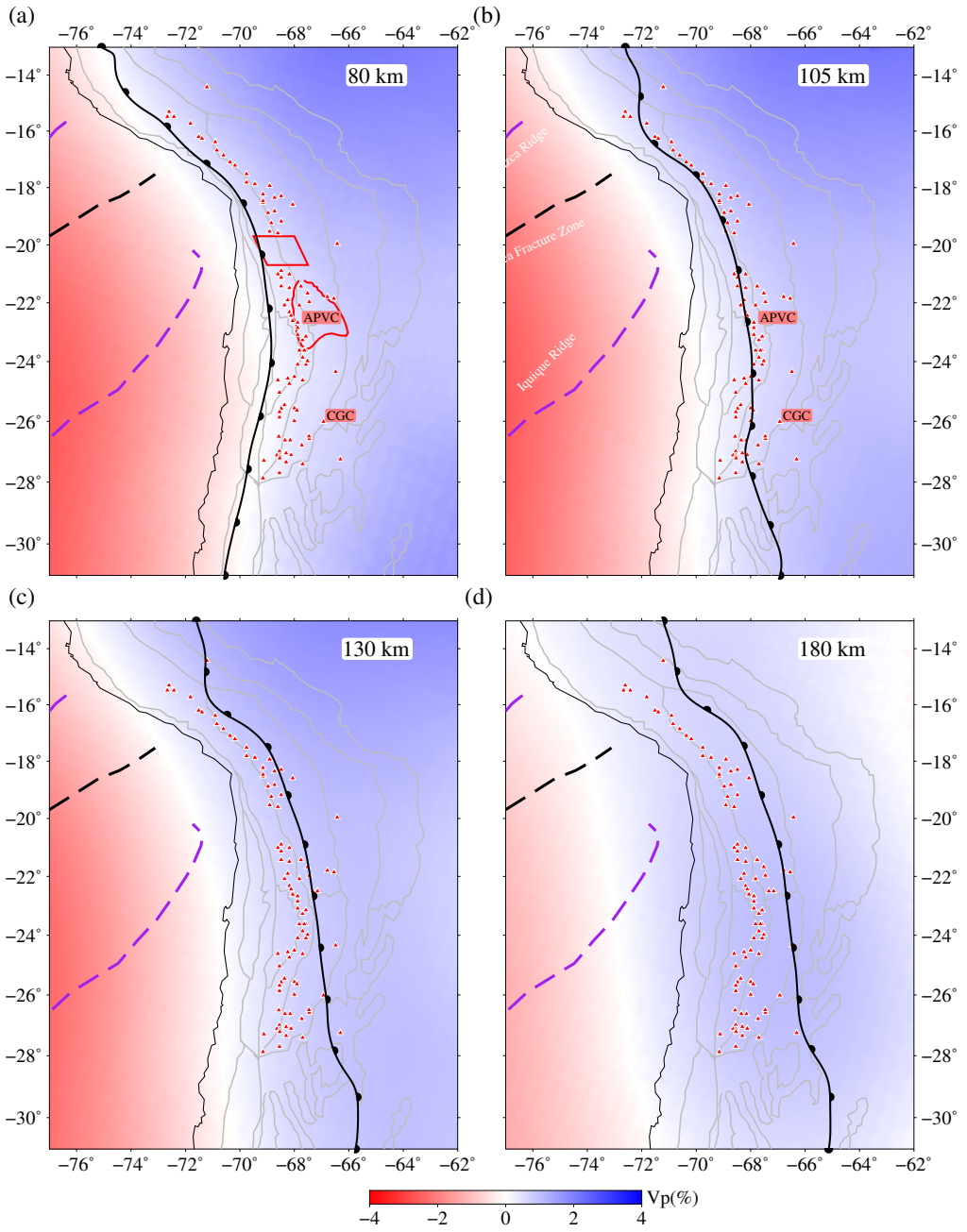

Fig. A.2: Isotropic V_P relative velocity horizontal slices for the upper mantle at 80 km (a), 105 km (b), 130 km(c) and 180 km (d) from the initial model. All velocity perturbations are relative to the depth-average 1D model of the CSEM mode (Figure 3 in main text).

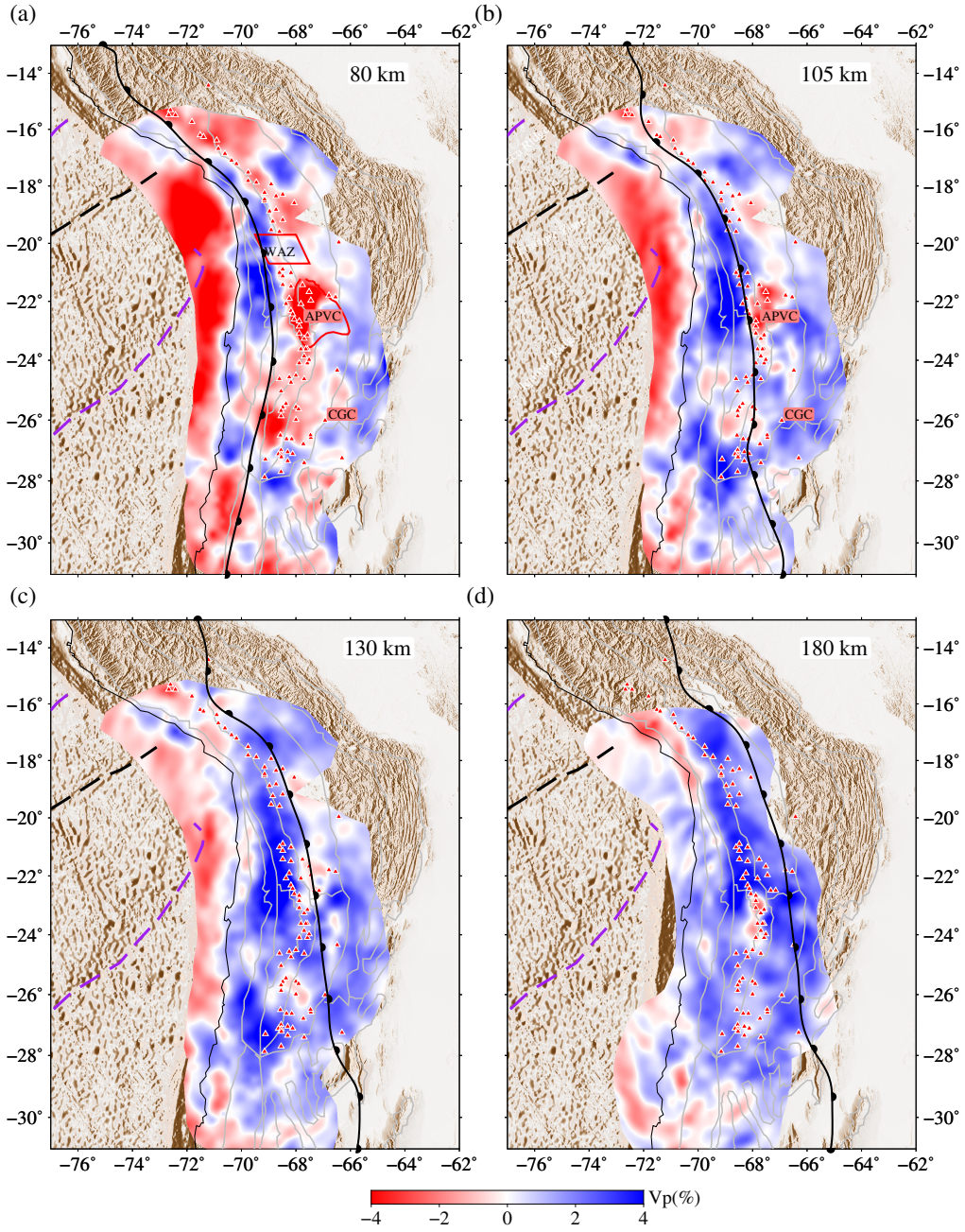

Fig. A.3: Isotropic V_P relative velocity horizontal slices for the upper mantle at 80 km (a), 105 km (b), 130 km(c) and 180 km (d) from the final model. All velocity perturbations are relative to the depth-average 1D model of the CSEM mode (Figure 3 in main text).

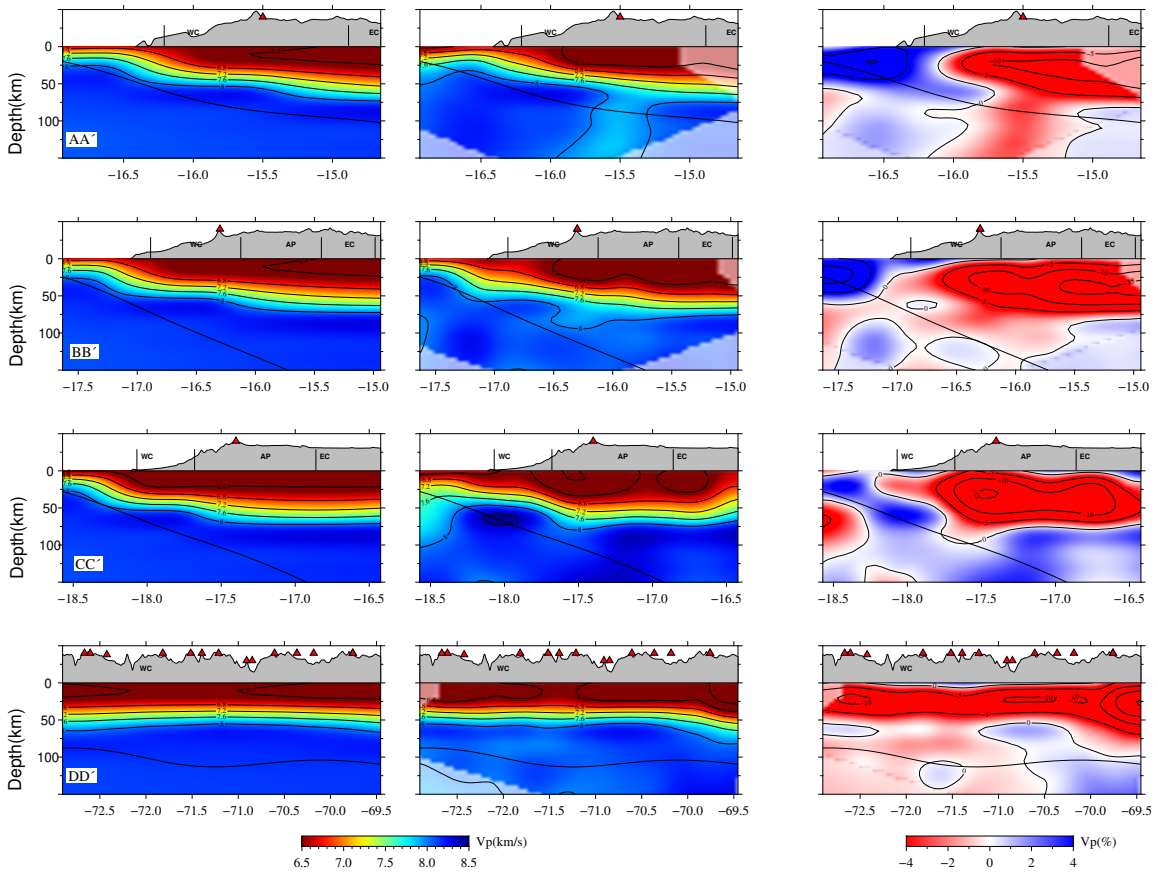

Fig. A.4: Cross sections of V_P for initial model and final model along AA'-DD'. The left panel: V_P cross sections of the initial model; middle: V_P cross sections of the final model; right: relative velocity of V_P cross sections of the final model. All velocity perturbations are relative to the depth-average 1D model of the CSEM mode (Figure 3 in main text).

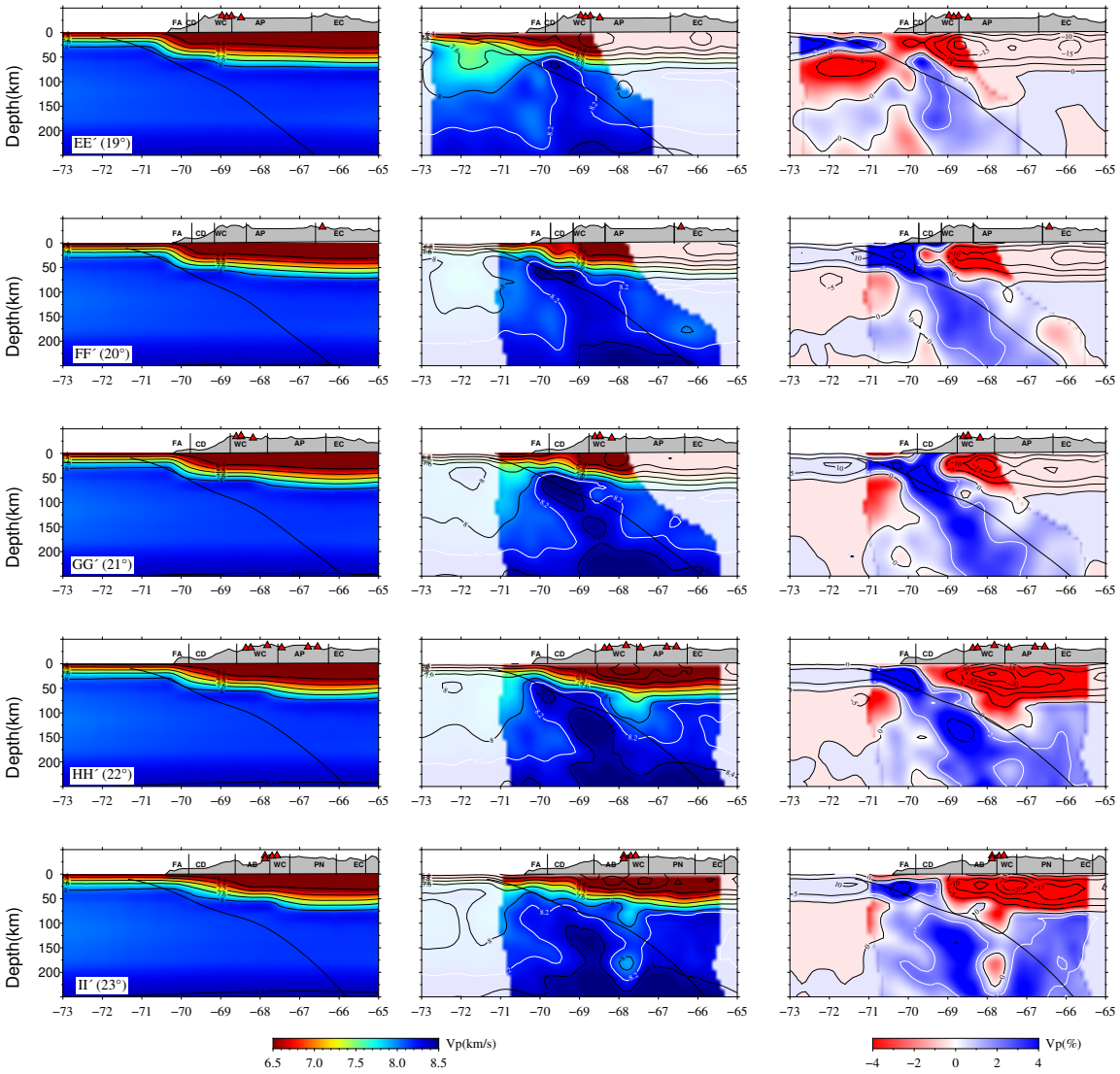

Fig. A.5: Cross sections of V_P for initial model and final model along EE'-II'. The left panel: V_P cross sections of the initial model; middle: V_P cross sections of the final model; right: relative velocity of V_P cross sections of the final model. All velocity perturbations are relative to the depth-average 1D model of the CSEM mode (Figure 3 in main text).

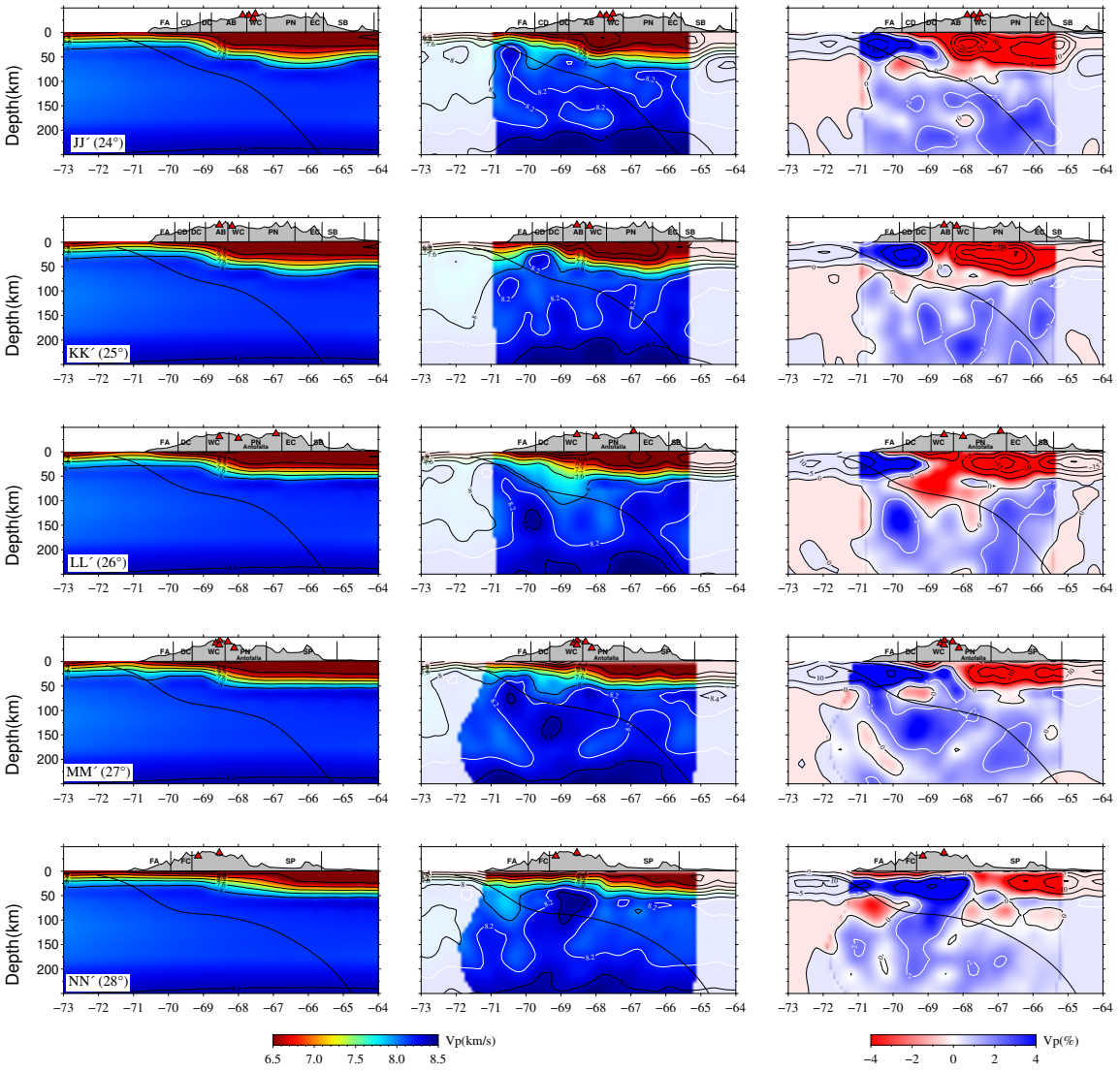

Fig. A.6: Cross sections of V_P for initial model and final model along JJ'-NN'. The left panel: V_P cross sections of the initial model; middle: V_P cross sections of the final model; right: relative velocity of V_P cross sections of the final model. All velocity perturbations are relative to the depth-average 1D model of the CSEM mode (Figure 3 in main text).

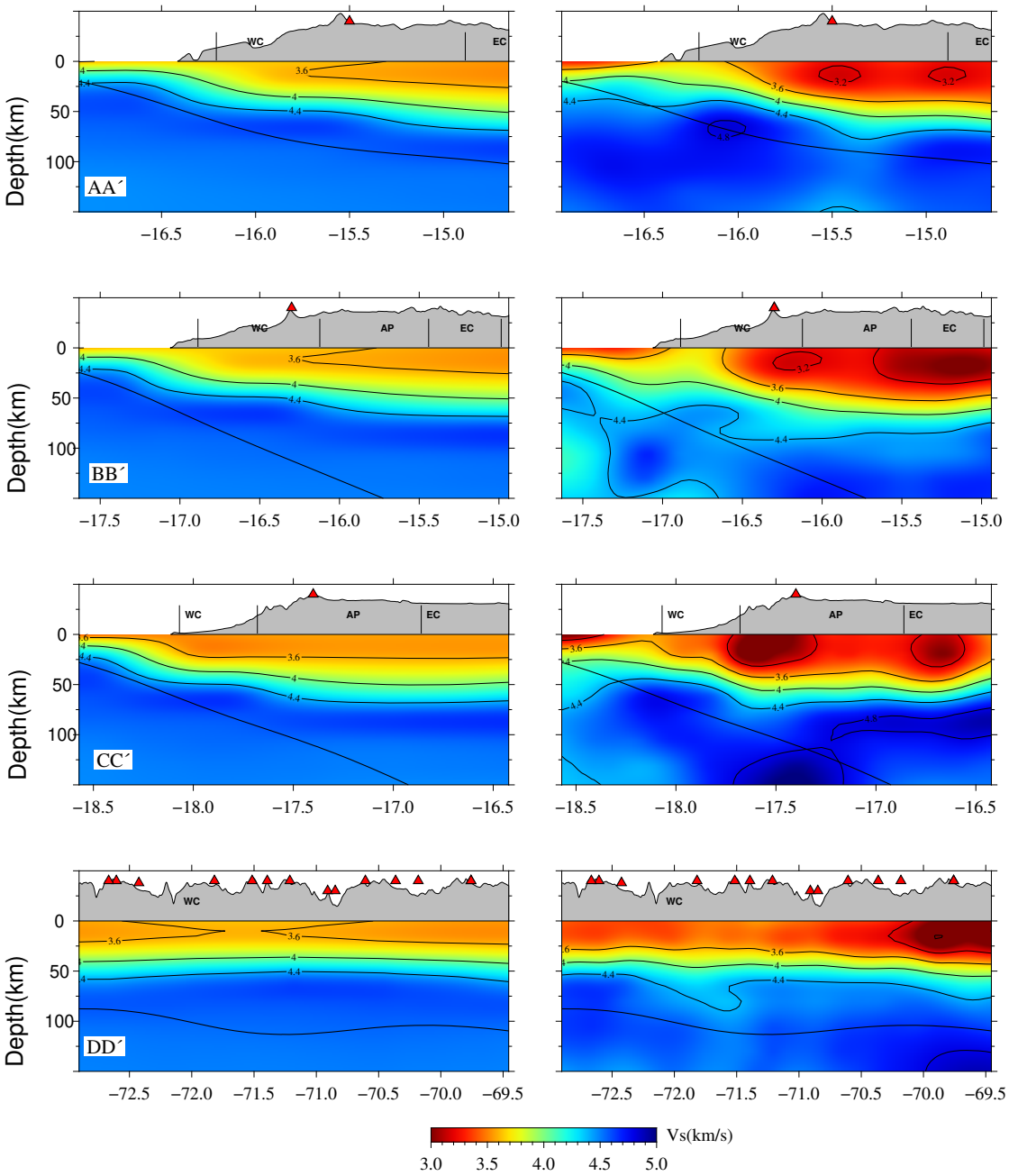

Fig. A.7: Cross sections of V_S for initial model and final model along AA'-DD'. The left panel: V_S cross sections of the initial model; right: V_S cross sections of the final model.

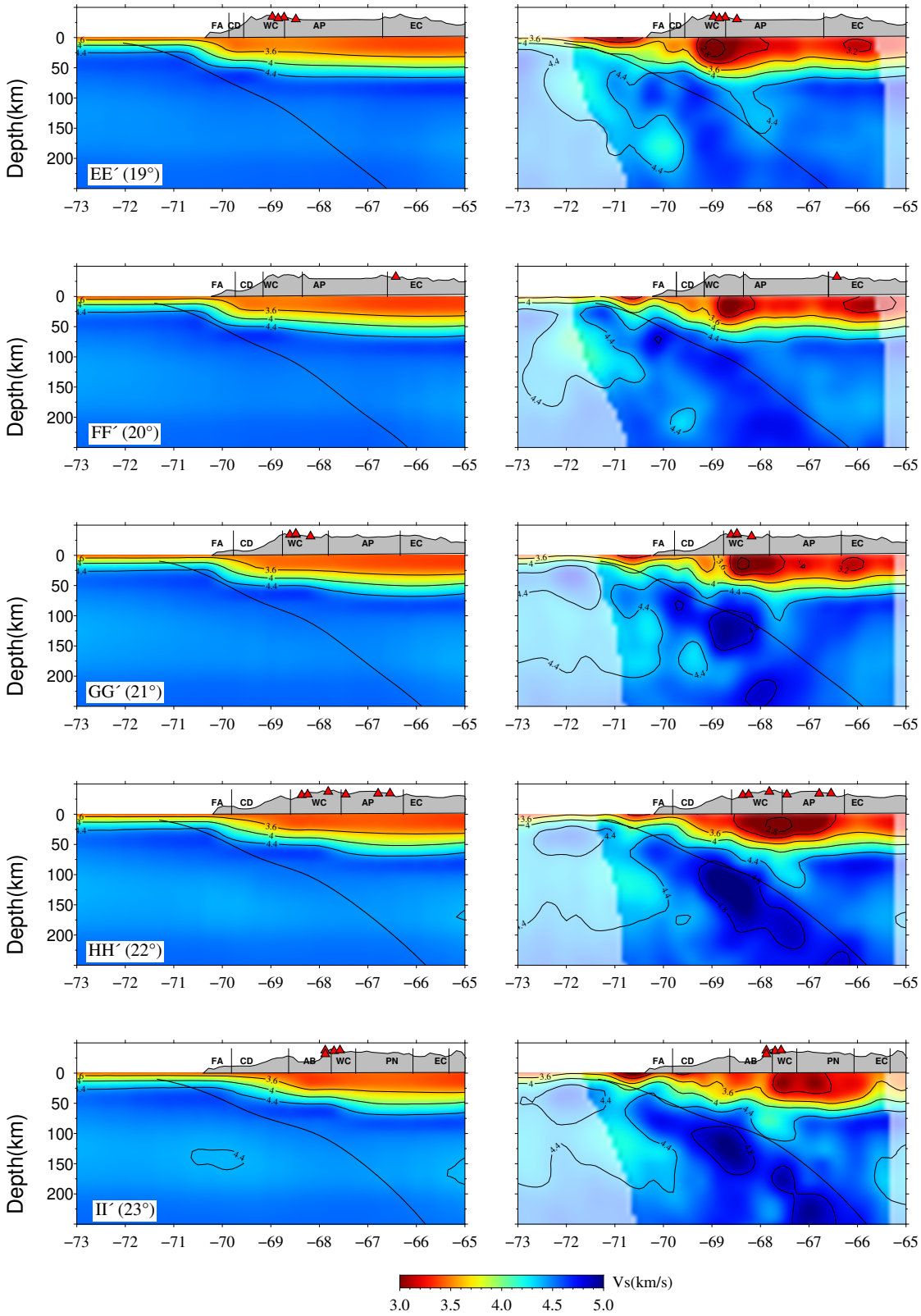

Fig. A.8: Cross sections of V_S for initial model and final model along EE'-II'. The left panel: V_S cross sections of the initial model; right: V_S cross sections of the final model.

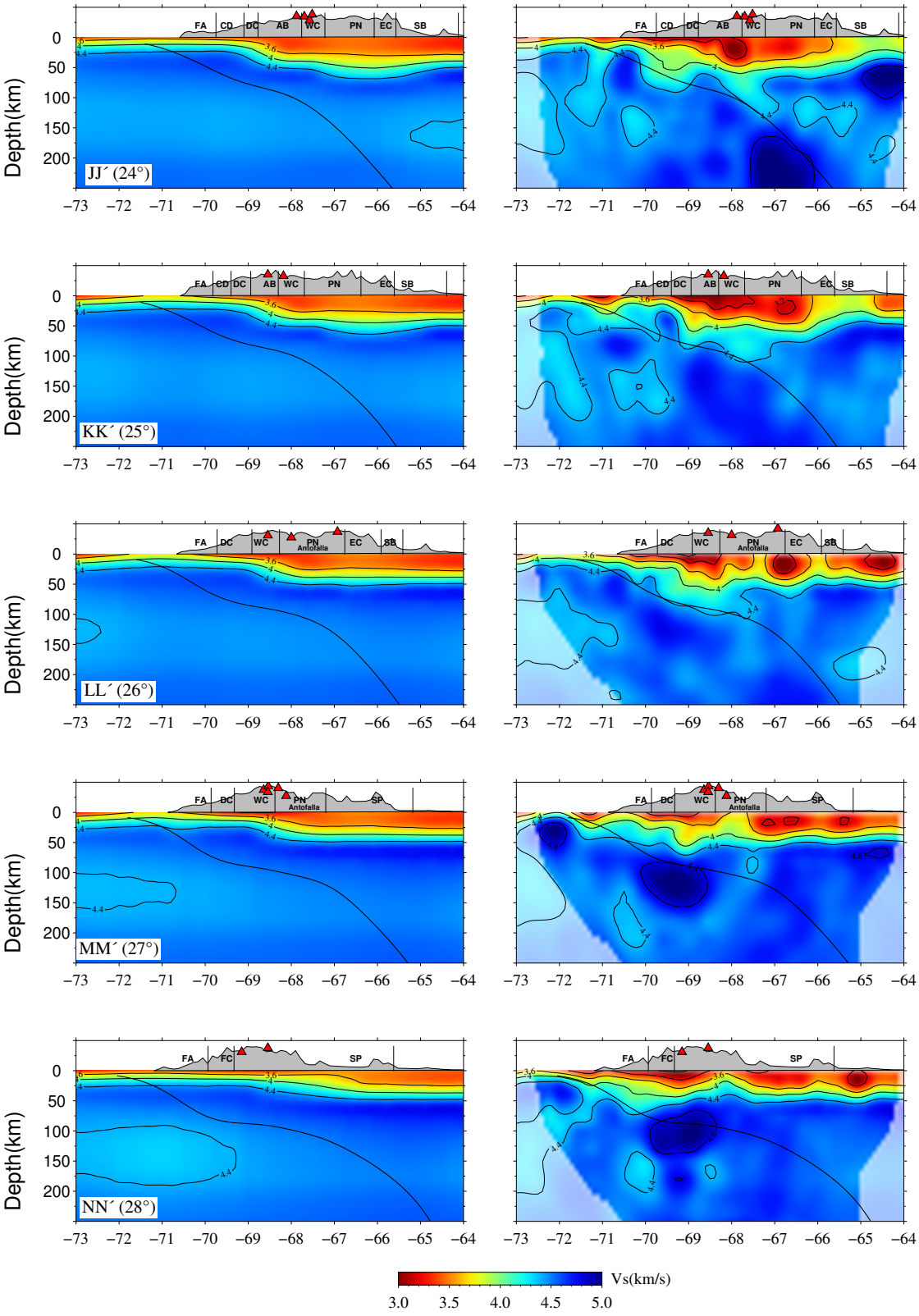

Fig. A.9: Cross sections of V_S for initial model and final model along JJ'-NN'. The left panel: V_S cross sections of the initial model; right: V_S cross sections of the final model.

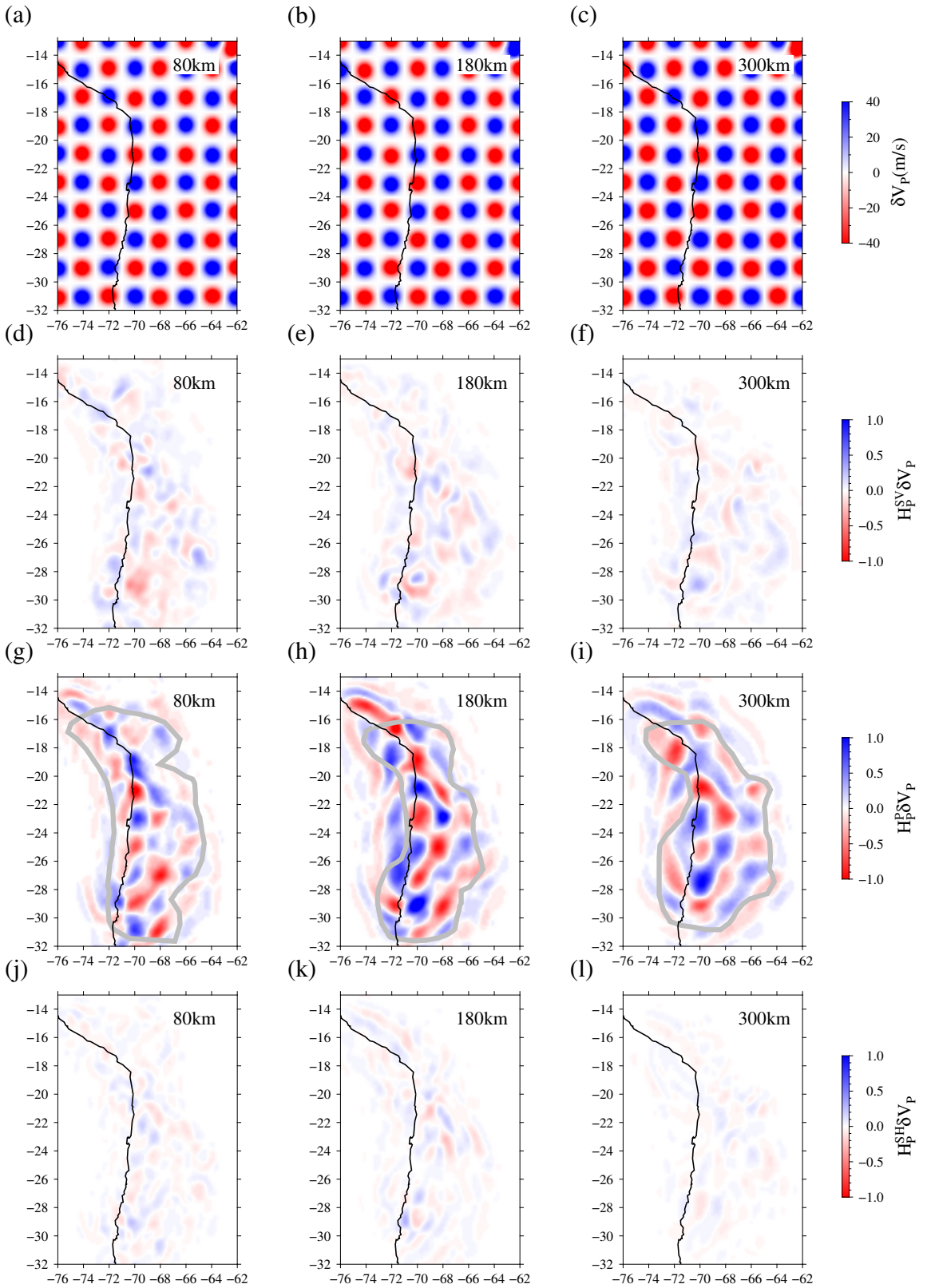

Fig. A.10: Point-spread function test respect to isotropic $\mathbf{V}_P$ perturbations ($\delta\mathbf{V}_P$). (a-c): horizontal slices of input 1% Gaussian $\mathbf{V}_P$ perturbations ($\delta\mathbf{V}_P$) with σ=40 km at 80 km, 180 km and 300 km depth in the upper mantle; (d-f): point-spread functions $\mathbf{H}_P^{SV}\delta\mathbf{V}_P$ with respect to isotropic V_P perturbations ($\delta\mathbf{V}_P$); (g-i): point-spread functions $\mathbf{H}_P^{P}\delta\mathbf{V}_P$; (j-l) point-spread functions $\mathbf{H}_P^{SH}\delta\mathbf{V}_P$; Gray thick lines denote the trust region for isotropic $\mathbf{V}_P$.

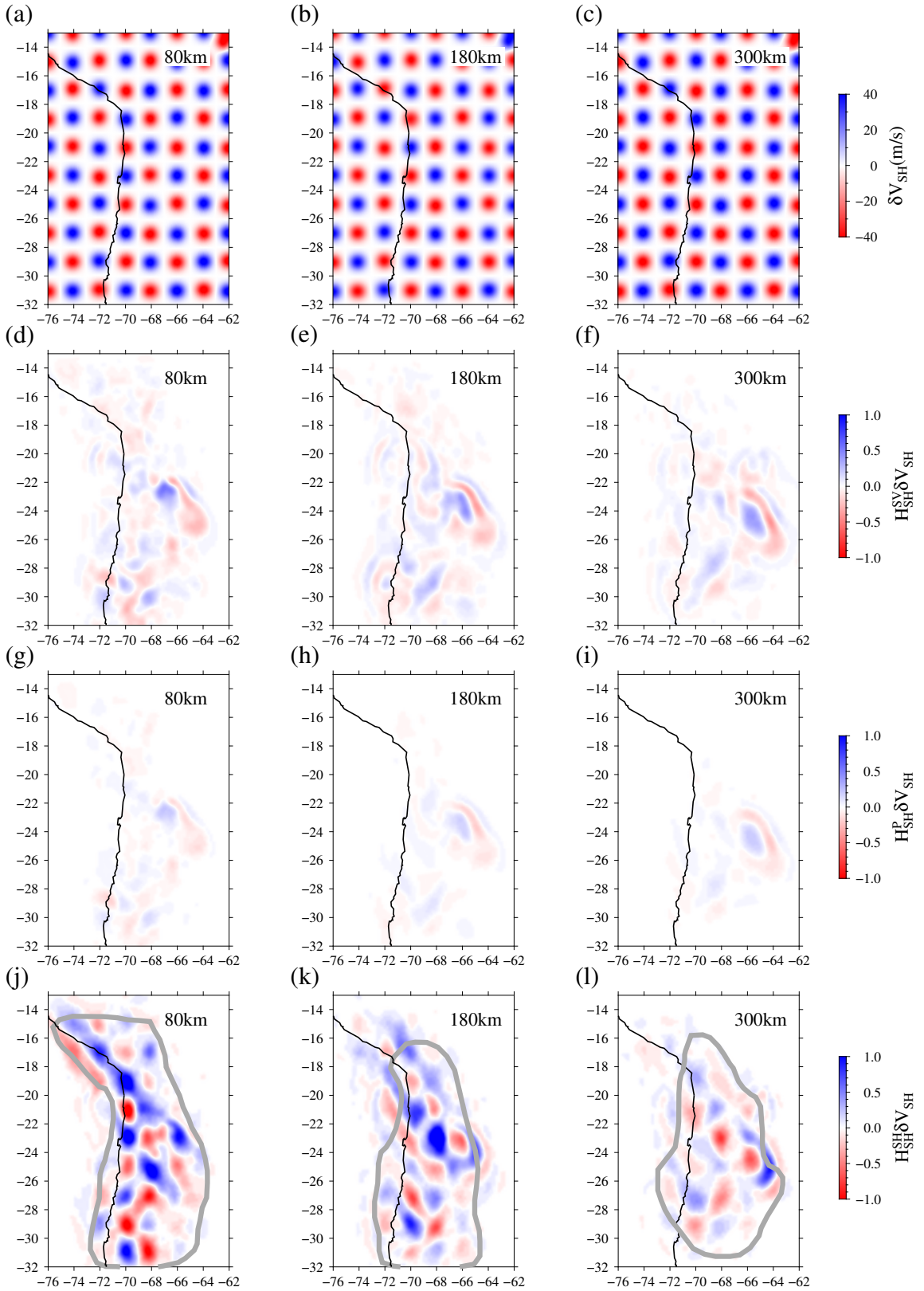

Fig. A.11: Point-spread function test respect to $\mathbf{V}_{SH}$ perturbations ($\delta\mathbf{V}_{SH}$). (a-c): horizontal slices of input 1% Gaussian $\mathbf{V}_{SH}$ perturbations ($\delta\mathbf{V}_{SH}$) with σ=40 km at 80 km, 180 km and 300 km depth in the upper mantle; (d-f): point-spread functions $\mathbf{H}^{SV}_{SH}\delta\mathbf{V}_{SH}$ with respect to isotropic $\mathbf{V}_{SH}$ perturbations ($\delta\mathbf{V}_{SH}$); (g-i): point-spread functions $\mathbf{H}^{P}_{SH}\delta\mathbf{V}_{SH}$; (j-l) point-spread functions $\mathbf{H}^{SH}_{SH}\delta\mathbf{V}_{SH}$; Gray thick lines denote the trust region for $\mathbf{V}_{SH}$.

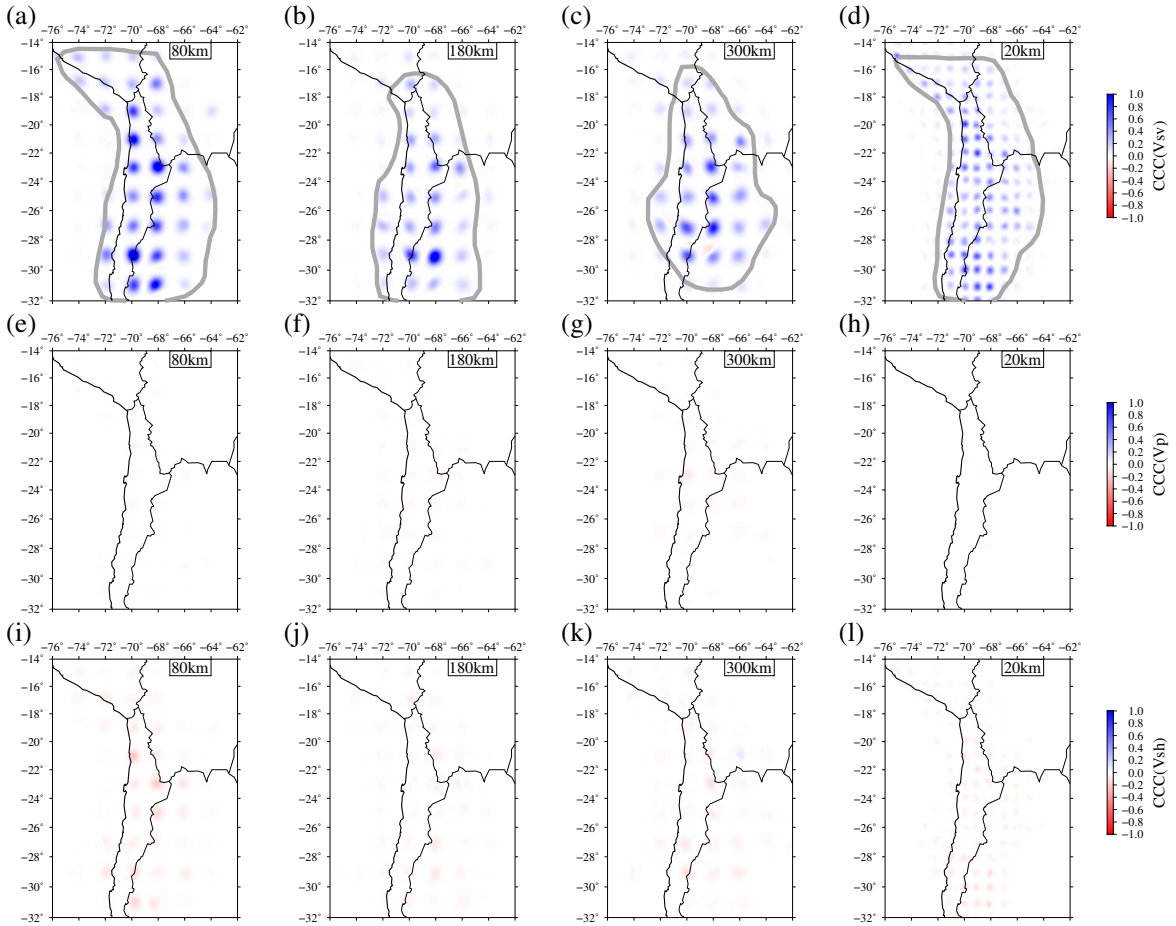

Fig. A.12: Normalised product between the $\delta\mathbf{V}_{SV}$ and point-spread functions $\mathbf{H}^{SV}_{SV}\delta\mathbf{V}_{SV}$ (a-d), $\mathbf{H}^{P}_{SV}\delta\mathbf{V}_{SV}$ (e-h) and $\mathbf{H}^{SH}_{SV}\delta\mathbf{V}_{SV}$ (i-l). All the results are normalised by the product of the maximum of $\delta\mathbf{V}_{SV}$ and the maximum of $\mathbf{H}^{SV}_{SV}\delta\mathbf{V}_{SV}$ for every depth level.

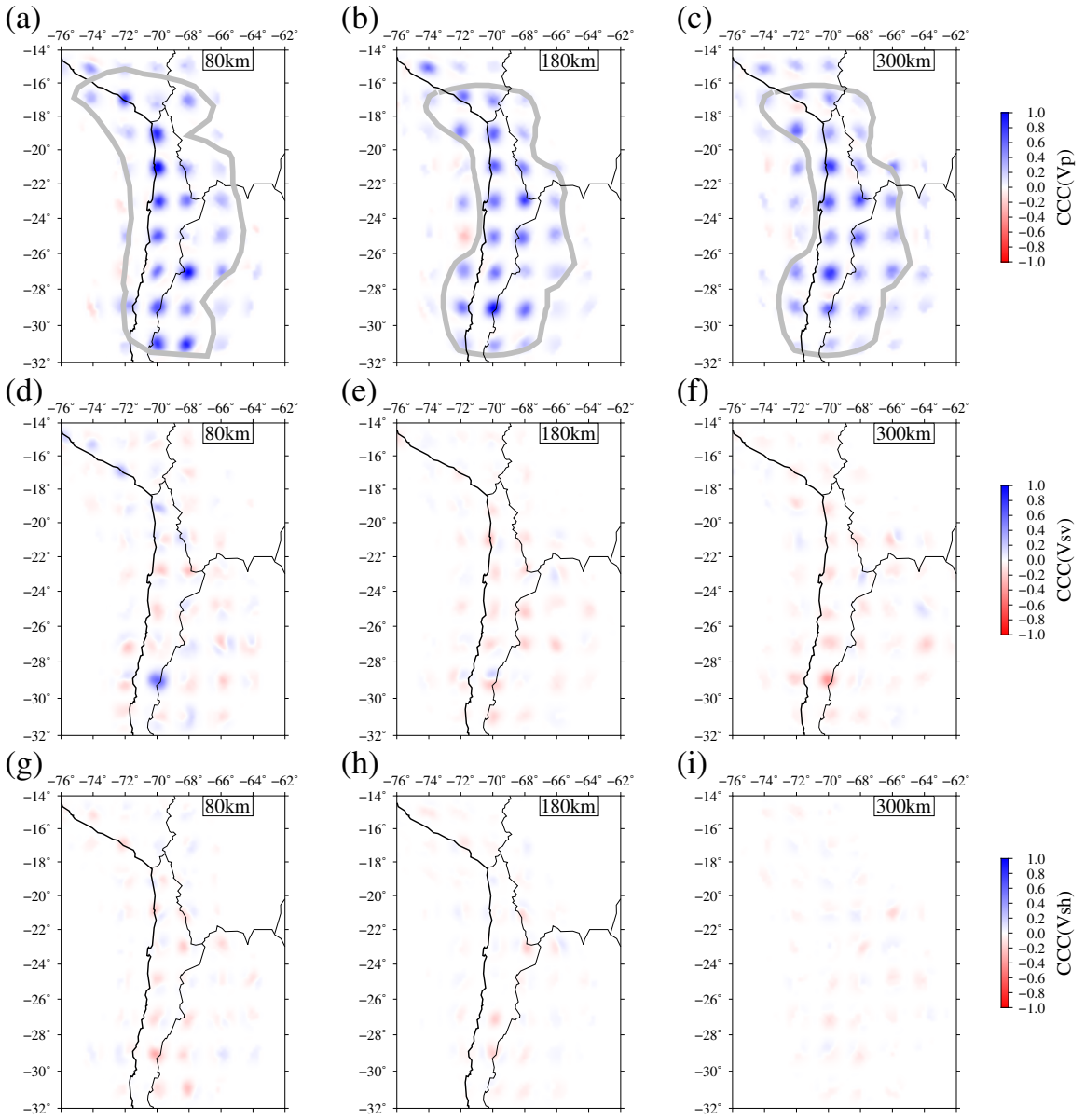

Fig. A.13: Normalised product between the $\delta\mathbf{V}_P$ and point-spread functions $\mathbf{H}_P^P\delta\mathbf{V}_P$ (a-c), $\mathbf{H}_P^{SV}\delta\mathbf{V}_P$ (d-f) and $\mathbf{H}_P^{SH}\delta\mathbf{V}_P$ (g-i). All the results are normalised by the product of the maximum of $\delta\mathbf{V}_P$ and the maximum of $\mathbf{H}_P^P\delta\mathbf{V}_P$ for every depth level.

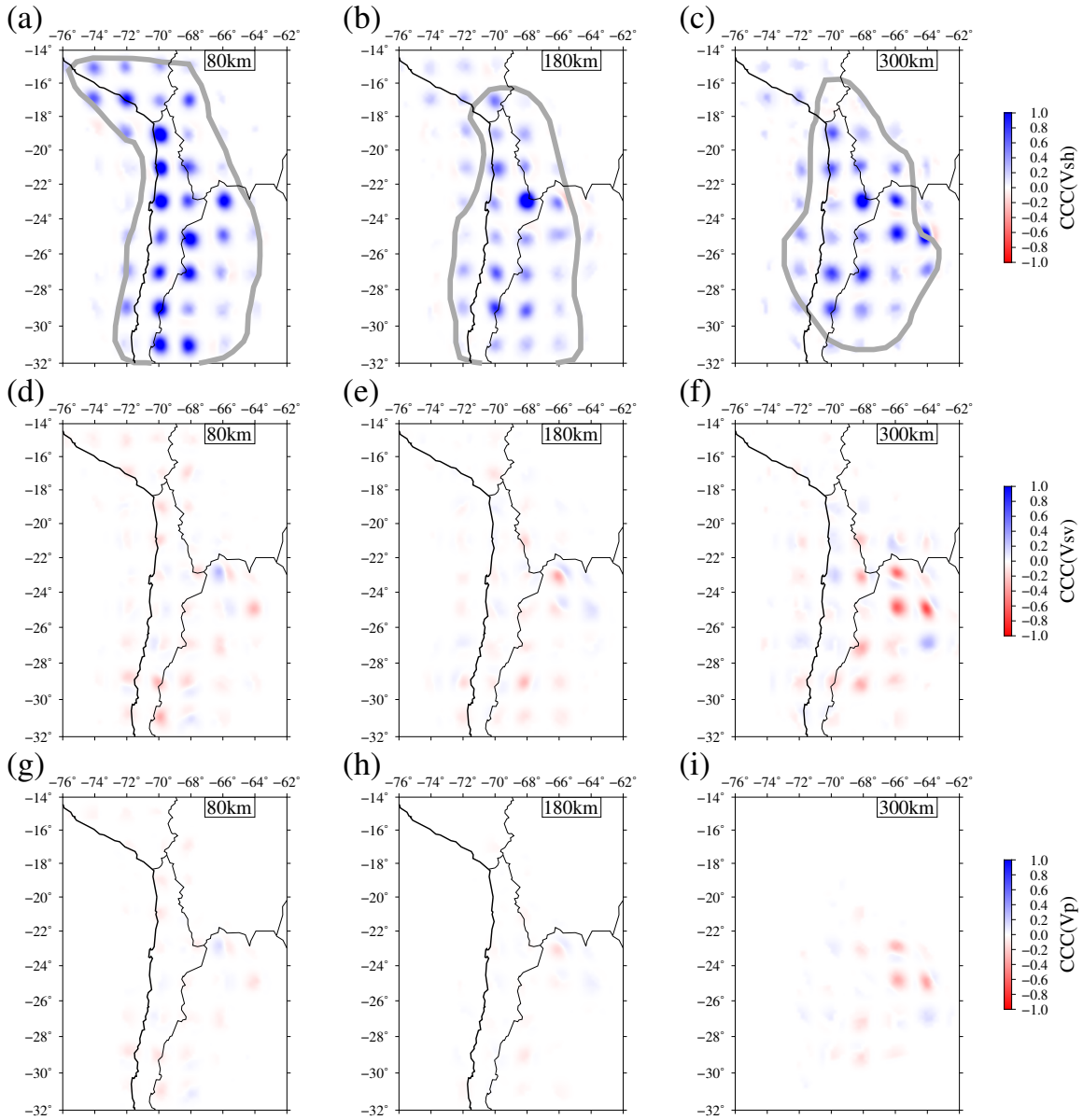

Fig. A.14: Normalised product between the $\delta \mathbf{V}_{SH}$ and point-spread functions $\mathbf{H}_{SH}^{SH}\delta \mathbf{V}_{SH}$ (a-c), $\mathbf{H}_{SH}^{SV}\delta \mathbf{V}_{SH}$ (d-f) and $\mathbf{H}_{SH}^{P}\delta \mathbf{V}_{SH}$ (g-i). All the results are normalised by the product of the maximum of $\delta \mathbf{V}_{SH}$ and the maximum of $\mathbf{H}_{SH}^{SH}\delta \mathbf{V}_{SH}$ for every depth level.

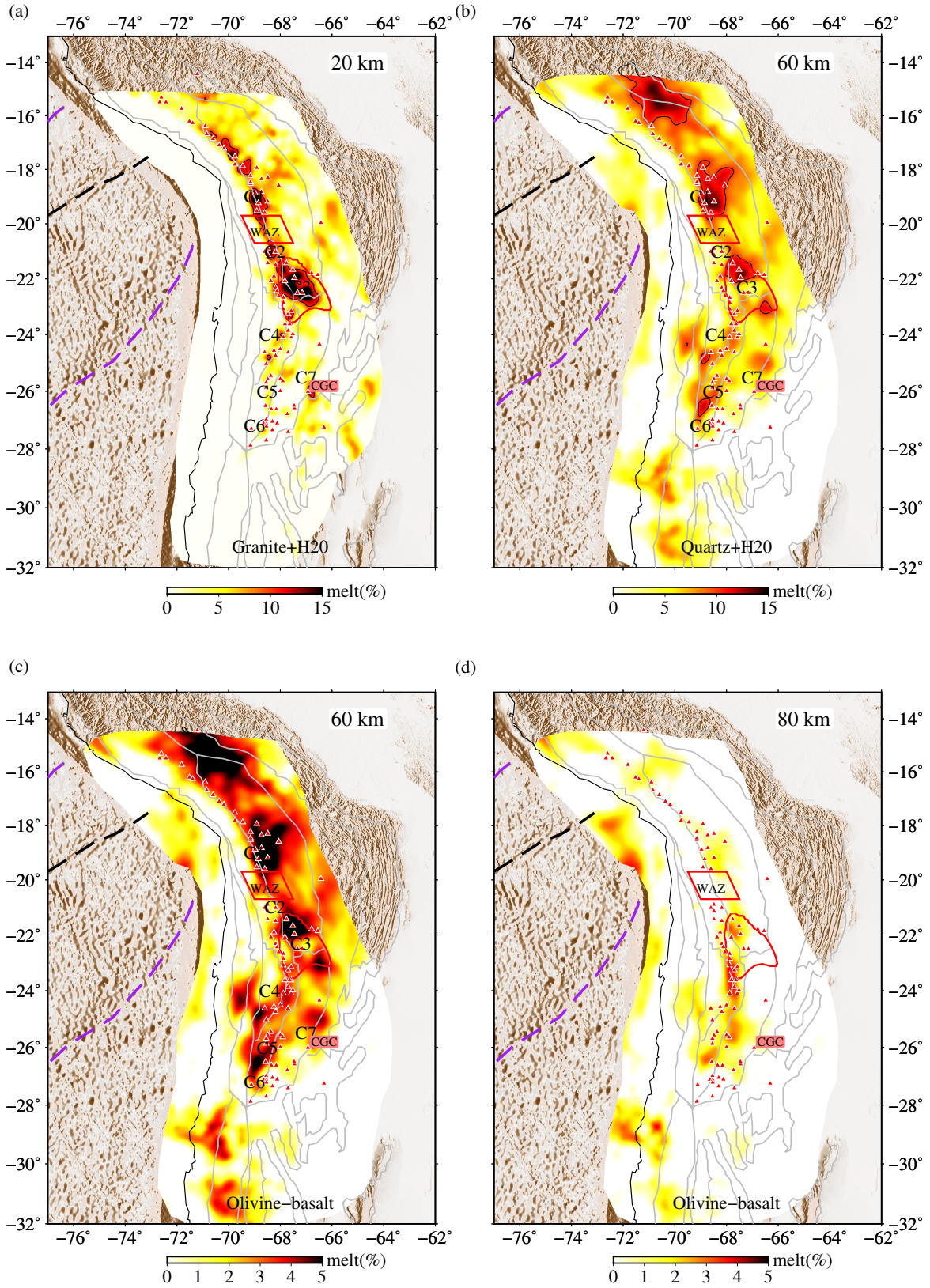

Fig. A.15: Partial melt fraction estimation within (a) the middle crust (20 km), (b,c) crust-mantle transition (60 km), with b,c representing different assumptions on the composition, and (d) uppermost mantle (80 km). Labels designate the assumed composition, see supplementary text for more detail.

Appendix B

Supplementary material for chapter 5

B.1 Inversion

S1: Model construction and inversion working flow Long-wavelength surface topography from the EGM2008 Geoid (Pavlis et al., 2012) and Earth2014 global topography model (Hirt & Rexer, 2015) with Earth ellipticity according to WGS84 and Moho topography from Crust1.0 (Laske et al., 2013) are implemented by deforming the mesh grid vertically. The surface and Moho topography have been filtered with maximum angular order $lmax = 128$, equivalent to a spatial resolution of 155 km. In order to constrain the deep structure of the upper mantle, we initiate our inversion from long-period surface wave data at 60–120 s and progress in seven stages to a final period range of 12–120 s (see Table B.2); the progressive extension to shorter periods mitigates the risk of falling into local minima. The model updates are driven by the Limited-Memory Broyden–Fletcher–Goldfarb–Shanno algorithm (Liu & Nocedal, 1989). We employ the Time-Frequency Phase Shift and Cross-Correlation-Coefficient misfits as misfit functions during stage I-V and VI-VII, respectively, following (Gao et al., 2021a) with the assistance of the *Large-scale Seismic Inversion Framework 2.0* (Krischer et al., 2015a; Thrastarson et al., 2021). The detailed misfit evolution chart and histograms based on events and seismic traces are shown in Figure B.4. Exemplary waveform fits from four events are illustrated in Figures B.33-B.37. More technical details about the inversion workflow can be found in Gao et al. (2021a).

S2: Point-spreading tests We analyse the resolution for the inversion and the trade-offs among the parameter types. In traditional ray theory tomography, the checkerboard test is popular and relatively robust with low computational costs, but it is computationally prohibitive for FWIs. In this study, we therefore approximate the Hessian-vector product $\mathbf{H}\delta\mathbf{m}$ for a test function $\delta\mathbf{m}$ (Fichtner & Trampert, 2011; Fichtner & Leeuwen, 2015; Zhu et al., 2015, 2017; Tao et al., 2018)

$$\mathbf{H}\delta\mathbf{m} = \mathbf{g}(\mathbf{m} + \delta\mathbf{m}) - \mathbf{g}(\mathbf{m}) \tag{B.1}$$

where $\mathbf{g}(\mathbf{m})$ denotes the summed gradient from the adjoint simulations for model $\mathbf{m}$, and $\mathbf{g}(\mathbf{m}+\delta\mathbf{m})$ indicates the gradient from the perturbed model $\mathbf{m}+\delta\mathbf{m}$.

If the synthetics from the final model provide a good fit of the observed data and the inversion thus has reached convergence, $\mathbf{H}\delta\mathbf{m}$ can be used to estimate the model resolution. Specifically, when the $\delta\mathbf{m}$ is nearly point-localised, the $\mathbf{H}\delta\mathbf{m}$ will be a linearised point-spread function.

In order to provide a visual representation of resolution throughout the model rather than just for a single model node, we perturbed our model by adding velocity perturbations $\delta\mathbf{m}$ in a three dimensional checkerboard pattern in the upper mantle made up of Gaussian spheres with $\pm 1\%$ maximum amplitude of the velocity for a specific depth and a Gaussian radius σ of 40 km. The horizontal and depth grid spacing of the Gaussian spheres are 2° and 100 km (Figure B.22). We calculate $\mathbf{H}\delta\mathbf{m}$ for this anomaly pattern for V_{SV}, V_{SH} and isotropic V_P separately (Figure B.22-B.24).

Table B.1: Seismic Network information

Code	Data Center	start	end	reference
C	IRISDMC	2007	2009	Chilean National Seismic Network
*C*1	IRISDMC	2012	-	Universidad De Chile (2013)
CX	GEOFON	2006	-	GFZ & CNRS-INSU (2006)
IU	IRISDMC	1988	-	Albuquerque Seismological Laboratory (ASL)/USGS (1988)
WA	IRISDMC	2011	-	West Central Argentina Network
2*B*	GEOFON	2007	2009	Heit et al. (2007b)
3*A*	IRISDMC	2010	2012	Maule Aftershock Deployment (UK)
3*H*	GEOFON	2014	2015	Lange et al. (2019)
G	IPGP	1982	-	IPGP & EOST (1982)
*X*6	IRISDMC	2007	2009	Sandvol & Brown (2007)
XH	IRISDMC	2008	2010	Gilbert (2008)
XS	RESIF	2010	2011	Vilotte & RESIF (2011)
XY	IRISDMC	2010	2010	Roecker & Russo (2010)
YC	IRISDMC	2002	2002	Beck & Terry (2000)
YM	IRISDMC	2010	2012	Waite (2010)
ZA	GEOFON	2002	2004	Asch et al. (2002)
ZB	GEOFON	1997	1997	Schurr et al. (1997)
ZE	GEOFON	2010	2011	Maule Aftershock Survey-GFZ
ZL	IRISDMC	2007	2009	Beck & Zandt (2007)
ZP	GEOFON	1999	2001	ISSA Southern Andes
ZQ	GEOFON	2004	2005	Cerro Blanco Project Central Andes
ZR	IRISDMC	2015	2018	Thurber (2015)
ZW	GEOFON	2005	2005	Rietbrock et al. (2004)

Through the multi-parameter point-spread tests, we could confirm that the resolution for the inversion parameters is mostly confined to the top 400 km, although V_{SV} and isotropic V_P even show some ability to resolve the structure down to 460 km. The resolution of V_{SH} is confined to 360 km depth. Therefore, we could extend our interpretation on both of the isotropic V_S and V_P down to about 400 km.

To further quantitatively assess the resolution, we also present the normalised product of the perturbations $\delta\mathbf{m}$ and the resultant Hessian product $\mathbf{H}\delta\mathbf{m}$ within and between parameter classes (Figure B.25-B.27).

S3: Model comparison In this section, we provide a simple comparison (Figure B.21) between our model with (Ward et al., 2013). Although the shape of the recovered anomalies is sometimes quite different, the basic features can generally be found in both models. For example, the forearc has higher velocities than the main volcanic arc, indicating colder temperatures. Importantly, in the middle crust (20 km) only moderately low velocities are found from 29°S to 32°S and spread over a wider distance in EW-direction, compared to the segments north and south with stronger anomalies confined to the active volcanic arc. In general, the anomalies imaged by us tend to be more focused and with larger amplitudes, compared to (Ward et al., 2013).

Table B.2: Overview of inversion stages. TF: Time Frequency, CCC: Cross Correlation Coefficient

No.	Periods	It.	Simulation time	Events	Windows	Misfit
I	60–120 s	5	450 s	71	7785	TF
II	40–120 s	7	450 s	93	10211	TF
III	30–100 s	7	450 s	93	12497	TF
IV	20–100 s	11	450 s	93	12497	TF
V	20–100 s	7	450 s	110	28399	TF
VI	15–100 s	9	450 s	120	61516	CCC
VII	12–100 s	8	450 s	139	74751	CCC

B.2 Supplementary Figures

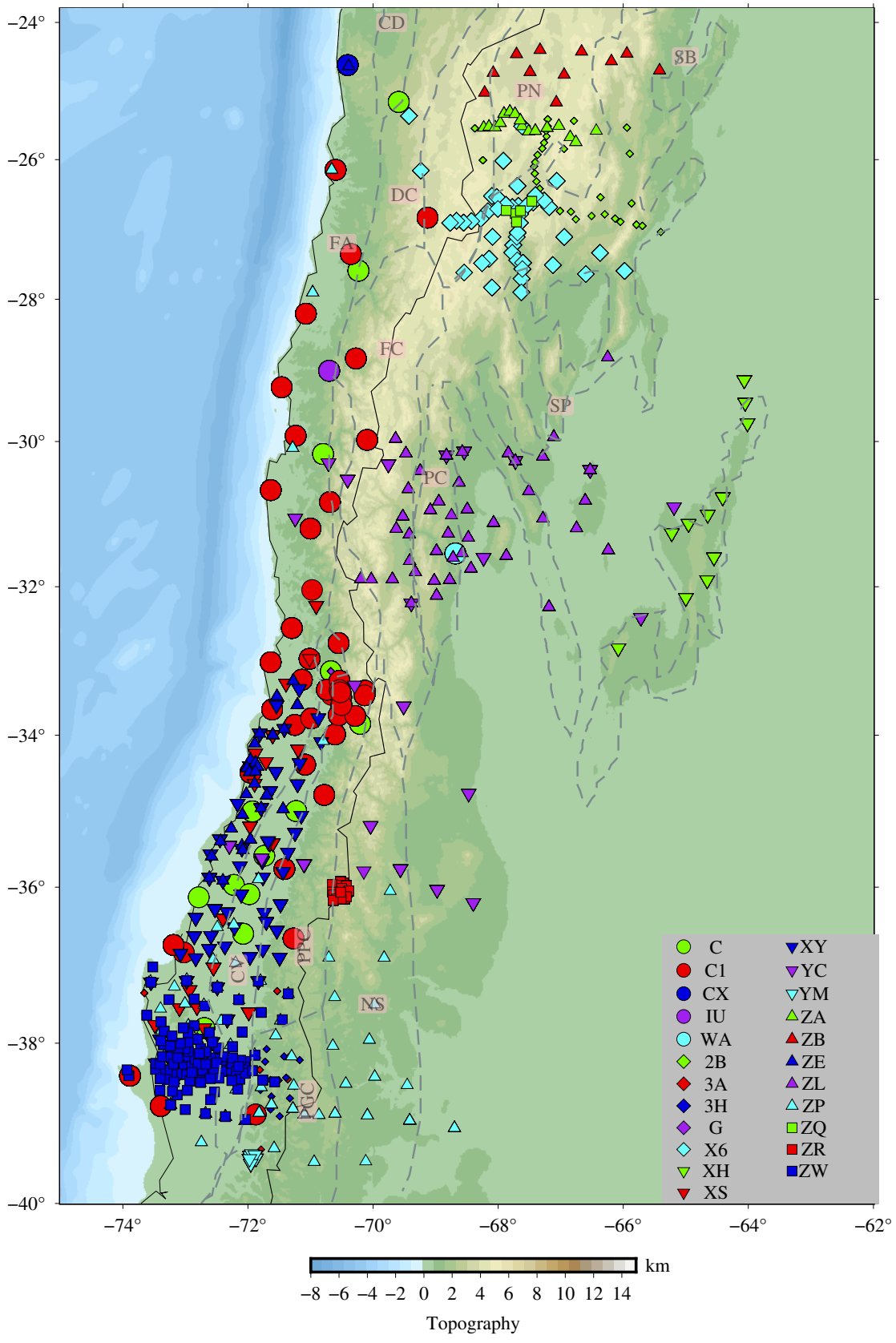

Fig. B.1: Map showing seismic stations of individual networks used in the study with circles marking the permanent stations. Detailed information about the networks is given in Table B.1

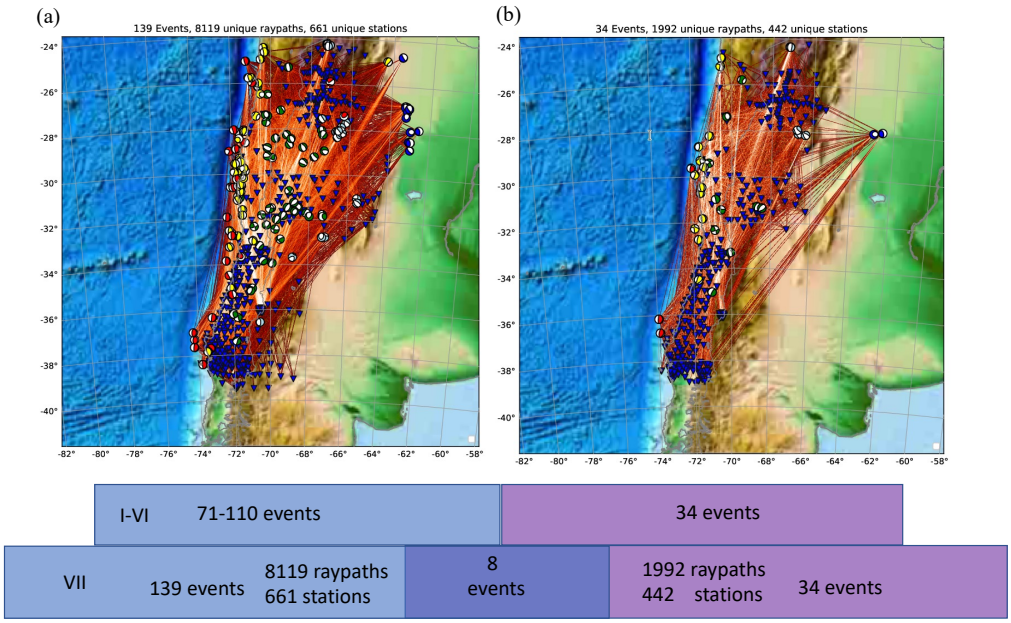

Fig. B.2: (a) Earthquakes, stations and ray-paths used for the inversion. (b) Earthquakes, stations and ray-paths for the validation dataset. 8 earthquakes are overlapped between the inversion data set and validation data set in the final inversion stage (VII). The waveforms in the validation dataset were not used in the inversion, but instead used to evaluate improvement of the model and avoid overfitting. See Fig. B.4 for a comparison of fit improvements in inversion and validation dataset.

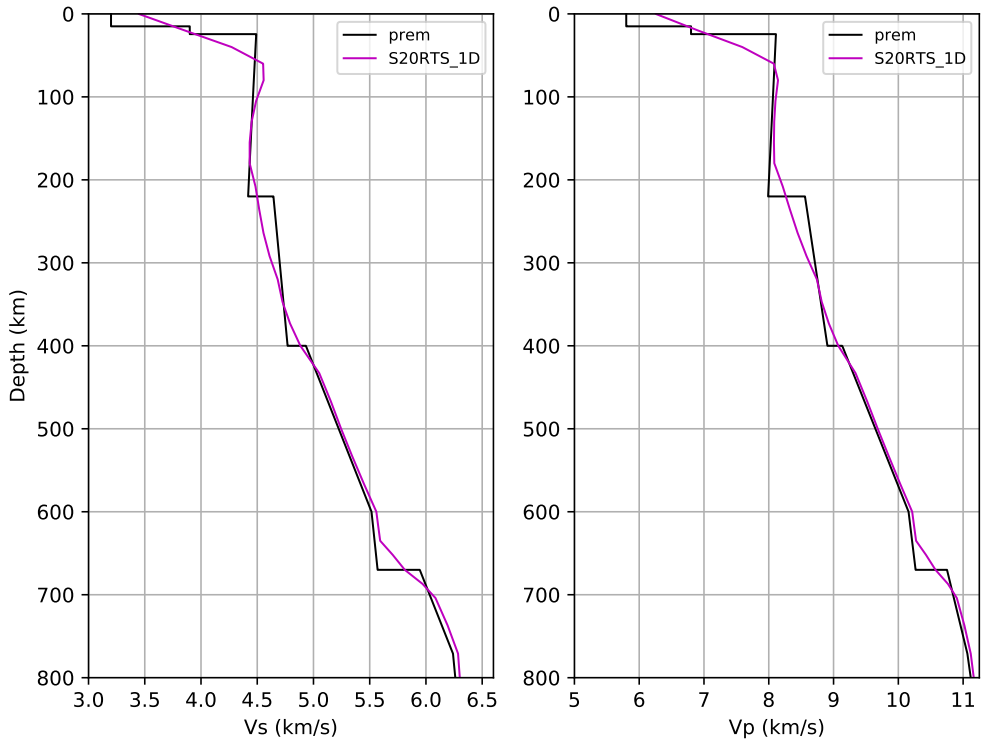

Fig. B.3: The reference 1D model derived from the depth-averaged initial SP12RTS Koelemeijer et al. (2015) model, compared with isotropic PREM Dziewonski & Anderson (1981).

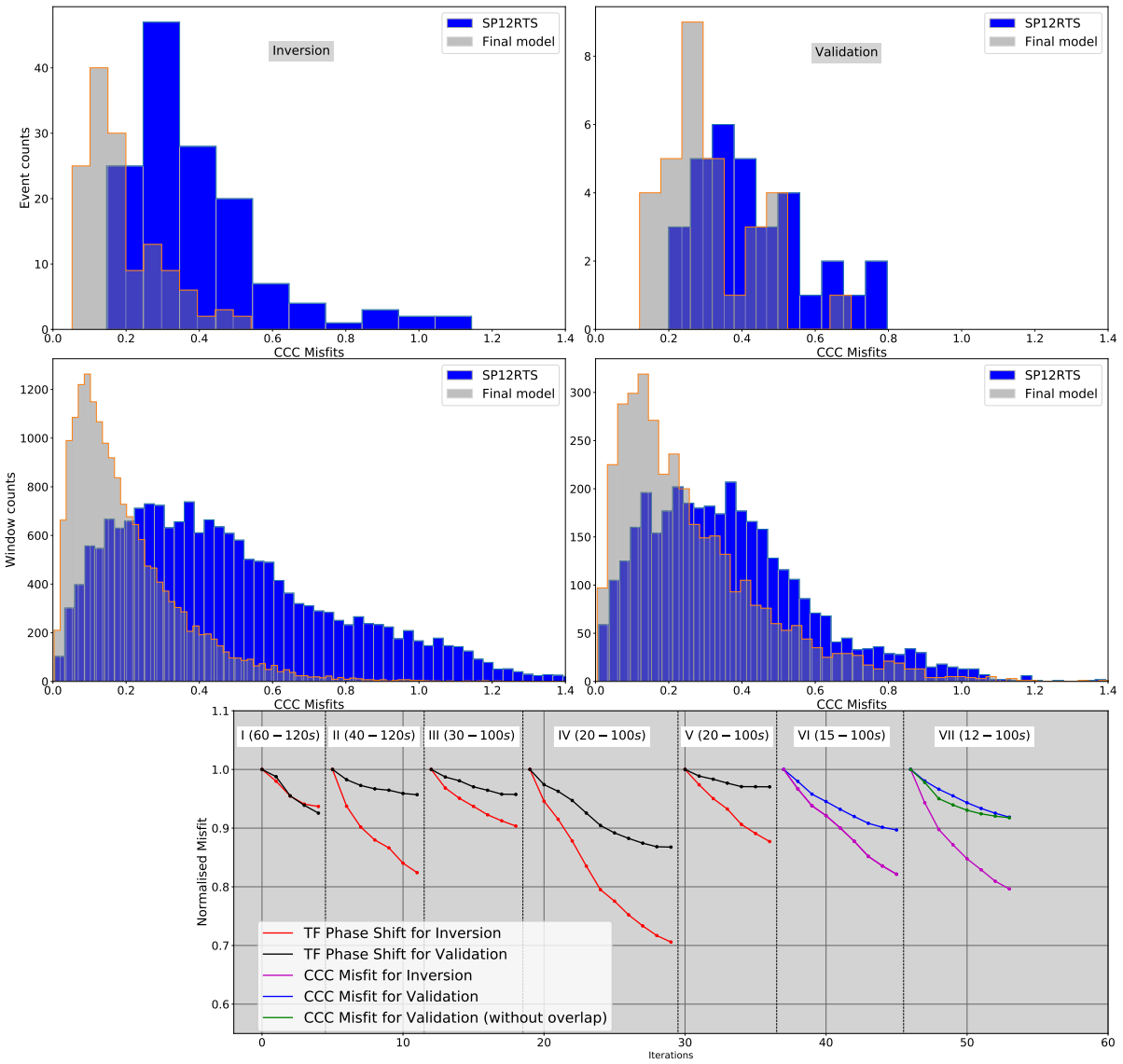

Fig. B.4: Top: Histogram of average cross corrrelation coefficient (CCC) misfits for each event for the starting model and after the final iteration; the left column shows the inversion, the right column the validation data set. Middle: Histogram of CCC misfits for each trace; Lower: Misfit evolution with iterations. See Fig. B.2 for more details on inversion and validation dataset.

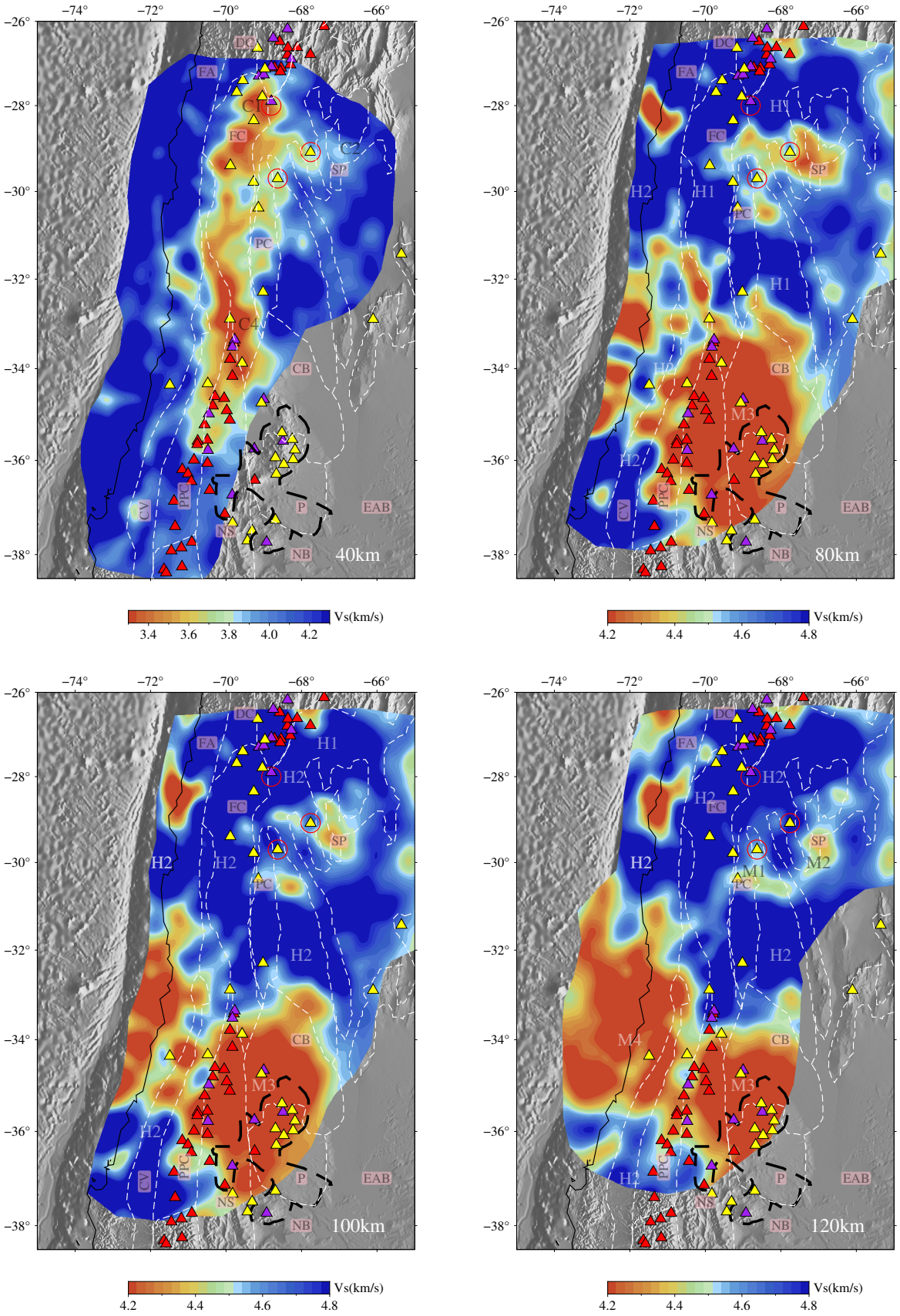

Fig. B.5: Horizontal slices for isotropic V_S model at 40 km, 80 km, 100 km and 120 km depth.

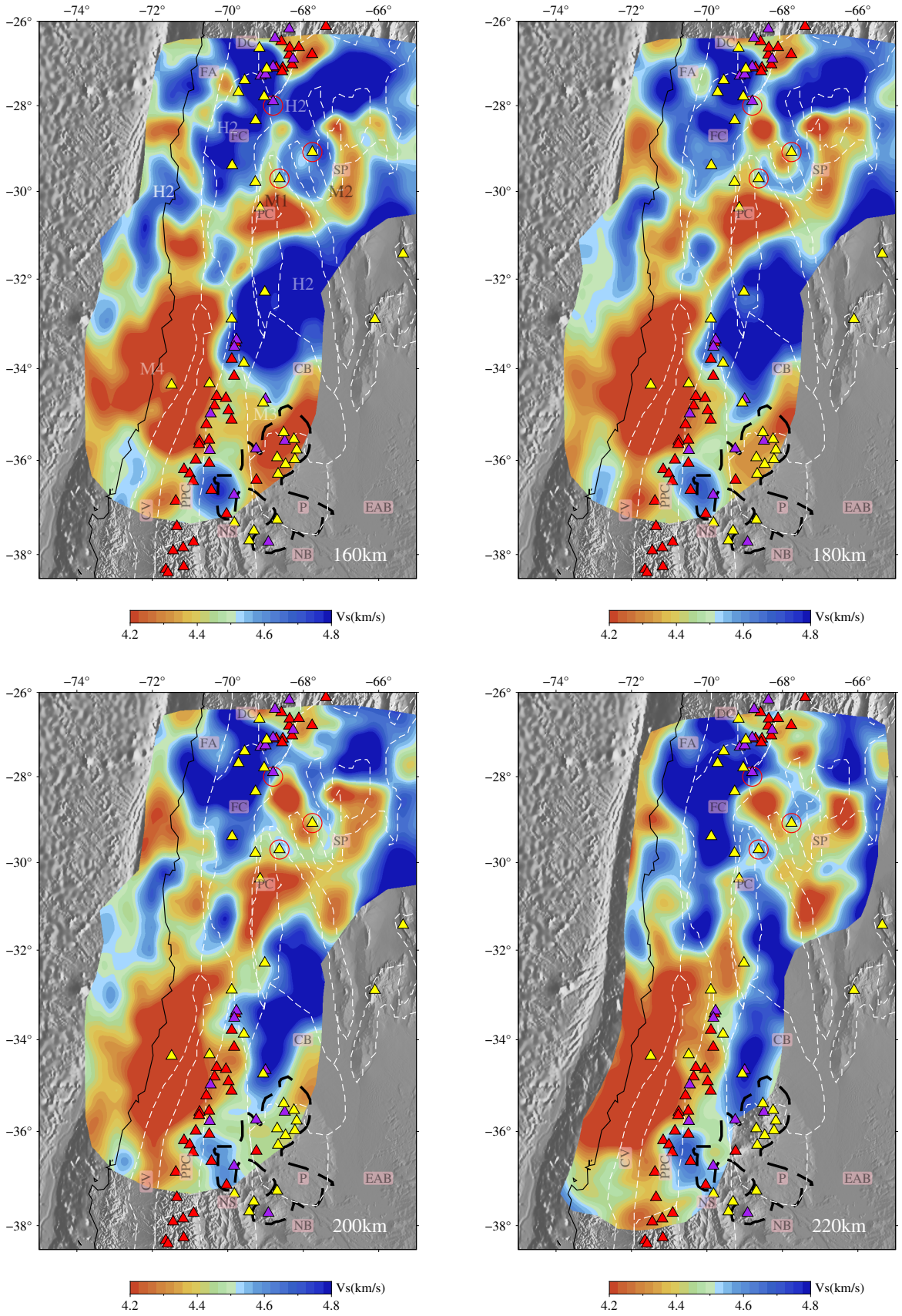

Fig. B.6: Horizontal slices for isotropic V_S model at 160 km, 180 km, 200 km and 220 km depth.

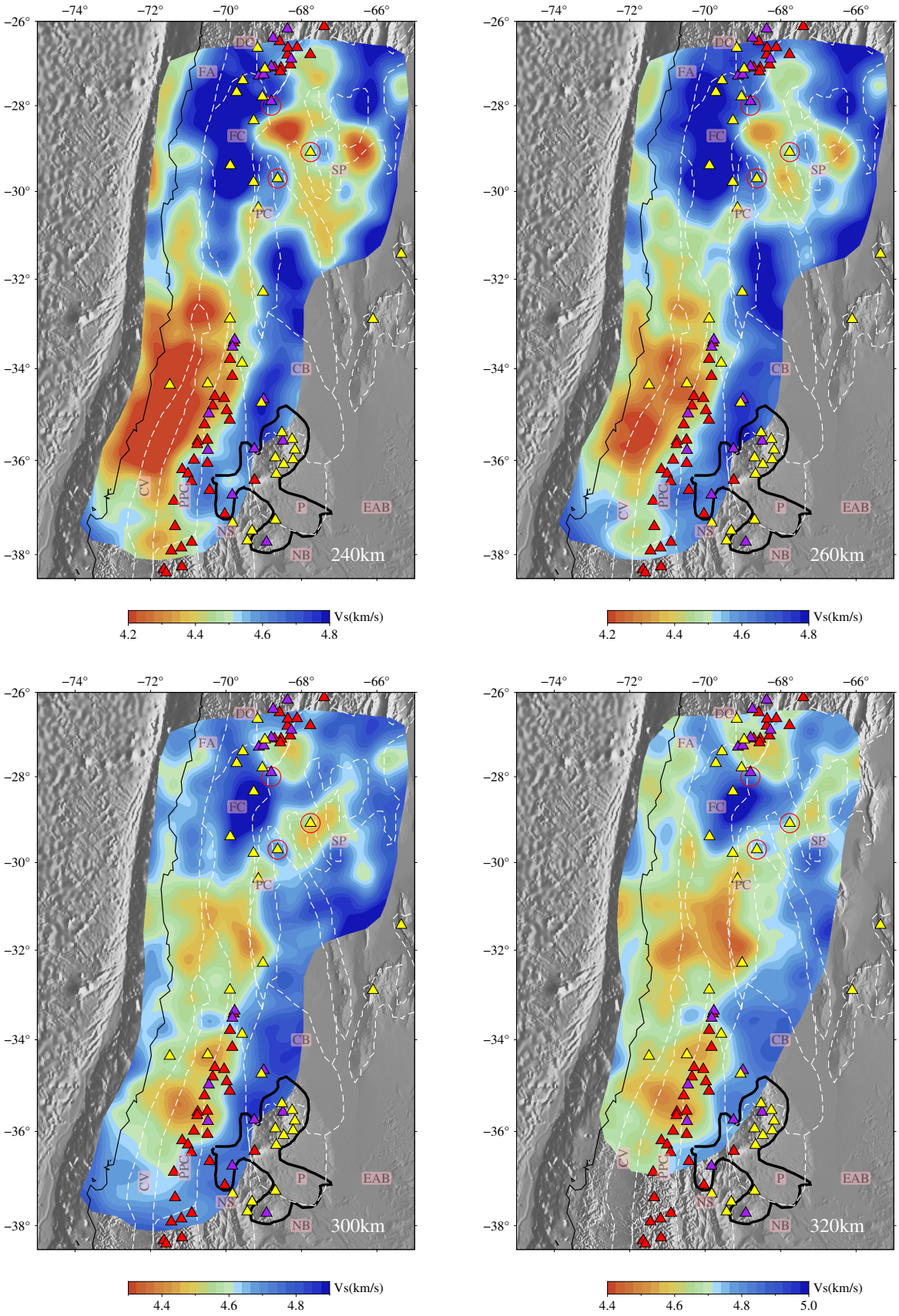

Fig. B.7: Horizontal slices for isotropic V_S model at 240 km, 260 km, 300km and 320 km depth.

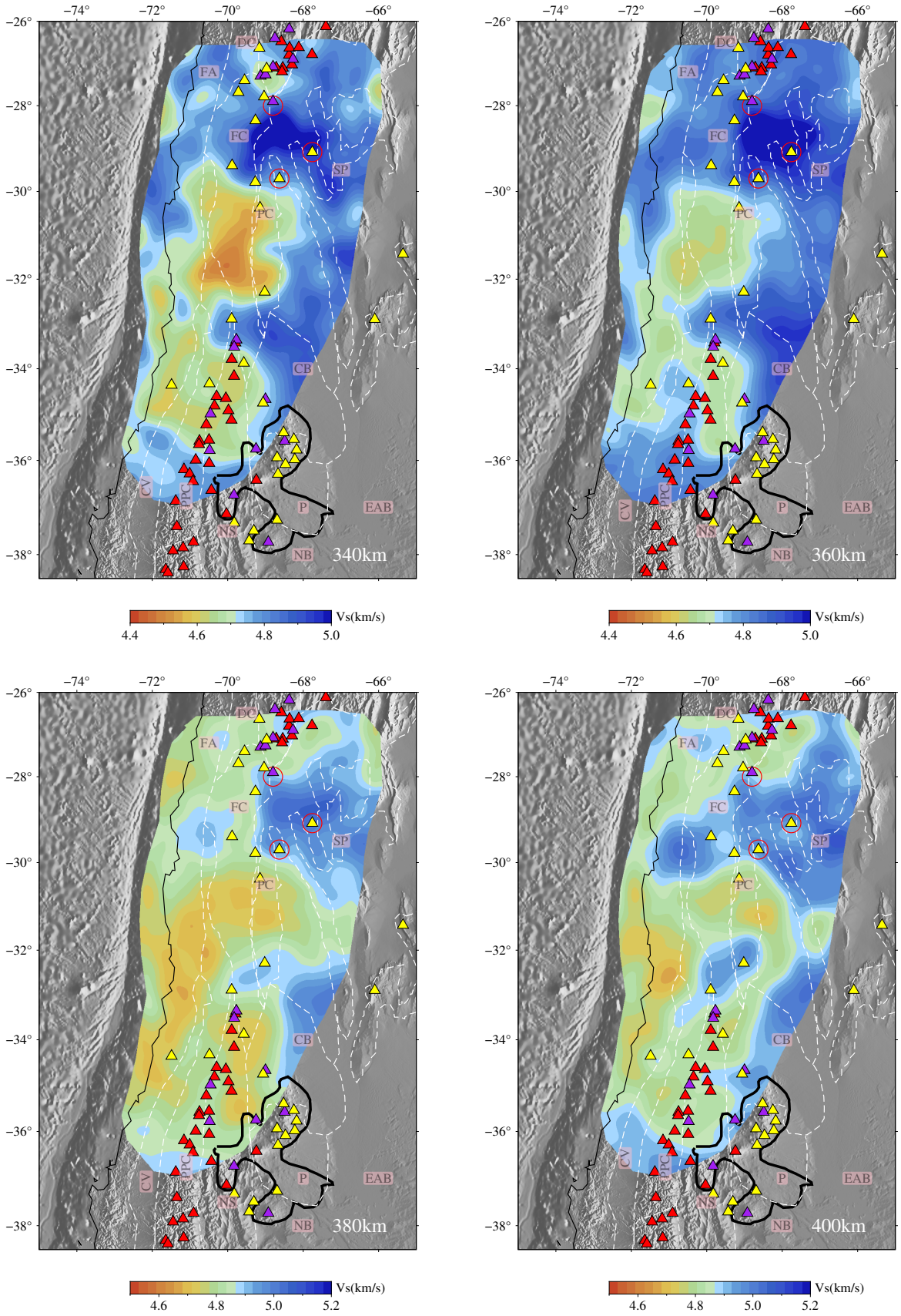

Fig. B.8: Horizontal slices for isotropic V_S model at 340 km, 360 km, 380 km and 400 km depth.

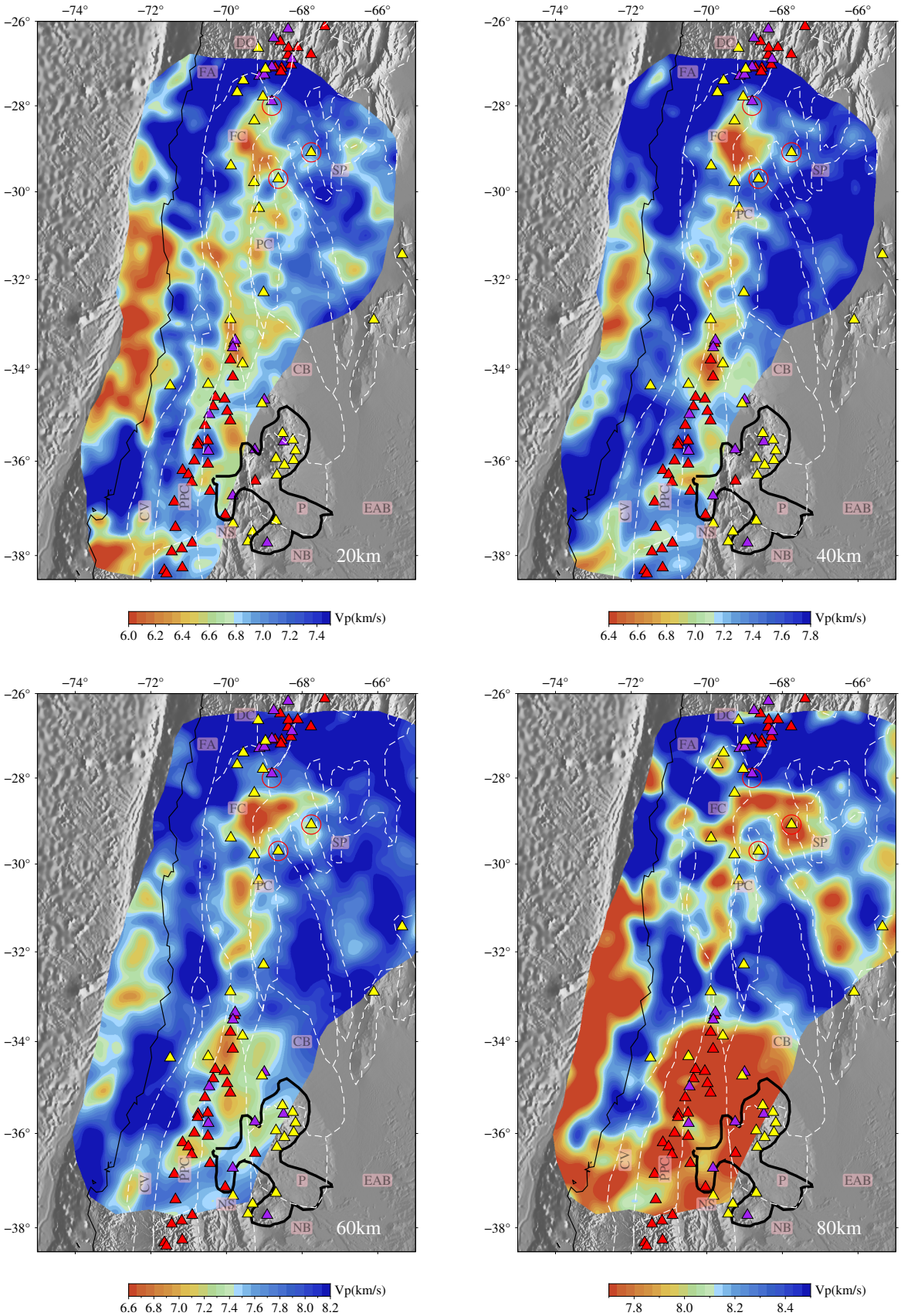

Fig. B.9: Horizontal slices for isotropic V_P model at 20 km, 40 km, 60 km and 80 km depth.

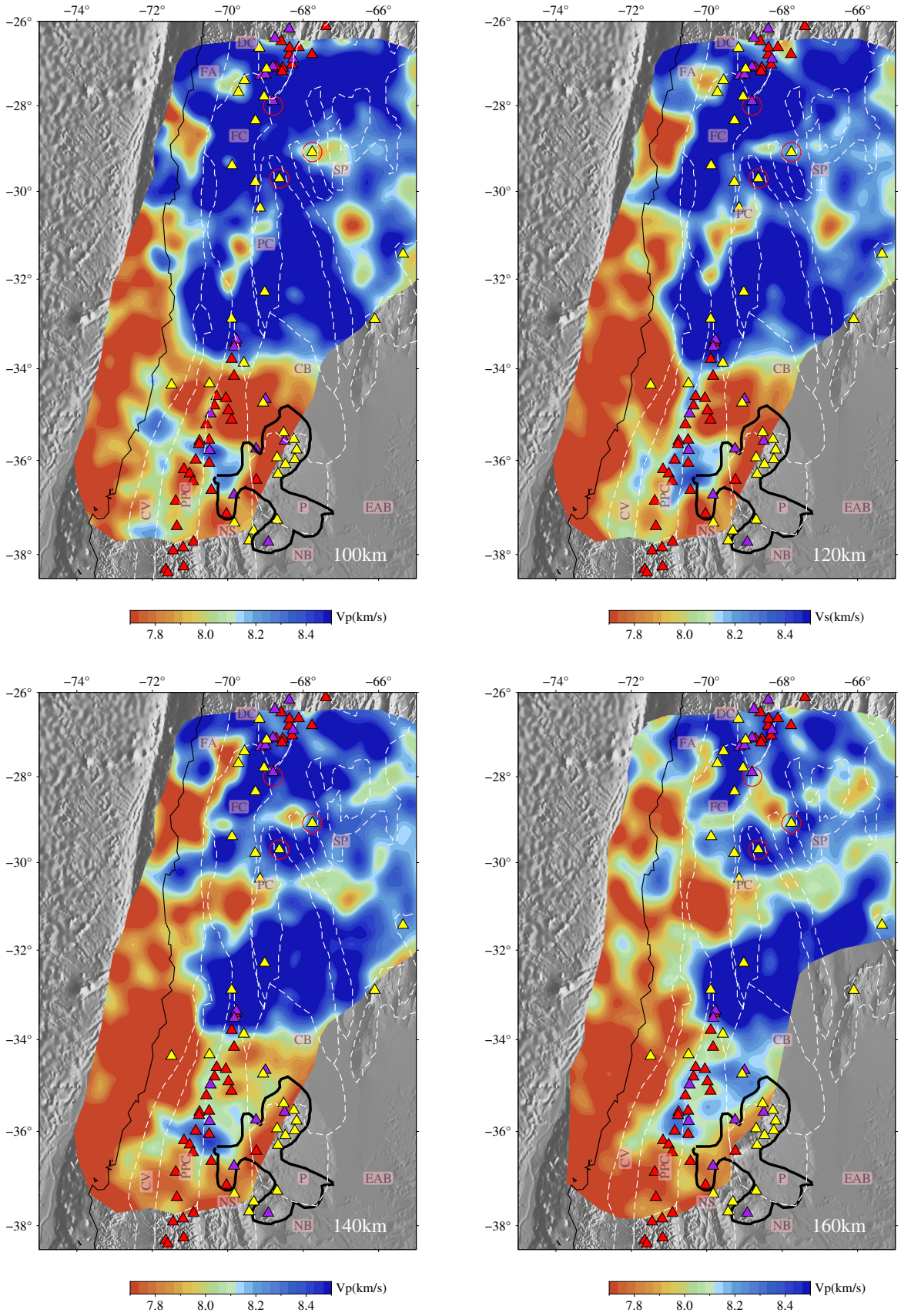

Fig. B.10: Horizontal slices for isotropic V_P model at 100 km, 120 km, 140 km and 160 km depth.

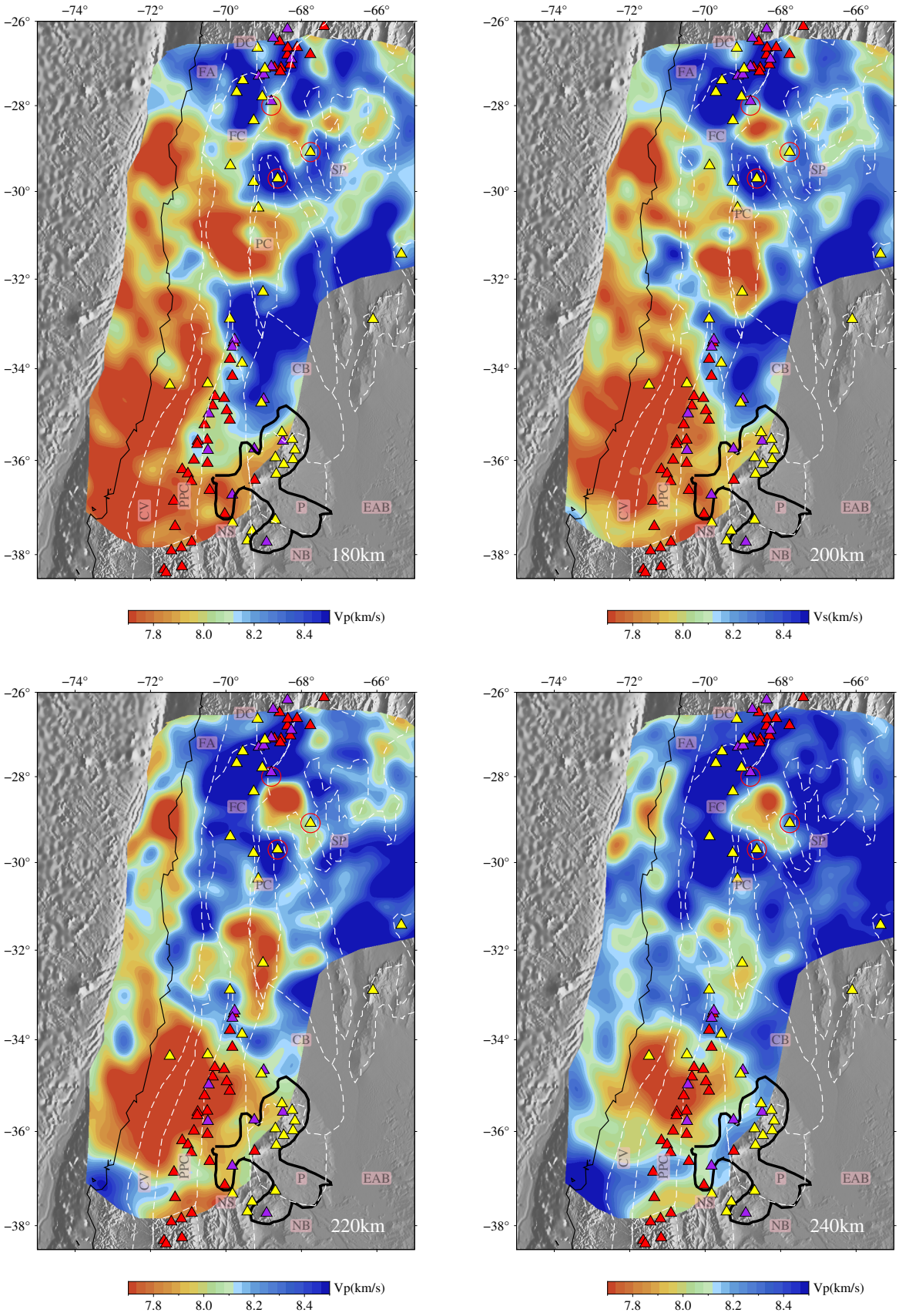

Fig. B.11: Horizontal slices for isotropic V_P model at 180 km, 200 km, 220 km and 240 km depth.

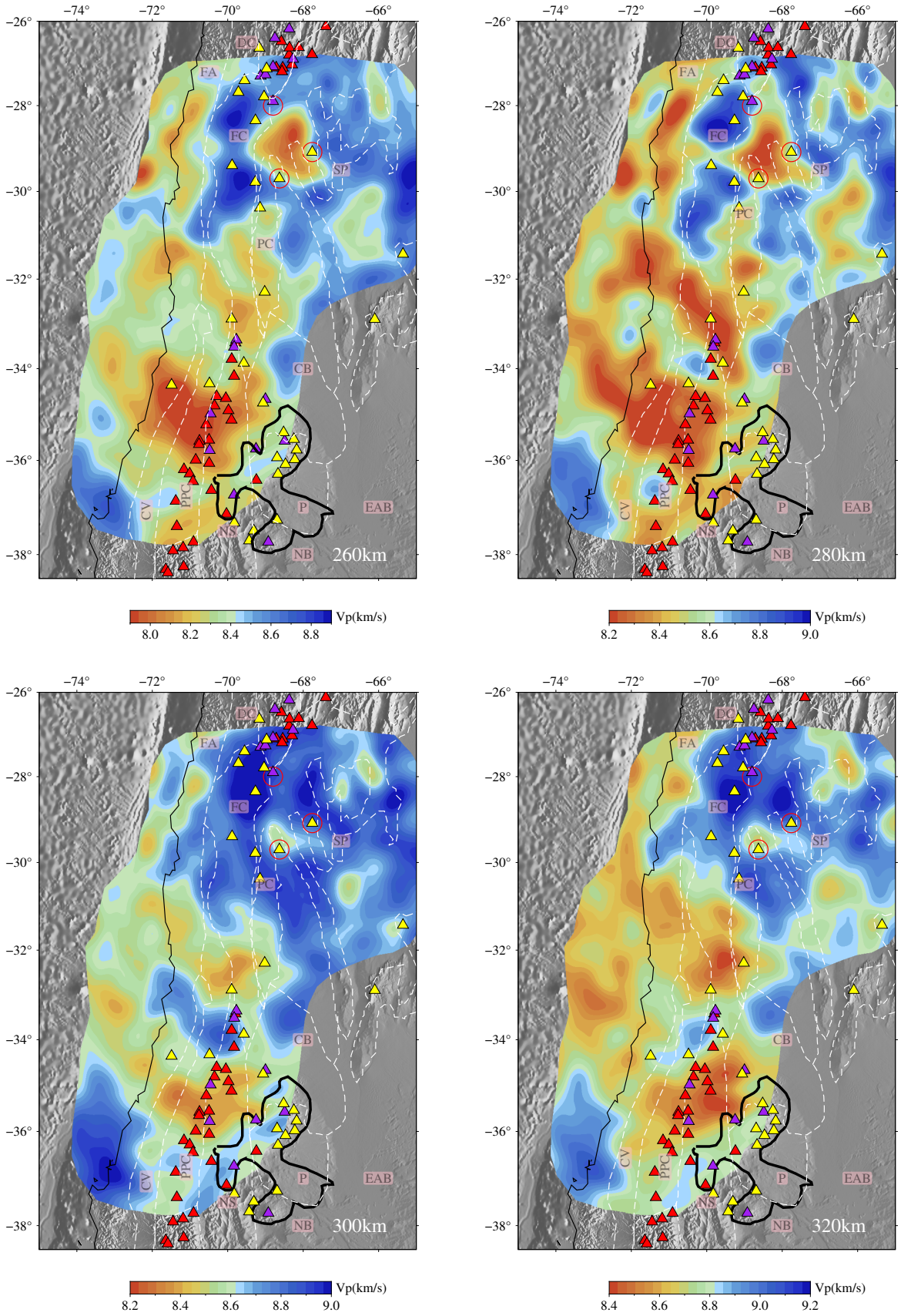

Fig. B.12: Horizontal slices for isotropic V_P model at 260 km, 280 km, 300 km and 320 km depth.

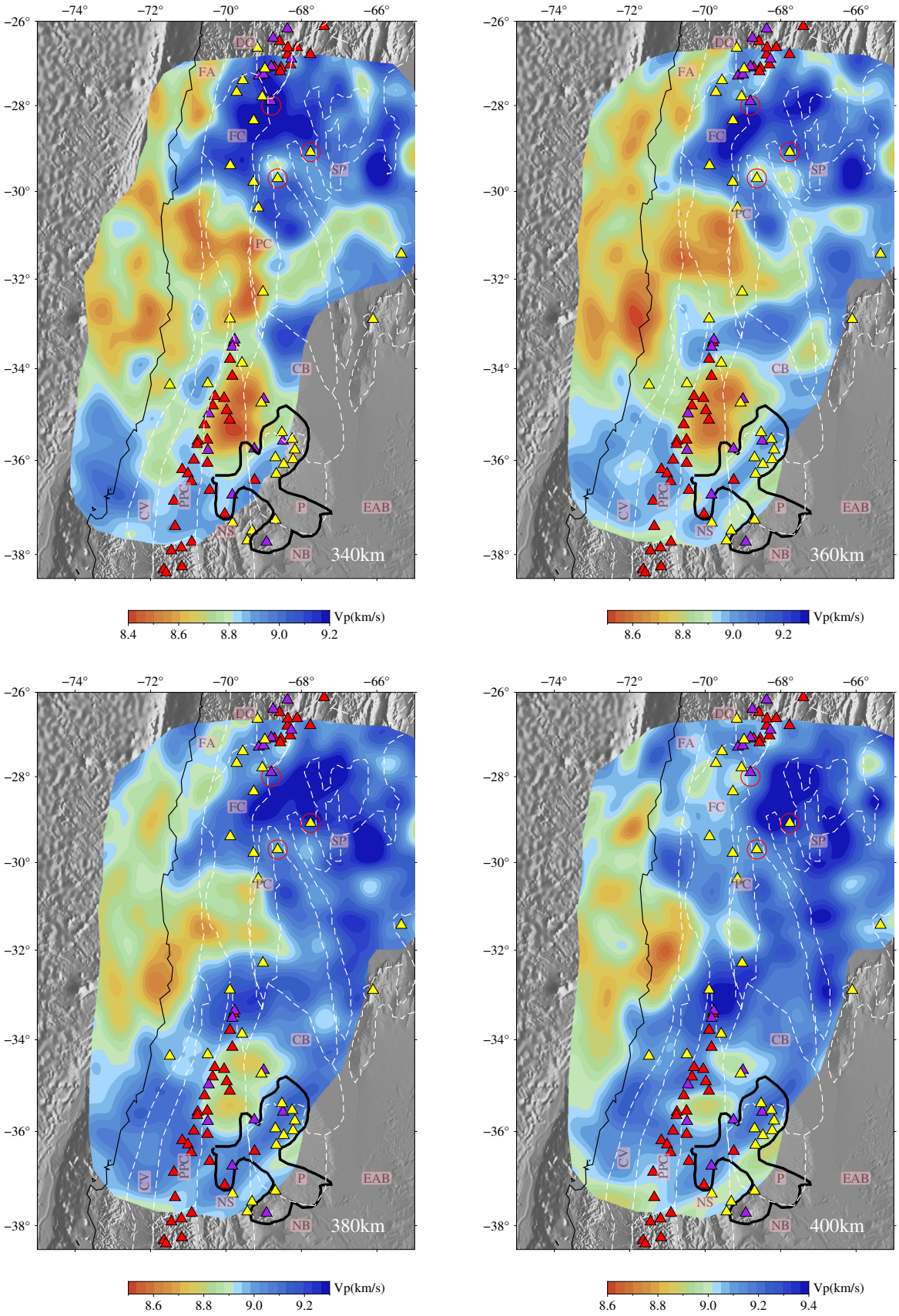

Fig. B.13: Horizontal slices for isotropic V_P model at 340 km, 360 km, 380 km and 400 km depth.

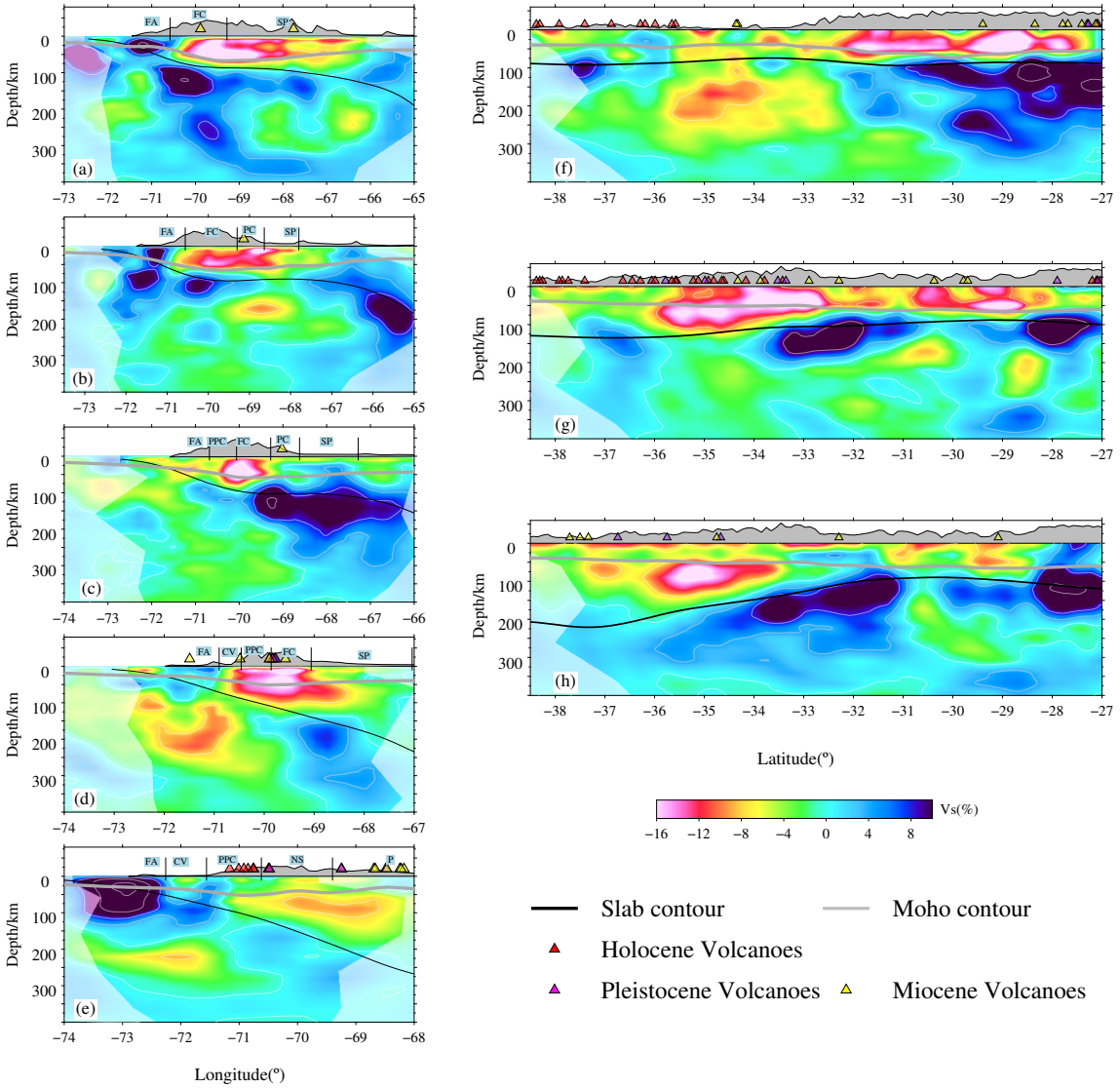

Fig. B.14: Same as Figure 5.3 but without seismicity. Cross-sections of isotropic V_s perturbations relative to the reference 1D V_s. The positions for the cross sections are defined in Figure 5.2(d) (see main text). Thick solid gray lines denote the continental Moho (Rivadeneyra-Vera et al., 2019) and thin solid black lines denote the slab contour from Slab 2.0 (Hayes et al., 2018). Magenta dots in b-d denote the seismicity relocated by (Sippl et al., 2021) and in other profiles are retrieved from ISC-EHB catalog.

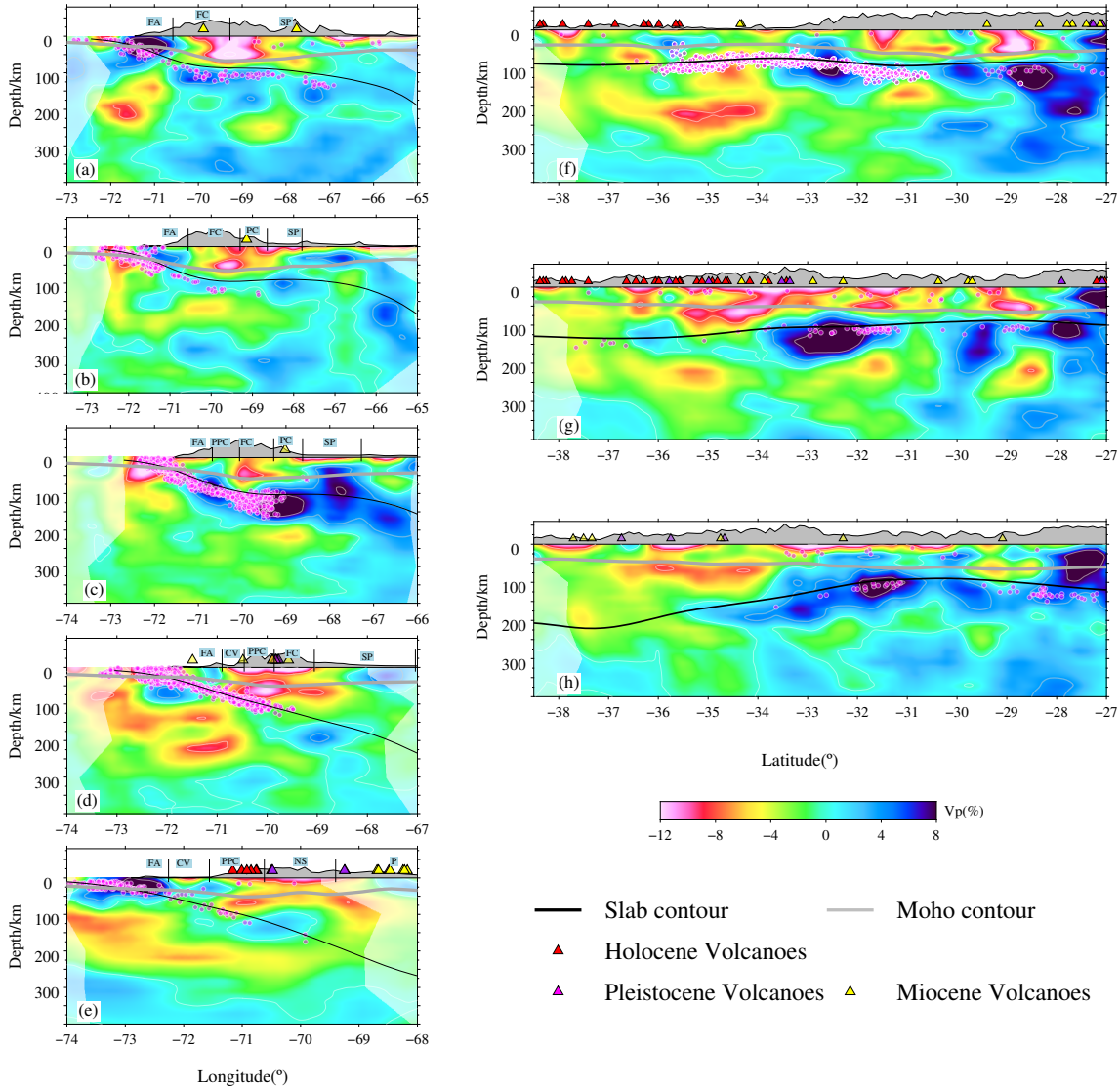

Fig. B.15: Cross-sections of isotropic V_p perturbations relative to the reference 1D V_p. The positions for the cross sections are defined in Figure 5.2(d) (see main text). Thick solid gray lines denote the continental Moho (Rivadeneyra-Vera et al., 2019) and thin solid black lines denote the slab contour from Slab 2.0 (Hayes et al., 2018). Magenta dots in b-d denote the seismicity relocated by (Sippl et al., 2021) and in other profiles are retrieved from ISC-EHB catalog.

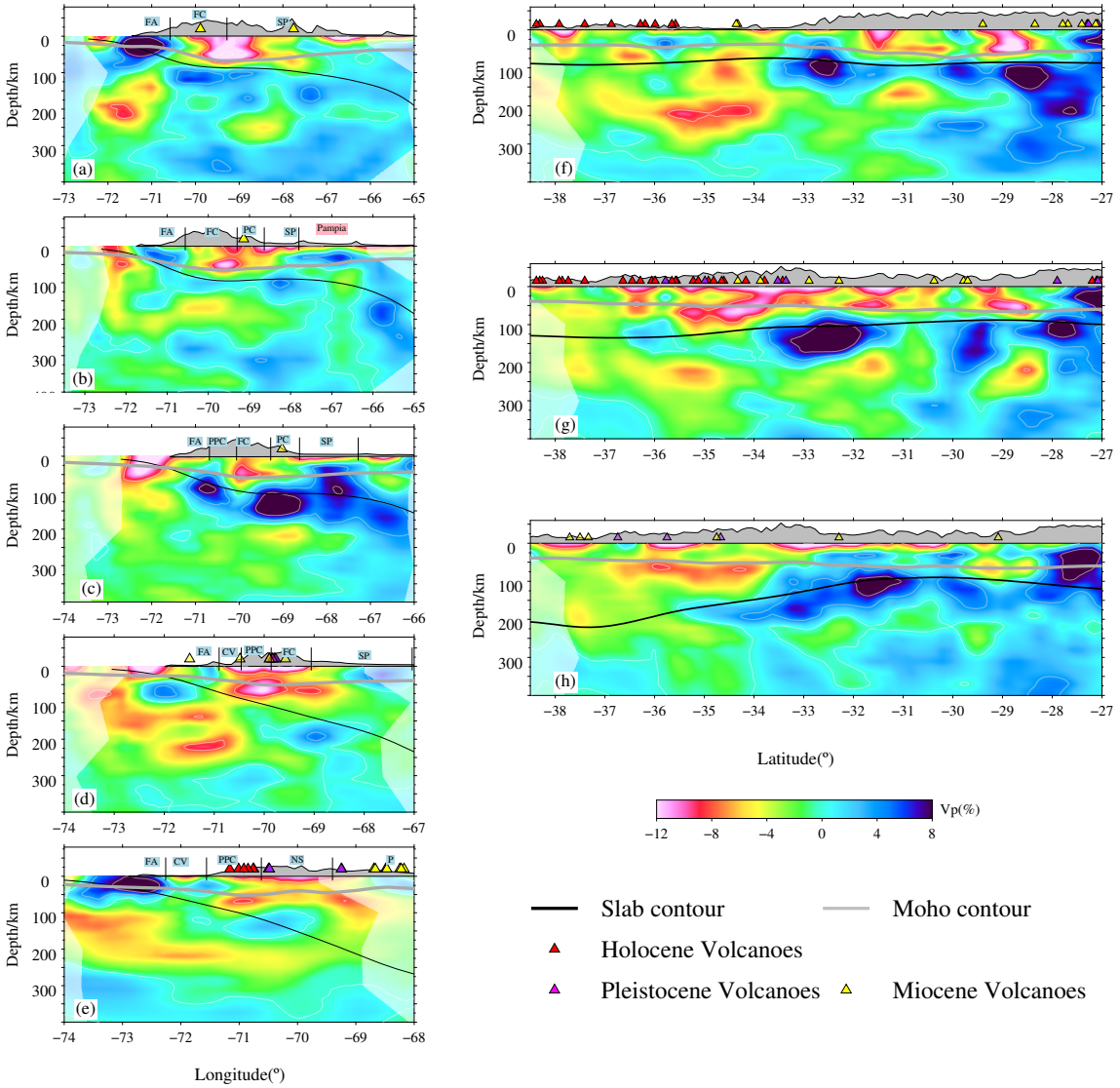

Fig. B.16: Same as Figure B.15 but without seismicity

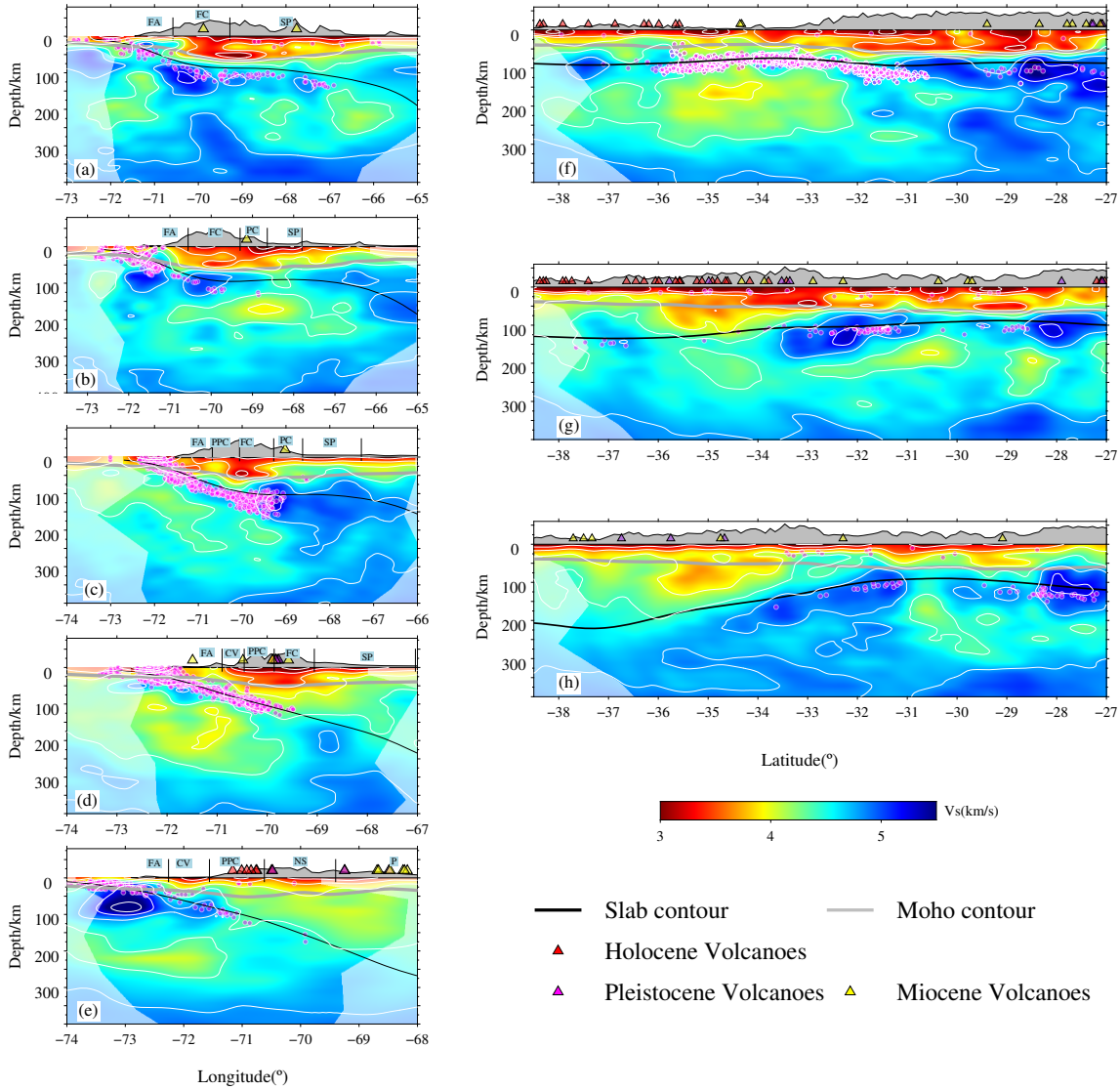

Fig. B.17: Isotropic absolute V_S cross-sections. For other figure elements see Fig. B.15.

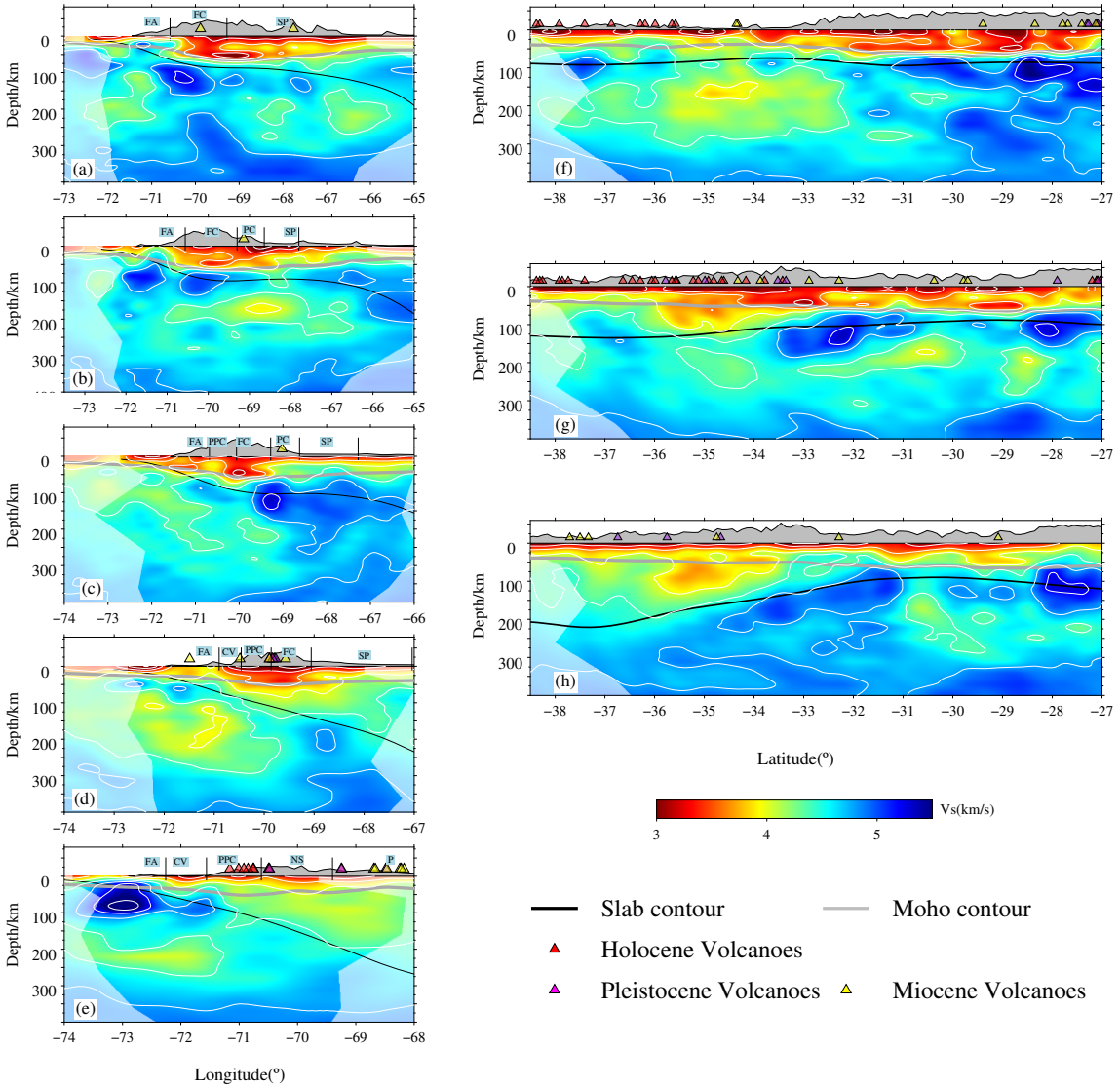

Fig. B.18: Same as Figure B.17 but without seismicity

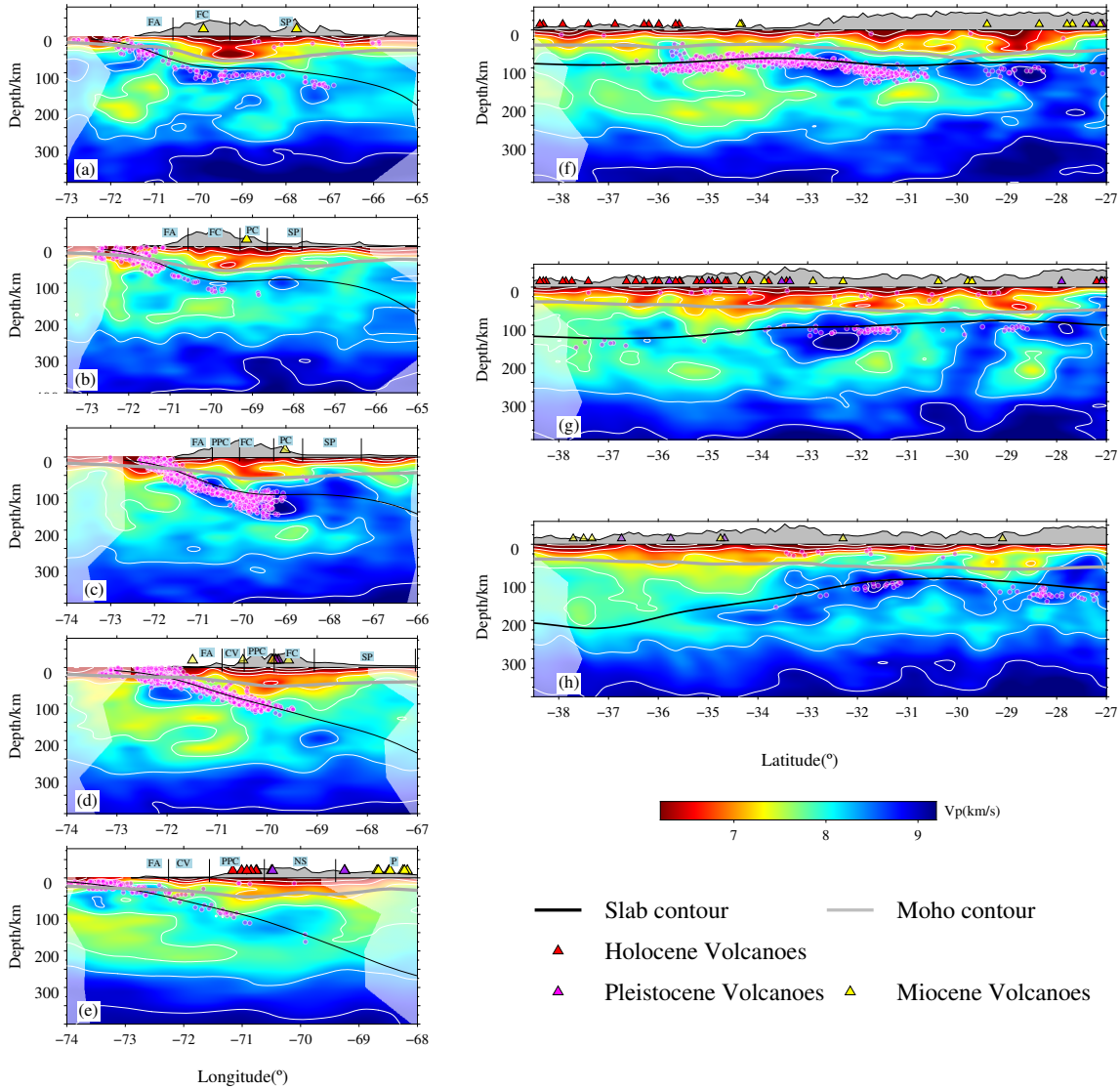

Fig. B.19: Isotropic absolute V_P cross-sections. For other figure elements see Fig. B.15

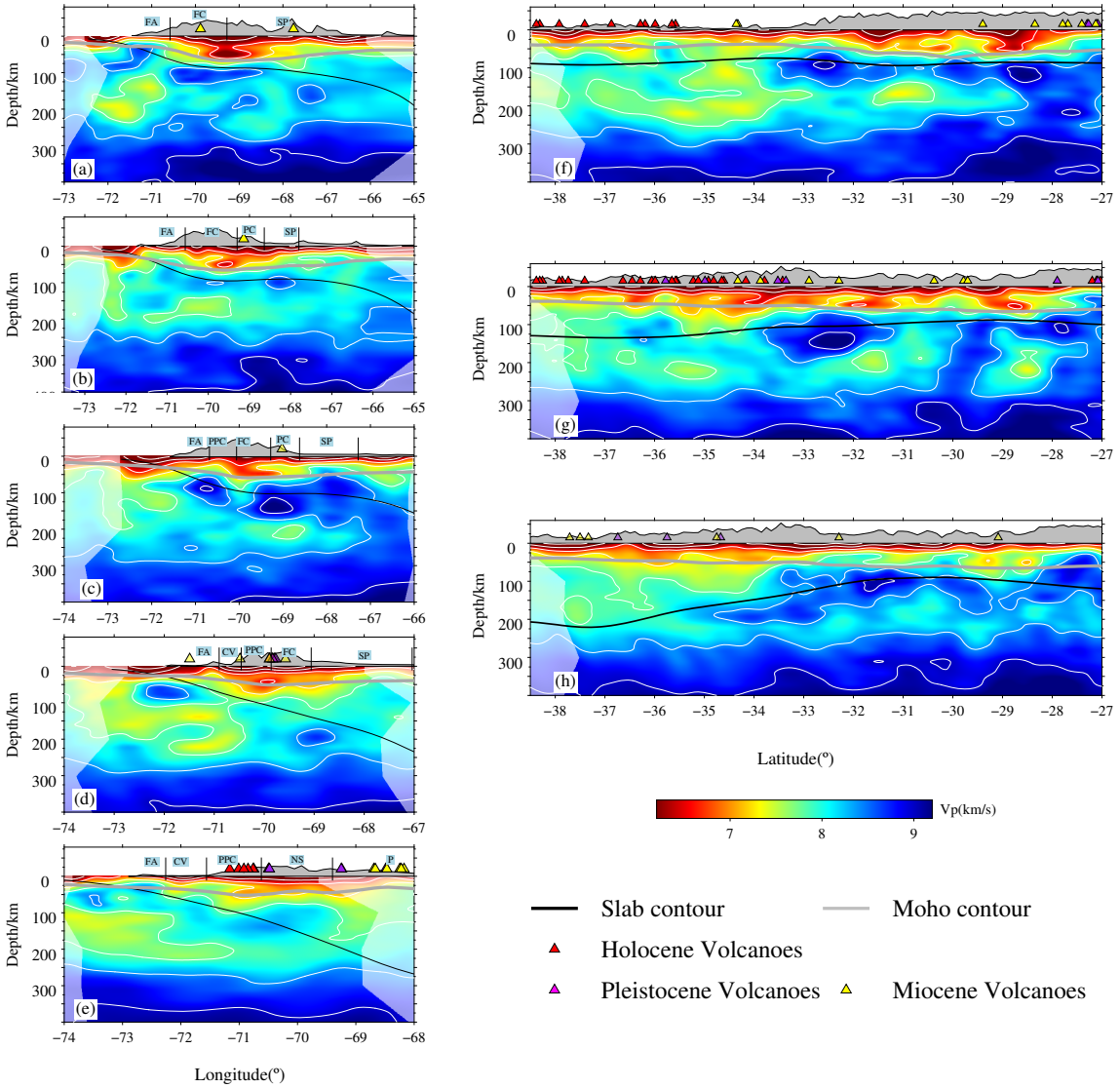

Fig. B.20: Same as Figure B.19 but without seismicity

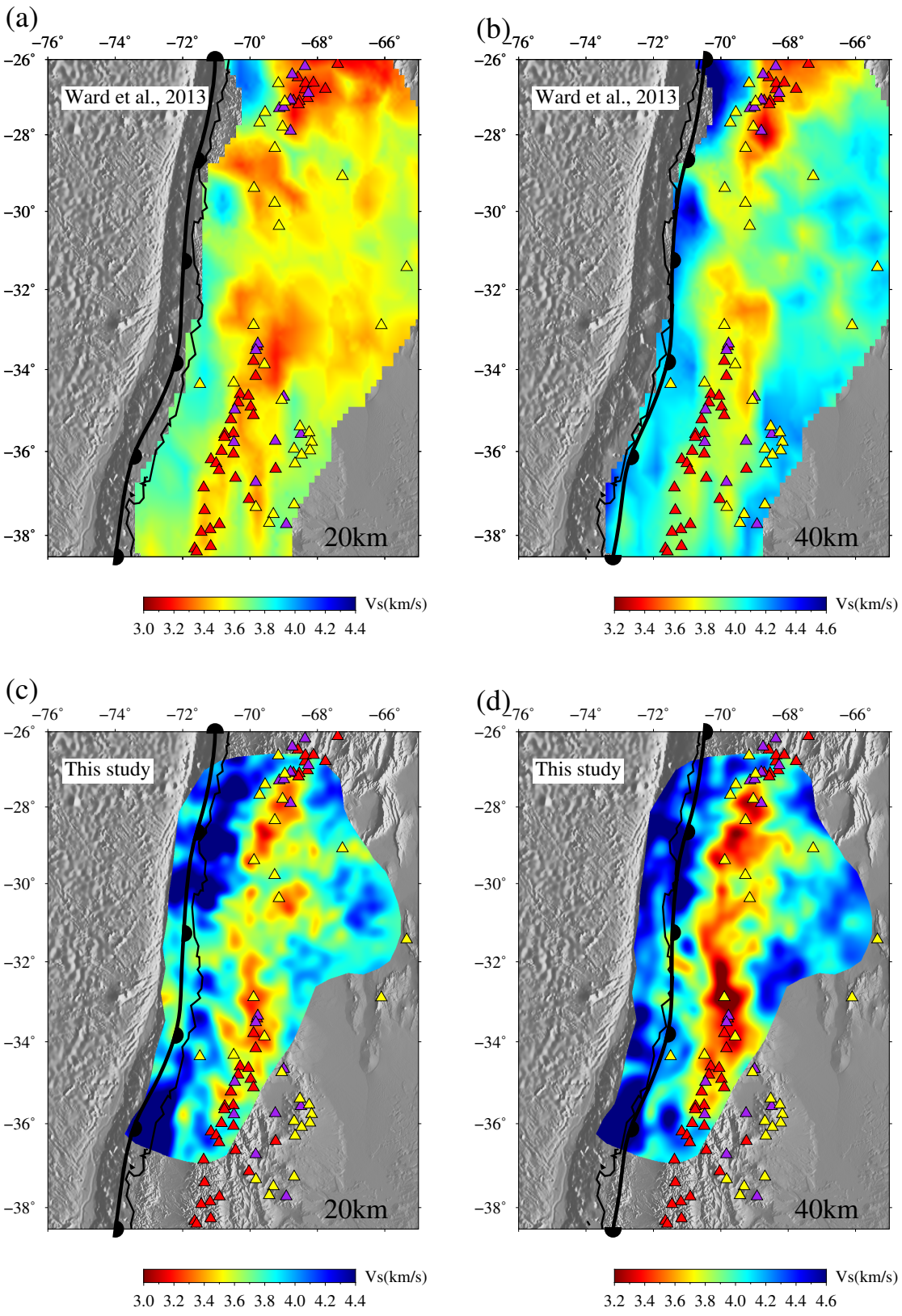

Fig. B.21: Comparison of the crustal structure inferred by the ambient noise tomography model of (Ward et al., 2013) (top) with our model (bottom).

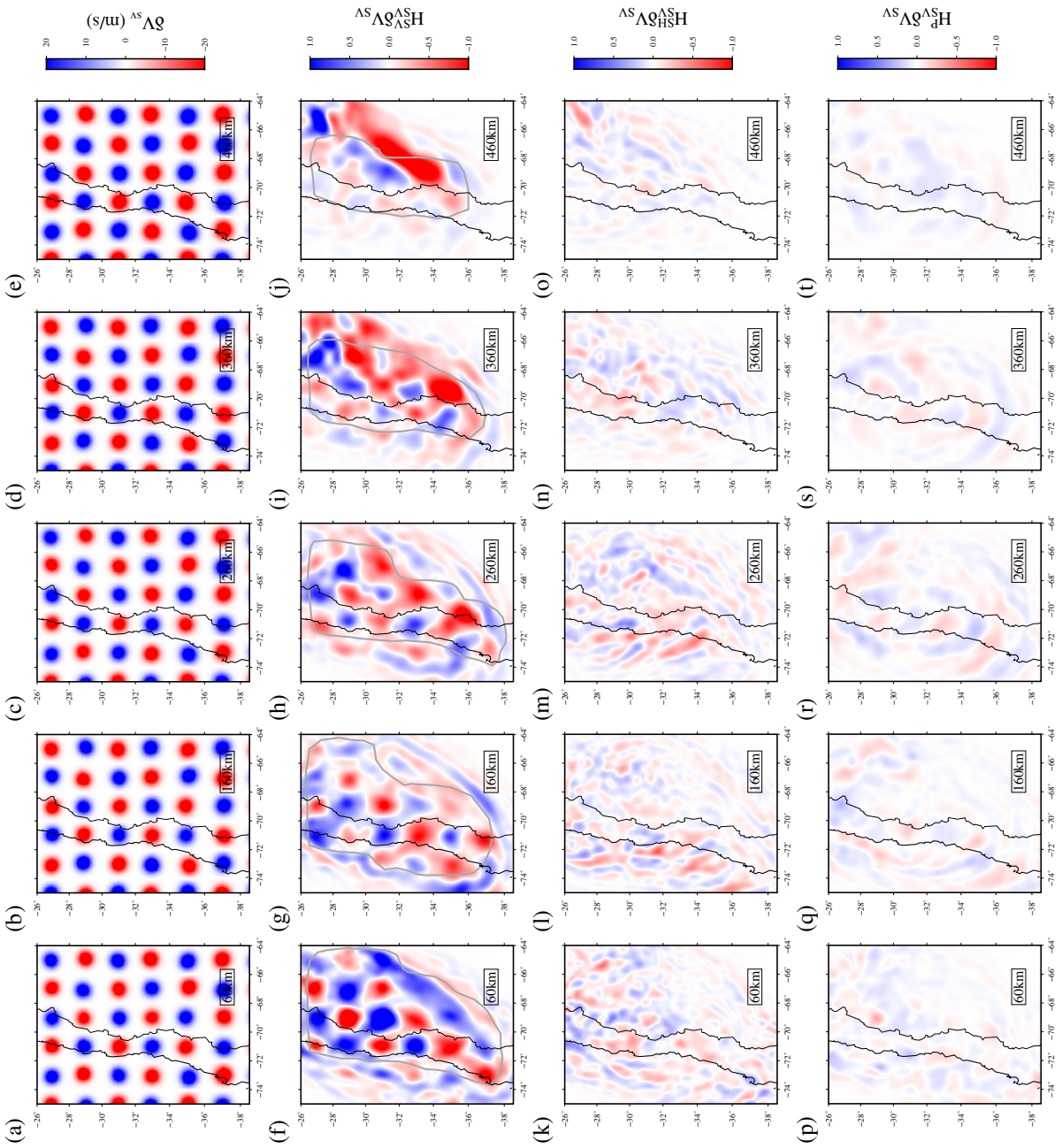

Fig. B.22: Point-spread function test with respect to $\mathbf{V}_{SV}$ perturbations ($\delta\mathbf{V}_{SV}$). (a-e): horizontal slices of input 1% Gaussian $\mathbf{V}_{SV}$ perturbations ($\delta\mathbf{V}_{SV}$) with σ=40 km at 60 km, 160 km, 260 km, 360 km and 460 km depth in the upper mantle; (f-j): point-spread functions $\mathbf{H}^{SV}_{SV}\delta\mathbf{V}_{SV}$ with respect to V_{SV} perturbations ($\delta\mathbf{V}_{SV}$) quantify the resolution for V_{SV}. (k-o): point-spread functions $\mathbf{H}^{SH}_{SV}\delta\mathbf{V}_{SV}$ quantify the cross-talk between V_{SV} and V_{SH}; (p-t) point-spread functions $\mathbf{H}^{P}_{SV}\delta\mathbf{V}_{SV}$ quantify the trade-off between V_{SV} and V_P. Gray thick lines in f-j denote the trust region for $\mathbf{V}_{SV}$ used for masking results plots.

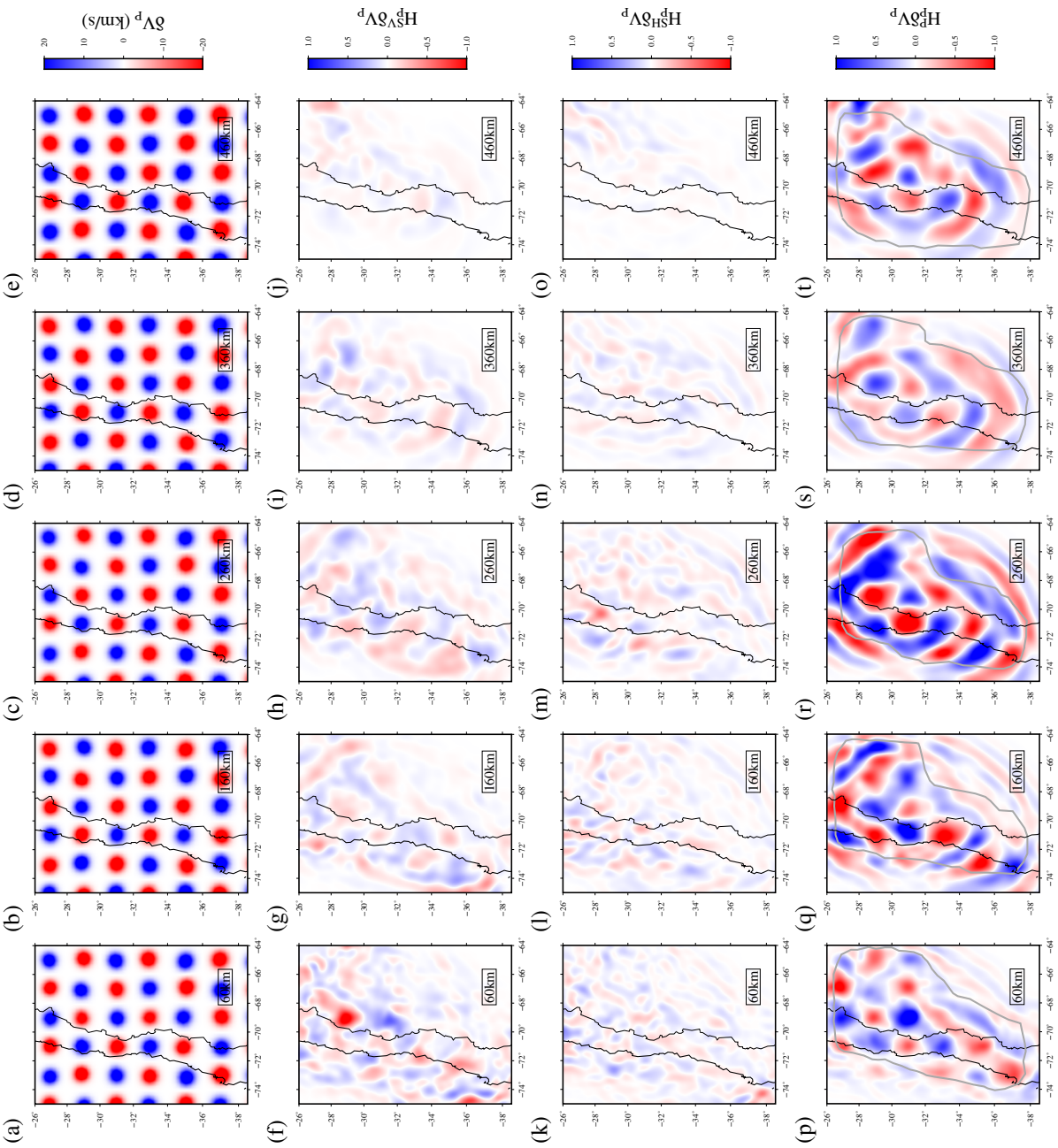

Fig. B.23: Point-spread function test with respect to isotropic $\mathbf{V}_P$ perturbations ($\delta\mathbf{V}_P$). (a-e): horizontal slices of input 1% Gaussian $\mathbf{V}_P$ perturbations ($\delta\mathbf{V}_P$) with σ=40 km at 60 km, 160 km, 260 km, 360 km and 460 km depth in the upper mantle; (f-j): point-spread functions $\mathbf{H}_P^{SV}\delta\mathbf{V}_P$ with respect to isotropic V_P perturbations ($\delta\mathbf{V}_P$); (k-o): point-spread functions $\mathbf{H}_P^{SH}\delta\mathbf{V}_P$; (p-t) point-spread functions $\mathbf{H}_P^{P}\delta\mathbf{V}_P$; Gray thick lines denote the trust region for $\mathbf{V}_P$.

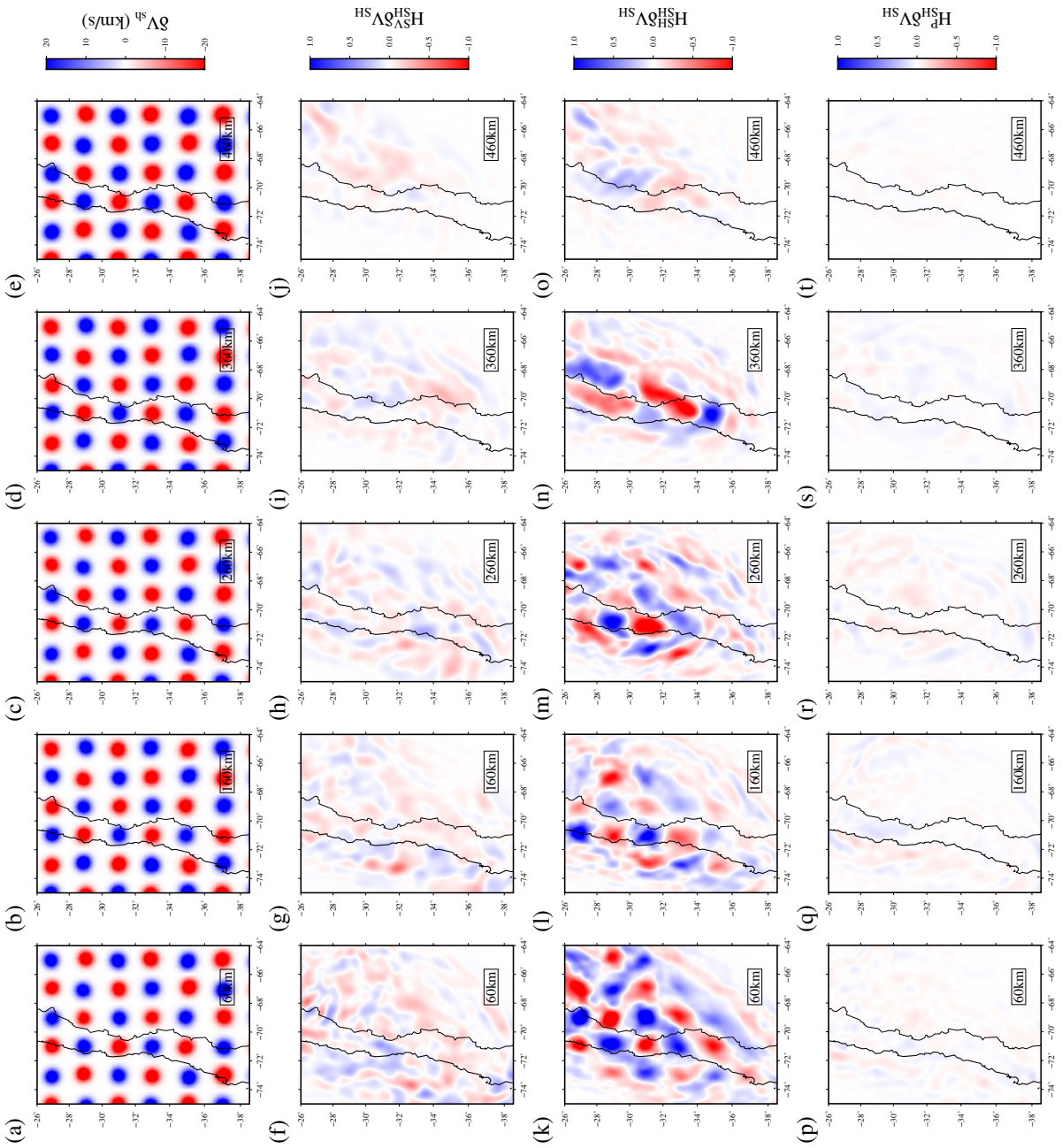

Fig. B.24: Point-spread function test with respect to $\mathbf{V}_{SH}$ perturbations ($\delta\mathbf{V}_{SH}$). (a-e): horizontal slices of input 1% Gaussian $\mathbf{V}_{SH}$ perturbations ($\delta\mathbf{V}_{SH}$) with σ=40 km at 60 km, 160 km, 260 km, 360 km and 460 km depth in the upper mantle; (f-j): point-spread functions $\mathbf{H}^{SV}_{SH}\delta\mathbf{V}_{SH}$ with respect to V_{SH} perturbations ($\delta\mathbf{V}_{SH}$); (k-o): point-spread functions $\mathbf{H}^{SH}_{SH}\delta\mathbf{V}_{SH}$; (p-t) point-spread functions $\mathbf{H}^{P}_{SH}\delta\mathbf{V}_{SH}$.

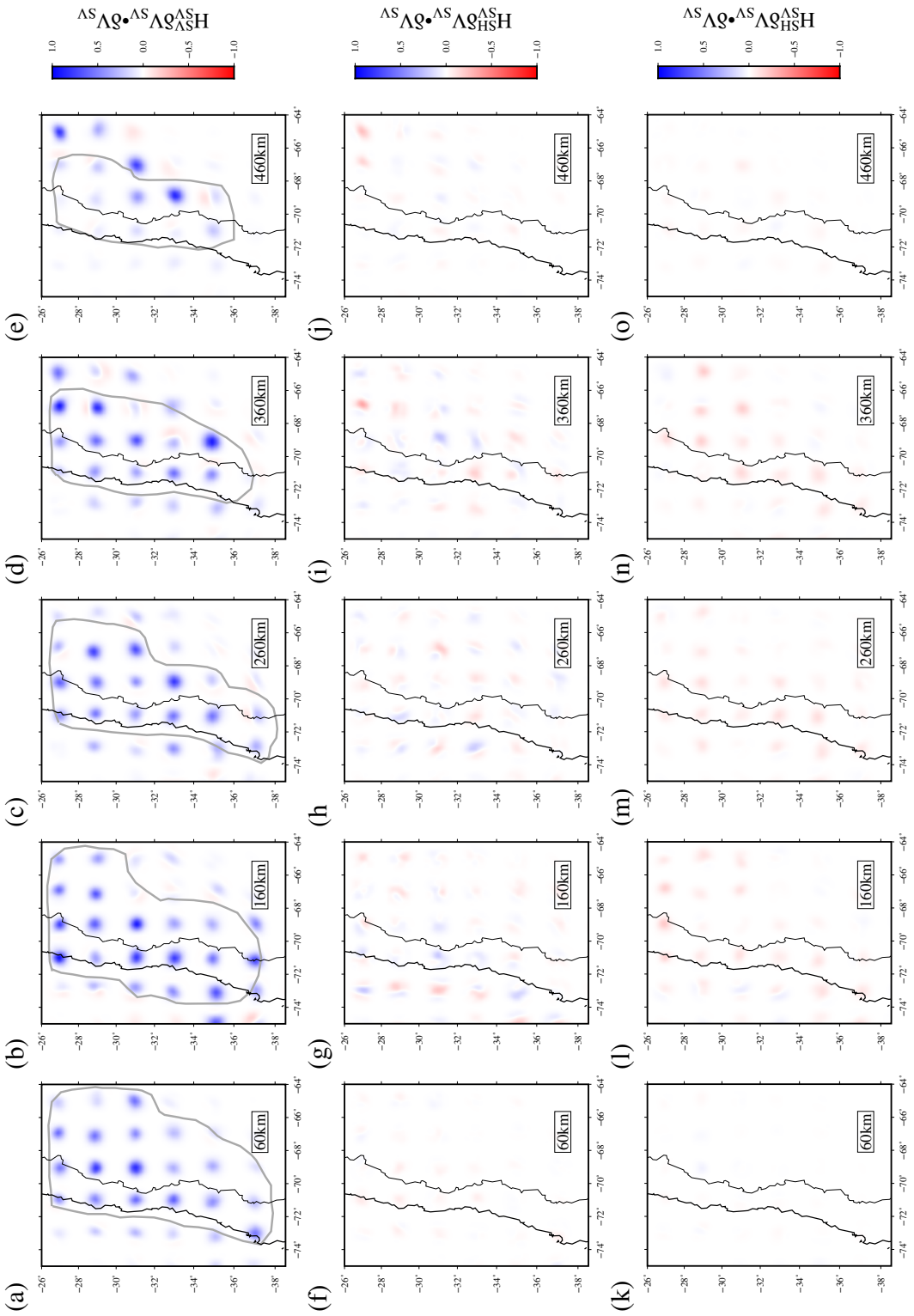

Fig. B.25: Normalised product between the $\delta\mathbf{V}_{SV}$ and point-spread functions $\mathbf{H}_{SV}^{SV}\delta\mathbf{V}_{SV}$ (a-e), $\mathbf{H}_{SV}^{P}\delta\mathbf{V}_{SV}$ (f-j) and $\mathbf{H}_{SV}^{SH}\delta\mathbf{V}_{SV}$ (k-o). All the results are normalised by the product of the maximum of $\delta\mathbf{V}_{SV}$ and the maximum of $\mathbf{H}_{SV}^{SV}\delta\mathbf{V}_{SV}$ for every depth level. The best resolution is indicated by blue dots of uniform amplitude for the same anomaly type (a-e); poor resolution by uneven recovery or red zones indicates failure to recover the basic anomalies. For perfect resolution the plots in f-o would be uniformly white; in fact minor cross-talk of parameters is observed. Note that this test focuses attention on recovery of correct anomaly polarities in the anomaly centres, giving a clearer picture in this regard than the raw checkerboard point spread recovery results, but that the importance of smearing effects is not visible. Both visualisations are therefore best considered together.

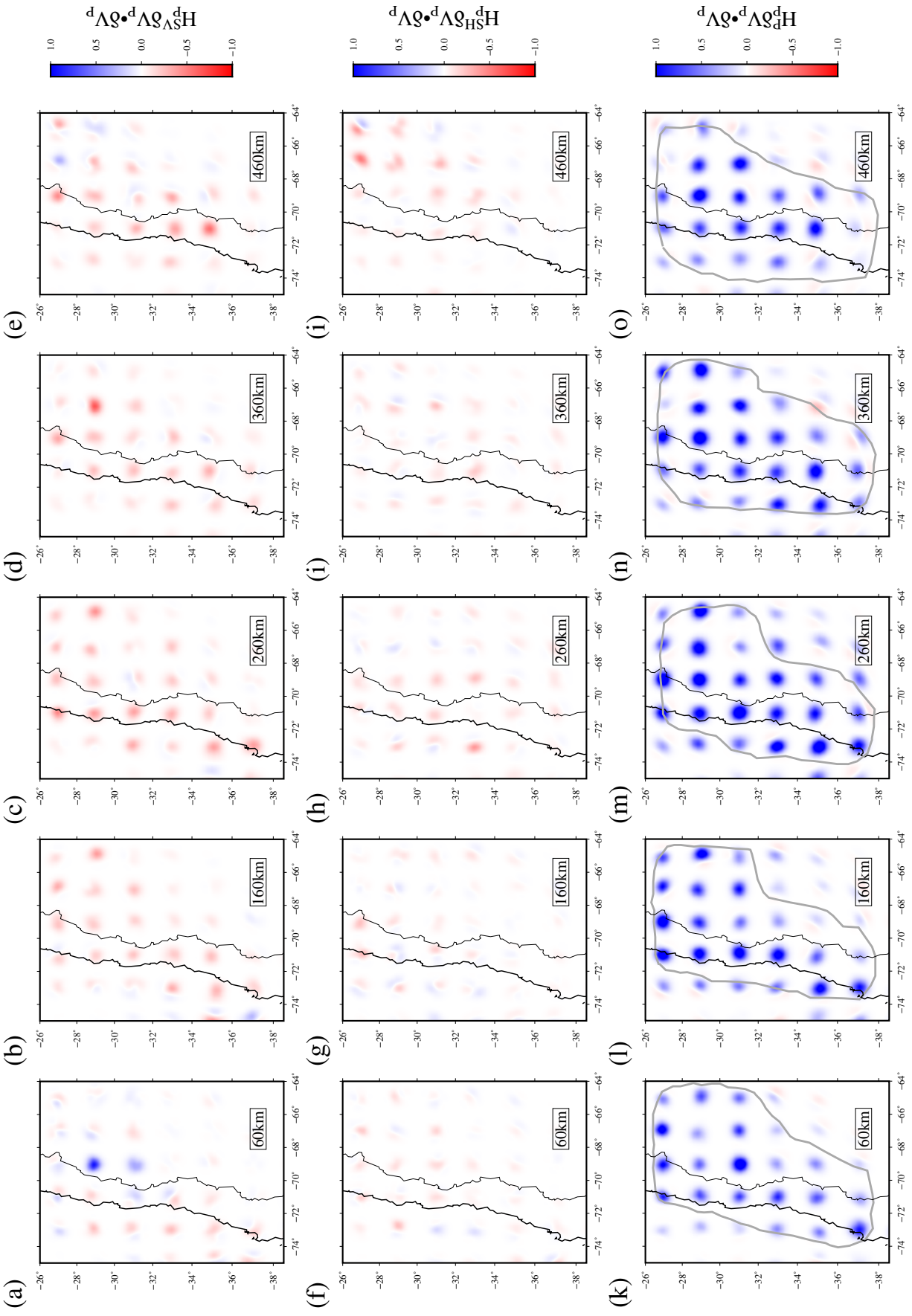

Fig. B.26: Normalised product between the $\delta\mathbf{V}_P$ and point-spread functions $\mathbf{H}^P_{SV}\delta\mathbf{V}_P$ (a-c), $\mathbf{H}^{SH}_P\delta\mathbf{V}_P$ (d-f) and $\mathbf{H}^P_P\delta\mathbf{V}_P$ (g-i). All the results are normalised by the product of the maximum of $\delta\mathbf{V}_P$ and the maximum of $\mathbf{H}^P_P\delta\mathbf{V}_P$ for every depth level.

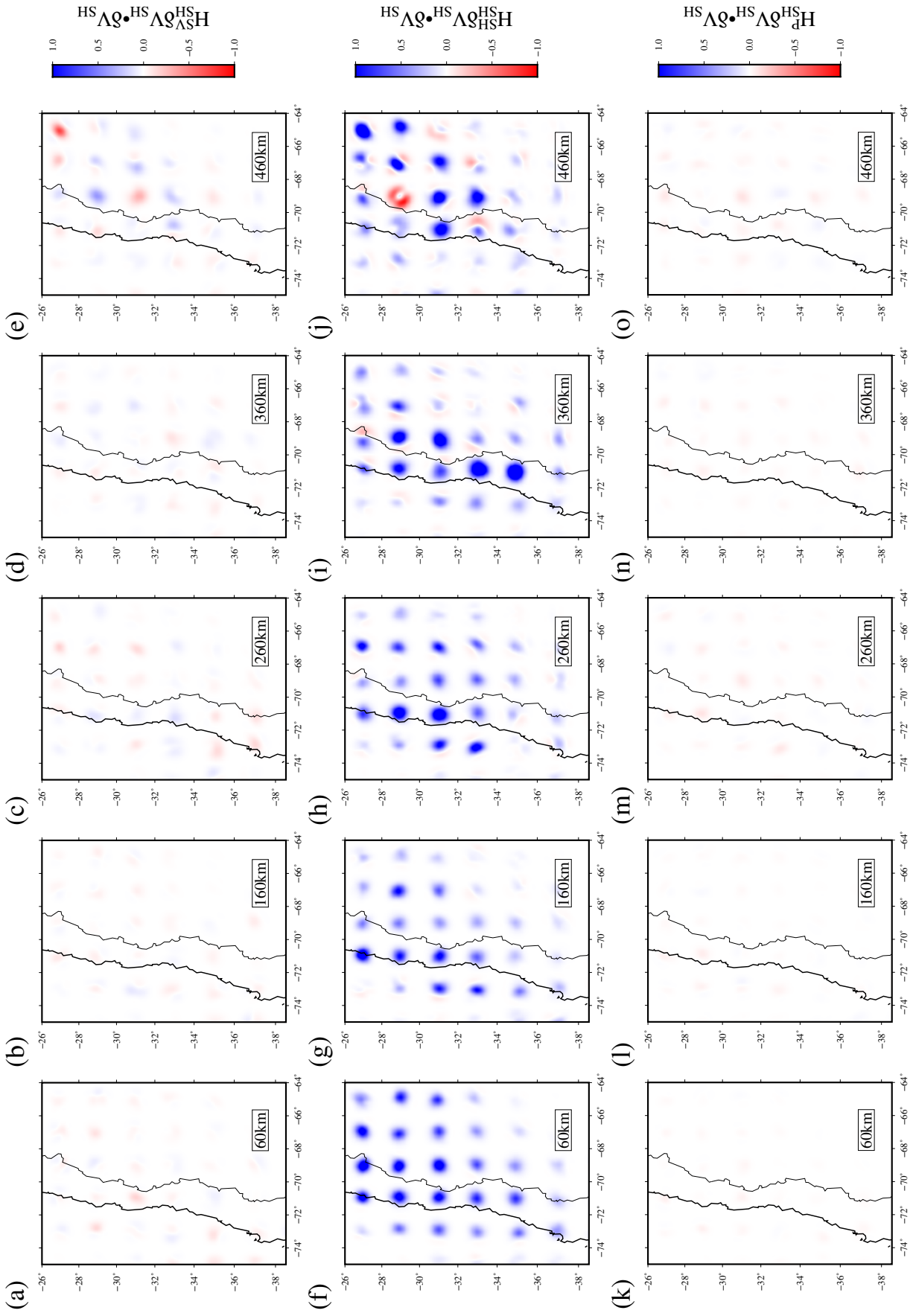

Fig. B.27: Normalised product between the $\delta \mathbf{V}_{SH}$ and point-spread functions $\mathbf{H}_{SV}^{SH}\delta \mathbf{V}_{SH}$ (a-c), $\mathbf{H}_{SH}^{SH}\delta \mathbf{V}_{SH}$ (d-f) and $\mathbf{H}_{P}^{SH}\delta \mathbf{V}_{SH}$ (g-i). All the results are normalised by the product of the maximum of $\delta \mathbf{V}_{SH}$ and the maximum of $\mathbf{H}_{SH}^{SH}\delta \mathbf{V}_{SH}$ for every depth level.

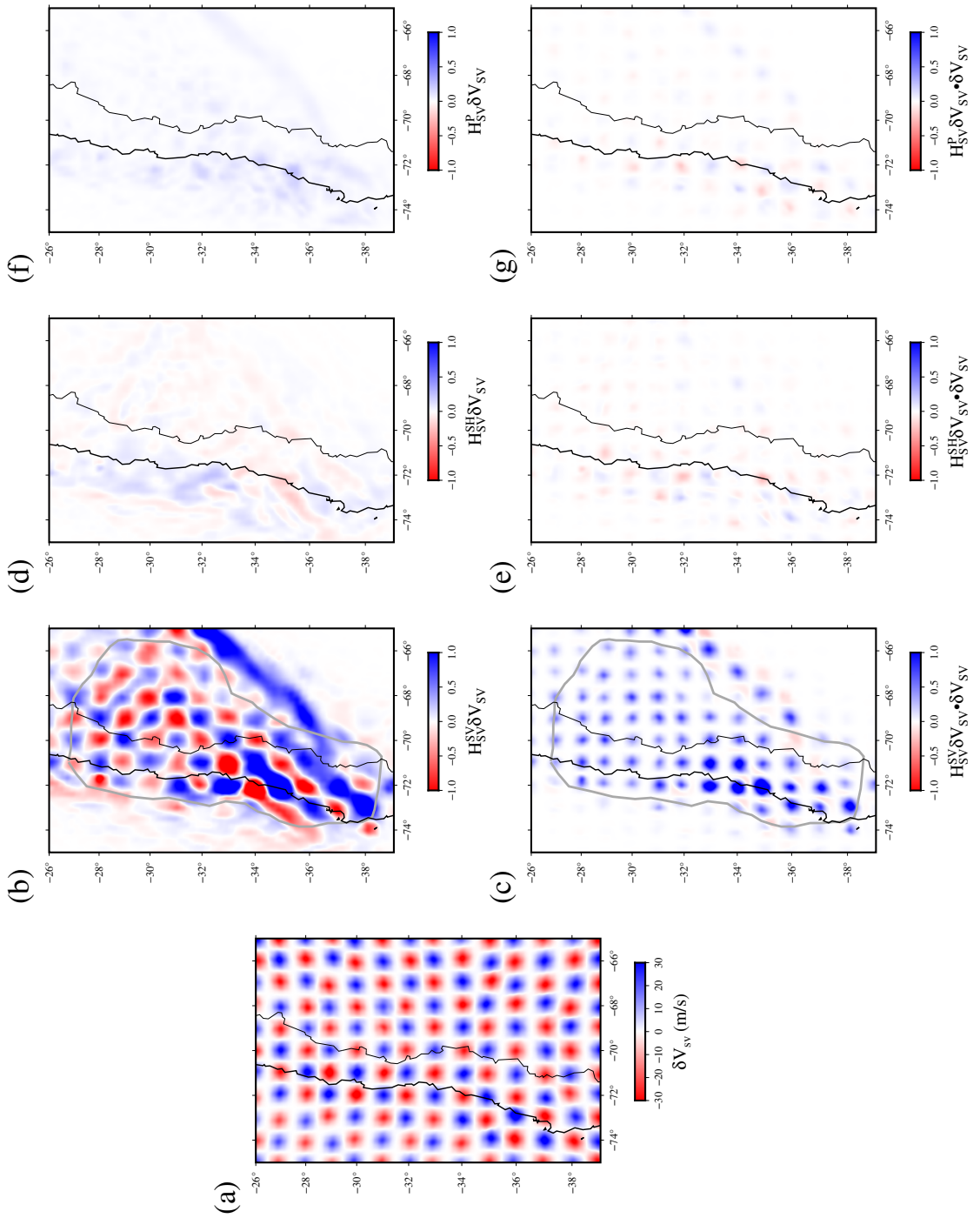

Fig. B.28: (a) Horizontal slice of input 1% Gaussian $\mathbf{V}_{SV}$ perturbations ($\delta\mathbf{V}_{SV}$) with σ=25 km at 20 km depth in the crust; (b), (d), (f) point-spread functions $\mathbf{H}^{SV}_{SV}\delta\mathbf{V}_{SV}$, $\mathbf{H}^{SH}_{SV}\delta\mathbf{V}_{SV}$, $\mathbf{H}^{P}_{SV}\delta\mathbf{V}_{SV}$ with respect to V_{SV} perturbations ($\delta\mathbf{V}_{SV}$), respectively. (c), (e), (g) Normalised product between the $\delta\mathbf{V}_{SV}$ and point-spread functions $\mathbf{H}^{SV}_{SV}\delta\mathbf{V}_{SV}$, $\mathbf{H}^{SH}_{SV}\delta\mathbf{V}_{SV}$, $\mathbf{H}^{P}_{SV}\delta\mathbf{V}_{SV}$, respectively. All the products are normalised by the product of the maximum of $\delta\mathbf{V}_{SV}$ and the maximum of $\mathbf{H}^{SV}_{SV}\delta\mathbf{V}_{SV}$

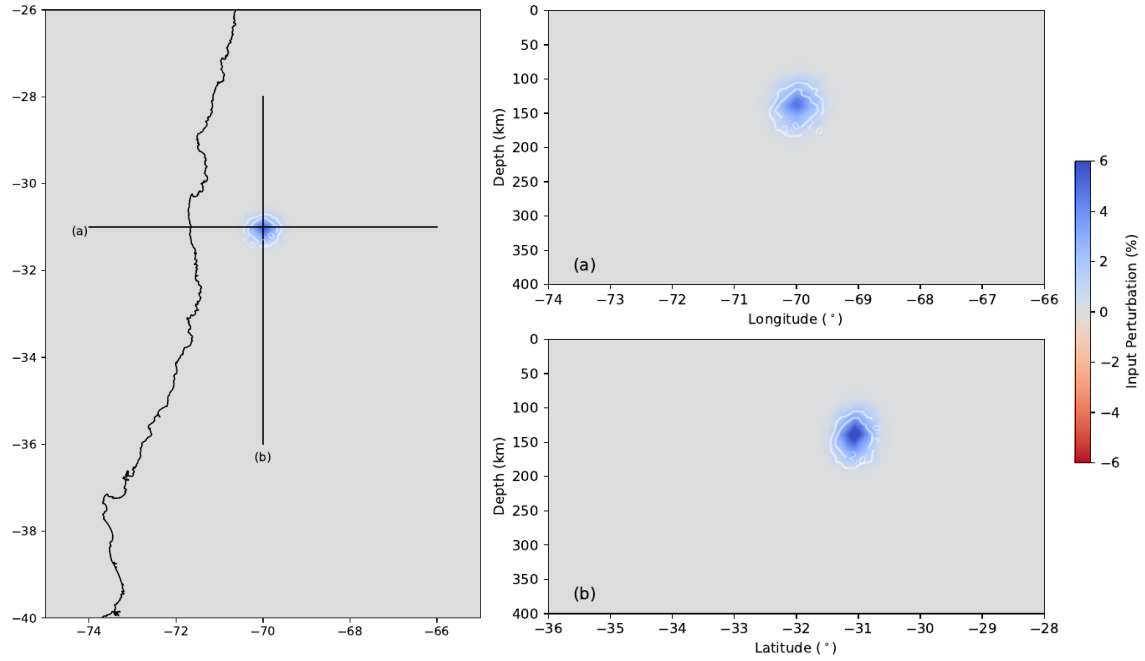

Fig. B.29: Left panel: horizontal slices of input 6% Gaussian $\mathbf{V}_{SV}$ perturbations ($\delta\mathbf{V}_{SV}$) with σ=20 km at 140 km; right two panels: vertical profiles displaying velocity perturbations along profile (a) and (b) defined in left.

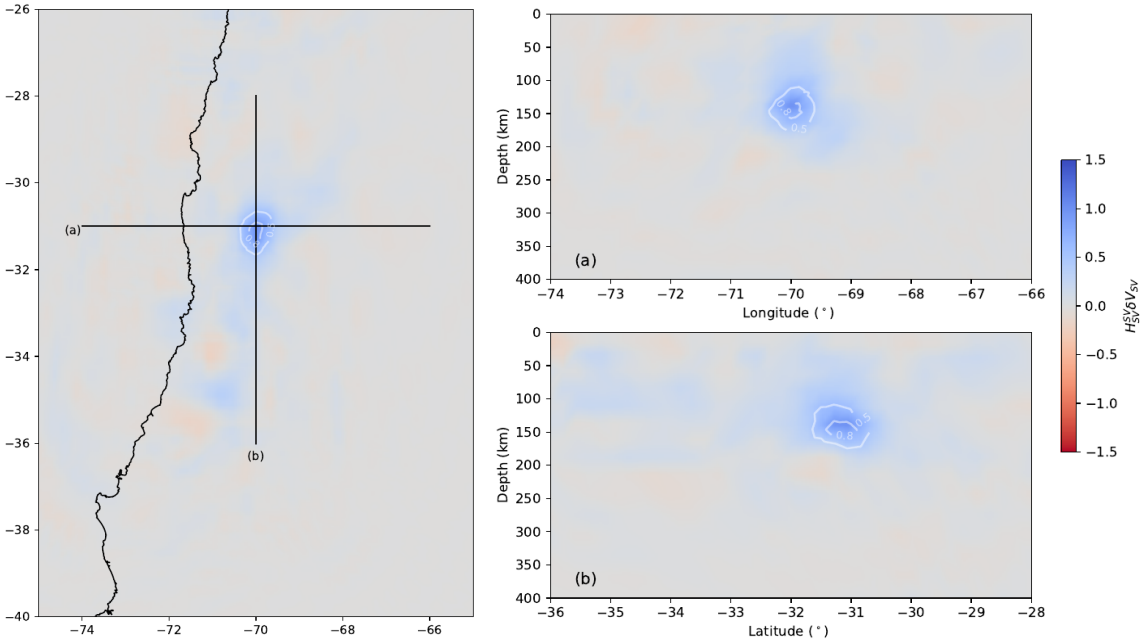

Fig. B.30: Point-spread functions $\mathbf{H}^{SV}_{SV}\delta\mathbf{V}_{SV}$ with respect to V_{SV} perturbations ($\delta\mathbf{V}_{SV}$) defined in Figure B.29 quantify the resolution for V_{SV}. Left: horizontal slices; Right: Vertical profiles.

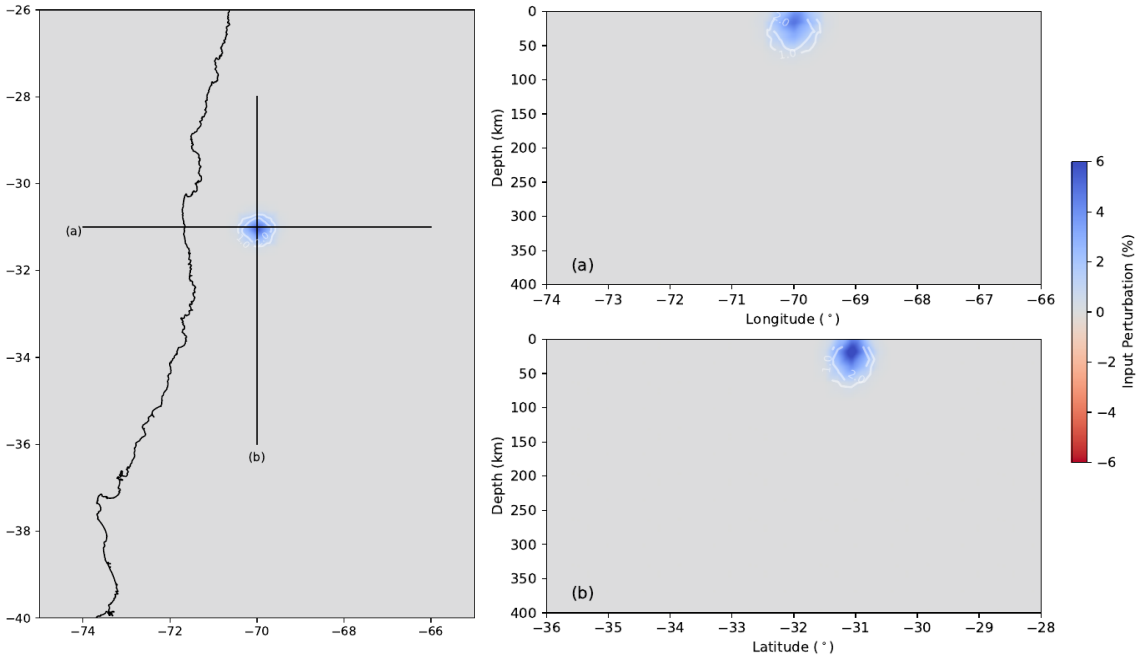

Fig. B.31: Left panel: horizontal slices of input 6% Gaussian $\mathbf{V}_{SV}$ perturbations ($\delta\mathbf{V}_{SV}$) with σ=20 km at 20 km; right two panels: vertical profiles displaying velocity perturbations along profile (a) and (b) defined in left.

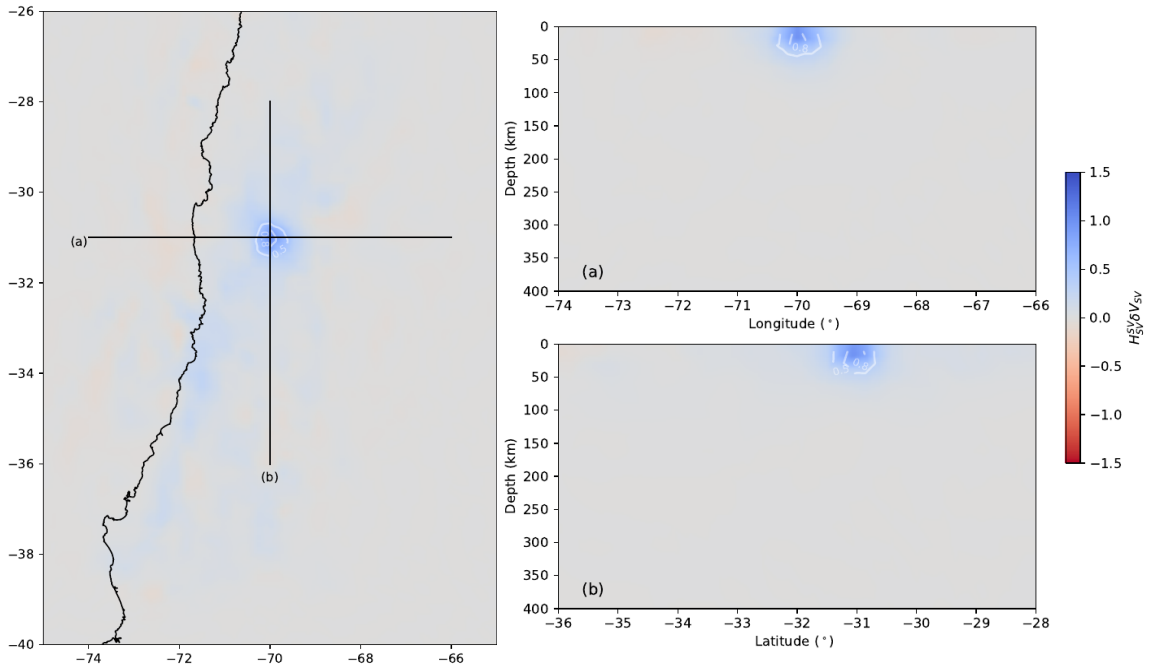

Fig. B.32: Point-spread functions $\mathbf{H}_{SV}^{SV}\delta\mathbf{V}_{SV}$ with respect to V_{SV} perturbations ($\delta\mathbf{V}_{SV}$) defined in Figure B.31 quantify the resolution for V_{SV}. Left: horizontal slices; Right: Vertical profiles.

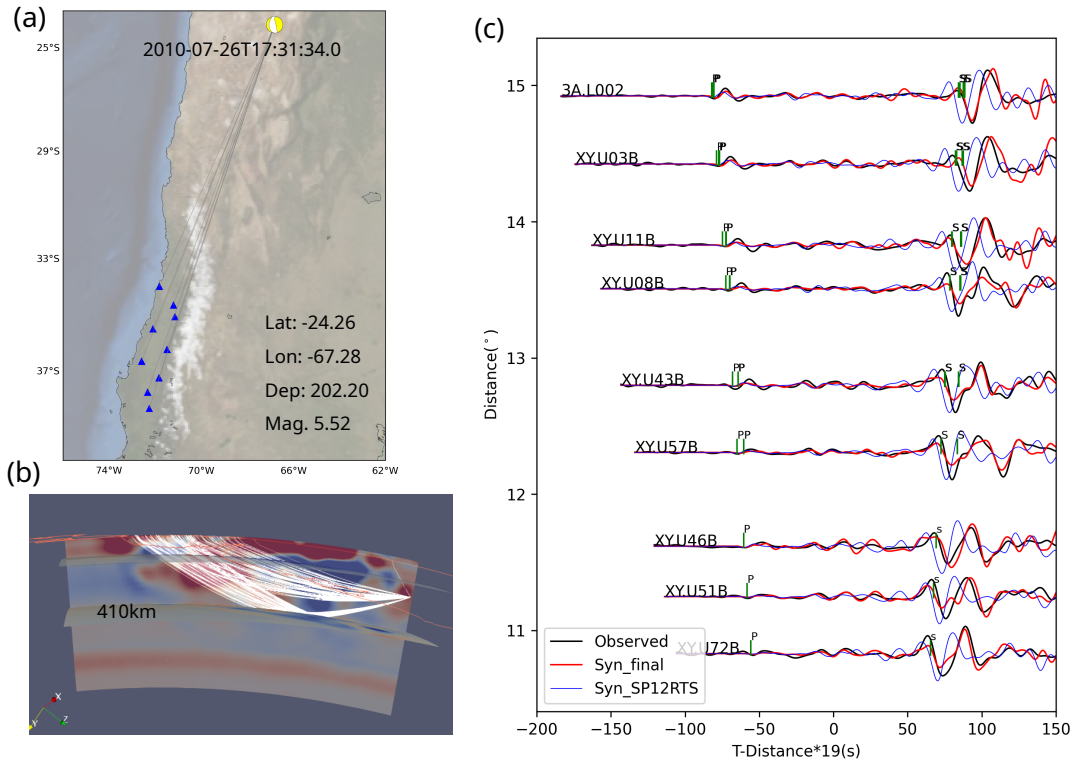

Fig. B.33: Z-component waveform comparison between the initial and final model. (a) Map for example event (centroid depth 202 km) and stations. (b) 3D ray-path illustration. (c) Observed (black lines) and synthetic waveforms (blue: initial model - SP12RTS; red: final model) for the indicated stations. Ray-path and arrival times are predicted for IASP91 using Taup toolkit in Obspy.

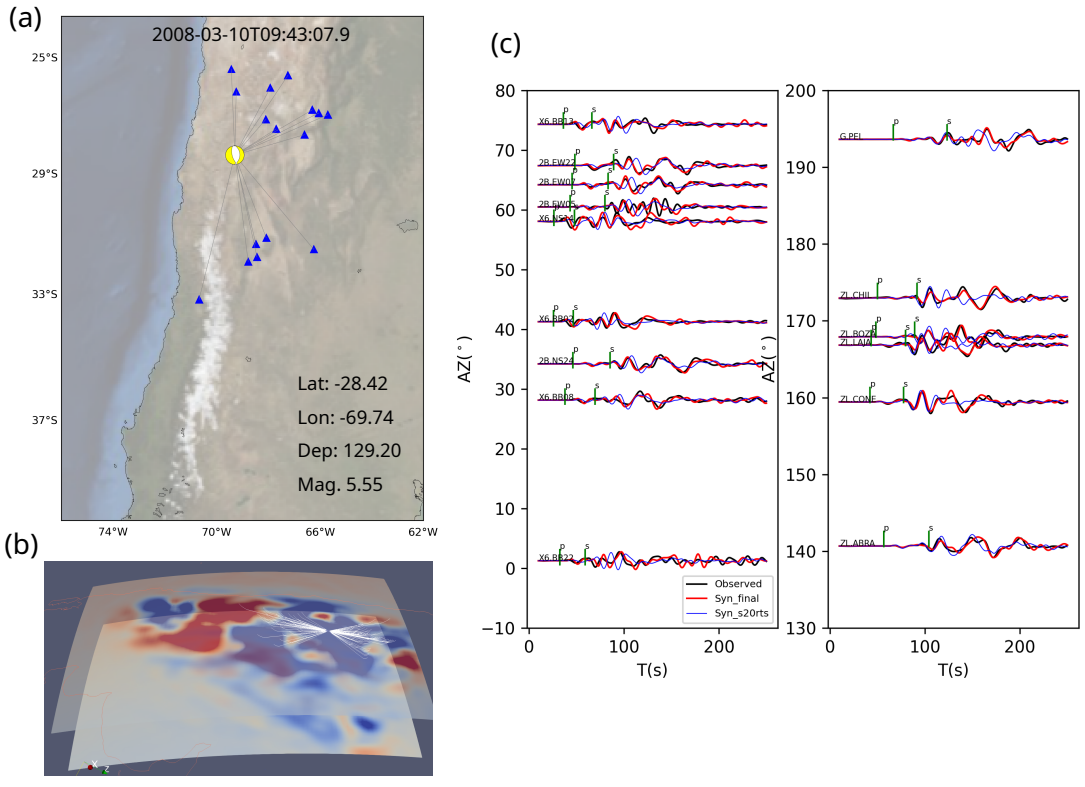

Fig. B.34: Z component waveform fits for inital nd final models for example event at centroid depth 129 km. For other figure elements see Fig. B.33.

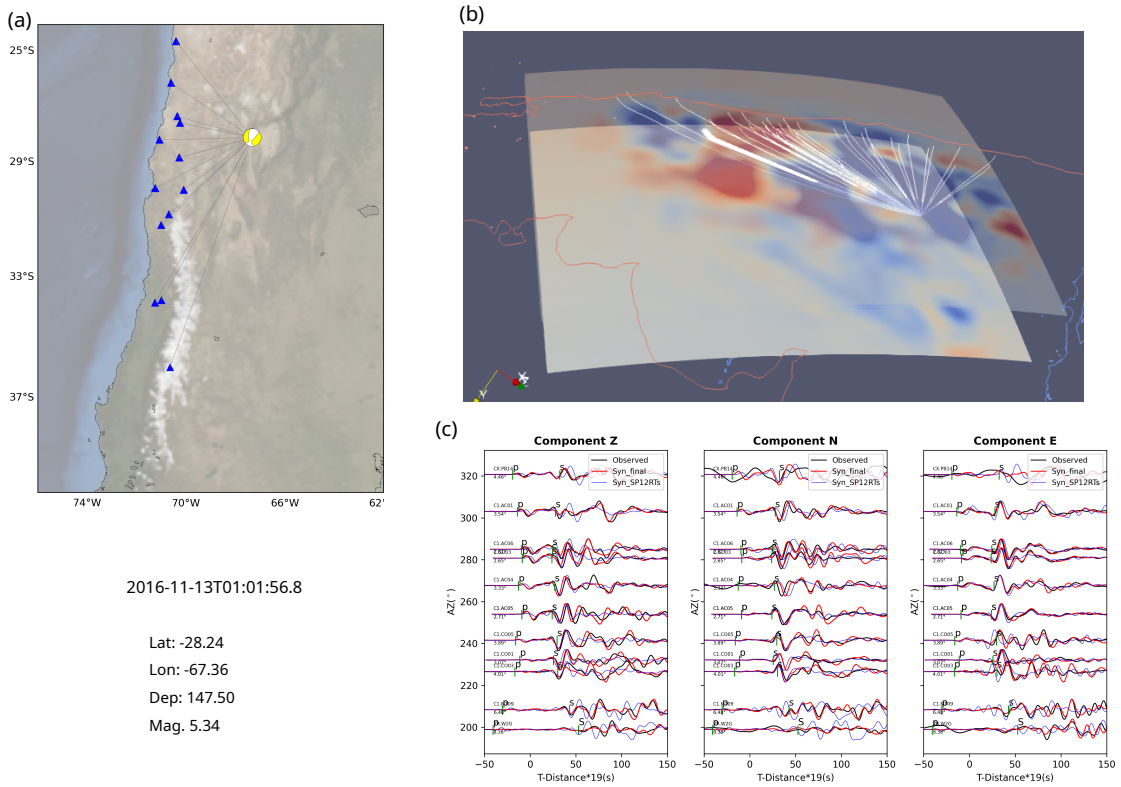

Fig. B.35: Three-component waveform comparison between the initial and final fits. (a) example event (centroid depth 148 km) and stations. (b) 3D ray-path illustration. (c) Observed (black lines) and synthetic waveforms (blue: initial model - SP12RTS; red: final model) for the indicated stations. Ray-path and arrival times are predicted for IASP91 using Taup toolkit in Obspy.

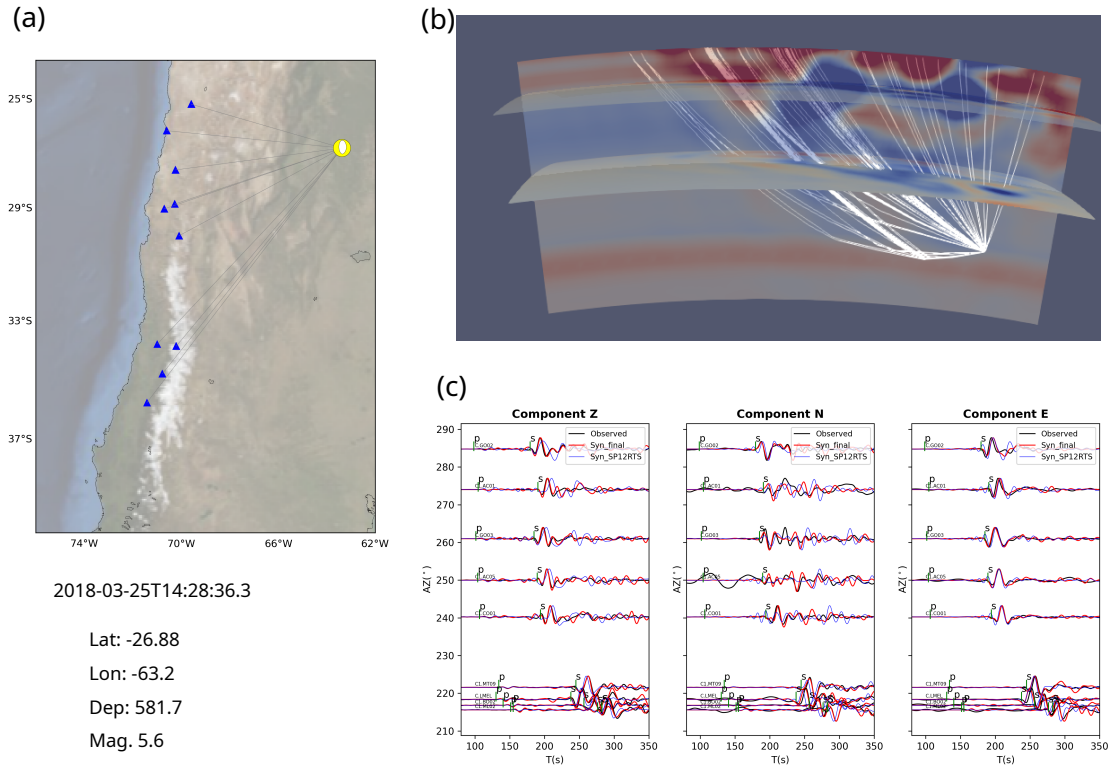

Fig. B.36: Three component waveform comparison between initial and final fits for event at centroid depth 582 km. For other figure elements see Fig. B.35.

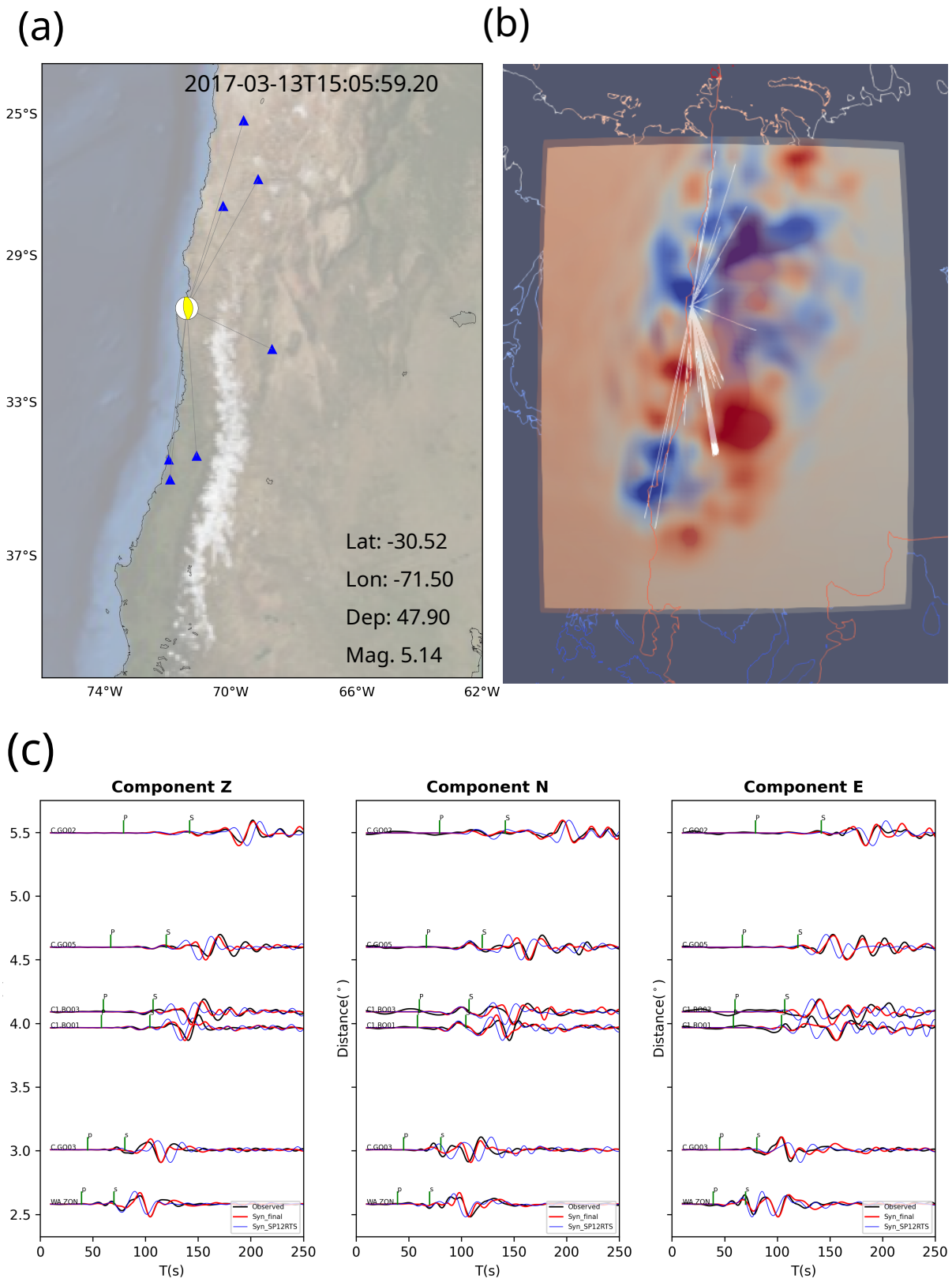

Fig. B.37: Three component waveform comparison between initial and final fits for event at centroid depth 48 km. For other figure elements see Fig. B.35.

Acknowledgements

This thesis arose from the funding from China Scholarship Council under the Freie Universität Berlin - China Scholarship Council program. I wrote this thesis while I was working at GFZ Potsdam and enrolled at the Freie Universität Berlin. Time-Dependent Seismology of Short Term Scientific Missions also supported me for a one-month visit to ETH, Zürich, Switzerland.

It is impossible to finish my thesis and my research project without significant supports from many people.

First of all, I would like to express my deepest appreciation to my principal supervisor Prof. Dr. Frederik Tilmann who is providing me encouragement and extreme patience towards my research, especially during my earlier failures of research topics. I am always inspired by his innovative scientific ideas and ambitious thoughts. Apart from his professional guidance, he also kindly provided me with amazing opportunities for international collaborations with other groups. His critical feedbacks and instructions improved and even reforged my manuscripts deeply which he corrected carefully with more patience than myself. He also provides a very harmonic working environment with his endless supports and persistent motivations. His strict but optimistic attitudes towards science and many other aspects always deserve my learning from which I believe he set a standard of excellence.

I thank Prof. Andreas Fichtner at ETH, Zürich. During my visits and many visual meetings with emails, his inspirations and knowledge about inverse theory and FWI always granted me enthusiasm to continue my practical applications of FWI to the real Earth science. His book 'Full Seismic Waveform Modelling and Inversion' is always a classic masterpiece for the FWI domain. Meanwhile, I obtained many supports from the members of 'Seismology and Wave Physics' in ETH, Zürich, including Dirk-Philip van Herwaarden, Sölvi Thrastarson, Michael Afanasiev, Lion Krischer and Mondaic AG for providing Salvus, based on which my Ph.D. and production work could move on and inspired new research ideas for my future research.

I am also grateful for my second supervisor Dr. Xiaohui Yuan. It is really helpful to discuss Earth science problems with him. I also thank Xiaohui and his kind wife Dr. Xueqing Li for preparing Chinese dinners hosting for us. I thank Ben Heit for his insight into the evolution of the Central Andes and his many explanations about the deformation history, which benefits my first long manuscript significantly. I also want to express my thanks to our lovely secretary Liane, who helped me a lot in daily office time.

I also want to thank my working group at GFZ, the former and current colleagues bestow me the enthusiasm for science and daily life, including Alexandra Mauerberger, Zhouchuan Huang, Wei Li, Felipe Orlando Vera Sanhueza, Tuo Zhang, Stefan Mroczek, Jannes Münchmeyer, Javier Quinteros, Felix Schneider, Kuan-Yu Ke, Joachim Saul with his cute boys, Peter Evans, Nasim Karam Zadeh, Peter Makus, Laura Hillmann, Yiming Bai, Jing Chen, Yanling Liang, Laura Hillmann, Luc Illien, Christoph Sens-Schönfelder with his Friday science chat, Susanne Hemmleb, Angelo Strollo and Michael Pons from section 2.5. Further, I am also grateful to Frederik Tilmann, Felix Schneider, Ben Heit and Xiaohui Yuan for proofreading different parts of this long thesis. In addition, I also thank Prof. Andreas Rietbrock for hosting me as a Postdoc researcher in the next few years during which I could extend my research.

Finally, I would like to thank my family for their endless support and understanding, especially during the hard times of Corona. Distance and disease will never erode love. Deep love to my parents, my sister

and brother-in-law, my lovely nephew, my grandparents though my grandpa will never see me.

Though the acknowledgment should end here, I want to express my deep love to the excellent natural, scientific and cultural environment in our group, in Potsdam, in Germany and the whole Europe. The fresh air alleviates the symptoms of my rhinitis. Traveling in Europe including Germany, Italy, France, Switzerland, Spain, Hungary, Croatia, etc makes me rejuvenate and also allows me to introspect about how to face lives optimistically.

oh, oh, by the way, I love espresso! Cheers!